OPTICAL FIBRE SENSORS AND THEIR APPLICATIONS IN THE INDUSTRIAL WEIGHING & AEROSPACE INDUSTRIES

STEVEN JOHN GRICE

Doctor of Philosophy

ASTON UNIVERSITY

July 2010

ASTON UNIVERSITY

OPTICAL FIBRE SENSORS AND THEIR APPLICATIONS IN THE INDUSTRIAL WEIGHING & AEROSPACE INDUSTRIES

STEVEN JOHN GRICE
Doctor of Philosophy, July 2010

Abstract

This thesis presents the design, fabrication and testing of novel grating based Optical Fibre Sensor (OFS) systems being interrogated using "off the shelf" interrogation systems, with the eventual development of marketable commercial systems at the forefront of the research.

Both in the industrial weighing and aerospace industries, there has been a drive to investigate the feasibility of using optical fibre sensors being deployed where traditionally their electrical or mechanical counterparts would traditionally have been. Already, in the industrial weighing industry, commercial operators are deploying OFS-based Weigh-In-Motion (WIM) systems. Likewise, in the aerospace industry, OFS have been deployed to monitor such parameters as load history, impact detection, structural damage, overload detection, centre of gravity and the determination of blade shape.

Based on the intrinsic properties of fibre Bragg gratings (FBGs) and Long Period Fibre Gratings (LPFGs), a number of novel OFS-based systems have been realised. Experimental work has shown that in the case of static industrial weighing, FBGs can be integrated with current commercial products and used to detect applied loads. The work has also shown that embedding FBGs in e-glass, to form a sensing patch, can result in said patches being bonded to rail track, forming the basis of an FBG-based WIM system. The results obtained have been sufficiently encouraging to the industrial partner that this work will be progressed beyond the scope of the work presented in this thesis.

Likewise, and to the best of the author's knowledge, a novel Bragg grating based systems for aircraft fuel parameter sensing has been presented. FBG-based pressure sensors have been shown to demonstrate good sensitivity, linearity and repeatability, whilst LPFG-based systems have demonstrated a far greater sensitivity when compared to FBGs, as well the advantage of being potentially able to detect causes of fuel adulteration based on their sensitivity to refractive index (RI). In the case of the LPFG-based system, considerable work remains to be done on the mechanical strengthening to improve its survivability in a live aircraft fuel tank environment. The FBG system has already been developed to an aerospace compliant prototype and is due to be tested at the fuel testing facility based at Airbus, Filton, UK.

It is envisaged by the author that in both application areas, continued research in this area will lead to the eventual development of marketable commercial products.

Key words: Optical fibre sensors, weighing, fuel level sensing

Dad.

Acknowledgements

I would like to thank the following for their continuing advice, support, encouragement and most important of all, patience, during my PhD. All of which kept me sane, especially when experiments didn't quite go to plan.

First and foremost I would like to express my sincere thanks and gratitude to my primary academic supervisor, Kate Sugden. I'd particularly like to thank Kate for her understanding during the early stages of my studies when I found myself in difficult circumstances due to the sudden death of my father. Without her support and understanding, this PhD would simply not have been possible.

I would also like to thank my secondary supervisors, David Webb, John O'Connell and Mike Ford for their input. Huge thanks also go to Wei Zhang and Peter Foote for their advice, support and guidance, especially regarding the experimental work.

I'd like to extend a special thanks to Bert Biggs for all his help with the day-to-day running of the departmental laboratories and equipment. My thanks also go to Helen Yard and Yuen Chu for their administrative support.

Acknowledgment must also go to the head of the Photonics Research Group, Ian Bennion.

My thanks to the Engineering and Physical Science Research Council and my PhD CASE sponsor, Avery Weigh-Tronix, for funding this research project.

A big thanks also goes to my fellow PhD Students who I have shared my time with at Aston – and great bunch of guys and gals!

My thanks also go to my Mom for her support and, well, just putting up with me! Besides, she'd kill me if I didn't give her a mention.

Lastly, and not withstanding the support from all mentioned above, the person I would like to thank most is my partner, Kelly, a.k.a. "the Missus". She has been a constant source of incalculable support and encouragement throughout my studies, and for that I can't thank her enough.

Table of Contents

Table of figures

Chapter 1:

Chapter 2:

Chapter 3:

Chapter 4:

Chapter 5:

Table of tables

Chapter 1:

Chapter 2:

Chapter 3:

Chapter 4:

Chapter 5:

Table of abbreviations

CW	Continuous Wave
FBG	Fibre Bragg grating
FSI	Fibre Sensor Interrogator
FWHM	Full-Width at Half-Maximum
GODC	Germanium Oxygen-Deficient Centres
LED	Light Emitting Diode
LP	Loading Point
LPFG	Long Period Fibre Grating
OFS	Optical Fibre Sensor
OSA	Optical Spectrum Analyzer
OTDR	Optical Time Domain Reflectometer
PPS	Polyphenylene sulphide
RI	Refractive Index
SG	Strain Gauge
SMF	Single Mode Fibre
SOA	Semiconductor Optical Amplifier
TDM	Time Division Multiplexing
TFBG	Tilted Fibre Bragg Grating
TiO_2	Titanium Oxide
UV	Ultraviolet
WDM	Wavelength Division Multiplexing
WIM	Weigh-In-Motion

1 Thesis introduction

1.1 The development of fibre Bragg grating based optical fibre sensors

Thanks to the boom in telecommunications research and commercialisation, optical fibre sensors (OFS) have, over the last 20 years or so, received an enormous amount of interest due to their sensing capabilities. When compared with electrical or electro-mechanical sensors and transducers, OFS flaunt many advantages, as described by Kersey *et al* [1] and Rao *et al* [2]. These advantages are:

- Immunity to electromagnetic interference
- Light and compact
- Remote interrogation
- Ability to operate on harsh and explosive environments
- Multiplexing capabilities

Over the years, OFS have been deployed in the development of numerous optical sensing systems for a wide range of industrial applications. For a significant number of these systems, the sensing device is a fibre Bragg grating (FBG), which acts as a mirror-like reflector, which in-turn acts as an optical filter at specific wavelength. The OFS converts physical measurands, such as strain and temperature, into a corresponding change in one or more optical characteristics. These include:

- Wavelength
- Amplitude
- Intensity
- Polarisation

Substantial progress has been made in implementing FBG sensors in applications involving either the measurement of strain and temperature, or the simultaneous measurements of both measurands. FBG sensors are usually bonded to, or embedded in, the structures, effectively making them “Smart” structures [2][3].

More recent developments regarding FBG-based OFS have been their implementation as structural health monitors [1], predominantly in the aerospace and civil engineering industries. The FBG is capable of providing a real-time profile of the measurand, to the extent that incorporating an array of FBG sensors can, in effect, map parameters such as stress and damage over time.

1.2 Fibre Bragg gratings

First demonstrated by Hill *et al* in 1978 [4], FBGs have been extensively researched and industrially utilised. In its most basic form, an FBG consists of a periodic modulation of the refractive index (RI) along the fibres' core. FBGs are photo-induced into the core using a variety of techniques, which usually involves exposing a pre-defined length of the fibre to radiation from an ultraviolet (UV) laser. The modulation of the RI within the core occurs due to the photosensitive properties of the core. The magnitude of the RI modulation, Δn, is dependant upon numerous factors including beam intensity, beam wavelength and the properties of the fibre itself. Figure 1.1 is a microscope image of a FBG immersed in oil. The periodic grating structure is clearly visible.

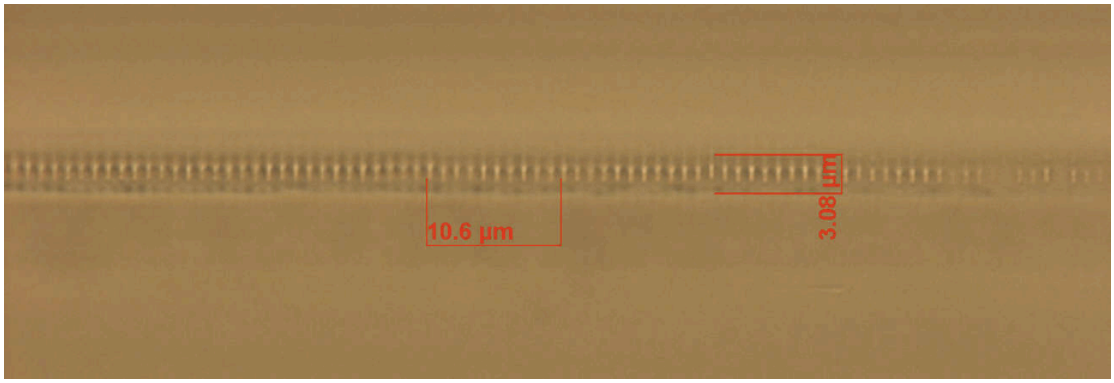

Figure 1.1 Microscope image of an FBG immersed in oil [5]

A FBG reflects light at a specific wavelength if the fibre is illuminated by a broadband light source, which transmits light through the fibre core. When the Bragg condition is satisfied, the reflected light from each grating plane constructively adds. This light is then reflected back along the fibre at a specific wavelength called the Bragg wavelength, λ_B. This Bragg wavelength is dependant on the effective refractive index, n_{eff}, and the grating period, Λ, and can be expressed as follows:

$$\lambda_B = 2n_{eff}\Lambda \qquad \textbf{Equation 1.1}$$

When certain physical measurands vary, it alters the values of the two Bragg wavelength dependant factors (effective refractive index and grating period). A change in either parameter changes the Bragg wavelength at which the light is reflected back. Therefore external measurand values can be inferred by measuring the shift of the reflected Bragg wavelength. Predominantly, the two main measurands FBGs sense are strain and temperature. Any variation in applied strain or ambient temperature will cause the Bragg wavelength to shift.

Table 1.1 gives a comparison between FBG sensors when compared to other fibre-optic sensors for smart structures.

Table 1.1 Advantages of FBG sensors over other fibre-optic sensors, FP: Fabry-Perot Interferometric Sensors, TM: Two Mode Fibre Optic Sensors and PM: Polarimetric Fibre-Optic Sensors [2].

Today, FBG sensors are deployed as transducers in numerous industries sensing measurands such as strain [6], temperature [7], flow rate [8], vibration [9], structural damage [10], pressure [11] and the detection of liquids and gases [12].

FBGs are unfortunately not without their drawbacks. One of the most significant disadvantages is that the de-coupling of measurands is required to obtain true values. An example of this is temperature compensation. Another drawback is that at present the technology is comparatively expensive, making the identification of niche markets and applications essential.

This thesis presents viable grating-based OFS solutions to applications in the industrial weighing and aerospace industries. In some cases, the work has focussed on novel methods

of integrating FBG sensors into current commercial systems. In other cases, completely novel devices have been designed, fabricated and tested.

1.3 Thesis outline

Chapter 2: Optical fibre sensors

Chapter 2 provides the reader with the required theoretical background essential for understanding the experimental work presented in following experimental chapters. The first section of the chapter details all the basic concepts of optical fibre, photosensitivity, FBGs and their fabrication. The sensitivity to physical measurands is then discussed to give the reader an in-depth knowledge of their effects on the FBG, as well as cross-sensitivity issues and compensation techniques. Interrogation techniques are then discussed, heavily focussing on both Wavelength-Division-Multiplexing (WDM) and Time-Division-Multiplexing (TDM) multiplexing techniques and their respective advantages and disadvantages. A brief description of the commercial interrogation systems used in this thesis is given. OFS are then introduced along with their advantages and disadvantages, as well as a brief section on their potential lifespan and reliability. Finally, Long Period Fibre Gratings (LPFGs) are introduced as a foundation to Chapter 5.

Chapter 3: Novel fibre Bragg grating techniques for static and dynamic industrial weighing applications

Chapter 3 serves as the first of three experimental chapters, and is entirely focussed on the industrial weighing application. Based on extensive market research, both static and dynamic weighing applications were identified for research. The static research presented initially is based on a FBG-based cantilever system before continuing on to investigate the feasibility of integrating FBG sensors into one of Avery Weigh-Tronix commercial systems. The dynamic weighing concentrates on rail Weigh-In-Motion (WIM), and used commercially made sensing patches to measure shear strain in rail track incorporating a novel FBG grating configuration.

From this work, Avery Weigh-Tronix are sufficiently convinced that this technology holds significant promise for applications in their current markets as well as new markets.

Some of the practical work was in this chapter was aided by Mike Ford of Avery Weigh-Tronix.

Chapter 4: Fuel level sensing techniques using single and multiple fibre Bragg grating based diaphragm systems

Chapter 4 is the first of two experimental chapters based on the UK Technology Strategy Board funded Integrated Wing collaborative R&T programme. The work is focussed on investigating the feasibility of utilising FBGs as aircraft fuel level sensors, with the eventual aim of replacing current electrical (capacitance) sensors. This chapter focuses on diaphragm-based systems with FBGs bonded to, or embedded in, the diaphragm material.

The first experiments involve a novel gasket-based approach incorporating a single FBG. To begin with, an aluminium gasket and steel diaphragm was used in a series of initial experiments before progressing on to work with aerospace compliant materials including Polyphenylene sulphide (PPS) and Kapton polyimide film. The design and fabrication of the aerospace compliant system was carried out in conjunction with Dr Peter Foote of BAE SYSTEMS.

Finally, a previously unreported level sensing tube concept is then presented, based on multiple sensors positioned at equidistant positions along the tube acting as pressure sensing diaphragms. The results from this series of tests are then presented and discussed.

The UK Technology Strategy Board funded the work presented in chapter.

Chapter 5: Fuel level sensing utilising long period fibre grating based refractive index sensors

Following on Chapter 4, Chapter 5 continues along the fuel level-sensing theme. The chapter presents in detail the experimental results obtained from the practical experiments utilising a 10 cm long uncoated LPFG with a periodicity of 1000 μm.

The advantages of a titanium oxide (TiO_2) coating, including its ability to increase the sensitivity of an LPFG as well as the bacterial repelling properties are then discussed. A 10 cm long / 1000 μm periodicity LPFG was sent to Dr Reeta Viitala of the Turku Biomaterials Centre, University of Turku, Finland, who coated the LPFG with a TiO_2 sol-gel coating. The experimental results are then presented and discussed.

The chapter then presents a novel concept of detecting free-water in fuel based on observing the minimum transmission value of two attenuation peaks for a specific mode coupling.

Finally, Optiwave IFO_Grating simulations are presented and discussed in section 5.12.

Some of the practical work was in this chapter was aided by Dr Wei Zhang of the Photonics Research Group, and again the work was funded by the UK Technology Strategy Board.

Chapter 6: Thesis conclusions

Chapter 6 provides a retrospective conclusion of the thesis

1.4 Chapter references

[1] A. D. Kersey, M. A. Davis, H. J. Patrick, M LeBlanc, K. P. Koo, M. A. Putnam and E. J. Friebele, "*Fiber grating sensors*", Journal of Lightwave Technology, vol. 15, Iss. 8, pp. 1442-1463, 1997

[2] Y. J. Rao, "*In-fibre Bragg grating sensors*", Measurement Science and Technology, vol. 8, pp.355-375, 1997

[3] Y. J. Rao, "*Recent progress in applications of in-fibre Bragg grating sensors*", Optics and Lasers in Engineering, vol. 31, Iss. 4, pp. 297-324, 1999

[4] K. O. Hill, Y. Fujii, D. C. Johnson and B. S. Kawasaki, "*Photosensitivity in optical fibre waveguides: application to reflection filter fabrication*", Applied Physics Letters, vol. 32, pp. 647-649, 1978

[5] Image taken from the Photonics Research Group image archive

[6] I. Read and P. D. Foote, "*Sea and flight trials of optical fibre Bragg grating strain sensing systems*", Smart Material Structures, vol. 10, pp. 1085-1094, 2001

[7] V. M. Murukeshan, P. Y. Chan, L. S. Ong and K. Seah, "*Cure monitoring of smart composites using Fiber Bragg Grating based embedded sensors*", Sensors and Actuators A, vol. 79, pp. 153-161, 2000

[8] Y. Zhao, K Chen and J. Yang, "*Novel target type flowmeter based on a differential fiber Bragg grating sensor*", Measurement, vol. 38, pp. 230-235, 2005

[9] H. Y. Tam, S. Y. Liy, B. O. Guan, W. H. Chung, T. H. T. Chan and L. K. Cheng, "*Fiber Bragg Grating Sensors for Structural and Railway Applications*", Proceedings of SPIE, vol. 5634, pp. 85-97, 2005

[10] I. Read, P. D. Foote and S. Murray, "*Optical fibre acoustic emission sensor for damage detection in carbon fibre composite structures*", Measurements and Science Technology, vol. 13, N5-N9, 2001

[11] T. Yamate, R. T. Ramos, R. J. Schroeder and E. Udd, "*Thermally Insensitive Pressure Measurements up to 300 degree C using Fiber Bragg Gratings Written onto Side Hole Mode Fiber*", 14th Conference on Optical Fibre Sensing, pp. 628-631, 2000

[12] S. Takashima, H. Asanuma and H. Niitsuma, "*A water flowmeter using dual fiber Bragg grating sensors and cross-correlation technique*", Sensors and Actuators A, vol. 116, pp. 66-74, 2004

2 Optical fibre sensors

2.1 Chapter preamble

This chapter is designed to introduce the reader to the theory of FBGs and their applications in sensing. For many years now FBGs have formed the basis for a huge amount of academic and industrial research activity. The advantages of FBGs, such as their multiplexing capabilities, small size, immunity to electromagnetic interference and their reliability have made them ideal for use in both the sensing and telecommunications industries.

This chapter begins by giving an introduction to optical fibres and their properties, to give the reader an understanding into the medium which FBG sensors are written. Staying with optical fibre, the chapter goes on to discuss the photosensitivity of optical fibres to UV irradiation and how photosensitivity can be enhanced by a number of techniques such as hydrogenation and co-doping. Following on from this the chapter gives an in-depth introduction to FBGs, including the numerous fabrication techniques that can be used to fabricate them and their sensitivity to measureands such as temperature, strain and pressure and how to compensate for cross-sensitivity. The chapter then introduces the techniques that can be employed to interrogate FBG sensors including the interrogation of a single FBG, as well as interrogating multiple gratings formed in an array by means of WDM, TDM, or a hybrid of both. The advantages and disadvantages of each technique are then presented. From there the chapter discusses the use of FBGs as sensors and the potential operating reliability and lifespan of such sensors.

2.2 Single Mode Fibre

The development of the laser and single mode fibre (SMF) has revolutionised both the optical communications and optical sensing industries. The construction of SMF consists of a high index core, typically with a diameter of approximately 8.2 μm, surrounded by a lower index cladding, which has a diameter in the region of 125 μm, such that the number of propagating modes is 1 [1]. The performance of SMF is largely dependant upon on the attenuation, birefringence and dispersion characteristics of the fibre [2]-[4]. Other physical parameters that can affect the performance of SMF include the difference between core and cladding refractive indices, the photosensitivity of the fibre core, the mechanical and

bending properties of the fibre and the dopant type/dopant concentration within the cladding and core.

2.3 Photosensitivity of optical fibres

Photosensitivity in co-doped silica optical fibres has been the foundation for the design, fabrication and implementation of a number of FBG based systems and devices. The first instance of photosensitivity in Germania-doped optical fibre was reported by Hill *et al* [5] in 1978, and built upon by work performed by Poumellec *et al* [6].

Photosensitivity in optical fibres essentially refers to the sensitivity of the fibre to permanent modifications of the RI of the fibre core, when the fibre is exposed to an interference pattern generated by a UV source. This permanent modification, or perturbation, of the RI axially along the fibres' core is in essence what forms a Bragg grating. It is therefore a necessary requirement that the fibres' core must be highly photosensitive to UV irradiation in order for FBGs to be fabricated, particularly high strength FBGs. By adding co-dopants to optical fibre, the photosensitivity to UV can be drastically increased. By common consensus, the most effective way of increasing photosensitivity is by co-doping germanosilicate optical fibres with boron [7], with demonstrated index changes as large as 10^{-2} in pre-hydrogenated fibre [8].

One of the most important factors when fabricating in-fibre optical devices, such as FBGs, for either sensing or communications applications is long-term stability and reliability. There is not any single factor that determines grating performance, factors include, but are not confined to:

- The UV irradiation power density
- Photosensitisation process
- Dopant concentration in the fibre core

2.3.1 Modelling of photosensitivity on optical fibres

To date, the most common and widely used modelling technique for modelling RI changes in optical fibres is known as the colour centre model. A colour centre is formed due to a defect being present in the glass structure of the fibre. The defect consists of a vacant negative ion site and an electron bound to that site. This defect absorbs light, making

normally a transparent region appeared coloured. The colour centre model makes the assumption that the change to the RI of the fibre core is related to the photo-induced changes in the absorption spectrum. The colour centre model states that any change in the RI can be calculated using the Kramers-Kronig relationship [9]:

$$\Delta n(\lambda') = \frac{1}{2\pi^2}\int_0^{\infty} \frac{\Delta\alpha(\lambda)}{(\lambda^2 - \lambda'^2)} d\lambda \qquad \textbf{Equation 2.1}$$

where $\Delta n(\lambda')$ is the change in the RI and $\Delta\alpha(\lambda)$ is the variation of the excess loss at any given wavelength.

The colour centre model is based upon breaking the germanium-oxygen oxygen vacancy defect bonds present in germanium-doped silica fibre when UV light is absorbed in the 244 nm wavelength region. When a photon is absorbed, the GeO bond is actually broken. The result is a colour centre forming due to the creation of a Si^+ hole and the release of an electron that is able to move around the glass structure. This freely moving electron can either return to the point of release or to a new defect site within the glass. When the electron is re-trapped, the shape of the molecule, which effectively changes the absorption properties of the doped silica glass to UV light, is reconfigured. The result is an increase in the RI, as described in the Kramers-Kronig relationship [9]. The colour centre model is further supported by work reported by Atkins *et al* [10]. In this work, it was reported that over a write/erase/write cycle, no change in photosensitivity was observed in terms of either the rate at which the grating grew, or the final grating strength/reflectivity. The colour centre model has also been used to account for changes in the absorption spectra in bismuth-based silicate glass [11] and rare-earth-doped fluorozirconate (ZBLAN) glasses [12].

The densification model reported by Poumellec *et al* [6] describes how the fibre core structure is compacted when exposed to UV irradiation. When UV absorption takes place, the structural matrix of the glass fibre is modified causing the core of the fibre to compress and take on a more compacted form, thus a denser form. It is this laser irradiation induced densification which causes the permanent modification of the RI of the glass, and is described by the Lorenz-Lorentz relationship. Work reported by Douay *et al* gives an in-depth overview of the densification model [13].

The stress relief model assumes that the chemical bonds are broken when the exposure to UV irradiation takes place, and upon these bonds breaking, the compressive internal

stresses in the glass are relieved. Hence the RI changes in the glass are induced by the photo-elastic stress relief during grating inscription [14].

It must be stated that no one model has described the RI changes. The colour centre model does account for a large proportion of the index changes induced in hydrogenated germanosilicate fibres, whilst the densification model accounts for much of the photosensitivity in non-hydrogenated germanosilicate fibres. Therefore it is probable that there is not one single mechanism taking place during UV inscription that is responsible for the RI modulation.

2.3.2 Photosensitivity enhancing techniques

To ensure repeatable high quality gratings can be written successfully and with relative ease, enhanced photosensitive fibres are highly advantageous. As a result, a number of photosensitising processes have been reported. Reported methods include:

- Hydrogen loading of germanosilicate fibres
- Co-doping germanosilicate fibres
- Flame brushing

2.3.2.1 Hydrogenation of germanosilicate fibres

One of the most common and effective methods of increasing photosensitivity in germanosilicate fibres is by pre-hydrogenating them prior to UV exposure [8][10]. The technique used is to load the fibre with hydrogen at high pressures in the region of 150-220 bar under temperature conditions in the region of 25°C to 80°C. Under these conditions, the hydrogen molecules defuse into the fibres' core prior to UV exposure. Post-hydrogenation, when the fibre is exposed to UV irradiation during grating inscription, the hydrogen molecules react with the Ge-O-Si glass sites producing OH groups and bleachable germanium oxygen-deficient centres (GODCs). The increase in photosensitivity resulting in permanent RI changes is attributed to the increased concentration of GODCs caused by thermal and photolytic reactions between germanium and hydrogen atoms. Post grating inscription, any un-reacted hydrogen in the core diffuses out over a period of time, resulting in a small shift in the Bragg wavelength [15]. Detailed models analysing the photosensitisation process has been previously reported [16].

The issue of the Bragg wavelength shifting owing to hydrogen out-diffusion from the fibre is neither trivial or something that can be omitted during the design and fabrication of FBGs. When compared to non-hydrogenated fibres, gratings inscribed in pre-hydrogenated fibres decay at a much faster rate as a direct result of this hydrogen molecule out-diffusion. The result is a less stable grating spectrum at high temperatures, which is undesirable when, for example, the grating is used in sensing applications. One such reported technique for improving thermal stability of gratings inscribed in hydrogen-loaded fibres has been reported by Guan *et al* [17] where prior to grating inscription, the fibres are pre-irradiated with a UV beam.

2.3.2.2 Co-doping of germanosilicate fibres

The addition of a variety of co-dopants such as boron [7], tin [18] and nitrogen [19] in germanosilicate fibres produces a significant increase in the UV photosensitivity. Boron co-doping germanosilicate fibre has been shown to produce RI changes up to four times larger than RI changes obtained from pure germanosilicate fibres [7], with index changes of 10^{-2} [8] and 10^{-3} [10] being achieved in hydrogenated and non-hydrogenated fibres respectively. Bennion *et al* have also reported Bragg gratings written in fluorozirconate fibres doped with cerium using a UV source with a wavelength of 248 nm. The same work also reported Bragg gratings written in aluminophosphosilicate fibres doped with europium and cerium [22].

2.3.2.3 Flame brushing of germanosilicate fibres

The technique known as flame brushing permanently increases the photosensitivity of germanosilicate optical fibres [23]. The technique involves immersing the fibre in a hydrogen/oxygen-fuelled flame at a temperature in the region of 1700°C for approximately 20 minutes. Such high temperatures allow the hydrogen to be absorbed into the fibre Ge-doped silica core, whilst the properties of the cladding remain unchanged. The cladding remains unaffected because the technique relies on hydrogen reacting with the germanosilicate, which mainly exists in the core. This technique has demonstrated that the photosensitivity of the fibre can be increased by as large as a factor of 10, and exposure to UV irradiation can induce changes in the RI of the fibre core, which can surpass 10^{-3} [23].

2.4 Fibre Bragg Gratings

A FBG is an in-fibre device induced by a uniform sinusoidal periodic modulation of the RI of the silica core of optical fibre, by exposing it to UV irradiation along the *n(z)* axis [5]. Exposure to UV irradiation generates a series of photo reflective mirrors known as fringes, which reflect light at discrete wavelengths. As broadband light propagates through the optical fibre, upon reaching the first fringe of the grating structure, a small amount of light is reflected back along the fibre core. As the light continues to propagate through the core, light from the subsequent fringes is also reflected. The light from each fringe arrives in phase thus constructively interferes at a certain wavelength, forming the grating structure. Figure 2.1 illustrates the grating structure.

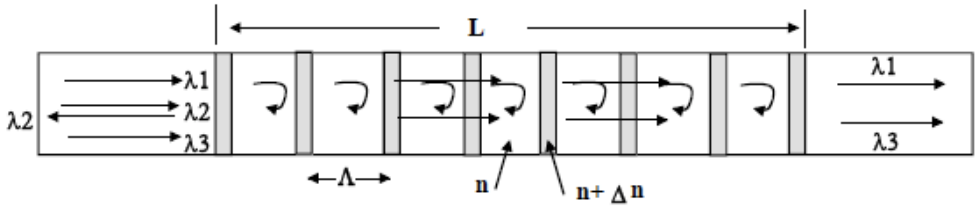

Figure 2.1 Basic grating structure

As the round trip distance is determined by the period Λ, and the RI of the fibre core *n*, the in-phase condition is only valid for discrete wavelengths. Therefore, all other wavelengths emitted by the light source propagate through the grating structure and are observed on the transmission spectra.

The Bragg condition, which defines the peak reflected wavelength, known as the Bragg wavelength λ_B is given as [25]:

$$\lambda_B = 2n_{eff}\Lambda \qquad \textbf{Equation 2.2}$$

where n_{eff} is the effective refractive index of the fibre core and Λ is the period of the grating. The RI modulation profile for a given grating structure is given by the following equation:

$$n(z) = n + \Delta n\left[1 + V\cos\left(\frac{2\pi z}{\Lambda}\right)\right] \qquad \textbf{Equation 2.3}$$

where Λ is the period of the grating, V is the UV fringe visibility, n is the RI of the fibre core before UV exposure and Δn is the amplitude of the RI change.

A useful technique for theoretically describing how the guided waves interact with the grating structure is to use coupled mode theory analysis. The reflectance *R* of a FBG of length *L*, with sinusoidal fringes is given as [22][24][26]:

$$R = \frac{k^2 \sinh^2(SL)}{\Delta\beta^2 \sinh^2(SL) + S^2 \cosh(SL)} \qquad k^2 > \Delta\beta^2 \qquad \textbf{Equation 2.4}$$

$$R = \frac{k^2 \sin^2(QL)}{\Delta\beta^2 - k^2 \cos(QL)} \qquad k^2 < \Delta\beta^2 \qquad \textbf{Equation 2.5}$$

where L is the Bragg grating length, k is the coupling coefficient, β is the mode propagation constant and is defined as $\beta = 2n/\lambda$. $S = \sqrt{k^2 - \Delta\beta^2}$ and $Q = \sqrt{\Delta\beta^2 - k^2}$. For a sinusoidal RI modulation of the fibre core, the coupling coefficient k, is defined as [22]:

$$k = \frac{\pi \Delta n}{\lambda_B} \eta \qquad \textbf{Equation 2.6}$$

where Δn is the extent of the change in the RI and η is the fraction of the normalised power within the fibres' core [22].

The differential Eigenmode propagation $\Delta\beta$, is defined as [22][26]:

$$\Delta\beta = \beta - \frac{p\pi}{\Lambda} \qquad \textbf{Equation 2.7}$$

where p is an integer value, $\beta = \frac{2\pi n}{\lambda}$ is the Eigenvalue propagation constant and λ is the free space wavelength.

For a uniform period grating, η is given by [25]:

$$\eta = 1 - \frac{1}{V^2} = 1 - \left[\left(\frac{\lambda}{2\pi a}\right)\frac{1}{n_1^2 - n_2^2}\right] \qquad \textbf{Equation 2.8}$$

where n_1 and n_2 are the refractive indices of the fibre core and cladding respectively, λ is the free space wavelength, a is the radius of the fibre core and V is the fibre V-parameter, given by [27]:

$$V = \frac{2\pi}{\lambda} aNA = \frac{2\pi}{\lambda} an_1\sqrt{2\Delta} \qquad \textbf{Equation 2.9}$$

where NA is the numerical aperture of the fibre. The V parameter for SMF is <2.405.

When $\Delta\beta = 0$, the maximum reflectivity R is achieved.

$$0 = \left(\beta - \frac{p\pi}{\Lambda}\right) = \left(\frac{2\pi n}{\lambda} - \frac{p\pi}{\Lambda}\right) = \left(\frac{2\pi n}{p\lambda} - \frac{2\pi n}{\lambda_B}\right) \qquad \textbf{Equation 2.10}$$

i.e. when the Bragg condition is met

$$p\lambda = 2n\Lambda \equiv \lambda_B \qquad \textbf{Equation 2.11}$$

The above equation gives the Bragg wavelength λ_B of a diffraction order p [22].

For the fundamental Bragg order, the strongest reflection is achieved when p=1. When $\Delta\beta = 0$, the equation for the peak reflectance given by equation 2.4 simplifies to:

$$R = \tanh^2(kL) \qquad \textbf{Equation 2.12}$$

Therefore it stands to reason that an increase in the reflectance of a Bragg grating is attributed to either an increase in the magnitude of the RI change in the fibre core, or by increasing the length of the grating structure.

The Full-Width at Half-Maximum (FWHM) of a Bragg grating is the difference between the two wavelengths located either side of the Bragg wavelength, where the grating reflectivity drops to ½. This difference in the two wavelength values $\Delta\lambda_{FWHM}$, is given by [28]:

$$\Delta\lambda_{FWHM} = \lambda_B \alpha \sqrt{\left(\frac{1}{2}\frac{\Delta n}{n}\right)^2 + \left(\frac{1}{N}\right)^2} \qquad \textbf{Equation 2.13}$$

where α is in the region of 1 for strong gratings, and 0.5 for weak gratings, N is number of grating fringes within the grating structure, and $\Delta n / n$ is the RI modulation, which is governed by exposure time and laser power for a given fibre type [29]. Two grating situations can be considered. If $\Delta n << \lambda_B / L$, then:

$$\frac{\Delta\lambda}{\lambda_B} = \frac{\lambda_B}{nL} \qquad \textbf{Equation 2.14}$$

Under this condition, the spectral bandwidth of the grating is inversely proportional to the length of interaction of the field with the grating L.

However, when $\Delta n >> \lambda_B / L$, then:

$$\frac{\Delta\lambda}{\lambda_B} = \frac{\Delta n}{n} \qquad \textbf{Equation 2.15}$$

Under this condition, the grating is already saturated and increasing the RI modulation increases the bandwidth of the grating. The bandwidth is no longer dependant on the grating length.

2.4.1 Fibre Bragg grating fabrication

Hill *et al* [5] first inscribed gratings into step-index fibre by guiding the light produced from an Argon Ion (Ar^+) laser with a wavelength of 488 nm. Known as *Hill gratings*, the creation of the grating was due to a hologram written in the core of the fibre generated by the sinusoidal pattern, produced by interference between the forward propagating light, and the light reflected back through the fibre from the fibre end. The counter-propagating light reflected from the fibre end was caused by Fresnel reflection generated by the silica/air boundary. The first internally written Bragg grating had been inscribed, unfortunately this particular fabrication technique has a significant draw back in that the Bragg wavelength of a given grating cannot be accurately selected. For *Hill* gratings, the Bragg wavelength is the write wavelength.

More than 10 years past before Meltz *et al* [25] reported that Bragg gratings could be inscribed in fibre by holographic exposure through the cladding using a side inscription technique. Lam *et al* [26] had previously demonstrated that *Hill Gratings* were generated by 2-photon absorption at the wavelength associated with the Ar^+ laser used in those initial experiments - 488 nm. Therefore by doubling the photon energy, 1-photon inscription could be implemented using a laser operating at 244 nm.

More recent developments in Bragg grating inscription techniques have been reported by Hill *et al* [30] and Anderson *et al* [31]. These two Bragg grating inscription techniques came to form the bedrock for all future grating fabrication, and are commonly referred to as the holographic interferometric technique and the phase mask technique.

2.4.1.1 Holographic interferometric inscription technique

The first significant break through for fabricating Bragg gratings using the holographic inscription technique came in 1989 by Meltz *et al* [25]. The principle of the inscription technique is illustrated in Figure 2.2.

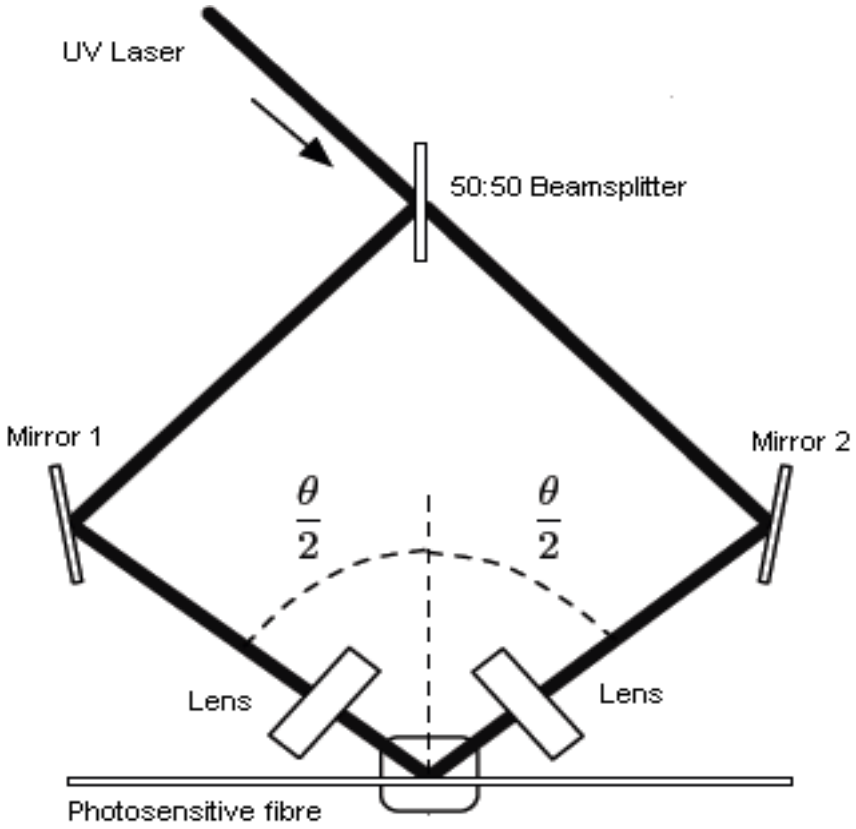

Figure 2.2 Kite-shaped holographic interferometric fabrication technique

This flexible inscription technique enabled the fabrication of FBGs by UV irradiation, which is aimed at the fibre core from the side, passing through the cladding layer. It should be noted that the fibre acrylate coating is removed by either mechanical or chemical stripping prior to fabrication. The principle of operation is that the UV laser light is first split by means of a 50:50 splitter, directed towards two mirrors which direct the respective incident beams towards cylindrical lenses, which in turn focus the incident light onto the fibre core. The period of the generated core index modulation was found to be a function of the laser wavelength and the incidence angle. Therefore it stands to reason that with a fixed laser wavelength, any adjustment to the incidence angle would result in a change in grating period. By adjusting the incidence angle, the Bragg wavelength of a given FBG can

be pre-designed and fabricated. The fact that this incidence angle can be widely varied means that numerous gratings can be written, each with a different Bragg wavelength.

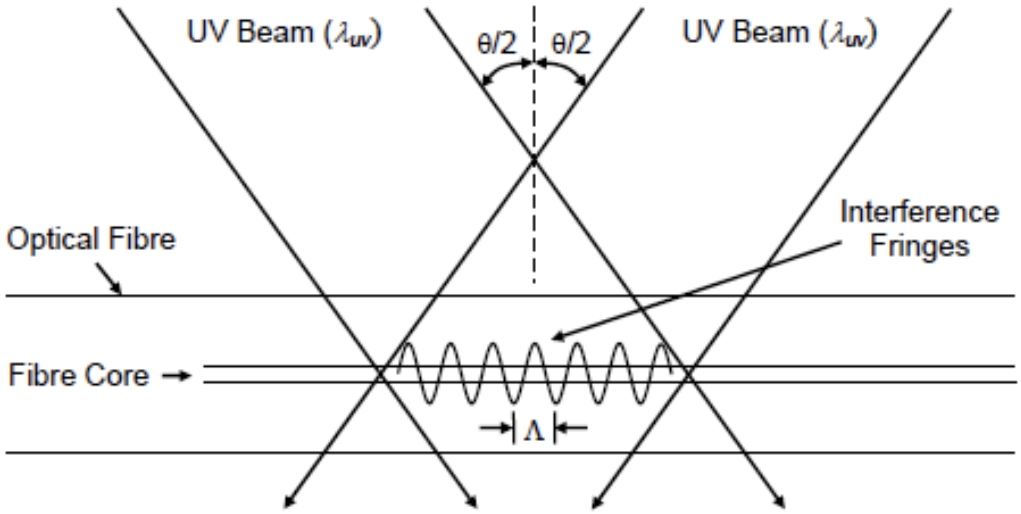

Figure 2.3 Two interfering UV beams generating a fibre Bragg grating

Equation 2.16 illustrates that that the grating period Λ, is dependant upon the laser wavelength λ_{UV} and the angle of interference θ.

$$\Lambda = \frac{\lambda_{UV}}{2\sin(\theta/2)} \qquad \textbf{Equation 2.16}$$

where $\theta/2$ is half the angle between the two incidence beams of wavelength λ_{UV}. This equation can be used to develop a statement for defining the Bragg wavelength of a given FBG, and is defined as:

$$\lambda_B = \frac{n_{eff}\lambda_{UV}}{\sin(\theta)} \qquad \textbf{Equation 2.17}$$

This technique unfortunately exhibited certain limitations. One such limitation is that in some instances it is required to inscribe gratings that are longer than the length of the interfering beams. However, this limitation can be over come by adding a beam-expanding telescope, which as the name suggests, expands the UV beam generated by the laser, allowing gratings of longer length to be fabricated. Another drawback of this technique is the grating profile can exhibit a chirped effect owing to the beam profile producing uneven exposure. Yet another disadvantage with the holographic interferometric technique is that

the grating quality relies heavily on the alignment of the optical system, which can for example be affected by vibrations in the system.

Despite the disadvantages listed above, Kashyap *et al* demonstrated an improved version of the side inscription technique based on wavefront splitting [32], and was the first reported instance of fabricating FBGs in the 1550 nm region. This modified technique used a Lloyd Interferometer providing total internal reflection in a prism, which replaced the Lloyd mirror. This milestone in grating fabrication saw a drastic upsurge in the amount of research, both industrial and academic, performed in this field owing to the fact that the telecommunications industry operated in the 1550 nm wavelength region.

2.4.1.2 Phase mask inscription technique

The alternative inscription technique was first reported by Hill *et al* in 1993 [30][31] which utilises a phase mask, and has since become the inscription technique of choice for reproducible grating fabrication. A phase mask, generally manufactured in a flat UV insensitive silica substrate, is in essence a diffractive element that can be used to define the interference pattern to be inscribed in the fibre core. The interference pattern is superimposed onto the substrate by means of photolithography. A significant advantage with photolithographic phase masks is that for a given interference pattern, the grating period can be varied along it's length, thus various types of gratings, such as Moiré phase shifted gratings [33], and apodised gratings [34] can be produced. The phase mask inscription technique is illustrated in Figure 2.4.

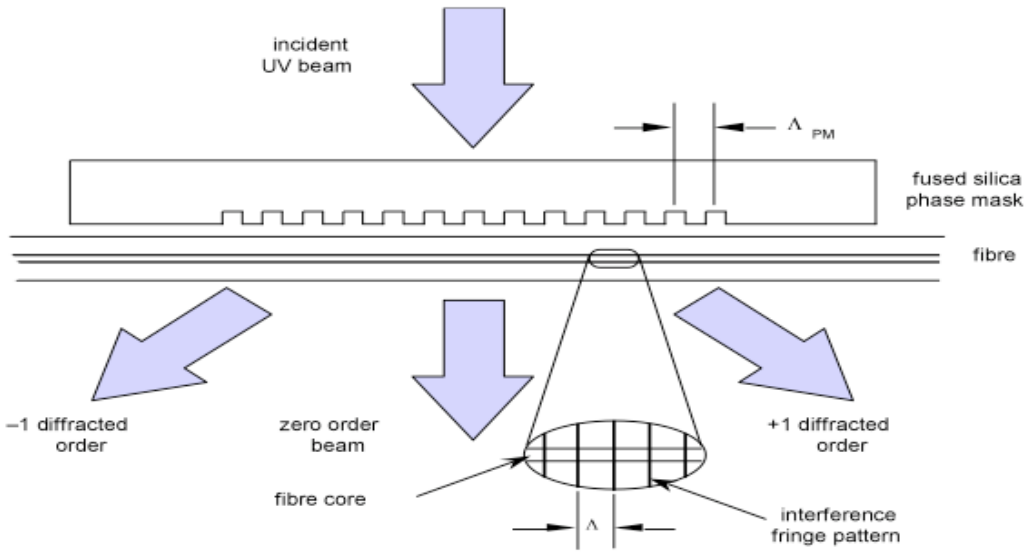

Figure 2.4 Phase Mask inscription technique

The principle of operation is that the incident UV beam passes through a cylindrical lens before reaching the phase mask. Upon reaching the phase mask, the beam splits into two diffraction orders - the first plus and minus diffraction orders. If the phase mask is positioned sufficiently close to the optical fibre, the fringe pattern produced by the interference of the plus and minus first order beams generate a modulation of the RI of the fibre core. The period of the interference fringes Λ_B, is half the phase mask period Λ_{pm}.

The phase mask inscription technique has a significant advantage over the holographic technique in that by utilising a translation stage, the grating length is not limited to the incident beam width, but rather to the length of the phase mask. Therefore gratings of much greater length can be fabricated. Another advantage is that the fibre can be angled relative to the phase mask, which allows the inscription of tilted fibre Bragg gratings (TFBGs) [35]. Another significant advantage of the phase mask technique is that it effectively de-skills the fabrication process.

The expression defining the Bragg wavelength for phase mask induced gratings is given as:

$$\lambda_B = 2n\Lambda\sqrt{1+(d/l)^2} \qquad \textbf{Equation 2.18}$$

where l is the length of the interference pattern on the phase mask and d is the distance between the fibre core and phase mask when the fibre is parallel to the phase mask. If the fibre is actually positioned parallel to the phase mask, $d = 0$ and the equation simplifies to:

$$\lambda_B = 2n\Lambda \qquad \textbf{Equation 2.19}$$

Unfortunately the obvious draw back of fabrication using this technique is that once the phase mask has been manufactured, the periodic pattern cannot be modified. Though not a direct solution to this problem, it is quite common that phase masks are produced with multiple interference patterns. There are some techniques, which can to some extent solve this issue. The most common technique was demonstrated and reported by Zhang *et al* in 1994 [36]. The technique involves pre straining the fibre before exposing it to UV irradiation. The resulting grating exhibits a slight blue shift in wavelength when the strain is alleviated from the fibre owing to a slight reduction in the grating period due to the fibre compressing. This technique is only limited by the mechanical strength of the fibre. Furthermore, it has been demonstrated by Byron *et al* that by varying the strain during UV

exposure, chirped gratings can be fabricated despite the interference pattern on the phase mask being uniform [37].

In both inscription techniques, there is a prerequisite that the protective acrylate coating be removed prior to fabrication as this protective coating actually absorbs UV irradiation at the common inscription wavelengths, namely 244 nm. The two most common techniques for removing this coating are mechanical stripping or chemical stripping, in both cases the fibre strength can be significantly reduced, increasing the possibility of the fibre breaking. The process of stripping the fibre, inscribing the grating and re-coating the fibre post-fabrication is also relatively time consuming and expensive. Optical fibre is generally manufactured using a draw tower, and Askins *et al* [38] demonstrated that it was possible to inscribe a grating at the fibre manufacturing stage, therefore the grating was inscribed before the coating was applied. Also, Starodubov *et al* [39] demonstrated a far more commercially viable option, whereby gratings could be inscribed through coated optical fibres using near-UV light at a wavelength of 344 nm. The drawback of fabricating gratings at the longer wavelength is that the fibre is not as photosensitive to the longer wavelengths, thus strong gratings are not possible in standard fibre.

2.4.1.3 Point-by-point inscription technique

The point-by-point inscription technique allows the direct writing of Bragg gratings, by locally inducing a modification of the RI of the fibre core. The laser inscription system will usually include a shutter, whereby the user can pre-enter the grating parameters and the shutter opens and closes as the translation stage moves from left to right, thus inscribing the grating one fringe at a time to form the complete grating structure.

Work reported by Malo *et al* documented how this point-by-point inscription technique could be used to fabricate such grating structures, using a KrF excimer laser, which illuminated a 15 μm slit and was focussed onto the fibre core using a 15 mm focussing lens [20]. The work resulted in a grating 360 μm in length, had a periodicity of 1.59 μm, and a reflectance of 70%. Such an inscription technique is highly versatile, and by pre-entering the desired grating parameters into the system software, complex grating structures, such as chirped gratings can be written. Also, the grating length is not limited by the length of the phase mask, hence longer gratings can be written.

There are two distinct methods for inscribing on a point-by-point basis. Either the UV laser beam is scanned parallel to the fibre whilst the fibre remains in a fixed position, or the UV beam remains fixed whilst the fibre is translated. In 1997, Asseh *et al* demonstrated that LPFGs could be written using the point-by-point inscription technique [21].

2.4.2 Types of photosensitivity

Depending upon the UV irradiation condition, the magnitude of the RI modulation and the type of photosensitive fibre utilised to fabricate the grating; four types of photosensitivity are defined. These are:

- Type I – Standard grating which can be written in either hydrogenated or non-hydrogenated fibre
- Type II – Damage written grating fabricated by a pulsed high power laser
- Type IA – Regenerated grating written after erasure of type I grating in hydrogenated germanosilicate fibre of all types
- Type IIA – Regenerated grating written after erasure of a type I grating in hydrogen-free germanosilicate fibre

2.4.2.1 Type I

A Type I FBG is inscribed in fibres of all types under hydrogenated conditions. They are generally produced using low-power UV irradiation below a threshold during a short fabrication period. The RI grows almost linearly with the UV exposure time and intensity. Type I gratings have low thermal stability. At temperature of approximately 300˚C and below, the index modulation remains relatively constant. However above 300˚C it begins to decay. The index modulation of a type I grating is typical less than 0.001. Type I gratings are the most common grating.

2.4.2.2 Type II

As the power of UV light used for fabrication exceeds the threshold value, a single excimer laser pulse can attain a large rise in the RI, typically in the order of 0.006 [40]. This kind of RI change is known as Type II. The Type II RI change has the highest stability at high temperatures. Under temperatures as high as 800˚C over a period of 24 hours, no significant changes in the index modulation strength were observed. One issue

however was that due to high power UV exposure; localised damage was detected, which may reduce the mechanical strength of the fibre.

2.4.2.3 Type IA and IIA

As a Type I grating is being fabricated, the grating strength increases to a point where it saturates after absorbing a certain amount of light. Once the grating has saturated, it begins to decrease until it has partially or completely been erased. If exposure continues, the grating will reappear. This re-grown grating is known as a Type IA grating if fabricated in hydrogenated fibre [41], or a Type IIA grating if in non-hydrogenated fibre [42]. A Type IA grating exhibits a red wavelength shift during fabrication, whilst a Type IIA exhibits a blue shift. Type IIA gratings are far more temperature stable than a Type I grating, and can survive in temperatures as high as 600˚C [42]. Type IA and IIA gratings exhibit larger index modulations than Type I gratings.

Canning *et al* has since proposed a series of new grating classifications [43].

2.5 Sensitivity to physical measurands

The properties of FBGs make them ideal candidates for deployment as sensors in a wide and varied range of applications, namely the fact that the measurand is wavelength encoded, eliminating factors such as source power fluctuations, scattering losses, bending losses, and reflection losses. However, the inherent sensitivity of FBGs to changes in the external temperature and strain result in a shift in the Bragg condition resulting in a wavelength shift when either or both parameters change. It is therefore essential to decouple these two parameters in order to obtain correct and accurate measurements.

2.5.1 Sensitivity to strain

When a longitudinal strain is applied to the optical fibre, the physical length of the fibre is elongated resulting in a change to the grating period, and also the effective refractive index changes due to photo elastic effects [44][45]. The result is a shift in the Bragg wavelength, λ_{BS}. The relationship between this Bragg wavelength and strain is given as [29]:

$$\lambda_{BS} = \lambda_B(1-\rho_e)\Delta\varepsilon \qquad \textbf{Equation 2.20}$$

where $\Delta\varepsilon$ is the applied longitudinal strain and ρ_e is the photo-elastic coefficient of the fibre given as:

$$\rho_e = \frac{n^2}{2}\left[\rho_{12} - \upsilon(\rho_{11} + \rho_{12})\right] \approx 0.22$$ **Equation 2.21**

where ρ_{12} and ρ_{11} are the components of the fibre optic strain tensor and υ is Poisson's ratio. Whilst accurate strain sensitivity varies from sensor to sensor based on factors such as the type of grating utilised and fibre type, it is widely accepted that at 1550 nm, 1 $\mu\varepsilon$ of applied strain will induce a wavelength shift of 1 pm, given by:

$$\frac{1}{\lambda_B}\frac{\partial\lambda_B}{\partial\varepsilon}$$ **Equation 2.22**

2.5.1.1 Effects of transverse strain

In most applications, FBGs simply measure the strain induced along the longitudinal axis. The measurement principle is simply based on monitoring the wavelength shift of the FBG peak. However for certain applications, a three dimensional state of strain is created. When a load is applied to a system housing a FBG, the transversal loading induces stress in the X and Y direction, one is tensile and other is compressive.

Light is essentially an electromagnetic wave, which has two polarizations, the X and Y direction. This is illustrated in Figure 2.5. When the RI profile is modified due to induced birefringence, a splitting of the resonant peak of the FBG is visible on the spectrum. The splitting is due to the birefringence being caused by the applied load, and is known as the photoelastic effect. The birefringence is a function of applied load, and increases with increasing load.

As a result of this phenomenon, the wavelength shift being observed is not simply due to axial strain, but a combination of both axial and transverse strain. A detailed review reporting the effects of transverse loading on uniform period FBGs has been reported by Gafsi *et al* [46].

Figure 2.5 Transverse view of an FBG system subjected to linear force distribution [46]

2.5.2 Sensitivity to temperature

The sensitivity of Bragg gratings to temperature is dependant upon a change in the effective refractive index of the glass induced by the thermo-optic effect and thermal expansion of the fibre resulting in a change in the grating period. The shift in the Bragg wavelength as a result of temperature variation is given as [47]:

$$\Delta\lambda_{BT} = \lambda_B(\alpha + \xi)\Delta T \qquad \textbf{Equation 2.23}$$

where ξ is the thermo-optic coefficient and α is the thermal expansion coefficient. In silica fibres, the primary cause of the wavelength shift is the thermo-optic effect. By substituting for ξ and α, equation 2.22 can be re-written as:

$$\Delta\lambda_B = \lambda_B\left[\left(\frac{\left(\frac{\partial\Lambda}{\partial T}\right)}{\Lambda}\right) + \left(\frac{\left(\frac{\partial n}{\partial T}\right)}{n}\right)\right]\Delta T \qquad \textbf{Equation 2.24}$$

Likewise with strain, though the exact wavelength shift induced by temperature variations is dependant upon grating and fibre type, it is widely accepted that at 1550 nm, a 1°C temperature change will induce a 10 pm shift in the Bragg wavelength, given as:

$$\frac{1}{\lambda B}\frac{\partial\lambda_B}{\partial T} \qquad \textbf{Equation 2.25}$$

2.5.3 Cross sensitivity of strain and temperature

As a Bragg grating sensor is affected simultaneously by both temperature and strain, the spectral shift of the Bragg wavelength is a combination of these two parameters. The Bragg wavelength can therefore be expressed as:

$$\Delta\lambda_B = \left[(1-p_e)\varepsilon + (\alpha+\zeta)\Delta T\right] \qquad \textbf{Equation 2.26}$$

Therefore the Bragg wavelength shift can be re-written as:

$$\Delta\lambda_B = \left[\left\{\left(1-\frac{n^2}{2}\right)\left[\rho_{12}-\upsilon(\rho_{11}+\rho_{12})\right]\right\}\varepsilon + \left[\frac{\left(\frac{\partial\Lambda}{\partial T}\right)}{\Lambda}\right] + \left(\frac{\left[\frac{\partial n}{\partial T}\right]}{n}\right)\Delta T\right]\lambda_B \qquad \textbf{Equation 2.27}$$

Table 2.1 gives some examples of the strain and temperature sensitivity of Bragg gratings written in silica fibre operating in different wavelength regions at room temperature [29].

Wavelength (nm)	Strain Sensitivity (pm/με)	Temperature Sensitivity (pm/°C)
830	0.64	6.8
1300	1.0	10
1550	1.2	13

Table 2.1. Wavelength shifts induced by strain and temperature variations in FBGs written in silica fibres operating in varying wavelength regions.

2.5.4 Compensating for cross sensitivity of strain and temperature

This issue of cross-dependence of FBGs to temperature and strain is an obvious one, in that without decoupling the two parameters, it is impossible to know what wavelength shift is attributed to a change in applied strain, and what is attributed to a variation in the external temperature. The most commonly used technique is to use a strain isolated grating, placed near to the strain sensing grating. This reference grating solely monitors temperature variations, therefore can be used to remove the temperature effect from the strain sensing grating, which is experiencing both strain an temperature effects. However, this is not the only technique reported to date. Patrick *et al* reported that a hybrid system comprising of a FBG and a LPFG could be used to isolate temperature and strain effects [48]. James *et al* demonstrated that by using two FBGs written in fibres of different diameters and spliced together resulting in a different strain response for each grating,

whilst the temperature response remains similar [49]. Simpson *et al* reported that by adjoining a Type I grating with a Type IA grating, the gratings are optically separated with different temperature coefficients [50]. Frazao *et al* reported a similar technique pairing a Type IIA grating with a Type I grating [51]. Xu *et al* demonstrated that using two FBGs operating in different wavelength regions, 800 nm and 1300 nm, each FBG has a different spectral response to temperature and strain [52].

2.5.5 Sensitivity to pressure

Another measurand, which FBGs are sensitive to, is pressure. For a change in external pressure, the Bragg wavelength shift induced is given by [29]:

$$\frac{\Delta\lambda_{BP}}{\lambda_B} = \frac{\Delta(n\Lambda)}{n\Lambda} = \left(\frac{1}{\Lambda}\frac{\partial\Lambda}{\partial P} + \frac{1}{n}\frac{\partial n}{\partial P}\right)\Delta P \qquad \textbf{Equation 2.28}$$

where ΔP is the change in pressure. The length and RI dependence induced by pressure variations are given by:

$$\frac{\Delta L}{L} = -\frac{(1-2\upsilon)}{E}P \qquad \textbf{Equation 2.29}$$

$$\frac{\Delta n}{n} = -\frac{n^2}{2E}(1-2\upsilon)(2\rho_{12}+\rho_{11}) \qquad \textbf{Equation 2.30}$$

where E is the Young's modulus of the optical fibre. As $\Delta L/L = \Delta\Lambda/\Lambda$, the normalised period-pressure is given by:

$$\frac{1}{\Lambda}\frac{\partial\Lambda}{\partial P} = \frac{(1-2\upsilon)}{E} \qquad \textbf{Equation 2.31}$$

and the refractive index-pressure is given by:

$$\frac{1}{n}\frac{\partial n}{\partial P} = \frac{n^2}{2E}(1-2\upsilon)(2\rho_{12}+\rho_{11}) \qquad \textbf{Equation 2.32}$$

Finally, by substituting equations 2.30 and 2.31 into 2.28, an expression for the overall wavelength shift induced by pressure can be derived, and is given as:

$$\Delta\lambda_{BP} = \left[\left(\frac{1-2\upsilon}{E}\right) + \frac{n^2}{2E}(1-2\upsilon)(2\rho_{12}+\rho_{11})\right]\Delta P \qquad \textbf{Equation 2.33}$$

2.5.6 Sensitivity to application-related measurands

As well as their sensitivity to strain and temperature, Bragg grating sensors have been demonstrated to be highly capable of measuring a whole host of other measurands over a huge range of applications. Wang *et al* has demonstrated that embedded FBGs can be used to measure dynamic loads [53]. Embedded FBGs for monitoring vibrations in railway structures has been reported by Tam *et al* [54]. The use of two FBGs written in series forming a Fabry-Perot cavity to measure acoustic emissions for use in the civil and marine industries has been reported by Takahashi *et al* [55]. The measurement of pipeline flow rates using a differential FBG sensor has been demonstrated by Zhao *et al* [56]. Suresh *et al* reported that shear forces could be obtained by measuring the strain induced in gratings embedded at angles [57]. Perez *et al* reported the use of FBGs to detect acoustic emissions [58]. Note that this is a small selection of application-related measurands rather than a comprehensive list.

2.6 Fibre Bragg grating interrogation techniques

Interrogation of a FBG basically requires the recovery of the wavelength-encoded measurand, for example recovering induced strain for a given wavelength shift. A number of techniques have been reported for interrogating single FBG sensors as well as multi-grating sensor arrays. Though it is obviously possible to interrogate single-sensor systems, a distinct advantage of FBGs is their ability to be multiplexed to form large sensing arrays. The formation of such a sensing array requires interrogation techniques that allow each sensor to be interrogated independently. The two most common forms of multiplexing are known as WDM [59] and TDM [60]. The work reported in this thesis is based on using these techniques in separate systems. However there are other techniques utilised to interrogate Bragg grating sensors, some of these include coherence multiplexing [61] and space division multiplexing [62].

2.6.1 Single FBG sensor interrogation

The simplest optical sensing system is one where the system need only interrogate a single Bragg grating sensor. There are a number of optical characteristics that can be measured in an optical system in order to extract the required data, these include:

- Wavelength shift

- Peak amplitude/loss/attenuation
- Phase
- Polarisation
- Dispersion

The accuracy and resolution of the optical system depends largely on the characteristics of the interrogation device, which can vary immensely in terms of complexity and cost. Two simple techniques can be employed when looking at a single grating, the first technique is to look at the transmission profile of the FBG, and the second is to look at the reflection profile of the FBG. Figure 2.6 illustrates these two interrogation techniques.

The disadvantage of these techniques is there is no compensation against external parameters such as temperature.

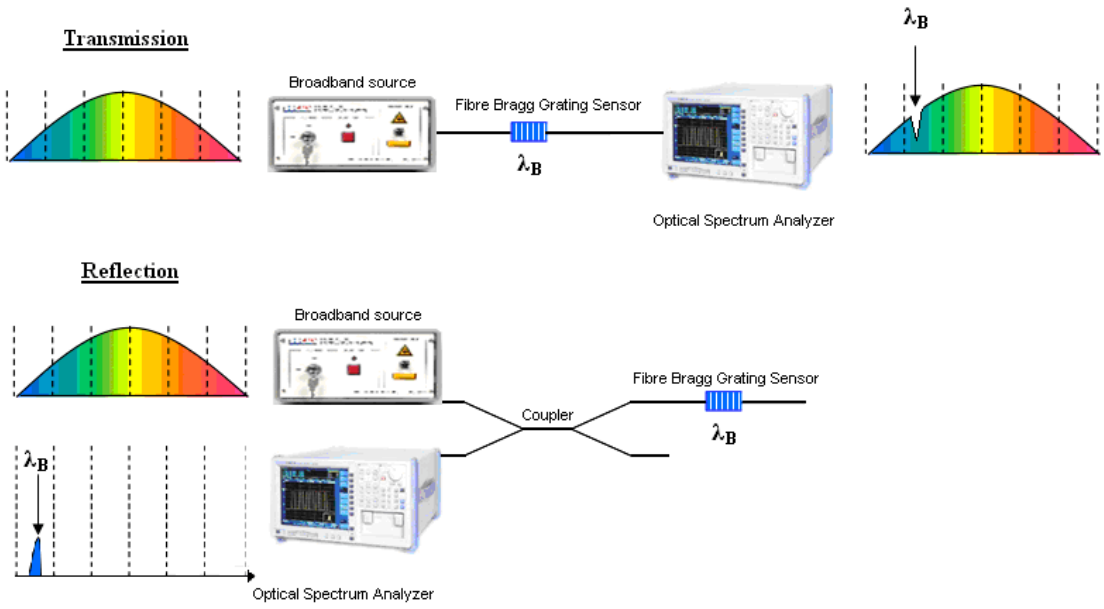

2.6 Basic transmission and reflection interrogation topology

The addition of a second FBG acting as a reference grating against the sensing grating allows the decoupling of external parameters affecting the measurand. The reference FBG is placed on a piezoelectric stage, which constantly tunes the wavelength of the reference FBG to match that of the sensing FBG. This technique is illustrated in Figure 2.7.

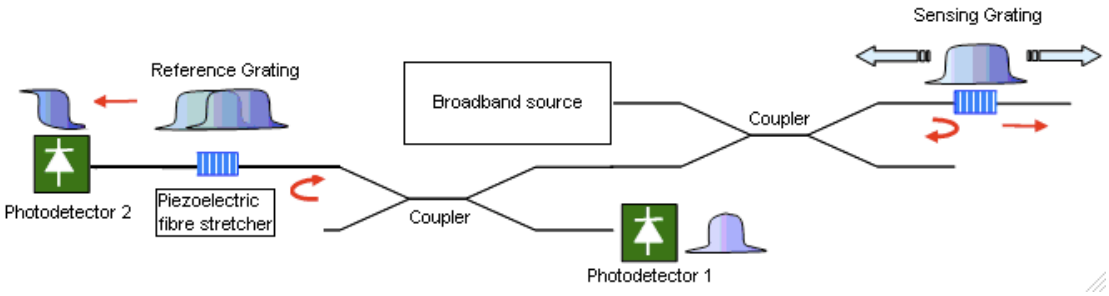

Figure 2.7 Topology of a matched FBG system

When the sensing grating is unstrained, the grating profiles of both FBGs completely match, resulting in all the light reflected from the grating also being reflected from the reference grating. When this occurs, photodetector 1 will detect maximum power, whilst photodetector 2 detects minimum power. However as the sensing grating is strained resulting in a Bragg wavelength shift, the grating spectrums no longer match. The reference grating is no longer filtering all the reflected light from the sensing grating; hence some light is now passing through the reference grating and is being detected by photodetector 2. Therefore by calculating a ratiometric value of both photodetectors, the amount of strain applied to the sensing grating can be determined. This approach can offer a low cost solution to some sensing applications, however this technique can suffer from effects such as source intensity and system loss. A system based on matched uniform period gratings has been reported by Lobo Ribeiro *et al* [64], as a well as a matched chirped grating system by Fallon *et al* [63].

2.6.2 Wavelength-division-multiplexing (WDM) interrogation

An optical system incorporating a single FBG sensor is all well and good, however there are many applications that require far more sensors. Such examples include structural monitoring of civil and aerospace structures. One of the most significant advantages of Bragg grating sensors is their ability to be multiplexed into a single fibre and can be interrogated independently by a single interrogation unit, differentiating between each sensing element by their respective Bragg wavelengths.

By far the most common technique is to use the WDM approach, allowing multiple gratings to be written into a single length of optical fibre at arbitrary locations. WDM techniques have been widely investigated [45]. The technique relies on multiple gratings being written each having a different resonant Bragg wavelength, essentially each sensor has its own wavelength operating window preventing cross-talk from other sensors

operating at different wavelengths corrupting the signal. When each respective sensor is strained or exposed to variations in temperature, the result is a shift in the Bragg wavelength of the grating. The technique requires a light source broad enough to illuminate all the gratings in the array, operating in their respective wavelength windows. Figure 2.8 illustrates a typical WDM optical sensing system incorporating multiple FBGs.

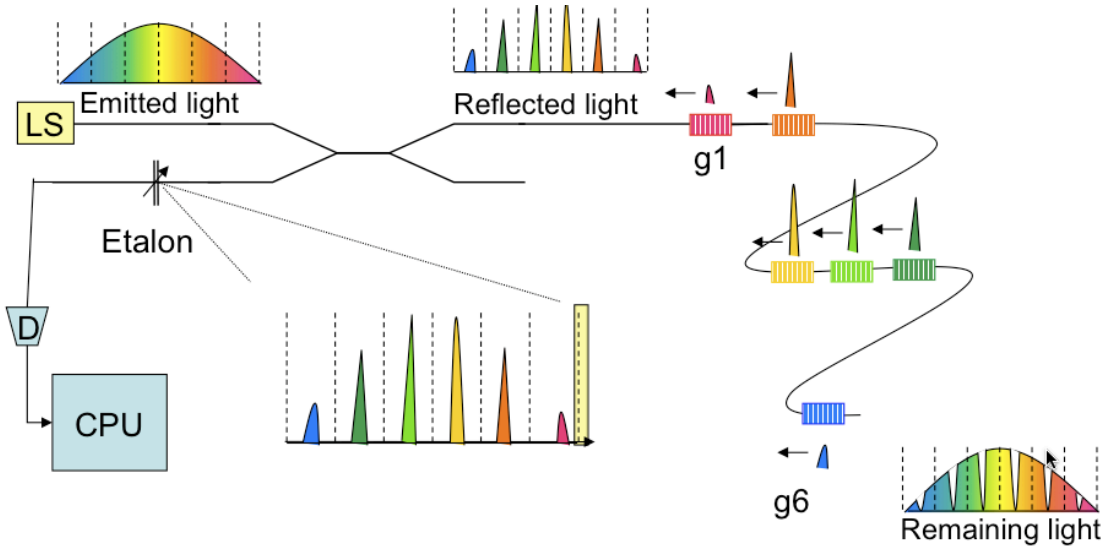

Figure 2.8 Typical topology of a WDM system

There are a number of WDM system techniques that can be incorporated into an optical system, and include series, parallel and branching. One of the limitations of WDM is that the number of sensors that can be incorporated into the system is limited by the bandwidth of light source. One such technique for overcoming this is to implement a WDM/TDM hybrid as reported by Chung *et al* [65], where multiple arrays are fabricated. Whereby for example two or more gratings of the same wavelength can be used, however as a known distance separates them, they can be differentiated in terms of time, hence making wavelength re-use possible. Figure 2.9 illustrates some WDM/TDM system topologies.

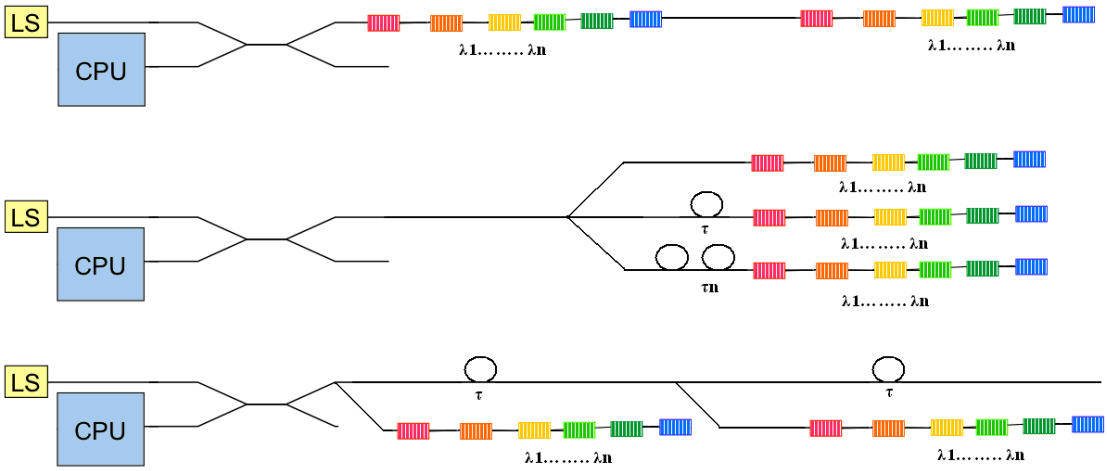

Figure 2.9 WDM/TDM hybrid topology for an FBG sensing array illustrating (a) Serial system with low reflectivity FBGs, (b) Parallel network and (c) Branching network.

Multiplexing techniques have been reviewed extensively by Kersey *et al* [45] and Rao *et al* [29].

2.6.2.1 Advantages of WDM

The advantages of WDM as a means of interrogating multiple sensors in a single grating array are numerous, and include:

- As each grating is written in its own operating window, the strength of each FBG can be made relatively strong, thus removing the issue of losses in the system
- As the system is interrogating each sensor in terms of its wavelength window rather than its position in the fibre, the restrictions on sensor spacing is far less stringent than with TDM techniques
- With the grating array appropriately designed such that each grating is operating in its own window, the sensors are free from interference from other gratings operating in different wavelength windows

2.6.2.2 Disadvantages of WDM

However there are some disadvantages to WDM interrogation techniques, these include:

- As each FBG operates in its own wavelength region, the parameters of each FBG need to be changed in order to produce a different Bragg wavelength. Therefore, for example, each FBG will require a different phase mask pattern. This will most

likely be extremely costly and time consuming, and require human intervention at some point during the fabrication process

- The number of sensors is restricted by the bandwidth of the light source. Broadband light sources can be extremely expensive; therefore to implement an array with a large number of gratings will also be expensive
- The operating windows for each sensor need to be sufficiently large to prevent crosstalk, keeping in mind that under strain, the wavelength shift can be as large as ~5-6 nm

2.6.3 Time-division-multiplexing (TDM) interrogation techniques

An alternative to WDM grating interrogation is to use a TDM scheme. The operation of a TDM system is based on optical time domain reflectometry (OTDR) technology. Figure 2.10 illustrates a typical topology of a TDM system. The principle of operation of a TDM system is that light from a narrowband pulsed source is launched into the optical fibre where an array of low reflectivity gratings is spatially positioned operating in the same wavelength window. When the input pulse duration is shorter than that of the round trip time between two sensors, the reflected light from the two sensors will be separated in the time domain, and can be detected using high speed electronics. An example of such a system is the Insensys Fibre Sensor Interrogator (FSI).

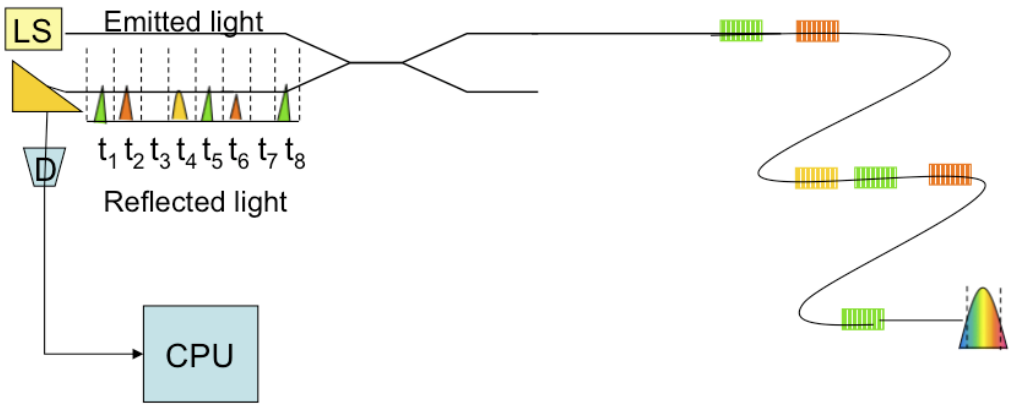

Figure 2.10 Typical topology of a TDM system

In a TDM system, the number of FBGs that can be multiplexed is greatly increased over a pure WDM system, as the restriction of source bandwidth is no longer a factor. This is because each FBG is fabricated at the same Bragg wavelength. Morey *et al* [66] has demonstrated that as many as 100 sensors can be multiplexed into a single fibre, with each grating have a reflectivity <0.13%.

2.6.3.1 Advantages of TDM

There are a number of advantages attributed to using a TDM topology, these include:

- As the system is not restricted by the operating bandwidth of the light source, a higher number of sensors can be deployed when compared with a WDM system
- As each sensing grating has the same parameters, effectively once the inscription system is set-up, it can run continuously to reel off a high number of sensors relatively quickly and can be fully automated
- As the gratings are quite weak, the gratings can be inscribed without the need to remove the coating at set intervals for grating inscription. This acts to maintain the mechanical strength of the fibre
- As the grating fabrication is far easier, quicker and cheaper, the end cost of the grating to the potential customer is significantly reduced

2.6.3.2 Disadvantages of TDM

There are however some disadvantages to a TDM system, these include:

- As the system is based on time-of-flight, the spacing between each sensor is dependant upon the speed of the gating electronics, and separation distances can run into metres for certain systems
- As the gratings are weak, the reflected power is also very low, which means losses in the system are far more of a factor. If too much loss is induced in the system, for example bending losses, the signal can be lost.

Table 2.2 gives a brief summary of FBG multiplexing techniques as outlined in the chapter [29].

	TDM	WDM
Multiplexing capacity	medium	good[1]
Spatial resolution	low	high
Usage of optical power	good[2]	good
Interchangeability	low	low
Potential cost	low	medium

Table 2.2 Brief summary of FBG multiplexing techniques

(1) In particular when combined with TDM forming a hybrid

(2) Poor SNR may occur when the number of sensors in the network is large

2.6.4 Interrogation units used in this thesis

This section introduces to the reader the two interrogation systems used in the experimental chapters of this thesis. The units used were:

- WDM system: Ibsen I-MON 400e
- TDM system: Insensys Fibre Sensor Interrogator (FSI)

2.6.4.1 Ibsen I-Mon 400e

The I-MON 400e interrogation unit is a real-time system monitoring the spectrums of FBG sensors. The system uses a high-resolution spectrometer, which spatially splits the wavelength spectrum. This allows FBG sensors operating in distinct operating windows to be processed in parallel. The I-MON 400e can detect up to 50 sensors spaced at 1200 pm, and has a maximum measurement frequency of 200 Hz. A diode array is used to measure the FBG sensor peaks. A USB interface and data acquisition software allows data to be captured via a LabVIEW interface.

2.6.4.2 Insensys Fibre Sensor Interrogator

The Insensys FSI system is based on a resonant cavity architecture utilising the high-speed switching properties of a Semiconductor Optical Amplifier (SOA). The SOA performs the operations of optical gating, optical amplification and sensor illumination. Using a broadband optical reflector, a cyclic optical signal is produced in the resonant cavity around the SOA. In doing so, a TDM de-multiplexing unit is created. The model of FSI used in this thesis was a two-channel device capable of interrogating up to 100 4%

reflectivity FBG sensors over a distance of 9 km per channel. Like the I-MON, the FSI has a USB interface which allows for data acquisition via a LabVIEW interface.

2.7 Optical fibre sensors

OFS have become increasingly popular since their inception, owing to their characteristic advantages over competing technologies. Compared to electrical sensors and transducers, OFS exhibit the following advantages:

- Immunity to electromagnetic interference. The advantage here is that OFS can be implemented where other sensor types, such as electrical, are affected by electromagnetic interference which may be generated by surrounding devices
- Light and compact. Typically optical fibres, such as Corning SMF-28 with the acrylate coating applied will have a diameter in the region of 250 μm
- Remote interrogation for long distance applications. The advantage here is that the actual interrogation device can be situated large distances from the sensing location
- Ability to operate in harsh and explosive environments, making them ideal for deployment in potentially flammable/explosive environments
- Multiplexing capabilities allows large grating arrays to be fabricated into the optical fibre, and can be interrogated in the wavelength domain, the time domain, or hybrid of both. This allows for applications where a large number of sensors are required for multi-position sensing

A study by Lee *et al* [67] in 2003 showed that by far the two most popular parameters to measure were strain and temperature, accounting for 24% and 17% of the over all parameters measured respectively. Other parameters included pressure/acoustic sensing (15%), current/voltage (12%), chemical/gas (11%), rotation (6%), vibration/acceleration (6%), bending/torsion (4%), displacement (3%) and bio (2%). The same report also showed that by a huge margin, the most popular sensing element was the fibre grating, accounting for 44% of the sensing elements used in optical sensing. Other technologies included interferometry (11%), scattering/reflection (10%), Faraday rotation (7%), fluorescence/luminescence/blackbody (7%), FOG (4%), low-coherence interferometry (4%) and other types (13%).

2.7.1 Potential lifespan and reliability of OFS

One of the factors to consider when choosing a sensor type is to consider the lifespan and reliability of such sensors. OFS are being deployed now more than ever before in a wide range of applications that are critical to the safety of the device or structure being monitored. One example would be sensors embedded in aircraft composites to monitor structural integrity and provide damage detection. The failure of such sensors would not only affect the safety aspect, but also the cost. Usually some components of an optical system are accessible and can be repaired or replaced if required. However repairing or replacing an embedded sensor is difficult to say the least.

With Bragg grating sensors, there are a number of reliability issues that can affect sensor performance. These include:

- The decay of the UV inscribed RI pattern. Erdogen *et al* [68]
- Weakening of fibre due to UV exposure. El Shalzey *et al* [69]
- Weakening of fibre due to coating removal and recoating. Tarpey *et al* [70]
- How the sensing element is integrated with the structure. Glisic *et al* [71]

Taking into account all these different factors, it is a difficult task to estimate accurately the lifespan and reliability of Bragg grating sensors. The reliability issues have been studied and are well managed, although failure is probabilistic.

2.8 Long Period Fibre Gratings

LPFGs, like FBGs, are in-fibre photo-induced optical devices formed by periodically perturbing the RI of the fibres' core. They can also be mechanically induced. LPFGs couple forward propagating light from the fundamental core mode (LP_{01}) to the co-propagating fibre cladding modes of SMF at discrete wavelengths, and typically range between 100 μm up to many cm in length.

In principle, the same process for fabricating Bragg gratings can also be employed to fabricate LPFGs, in that the RI of the core is modified typically in the region of $\Delta n \sim 10^{-4}$. It should be noted that this index change is of a much smaller magnitude than that of their FBG counterparts, which has been shown to produce LPFGs that are stable of over a longer period of time [72].

With FBGs, the forward propagating mode in the core is coupled to backwards propagating modes, requiring a much smaller grating period. Therefore Bragg gratings can be interrogated in either reflection or transmission, as discussed at length earlier in this chapter. However, in the instance of LPFGs, light is coupled at discrete wavelengths out of the core to one or more of the numerous forward co-propagating cladding modes [73].

LPFGs have a number of characteristics that are advantageous over other sensors. As with their FBG counterparts, these include lightness and compactness and low insertion loss. They are also relatively easy to fabricate when compared to FBGs and have a larger RI coefficient than FBGs. Also, for a FBG to be sensitive to the external medium, the cladding has to be etched to gain access to the evanescent field of the guided mode, which reduces the mechanical strength of the fibre. This is not necessary with LPFGs.

2.8.1 Principle of operation

Vengsarkar *et al* first reported the principle of operation for LPFGs in 1995 as a spectrally selective band rejection filter [74]. The principle of operation is illustrated diagrammatically in Figure 2.11. It highlights how the light in the fundamental core mode (LP_{01}) is being perturbed upon reaching the LPFG structure in the fibre core.

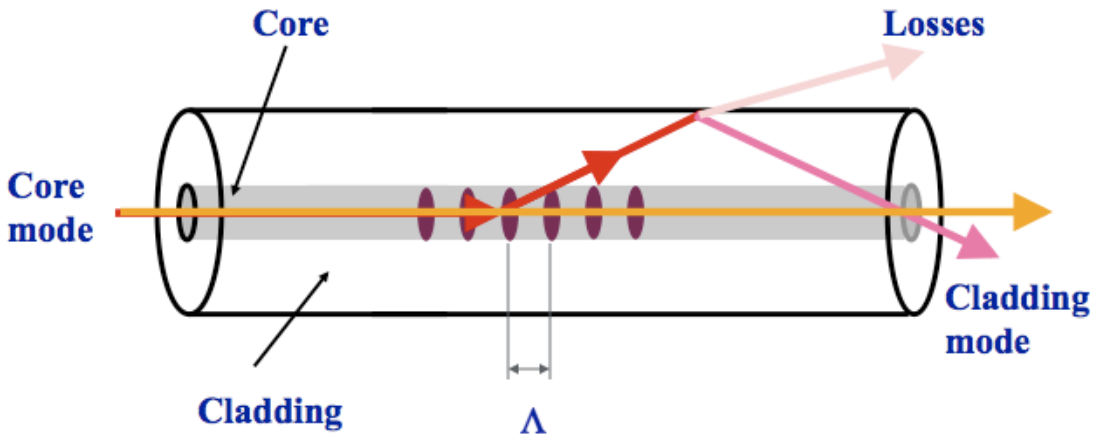

Figure 2.11 A schematic diagram of a LPFG illustrating coupling of the fundamental core mode to co-propagating cladding modes

When light from an optical source propagating along the fibre reaches the grating structure, elements of the light are diffracted from the fibre core mode to the co-propagating cladding modes. The elements that are coupled to the cladding modes appear lost when observing the transmission spectrum. These lost light elements are known as attenuation or loss bands and appear at discrete resonant wavelengths. After light is

coupled to into the cladding it quickly decays due to scattering losses. The wavelengths of these attenuation bands are dependant on the grating period Λ, and the refractive indices of the fibre core, fibre cladding, and the surrounding medium. Thus when a LPFG is exposed to perturbations of the RI of the external surrounding medium, the result is a change in the minimum attenuation value and/or resonant wavelength of one or more of the attenuation bands. This will be discussed further in section 2.8.3.

2.8.2 The phase matching condition

LPFGs can phasematch the coupling of power between core and cladding modes propagating in an optical fibre. To induce this power transfer, the phase of one of the propagating modes can be perturbed such that it matches the phase of another co-propagating mode. This is known as the phase matching condition.

The general expression for the phase matching condition of fibre gratings is given as:

$$\beta_{01} - \beta = \Delta\beta = \frac{2\pi}{\Lambda} \qquad \textbf{Equation 2.34}$$

where β_{01} is the propagation constant of the fundamental core mode, β is the propagation constant of the co-propagating cladding mode to which the light is coupled, and Λ is the grating period. As previously stated, LPFGs couple light from the fundamental core mode to the co-propagating cladding, hence for LPFGs $\beta = \beta_{cl}^{m}$ for a given coupling, where β_{cl}^{m} is the propagation constant for the m^{th} cladding mode.

As $\beta = 2\pi n / \lambda$, equation 2.34 can be rewritten as [74]:

$$\lambda_{res} = \left(n_{co}^{eff} - n_{cl,m}^{eff}\right)\Lambda \qquad \textbf{Equation 2.35}$$

Where λ_{res} is the resonant wavelength, Λ is the grating period and $n_{co}^{eff}$and $n_{cl,m}^{eff}$ are the effective refractive indices of the fundamental core mode and the m^{th} cladding mode, respectively. Equation 2.35 states that any change in grating period or perturbation of the effective refractive indices of the core and cladding results in a modification of the LPFG spectrum. The wavelength dependency of the effective refractive indices is due to waveguide and material dispersion. It can be assumed that the material dispersion has the same effect on both n_{co}^{eff} and $n_{cl,m}^{eff}$, therefore the foremost factor for a change in the LPFG spectrum is waveguide dispersion [75]. Differentiating equation 2.35 gives:

$$\frac{d\lambda_{res}}{d\Lambda} = \frac{\left(n_{co}^{eff} - n_{cl,m}^{eff}\right)}{\left\{1 - \Lambda\left[\frac{dn_{co}^{eff}}{d\lambda} - \frac{dn_{cl,m}^{eff}}{d\lambda}\right]\right\}}$$ **Equation 2.36**

As only the cladding modes interact with the surrounding medium, any perturbation in the surrounding medium, such as a change in temperature or RI, will also affect the LPFG spectrum. For variations of the surrounding RI n_{sur}, n_{co}^{eff} can be regarded as independent of n_{sur}, however $n_{cl,m}^{eff}$ can not. This is because the light in the core is bound within the core, thus not interacting with the surrounding medium. Therefore only the cladding modes that extend out of the fibre are affected by changes to the RI of the surrounding medium. Using equation 2.35, the expression for the surrounding RI sensitivity can be derived [76]:

$$\frac{d\lambda_{res}}{n_{sur}} = \lambda_{res}.\gamma.\left(\Gamma_{sur}\right)$$ **Equation 2.37**

where Γ_{sur} represents the RI dependence, and γ is the waveguide dispersion, derived as [75]:

$$\gamma = \frac{\frac{d\lambda_{res}}{d\Lambda}}{\left(n_{co}^{eff} - n_{cl,m}^{eff}\right)}$$ **Equation 2.38**

This waveguide dispersion γ is a general sensitivity factor and is independent of n_{sur}. It describes the sensitivities of the various modes related to just the LPFG properties. Therefore it stands to reason that certain coupled cladding modes are more sensitive to variations of the surrounding medium than others.

The RI dependence Γ_{sur}, is derived as:

$$\Gamma_{sur} = -\frac{u_m^2 \lambda_{res}^3 n_{sur}}{8\pi r_{cl}^3 n_{cl}\left(n_{co}^{eff} - n_{cl,m}^{eff}\right)\left(n_{cl}^2 - n_{sur}^2\right)^{3/2}}$$ **Equation 2.39**

where u_m is the mth root of the zero order Bessel function of the first kind, and n_{cl} is the RI of the cladding. Whilst equation 2.39 is relatively complex, a good approximation of Γ_{sur} is:

$$\Gamma_{sur} \approx -\frac{1}{\left(n_{co}^{eff} - n_{cl,m}^{eff}\right)\left(n_{cl}^2 - n_{sur}^2\right)^{3/2}}$$ **Equation 2.40**

Equation 2.40 stipulates that the sensitivity of a LPFG will increase as the surrounding RI approaches that of the cladding RI, so long as the surrounding RI is less than the cladding RI, fulfilling the condition $n_{sur} < n_{cl}$. At the condition where the surrounding RI is equal to the RI of the cladding, fulfilling the condition $n_{sur} = n_{cl}$, the cladding is considered to be infinite and therefore cannot support any modes, resulting in no attenuation bands present when observing the transmission spectrum. If the surrounding RI is higher than the cladding RI, fulfilling the condition $n_{sur} > n_{cl}$, the interface between the cladding and surrounding medium is no longer acting as a waveguide as total internal reflection cannot take place. In this case the sensitivity of the attenuation bands, with regard to wavelength shift and transmission value, is significantly reduced. For this condition, attenuation bands exist due to Fresnel reflection [77]. The work presented in this chapter is restricted to the condition $n_{sur} < n_{cl}$.

2.8.3 The minimum transmission value

Cladding modes experience high attenuation values and depend upon both the efficiency of the coupling between the core and cladding modes, and the LPFG length [77]. For a given LPFG, the minimum transmission value is given by:

$$T(L) = \sin^2(kL) \qquad \textbf{Equation 2.41}$$

where L is the LPFG length and k is the coupling coefficient.

When the LPFG is partially immersed into any liquid that possesses a different RI than air, then effectively two separate LPFGs are formed in series. Usually, for each coupled cladding mode, two distinct attenuation bands are visible. One attenuation band will be at the coupling wavelength for that of air (X), and another at the coupling wavelength for the liquid to which the LPFG has been immersed (Y). The effective length of these two LPFGs is attributed to how much of the LPFG has been immersed. By using equation 2.41, the minimum transmission values for the respective attenuation bands X and Y can be expressed as:

$$T_X(l,L) \propto \sin^2\left[\frac{\pi}{2}\left(\frac{l}{L}\right)\right] \qquad \textbf{Equation 2.42}$$

$$T_Y(l,L) \propto \sin^2\left[\frac{\pi}{2}\left(\frac{L-l}{L}\right)\right] \qquad \textbf{Equation 2.43}$$

where l is immersed length. Equations 2.42 and 2.43 are valid for the condition $0 < l < L$. Figure 2.12 diagrammatically illustrates this concept.

However if the dispersion condition of the LPFG is properly chosen by choosing the appropriate grating period, the combined spectral response of this pair of LPFGs exhibits a shift in the resonant wavelength of the attenuation band at the rate associated with the immersed length. When the LPFG is fully immersed in the liquid, the spectral response is that of the LPFG with the external RI of the liquid.

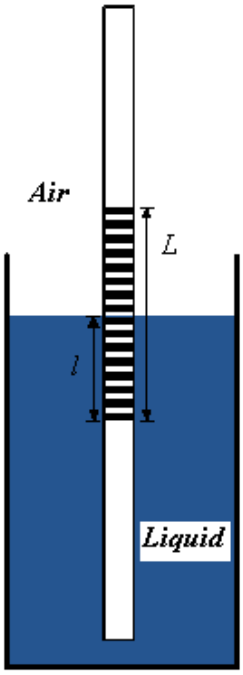

Figure 2.12 Concept of two LPFGs formed in series by partial immersion

2.8.4 Long period fibre grating fabrication

LPFGs can be manufactured either by mechanical induction, or by photo-inducing a modulation of the RI of the core of SMF, which is achieved by exposing the fibre to UV irradiation. The latter manufacturing technique can either be inscribing on a point-by-point basis, or by exposing the entire length of fibre continuously by means of a phase mask. By observing the transmission spectrum, distinct attenuation bands are evident at discrete wavelengths.

The photo-induced LPFGs utilised in Chapter 5 were fabricated by exposing presensitised Corning SMF-28 fibre to UV irradiation of 244 nm from a continuous wave (CW) argon

laser using the point-by-point inscription technique. The laser system configuration is shown in Figure 2.13.

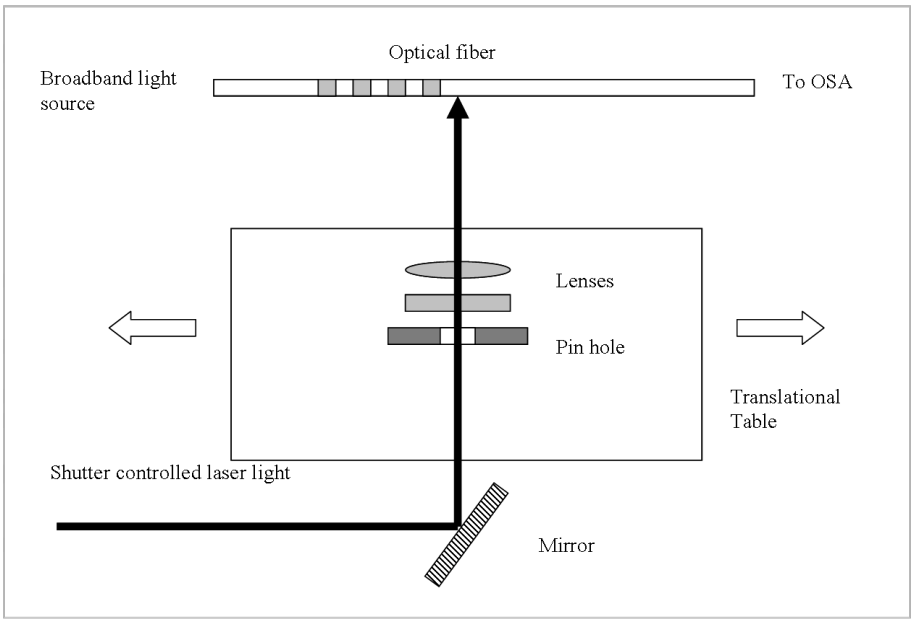

Figure 2.13 Laser system arrangement for writing an LPFG using the point-by-point inscription technique

The principal of operation for this system is that the incident laser light is focused onto the optical fibre, perpendicular to the fibre core axis, by means of cylindrical focusing lenses, which focuses the light in the x direction via a microscope objective. The system also comprises of a controllable motorised translation stage, which translates from left to right along the fibre, enabling the pre-programmed shutter-controlled laser light to periodically inscribe the LPFG on a point-by-point basis. The parameters that can be pre-programmed into the system are the grating period Λ, and the speed of the translation stage. These are programmed to suit the required grating specifications. The accuracy of this system largely depends upon the positional accuracy of the motor, and is typically < 0.1 nm per grating fringe.

Prior to fabrication, the fibre was first presensitised by hydrogen loading at 80°C / 180 bar for 60 hours before exposing it to the UV light. The hydrogen in the core acts to increase the photosensitivity of the fibre, with any unused hydrogen diffusing out over a period of time after the exposure. Once the gratings were written, they were placed in an oven for 24 hours at 80°C for annealing, this acts to stabilise the grating spectrum. Should the newly fabricated LPFG not be annealed, the hydrogen would still deplete from the fibre, however at a much slower rate resulting in spectrum instability.

An in-depth analysis of UV inscription, presensitising of optical fibres and thermal annealing has been extensively discussed earlier in this chapter.

2.9 Chapter conclusion

This chapter has presented an overview of the advancements in FBG technology since its inception. It has given the reader an understanding of optical fibres and the photosensitivity enhancement techniques that can be utilised. It has also given insight to FBGs and the inscription techniques used to write them, such as inscription by holographic interferometry, phase mask and direct writing.

The chapter has provided an insight to the numerous measurands that FBGs can measure, such as strain, temperature and pressure. It has also given insight to cross-sensitivity between these parameters and how they can be compensated for.

The two predominant multiplexing techniques, WDM and TDM, for interrogating single-sensor elements and multiple-sensor arrays have been introduced and evaluated. The evaluation has shown that each technique has its own advantages and disadvantages.

The chapter has introduced optical fibre sensors, their advantages over their electrical/electro-mechanical counterparts and the factors that need to be considered when evaluating sensor lifespan and reliability.

Finally the chapter has introduced LPFGs which were used for work conducted in Chapter 5.

This chapter serves as the basis for the following experimental chapters.

2.10 Chapter references

[1] R. Ulrich, "*Polarization stabilization on single mode fiber*" Applied Physics Letters, vol. 35, Iss. 11, pp. 840-842, 1979

[2] T. Okoshi, "*Polarization state control schemes for heterodyne and homodyne optical fiber communications*" Journal of Lightwave Technology, vol. LT-3, Iss. 6, pp. 1232-1237, 1985

[3] K. H. Wanser and N. H. Safar, "*Remote polarization control for fiber optic interferometers*" Optics Letters, vol. 12, Iss. 3, pp. 217-219, 1987

[4] A. D. Kersey, A. Dandridge and A. B. Tveten, "*Elimination of polarization induced signal fading in interferometric fiber sensors using input polarization control*" Proceedings 5th International Conference on Optical Fiber Sensors, (OFS-5, New Orleans, USA), Technical Digest, pp. 44-47, 1988

[5] K. O. Hill, Y. Fujii, D. C. Johnson and B. S. Kawasaki, "*Photosensitivity in optical fibre waveguides: application to reflection filter fabrication*", Applied Physics Letters, vol. 32, pp. 647-649, 1978

[6] B. Poumellec, P. Niay, M. Douay and J. F. Bayons, "*The uv-induced refractive index grating in Ge:SiO_2 preforms: Additional CW experiments and the macroscopic origin of the change in index*", Journal of Physics. D: Applied Physics., 29, pp. 1842-1856. 1996

[7] D. L. Williams, B. J. Ainsile, J. R. Armitage, R. Kashyap and R. Campbell, "*Enhanced UV photosensitivity in Boron Co doped Germanosilicate Fibres*" Electronics Letters, vol. 29, Iss.1, pp. 45-47, 1993

[8] P. J. Lemaire, R. M. Atkins, V. Mizrahi and W. A. Reed, "*High-Pressure H-2 Loading As a Technique For Achieving Ultrahigh UV Photosensitivity and Thermal Sensitivity in Geo2 Doped Optical Fibres*", Electronics Letters, vol. 29, Iss. 13, pp. 1191-1193, 1993

[9] A. Othonos and K. Kalli, "Fibre Bragg Gratings", Artech House Publishers, ISBN 0890063443, 1st Edition, 1999

[10] R. M. Atkins, P. J. Lemaire, T. Erdogan and V. Mizrahi, "*Mechanisms of enhancing UV photosensitivity via hydrogen loading in germanosilicate glasses*" Electronics Letters, vol. 29, Iss. 14, pp. 1234-1235, 1993

[11] Z. Yang, Q. Zhang and Z. Jiang, "*Photo-induced refractive index change of bismuth-based silicate glass*", J.Phys. D: Appl. Phys. vol. 38, pp. 1461-1463, 2005

[12] G. M. Williams, T. Tsung-Ein, C. I. Merzbacher and E. J. Friebele, "*Photosensitivity of rare-earth doped ZBLAN fluoride glasses*", Journal of Lightwave Technology, vol. 15, Iss. 8, pp. 1357-1362, 1997

[13] M. Douay, W. X. Xie, T. Taunay, P. Bernage, P. Niay, P. Cordier, B. Poumellec, L. Dong, J. F. Bayon, H. Poignant and E. Delevaque, "*Densification involved in the UV-based photosensitivity of silica glasses and optical fibres*", Journal of Lightwave Technology, vol. 15, Iss. 8, pp. 1329-1342, 1997

[14] M. G. Sceats, G. R. Atkins and S. Poole, "*Photo-induced index changes in optical fibres*", Annual Reviews in Material Science, vol. 23, pp. 381-410, 1993

[15] B. Malo, J. Albert, K. O. Hill, F. Bilodeau and D. C. Johnson, "*Effective index drift from molecular hydrogen diffusion in hydrogen-loaded optical fires and its effect on Bragg grating fabrication*" Electronics Letter, vol. 30, pp. 442-443, 1994

[16] J. Canning, M. Aslund and P. Hu, "*Ultraviolet-induced absorption losses in hydrogen-loaded optical fibres and in presensitized optical fibres*", Optics Letters, vol. 25, Iss. 22, pp. 1621-1623, 2000

[17] B. O. Guan, H. Y. Tam, X. M. Tao and X. Y. Dong, "*Highly stable fiber Bragg gratings written in hydrogen-loaded fiber*", IEEE Photon Technology Letters, vol. 12, Iss. 10, pp. 1349-1351, 2000

[18] L. Dong, J. L Cruz, L. Reekie, M. G. Xu and D. Payne, "*Enhanced photosensitivity in tin co-doped germanosilicate optical fibres*", IEEE Photonics Technology Letters, vol. 7, pp. 1048-1050, 1995

[19] E. M. Dianov, K. M. Golant, V. M. Mashinsky, O. I. Medvedkov, I. V. Nikolin, O. D. Sazhin and S. A. Vasilev, "*Highly photosensitive nitrogen-doped germanosilicate fibre for index grating writing*", Electronics Letters, vol. 33, pp. 1334-1336, 1997

[20] B. Malo, K. O. Hill, F. Bilodeau, D. C. Johnson and J. Albert, "*Point-by-point fabrication of micro-Bragg gratings in photosensitive fibre using single excimer pulse refractive index modification techniques*", Electronics Letter, vol. 29, pp. 1668-1669, 1993

[21] A. Asseh, H. Storoy, B. E. Sahgren, S. Sandgren and R. A. H. Stubbe, "*A writing technique for long fiber Bragg gratings with complex reflectivity profiles*", Journal of Lightwave Technology, vol. 15, pp 1419-1423, 1997

[22] I. Bennion, J. A. R. Williams, L. Zhang, K. Sugden and N. J. Doran, "*UV-written in-fibre Bragg gratings*", Optical and Quantum Electronics, vol. 28, pp. 93-135, 1996

[23] F. Bliodeau, B. Malo, J. Albert, D. C. Johnson, K. O. Hill, Y. Hibino, Y. Abe and M. Kawachi, "*Photosensitisation of optical fibre and silica-on-silicon/silica waveguides*", Optics Letters, vol. 18, pp. 953-955, 1993

[24] A. Yariv, "*Coupled Mode Theory for guided wave optics*", Journal of Quantum Electronics, vol. QE-9, Iss. 9, pp. 919-933, 1973

[25] G. Meltz, W. W. Morey and W. H. Glenn, "*Formation of Bragg Gratings in Optical Fibres By a Transverse Holographic Method*" Optics Letters, vol. 14, Iss. 15, pp. 823-825, 1989

[26] D. Lam and B. Garside, "*Characterization of single-mode fibre filters*", Applied Optics, vol. 20, pp. 440-445, 1981

[27] J. Senior, "*Optical Fibre Communications*", Prentice Hall, 1st Edition, 1992

[28] P. Russell, J. L Archambault and L. Reekie, "*Fibre gratings*", Physics World, vol. 6, pp. 41-46, 1993

[29] Y. J. Rao, "*In-fibre Bragg grating sensors*", Measurement Science and Technology, vol. 8, pp.355-375, 1997

[30] K. O. Hill, B. Malo, F. Bilodeau, D. C. Johnson and J. Albert, "*Bragg gratings fabricated in monomode photosensitive optical fibre by UV exposure through a phase mask*", Applied Physics Letters, vol. 62, pp. 1035-1037, 1993

[31] D. Z. Anderson, V. Mizrahi, T. Erdogan and W. White, "*Production of in-fibre gratings using a diffractive optical element*", Electronics Letters, vol. 29, pp. 556-567, 1993

[32] R. Kashyap, J. J. Armitage, R. Wyatt, S. T. Davey and D. L. Williams, "*All-fibre narrowband reflection gratings at 1550 nm"*, Electronics Letters, vol. 26, pp. 730-731, 1990

[33] J. Albert, K. O. Hill, D. C. Johnson, F. Bilodeau and M. J. Rooks, "*Moiré phase masks for automatic pure apodization of fibre Bragg gratings*", Electronics Letters, vol. 32, pp. 2260-2261, 1996

[34] J. Albert, K. O. Hill, B. Malo, S. Theriault, F. Bilodeau, D. C. Johnson and L. E. Erickson, "*Apodization of the spectral response of fibre Bragg gratings using a phase mask with variable diffraction efficiency*", Electronics Letters, vol. 31, pp. 222-223, 1995

[35] A. Othonos and X. Lee, "*Novel and improved methods of writing Bragg gratings with phase masks*", Photonic Technology Letters, vol. 7, No 10, pp. 1183-1185, October 1995

[36] Q. Zhang, D. A. Brown, L. Reinhart, T. F. Morse, J. Q. Wang and G. Xiao, "*Tuning Bragg Wavelength By Writing Gratings On Pre-Strained Fibres*" IEEE Photonics Letters, vol. 16, Iss. 7, pp. 839-841, 1994

[37] K. C. Byron and H. N. Rourke, "*Fabrication of Chirped Fibre Gratings By Novel Stretch and Write Technique*" Electronics Letters, vol. 31, Iss. 1, pp. 60-61, 1995

[38] C. G. Askins, M. A. Putnam, H. J. Patrick and E. J. Friebele, "*Fibre strength unaffected by on-line writing of single-pulse Bragg gratings*", Electronics Letters, vol. 33, pp. 1333-1334, 1997

[39] D. S. Starodubov, V. Grubsky and J. Feinberg, *"Efficient Bragg grating fabrication in a fibre through its polymer jacket using near-UV light"* Electronics Letters, vol. 33, pp. 1331-1333, 1997

[40] J. L. Archambault, L. Reekie and P. J. Russell, "*100% reflectivity Bragg reflectors produced in optical fibres by single excimer laser pulses*", Electronics Letters, vol. 29, pp. 453-455, 1993

[41] Y. Liu, J. A. R. Williams, L. Zhang and I. Bennion, "*Abnormal spectral evolution of fiber Bragg gratings in hydrogenated fibres*", Optics Letters, vol. 27, pp. 586-588, 2002

[42] L. Dong, W. F. Liu and L. Reekie, "*Negative-index gratings formed by a 193-nm excimer laser* ", Optics Letters, vol. 21, pp. 2032-2034, 1996

[43] J. Canning, "*Fibre gratings and devices for sensors and lasers*", Laser & Photonics Reviews, vol. 2, pp. 275-289, 2008

[44] V. M. Murukeshan, P. Y. Chan, L. S. Ong and A. Asundi, "*Intracore fiber Bragg gratings for strain measurement in embedded composite structures*", Applied Optics, vol. 40, pp. 145-149, 2001

[45] A. D. Kersey, M. A. Davis, H. J. Patrick, M. LeBlanc, K. P. Koo, M. A. Putnam and E. J. Friebele, "*Fiber grating sensors*", Journal of Lightwave Technology, vol. 15, Iss. 8, pp. 1442-1463, 1997

[46] R. Gafsi and M. A. El-Sherif, "Analysis of Induced-Birefringence Effects on Fiber Bragg Gratings", Optical Fiber Technology, vol. 6, pp. 299-323, 2000

[47] S. Pal, T. Sun, K. T. V. Grattan, S. A. Wade, S. F. Collins, G. W. Baxter, B. Dussardier and G. Monnom, "*Strain-independent temperature measurement using type-I and type IIA optical fiber Bragg grating combination*", Review of Scientific Instrumentation, vol. 75, Iss. 5, pp. 1327-1331, 2004

[48] H. J. Patrick, G. M. Williams, A. D. Kersey, J. R. Pedrazzani, A. M. Vengsarkar, "*Hybrid fiber Bragg grating/long period grating sensor or strain/temperature discrimination*", Photonics Technology Letters, vol. 8, pp.1223-1225, 1996

[49] S. W. James, M. L. Dockney and R. P. Tatam, "*Simultaneous independent temperature and strain measurement using in-fibre Bragg grating sensors*", Electronics Letters, vol. 32, pp. 1133-1134, 1996

[50] G. Simpson, K. Kalli, K. Zhou, L. Zhang and I. Bennion, "*An idealised method for the fabrication of temperature invariant Ia-I strain sensor*", Proceedings 16th International Conference on Optical Fibre Sensors, (OFS-16, Nara, Japan), Post-deadline paper PD4, 2005

[51] O. Frazao, M. J. N. Lima and J. L. Santos, "*Simultaneous measurement of strain and temperature using type I and type IIA fibre Bragg gratings*", Journal of Optics a-Pure and Applied Optics, vol. 5, Iss. 3, pp. 183-185, 2003

[52] M. G. Xu, J. L. Archambault, L. Reekie and J. P. Dakin, "*Discrimination between strain and temperature effects using dual-wavelength fiber grating sensors*", Electronics Letters, vol. 30, pp. 1085-1087, 1994

[53] K. Wang, Z. Wei, B. Chen and C. Hong-Liang, "*A Bridge-Style Fiber-Optic Weigh-In-Motion Sensor For Military Vehicle Monitoring*", Proceedings of SPIE, vol. 5778, part 1, pp.220-225, 1999

[54] H. Y. Tam, S. Y. Liy, B. O. Guan, W. H. Chung, T. H. T. Chan and L. K. Cheng, "*Fiber Bragg Grating Sensors for Structural and Railway Applications*", Proceedings of SPIE, vol. 5634, pp. 85-97, 2005

[55] N. Takahashi, K. Yoshimura, S. Takahashi and K. Imamura, "*Development of an optical fibre hydrophone with Fibre Bragg grating*", Ultrasonics, vol. 38, pp. 581-585, 2000

[56] Y. Zhao, K Chen and J. Yang, "*Novel target type flowmeter based on a differential fiber Bragg grating sensor*", Measurement, vol. 38, pp. 230-235, 2005

[57] R. Suresh, S. C. Tjin and N. Q. Ngo, "*Shear force sensing by strain transformation using non-rectilinearly embedded fiber Bragg gratings*", Sensor and Actuators A, vol. 116, pp. 107-118, 2004

[58] I. Prerez, H-L. Cui and E. Udd, "*Acoustic Emission Detection Using Fiber Bragg Gratings*", Proceedings of SPIE, vol. 4328, pp. 209-215, 2001

[59] M. A. Davies and A. D. Kersey, "*All fibre Bragg grating strain sensor demodulation technique using a wavelength division coupler*", Electronics Letters, vol. 30, Iss. 1, pp. 75-77, 1994

[60] A. D. Kersey, A. Dandridge and A. B. Tveten, "*Time division multiplexing of interferometric fiber sensors using passive phase generated carrier interrogation*", Optics letters, vol. 12, Iss. 10, pp. 775-777, 1987

[61] J. L. Brooks, R. H. Wentworth, R. C. Youngquist, M. Tur, B. Y. Kim and H. Shaw, "*Coherence multiplexing of fiber optic interferometric sensors*", Journal of Lightwave Technology, vol. LT-3, Iss. 5, pp. 1062-1072, 1985

[62] P. J. Henderson, D. J. Webb, D. A. Jackson, L. Zhang and I. Bennion, "*Highly multiplexed grating sensor for temperature referenced quasi static measurements of strain in concrete bridges*", in Proceedings 13th International Conference on Optical Fibre Sensors, OFS-13, Technical Digest, pp. 134-140, 1994

[63] R. W. Fallon, L. Zhang, A. Gloag and I. Bennion, "*Identical broadband chirped grating interrogation technique for temperature and strain sensing*", Electronics Letters, vol. 33, pp. 705-707, 1997

[64] A. B. Lobo Ribeiro, L. A. Ferreira, J. L. Santos and D. A. Jackson, "*Analysis of the reflective-matched fibre Bragg grating sensing interrogation scheme*", Applied Optics, vol. 36, pp. 935-939, 1997

[65] W. H. Chung and H-Y. Tam, "*Time- and Wavelength-Division Multiplexing of FBG Sensors Using a Semiconductor Optical Amplifier in Ring Cavity Configuration*", IEEE Photonics Technology Letters, vol. 17, pp. 2709-2711, 2005

[66] W. W. Morey, J. R. Dunphy and G. Meltz, "*Multiplexing fiber Bragg grating sensors*", Proceedings of SPIE, vol. 1585, pp. 216-224, 1991

[67] B. Lee, "*Review of the present status of optical fibre sensors*", Optical Fibre Technology, vol. 9, pp. 57-79, 2003

[68] T. Erdogen, V. Mizrahi, P. J. Lemaire and D. Monroe, "*Decay of ultraviolet induced fiber Bragg gratings*", Journal of Applied Physics, vol. 76, pp. 73-80, 1994

[69] Y. M. El Shazly and S. N. Kukureka, "*Reliability of optical fibre for optical fibre Bragg grating strain sensors*", Proceedings of SPIE, vol. 5502, pp. 188-191, 2004

[70] A. J. Tarpey, S. N. Kukureka and K. Jerkschat, "*The mechanical reliability of stripped and recoated fibre Bragg gratings for optical fibre sensors*", Proceedings of SPIE, vol. 4639, pp. 22-34, 2002

[71] B. Glisic and D. Inaudi, "*Sensing tape for easy integration of optical fiber sensors in composite structures*", Proceedings 16th International Conference on Optical Fiber Sensors, (OFS-16, Nara, Japan), Technical Digest, pp. 482-486, 2003

[72] F. Bakhti, J. Larrey and P. Sansonetto, "*Annealing of long period gratings in standard hydrogen-loaded fibre*", Conference: Bragg gratings, photosensitivity and poling in glass fibres and waveguides, Williamsburg, U.S.A, Technical Digest, 1997

[73] T. Erdogan, "*Cladding-mode resonances in short- and long-period fibre grating filters*", Journal of the Optical Society of America, vol. 14, pp. 1760-1773, 1997

[74] A. M. Vengsarker, P. J. Lemaire, J. B. Judkins, V. Bhatia, T. Erdogan, J. E. Sipe. "*Long Period Fiber Gratings As Band-Rejection Filters*" Journal of Lightwave Technology, vol. 14, pp. 58-64, 1996

[75] T. W. MacDougall, S. Pilevar, C. W. Haggans, and M. A. Jackson, "*Generalized expression for the growth of long period gratings*", *IEEE, Photonics Technology Letters*, vol. 10, pp. 1449–1451, 1998

[76] X. Shu, T. Allsop, B. Gwandu, L. Zhang, and I. Bennion, "*Room-temperature operation of widely tunable loss filter*", *Electronics. Letters*, vol. 37, pp. 216–218, Feb. 2001

[77] O. Duhem, J. F. Henninot, M. Warenghem and M. Douay, "*Demonstration of long-period grating efficient couplings with an external medium of a refractive index higher than that of silica*" Applied Optics, vol. 37, pp. 7223–7228, 1998

3 Novel fibre Bragg grating techniques for static and dynamic industrial weighing applications

3.1 Chapter preamble

Avery Weigh-Tronix is a market leading company specialising in weighing systems, both in the UK and internationally, and has a history stretching back to the 18th century. The majority of Avery's products are electronic and are based on two technologies: strain gauge technology, which has been employed for over 30 years, and vibrating beam technology which has been employed for over 10 years. As a company operating on the cutting edge of technology, Avery decided to look for other innovative ways of load sensing that could be applied to the weighing and measuring markets. The PhD project was designed to identify a commercial opportunity using Bragg grating sensors in the weighing industry, and then formulate and test novel concepts to meet the needs of those commercial opportunities.

From the offset of this project, Avery explicitly expressed a desire to integrate Bragg grating technology into their current products rather than develop completely new systems. Therefore the novelty in this work arises primarily from the integration techniques rather than from the design of new products for the Avery product catalogue.

The chapter begins with presenting the results of a series of market research presentation & brainstorm sessions highlighting the current and potential markets for this technology. From there, a brief description of Avery's current electrical strain gauge and vibrating beam technology is introduced to the reader.

The chapter presents the initial experiments with an in-house designed cantilever system. These experiments were designed to demonstrate to Avery the characteristics of a FBG sensor as a means of measuring load, as well as investigating the potential linearity, repeatability and sensitivity of the system.

The chapter then goes on to introduce the T702 beam and the experimental configuration and procedure is then given, followed by the results obtain for the static loading tests. Continuing on, the chapter discusses the design and fabrication of e-glass patches with embedded FBGs for dynamic loading applications, including the bonding procedure. The experimental arrangement and procedure for the single-FBG patch is then presented

followed by the results obtain from said system. Directly following on, the experimental arrangement and procedure, and the results for the double-FBG patch are presented. Conclusions from the work are then presented, as are avenues of future work.

3.2 Market research

This project was Avery's first venture into FBG technology, therefore before conducting any experimental research, it was vital to first educate the relevant Avery personnel about the technology, and once familiar with the technology and its advantages and limitations, discuss the possible markets and applications (current and new) where this technology could be deployed.

Conducting a series of presentations and brainstorming sessions with Avery engineers, marketers, business strategists and executive managers facilitated the identification of such applications and markets. In all, four sessions were conducted, these were:

1. UK and US Engineers. 20.July.2006
2. Marketing UK. 04.August.2006
3. RailWeight UK. 10.August.2006
4. US Production Managers 11.September.2006

The results of the sessions were as follows:

Session 2: UK & US Engineers 20.July.2006

The following is a list of applications proposed at this session:

- Axle loading monitoring on bridge structures
- WIM
- Temperature and flat wheel monitoring
- On board weighing
- Deck scales
- Deployed in radioactive environments
- Sorting Applications

Session 2: UK Marketing 04.August.2006

The following is a list of applications proposed at this session:

- WIM speed camera systems to detect overloading, where subsequent fines could be imposed on offenders
- Lorry trailer weighing
- Static weighing
- Mobile mat device
- On board weighing built into chassis of vehicles
- Marine applications (freight shipping and fishing trawlers)
- Tank farms where fibre runs the circumference of the tank
- Neural networks for shape recognition
- Security and forensic activities
- Medical applications (weighing patients in hospital bed)
- Cement and flour silo monitoring

Session 3: RailWeight UK 09.August.2006

The following is a list of applications proposed at this session:

- Flat spot and wheel defection detection
- Temperature measurement
- Wheel counting for signalling applications
- Vehicle determination
- Load cell within sleeper (‘active sleeper’)

Session 4: Production Managers US 11.September.2006

The following is a list of applications proposed at this session:

- Front end loading
- Floor scales
- Marine applications (freight shipping and fishing trawlers)
- Sensors embedded into pallets (‘smart pallet’)
- Oil & Gas applications
- Flow rate (oil & gas, mining, aggregates, food)

- Inventory management system on shelves with RF ID tag
- Pressure monitoring particularly high pressures

Also, an evaluation of the current Avery markets was conducted against advantages of FBG technology, the results clearly tallied in with the findings from the presentation/brainstorm sessions, highlighting the transportation and logistics industry as the most suitable candidate to focus the attention of this research. The results are summarised in Table 3.1.

	ADVANTAGES						
	Compact	Multiplexing	Embedding/Bonding	Immune to EMF and Nuclear Radiation	Safe in explosive environments	Work in harsh environments	Hygiene
Food and Beverage			☑			☑	☑
Chemical and Petrochemical				☑	☑	☑	
Waste, Mining and Aggregates	☑	☑	☑			☑	
Transportation and Logistics	☑	☑	☑	☑	☑	☑	
Retail		☑					☑

Table 3.1 Advantages of FBG technology applied to current Avery markets.

Clearly not all applications identified in the four sessions could be investigated due to time constraints, therefore it was decided that two areas would be addressed, these are:

- Static loading (Static load cell)
- Dynamic loading (Rail WIM)

3.3 Static loading

Electrical load cells are used in a number of industries, from oilrig construction to Formula 1 racing cars. In the weighing industry, load cells are required to meet strict performance criteria, which is set out by the International Regulatory Body (OIML R60), and rigorously policed by the National Weights and Measurements authority of the country in which the load cell is deployed. It must be stressed that the work in the chapter is designed to research the feasibility of developing an optical equivalent of an Avery electrical load cell, and not to develop a commercial product to meet the OIML R60 requirements.

Despite there being a number of optical load cell techniques reported [1]-[3], Avery currently only use electrical strain gauge load cells, of which there are three main types, these are:

- Single point – this consists of a single cell bolted directly to a weighing platform. These are used in shop scales and the smaller industrial scales. The system can measure in a range of grams to 1000 kg. The concept is based on using bending strain

- Beam cell – using four cells, one in each corner of a weighing platform. These are commonly used in the larger industrial scales. This system can measure in the region of 500 kg up to 10,000 kg. This concept is based on measuring shear strain in the web of an I-beam

- Compression cell – this can comprise of four, six or eight cells supporting a weighbridge. Common applications are in road transport load monitoring. Typically this system can measure from 5000 kg to 100 tonne. The concept is based on directly measuring compressive strain

All three concepts are based on the Wheatstone Bridge principle, as this offers inherent thermal stability and a low signal to noise ratio. All four resistors in these systems are active, which increases the output and therefore the resolution available can also be increased. Figure 3.1 illustrates the basic concept of a Wheatstone bridge load cell. Strain gauges SG 1 and SG 3 will increase in resistance, SG 2 and SG 4 will decrease. The change in the resistance of the strain gauge is a direct result of a change in mechanical stress on the surface of the load cell element. The stress change itself being caused by a change in the measured load.

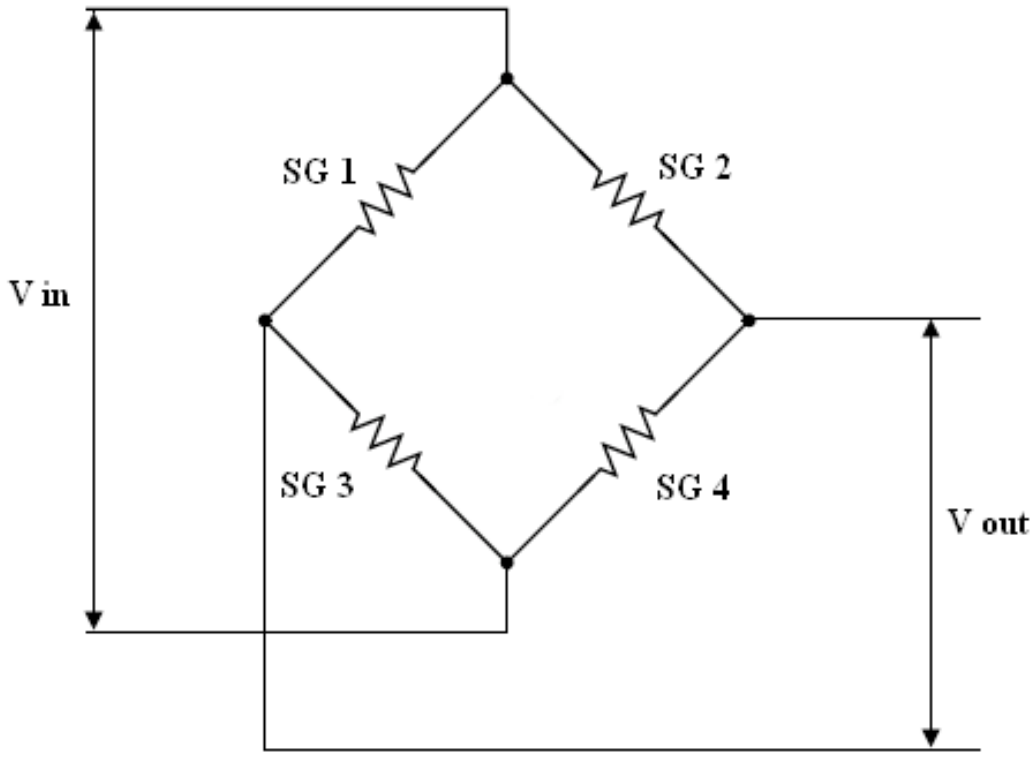

Figure 3.1 Wheatstone bridge

For each of the three strain gauge types described above, Avery offers numerous variants. The aim of the work presented in this chapter was to investigate the feasibility of making an optical variant of their T702 vibrating beam system. Current applications for said system are in shop scales, post office counter scales and airport baggage scales.

Prior to working on the T702, Avery wished to pursue a cantilever type approach to analyse the sensitivity, linearity and feasibility of such a system.

3.3.1 FBG-based cantilever system

The concept of this experiment is based on the elongation of a FBG sensor bonded to a cantilever. The aluminium cantilever was designed in-house and fabricated by RPS Engineering. The cantilever had a 200 μm V-groove running along the centre line and it is here where the FBG is bonded. The FBG is bonded 30 mm from the near end of the cantilever.

3.3.1.1 Cantilever experimental configuration and procedure

Figure 3.2a is a diagram of the experimental arrangement. Figure 3.2b is a picture of the cantilever housed in the loading system; note the hook to hang the weights off.

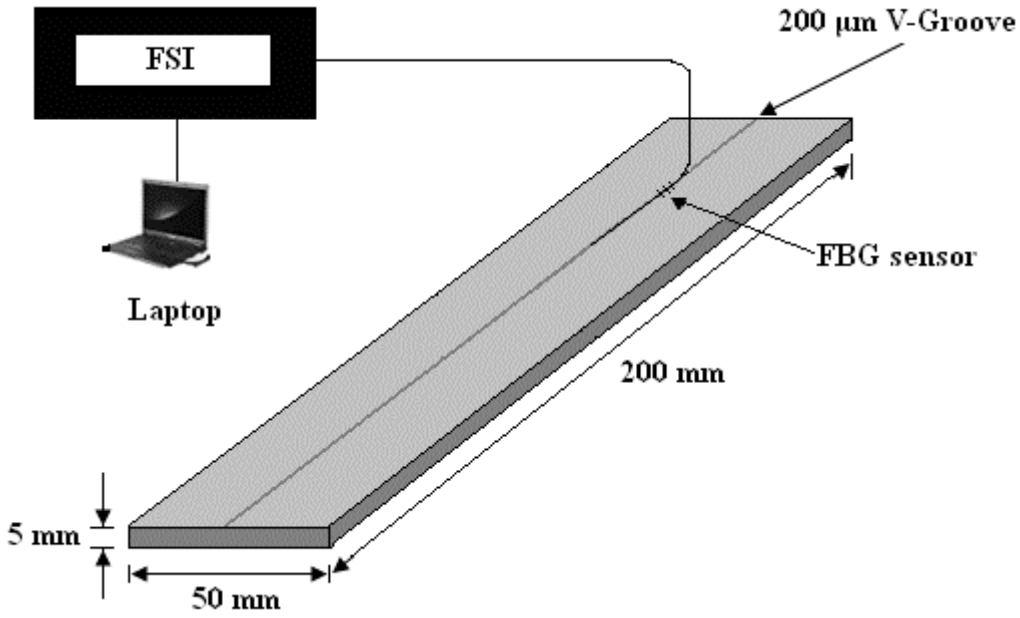

Figure 3.2a Aluminium cantilever experimental configuration

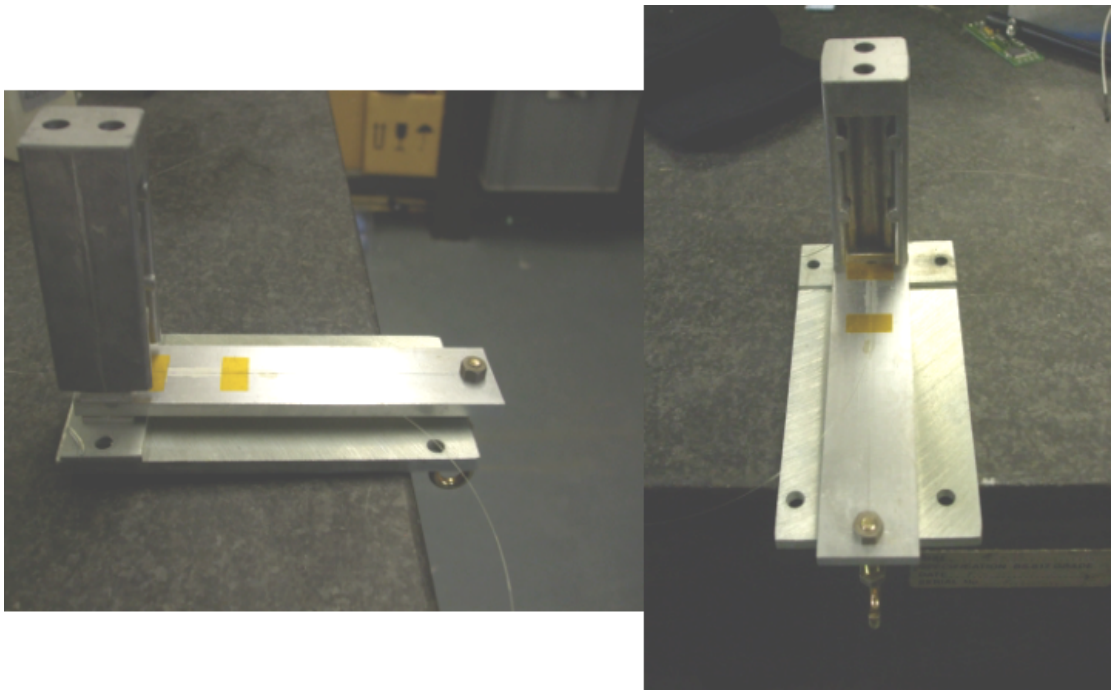

Figure 3.2b Picture of the cantilever system

The FBG was bonded in the V-groove using Micromeasurements 610 epoxy and left to cure at room temperature for 24 hours.

The experimental procedure simply consisted of hanging a series of loads from the hook, and measuring the wavelength shift of the FBG using the Insensys FSI.

3.3.1.2 Cantilever experimental results

The results presented in this section are taken from a series of tests conducted on the cantilever set-up. Note that all tests were conducted in a temperature-controlled environment to remove the temperature effect from the FBG sensors' response. Prior to conducting the series of tests, both the cantilever and weights were placed in the temperature-controlled environment and allowed to "soak" for a period of three hours.

Figure 3.3 illustrates a 1 kg load cycle. The wavelength shift induced by the 1 kg load is approximately 112 pm.

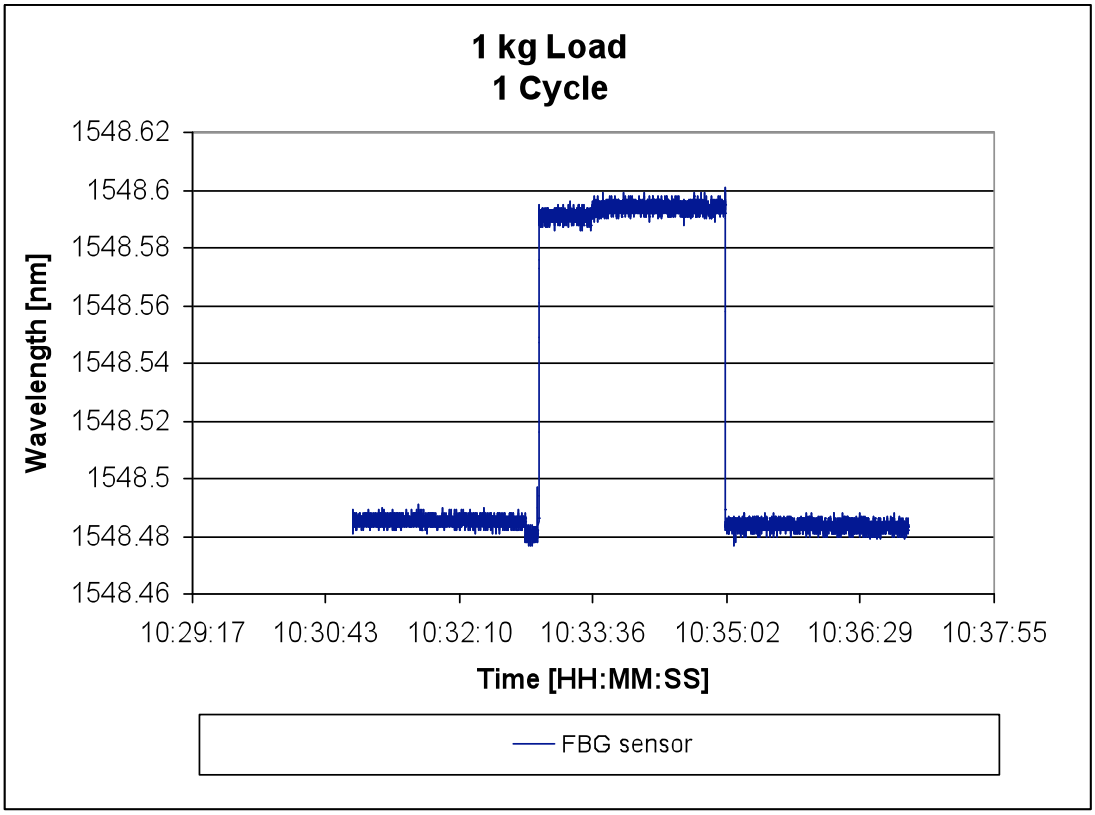

Figure 3.3 Cantilever 1 kg cycle

The next test shows a 2 kg cycle. The load was added and removed in 1 kg increments. Figure 3.4a shows the result of wavelength shift as a function of time, Figure 3.4b shows the same result as a function of load.

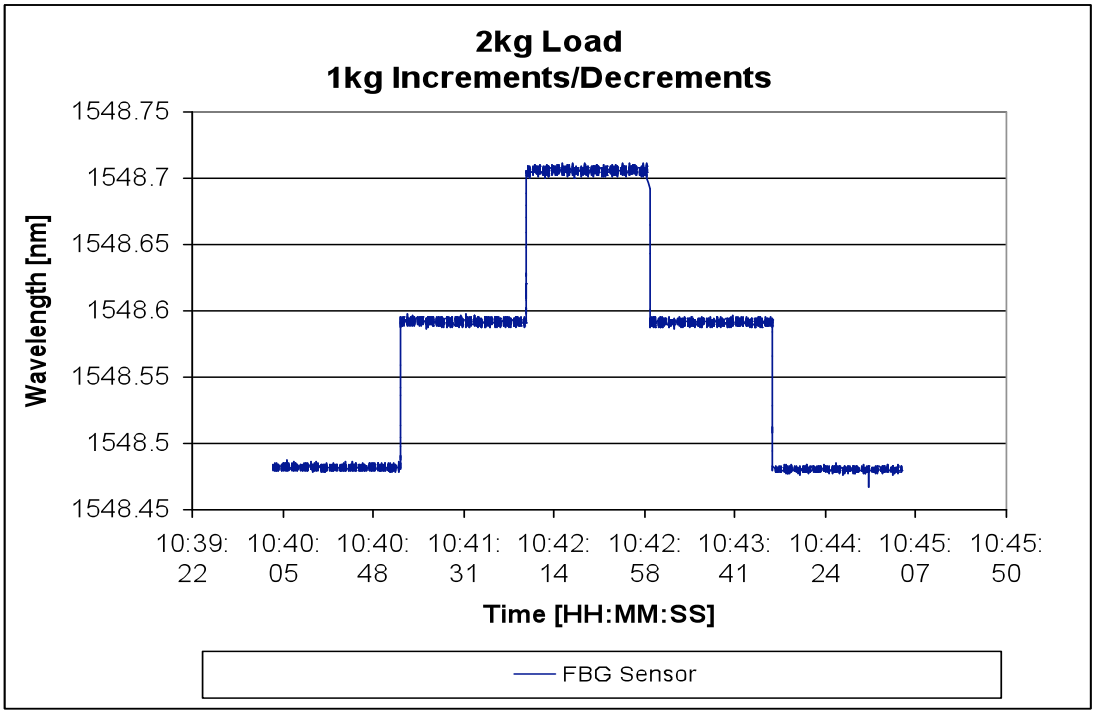

Figure 3.4a 2 kg cycle in 1 kg increments/decrements (function of time)

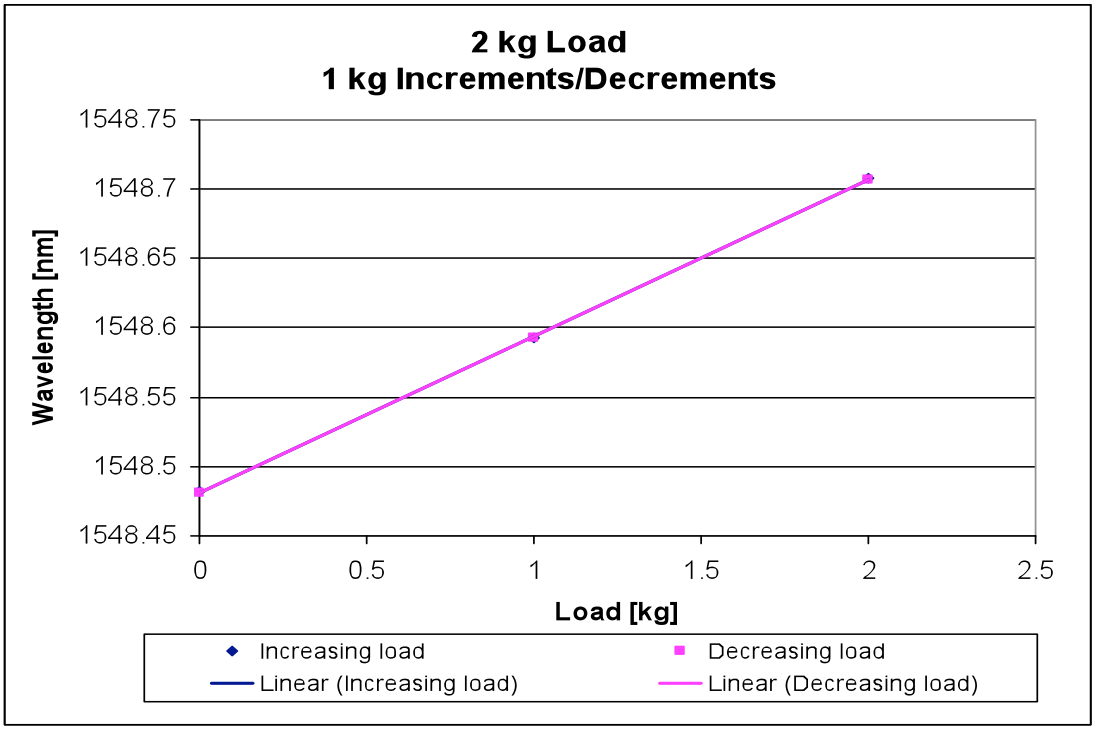

Figure 3.4b 2 kg cycle in 1 kg increments/decrements (function of load)

The next test increased the load to 10 kg, loading and unloading the system in 2 kg increments/decrements. Figures 3.5a and 3.5b shows the results of wavelength shift as a function of time and load respectively.

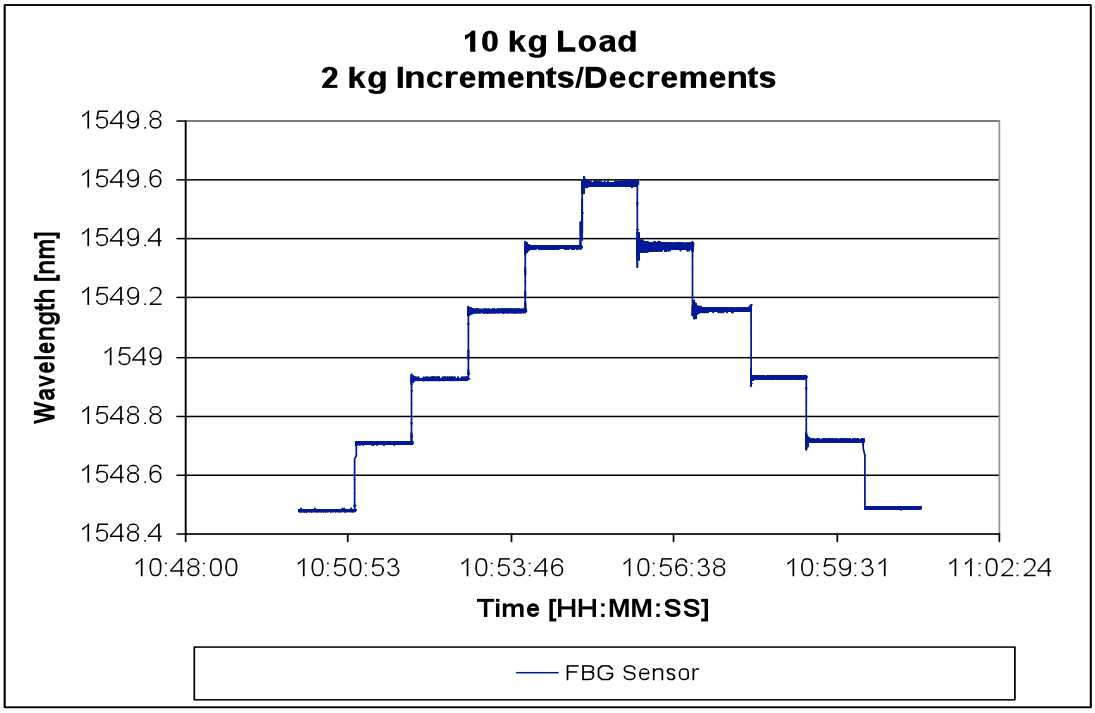

Figure 3.5a 10 kg cycle in 2 kg increments/decrements (function of time)

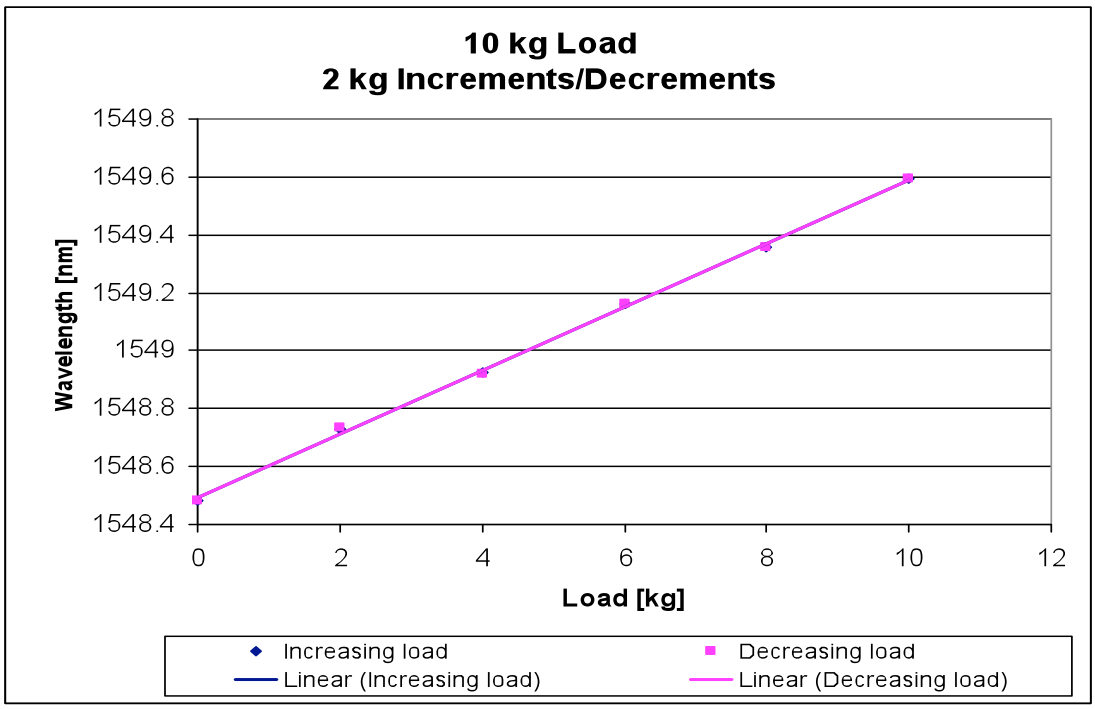

Figure 3.5b 10 kg cycle in 2 kg increments/decrements (function of load)

The results presented have shown the system is highly linear over the complete measurement range. Another factor, which is vital to the accurate measurement of load is repeatability. Figures 3.6a and 3.6b show five 2 kg incremental and decremental 10 kg cycles respectively.

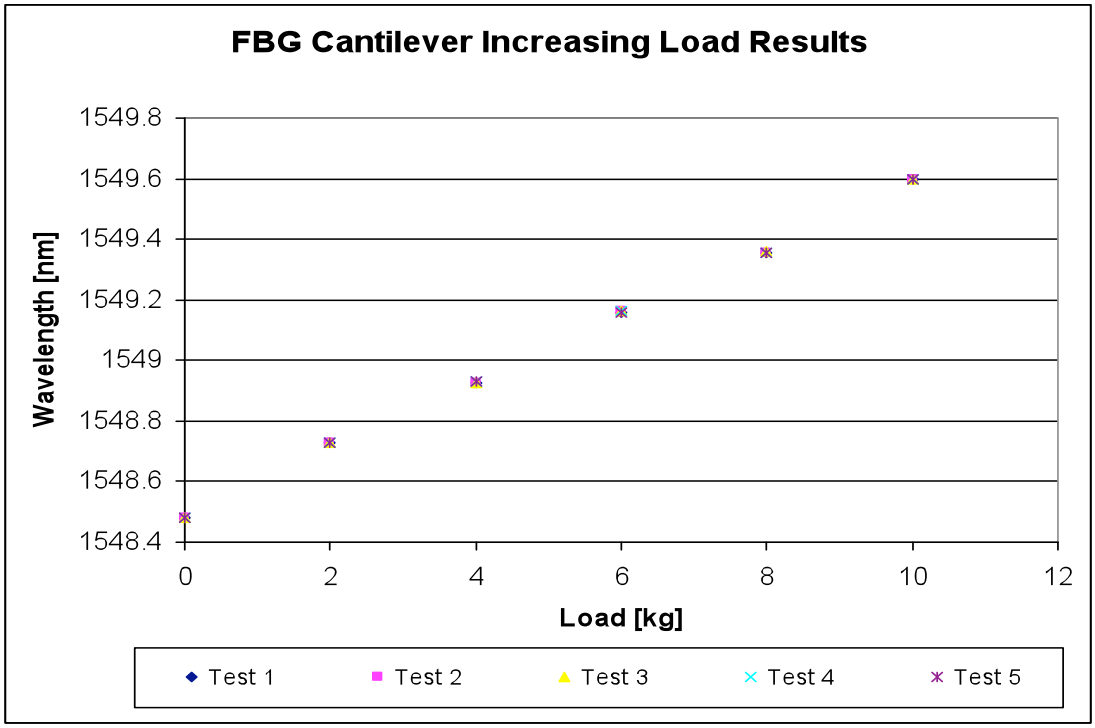

Figure 3.6a Five 10 kg load cycles – increasing load

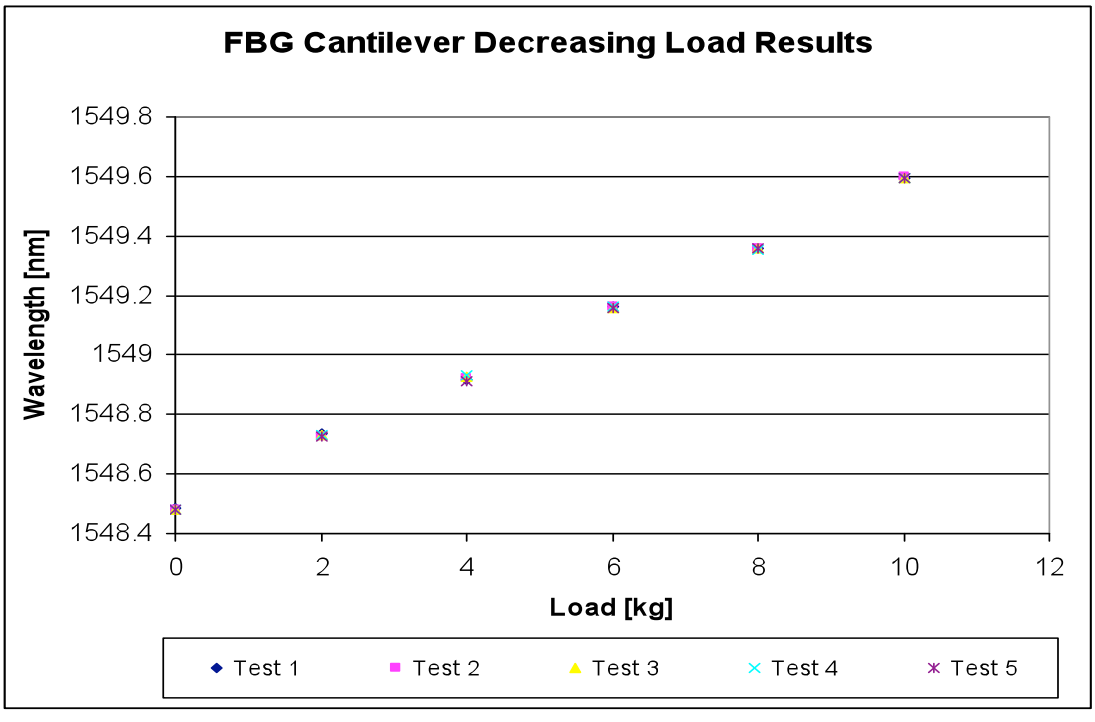

Figure 3.6b Five 10 kg load cycles – decreasing load

To stress the repeatability of the above results, the wavelength values for the five increasing tests and decreasing tests are shown in Tables 3.2a and 3.2b respectively.

Load [kg]	Test 1 Wavelength [nm]	Test 2 Wavelength [nm]	Test 3 Wavelength [nm]	Test 4 Wavelength [nm]	Test 5 Wavelength [nm]
0	1548.482	1548.482	1548.483	1548.483	1548.483
2	1548.729	1548.728	1548.73	1548.729	1548.728
4	1548.924	1548.924	1548.928	1548.931	1548.93
6	1549.16	1549.161	1549.161	1549.162	1549.159
8	1549.357	1549.356	1549.358	1549.357	1549.357
10	1549.596	1549.597	1549.596	1549.596	1549.597

Table 3.2a Wavelengths at incremental loads

Load [kg]	Test 1 Wavelength [nm]	Test 2 Wavelength [nm]	Test 3 Wavelength [nm]	Test 4 Wavelength [nm]	Test 5 Wavelength [nm]
0	1548.484	1548.482	1548.482	1548.481	1548.482
2	1548.737	1548.727	1548.731	1548.729	1548.727
4	1548.919	1548.929	1548.929	1548.93	1548.91
6	1549.161	1549.16	1549.16	1549.161	1549.16
8	1549.359	1549.357	1549.357	1549.355	1549.356
10	1549.596	1549.597	1549.596	1549.596	1549.597

Table 3.2b Wavelengths at decremental loads

The overall wavelength shift when 10 kg of load is applied in approximately 1114 pm, it is feasible that a sensitivity in the region of 111 pm/kg.

One final result, to demonstrate the sensitivity of the system was to load the system with lighter loads. Figures 3.7a and 3.7b illustrates a 250 g cyclic test, loading and unloading in 50 g increments/decrements.

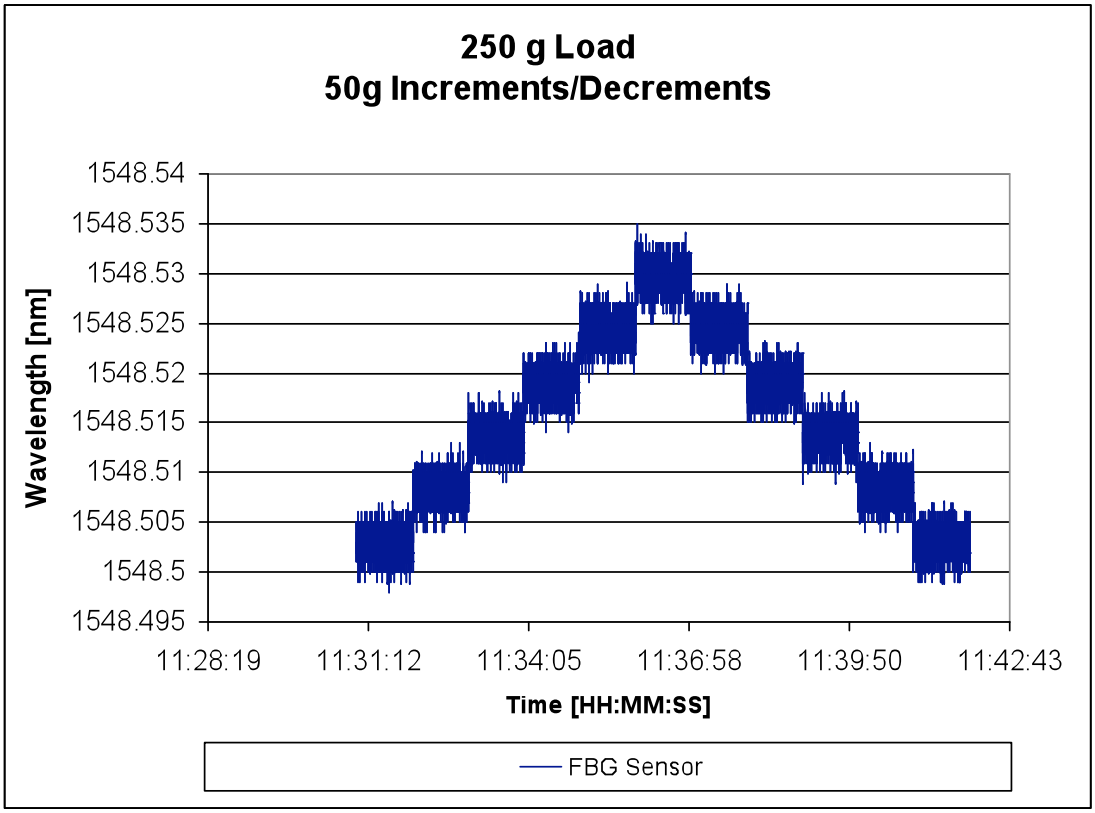

Figure 3.7a 250 g cycle in 50 g increments/decrements (function of time)

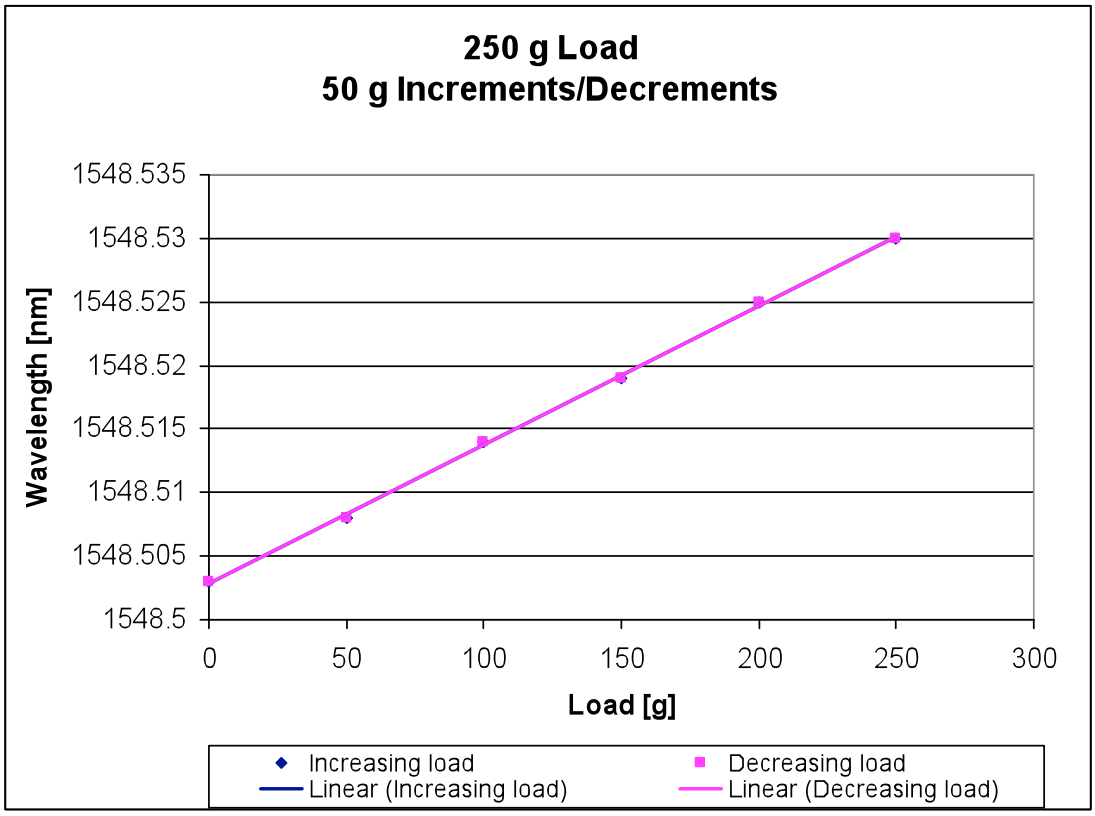

Figure 3.7b 250 g cycle in 50 g increments/decrements (function of load)

The noise present on this result is most likely to be due to instrument resolution limitation. The Insensys FSI has a maximum resolution of 0.8 μs / 0.8 pm, therefore when measuring smaller loads, the noise level on the signal will obviously increase. That said, even when measuring relatively small load (50 g) increments and decrements as shown in Figure 3.7a, the wavelength increase and decrease is distinctly evident. The result maybe further clarified by adding an additional averaging function.

3.3.2 FBG-based T702 system

The T702 comprises of a Berillium copper 30 kg beam. Figure 3.8 is a technical drawing of the T702 beam, provided by Avery Weigh-Tronix.

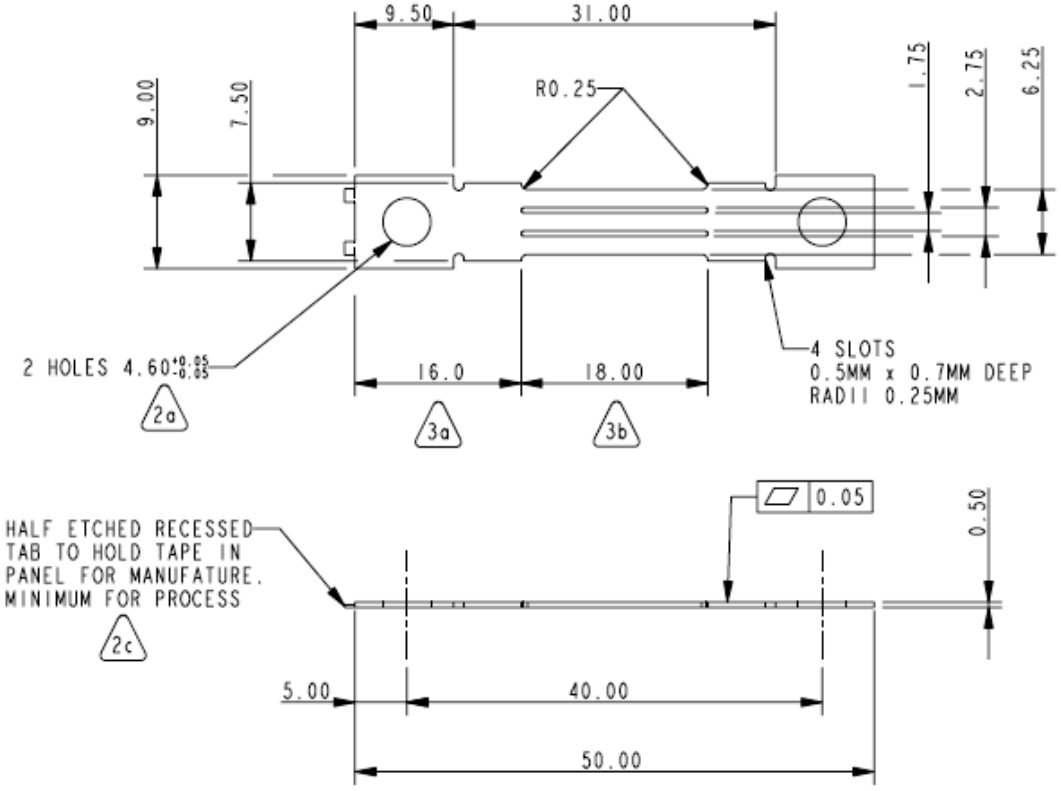

Figure 3.8 Technical drawing of a T702 30 kg beam

The concept of operation for vibrating beam technology is to etch out three narrow beams in the mid region of the Berillium beam, whilst the ends remain joined. A film of piezoelectric material is then deposited on each end so that the beams are driven in such a way that the centre of the middle beam rises, and the centres of the outer beams fall, and vice versa. The result is an oscillating device, resonating at a frequency which varies depending on the tension applied to the beam. Using digital signal processing, the

oscillating frequency can then be measured, inferring the applied strain. Current applications for vibrating beam technology including monitoring deflections in jet engine compressor blade roots in Rolls Royce Trent 500 and 600 engines.

The optical / FBG-based concept was to machine out a 200 micron V-groove along the centre line of the middle beam, bonding the FBG at the centre point. The idea being that as load was applied, the centre beam would rise, causing a red wavelength shift. Figure 3.9 is a picture of the vibrating beam with V-groove. Avery supplied the vibrating beam; RPS Engineering machined the V-groove.

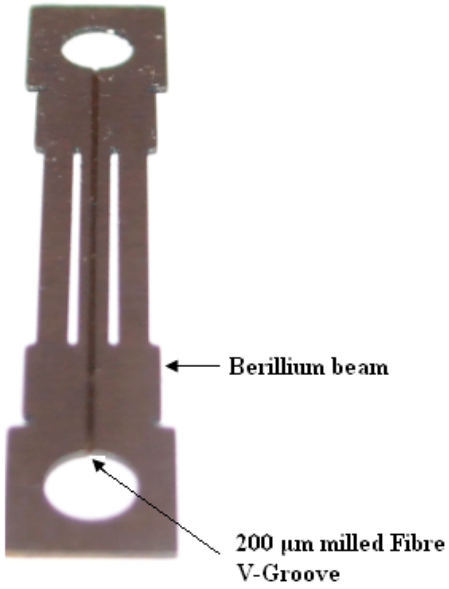

Figure 3.9 Picture of a T702 30 kg beam

3.3.2.1 T702 experimental configuration and procedure

As with Avery's electrical system, the T702 beam is housed in an aluminium FX220 cell support, which has the weighing pan bolted directly to it. With the housing fixed at one end, any load applied to the pan will in turn cause the centre beam to rise. With the FBG bonded in place, this elongation of the centre beam will result in an increase in the Bragg wavelength, which can than be interrogated. The measured wavelength shift can then be used to infer the applied load.

The FBG used in these tests was 10 mm in length and had a ~4% reflectivity. The FBG was fabricated, using a phase mask, at a central wavelength of 1550 nm. The design of the

FBG was in conjunction with the Insensys FSI requirements. The basic experimental arrangement is illustrated in Figure 3.10. The FBG was bonded using Micromeasurements 610 epoxy. All tests were conducted in a temperature-controlled environment, with the temperature being maintained at 22 °C.

Before conducting any experiment, all equipment used was "temperature soaked" to thermally stabilise.

Loads were manually applied and removed; the data was captured using the FSI.

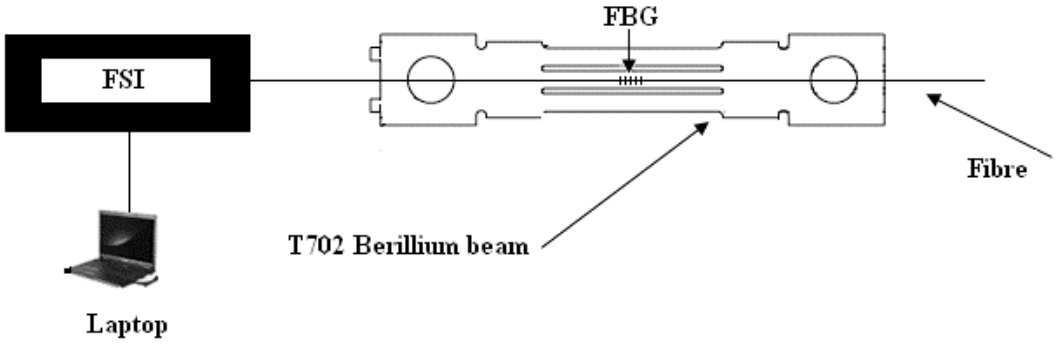

Figure 3.10 T702 basic experimental arrangement

Figure 3.11a is a picture of the T702 incorporated with the FX220. Figure 3.11b is a picture of the complete system and weighing pan. LP 1 – LP 5 are the loading points.

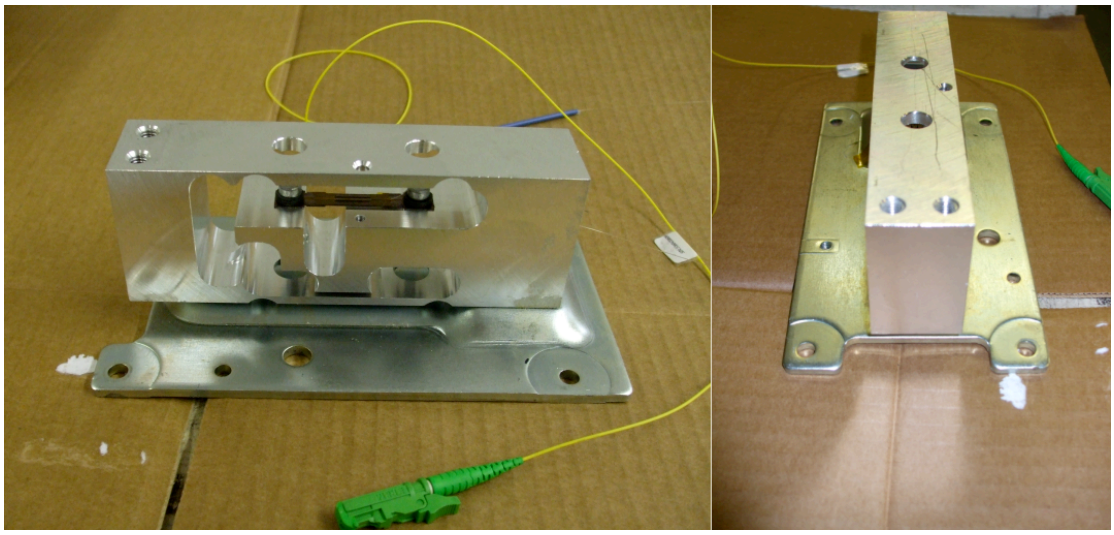

Figure 3.11a T702 incorporated into FX220

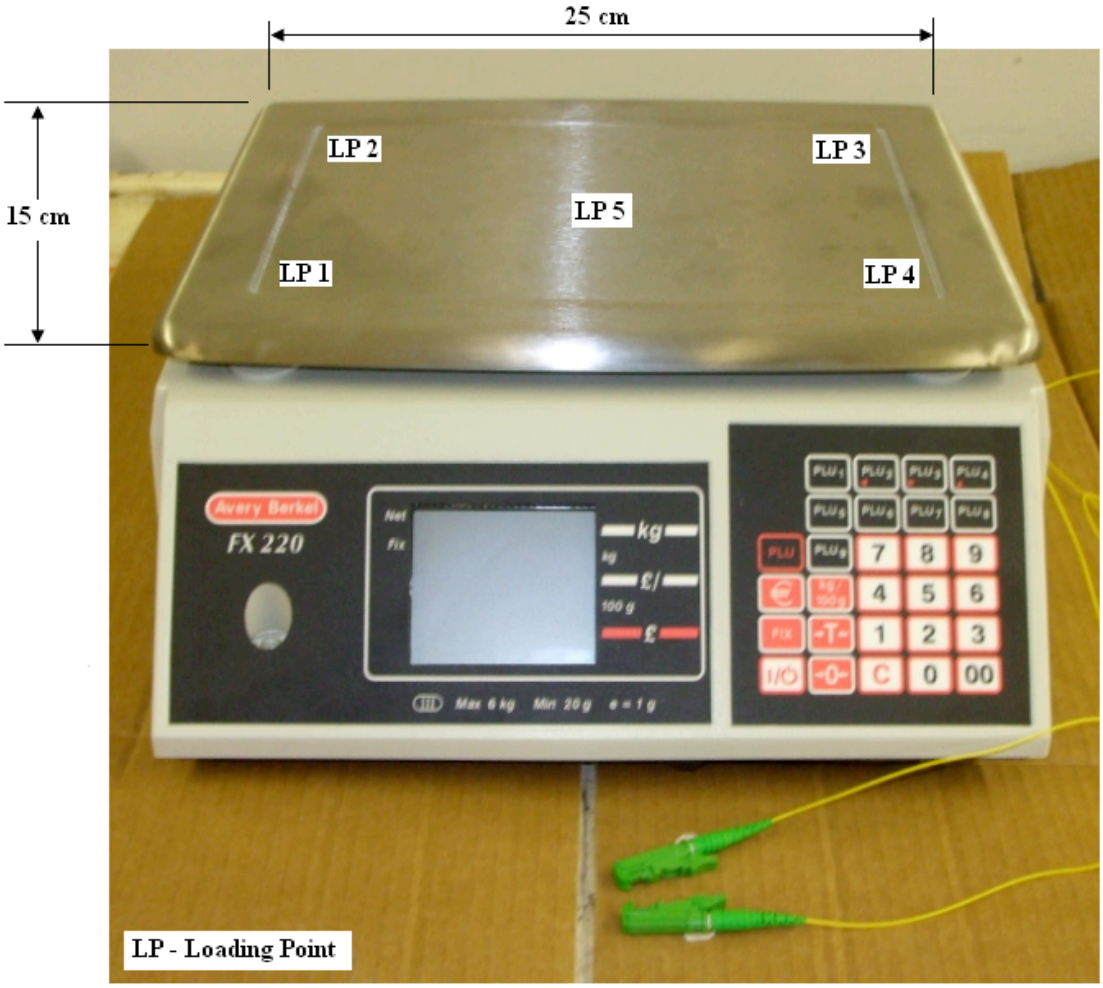

Figure 3.11b T702 complete experimental arrangement

3.3.2.2 FBG vibrating beam results

The first result, illustrated in Figure 3.12, shows the result of a 15 kg load cycle applied to the centre of the loading pan. The load induces a wavelength shift of 620 pm, which could yield a sensitivity of 41.3 pm/kg.

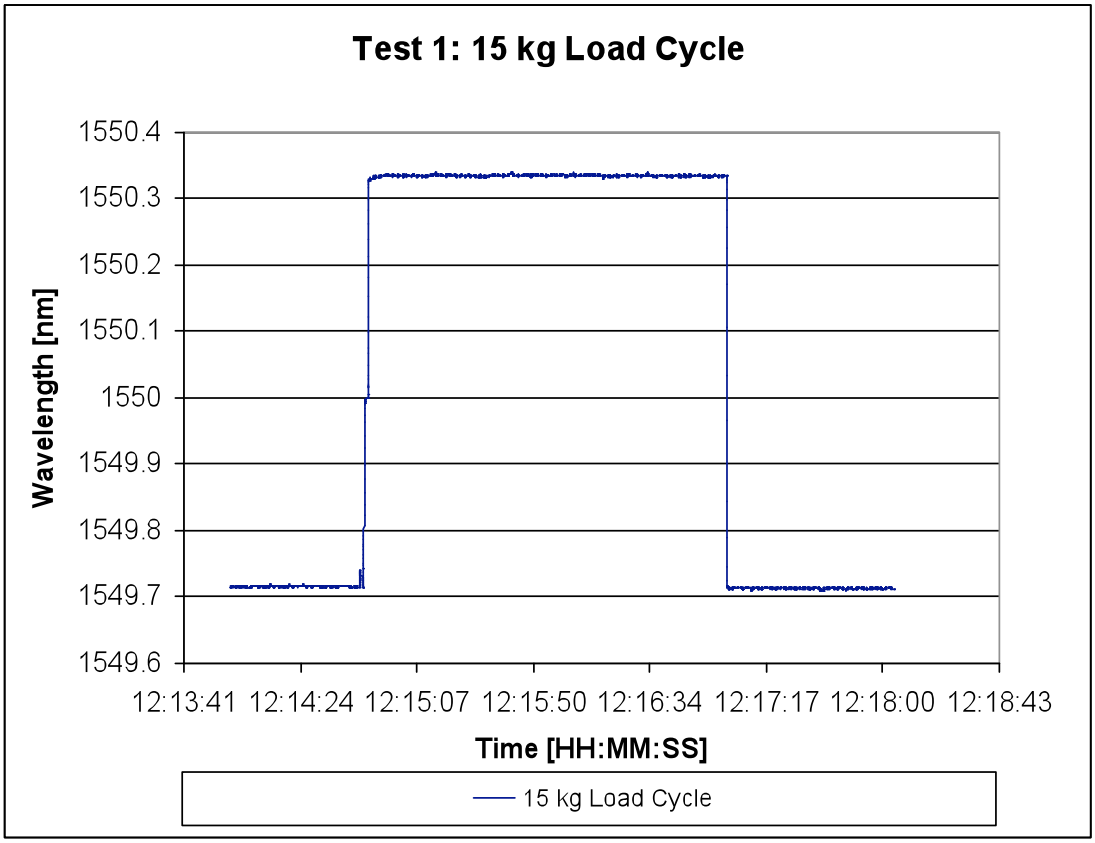

Figure 3.12 15 kg load cycle

The next result, illustrated in Figures 3.13a and 3.13b, shows the central loading and unloading of the weighing pan up to 6 kg in 1 kg increments and decrements. Figure 3.13a shows the result taken directly from the FSI captures file, Figure 3.13b is the same result with the wavelength shift plotted as a function of applied load.

The incremental increase and decrease in load clearly is evident in Figure 3.13a by the "step-up" and "step-down" nature of the trace. Also, the linearity of the result is clear from the linear trend lines plotted in Figure 3.13b.

Whilst the result illustrated in Figure 3.13b shows good linearity, there are errors in the result. For example, consider the result illustrated in Figure 3.13b. The load, which produced the largest error between incremental and decremental loads, was 5 kg.

The average wavelength at 5 kg (incremental loading) was 1549.903 nm, whereas the 5 kg average wavelength value (decremental loading) was 1549.901 nm. This result yields a difference of 2 pm between incremental and decremental loads. Given that the resolution of the FSI is 0.8 pm, it is suggested that this error is system limited rather than instrumentation limited.

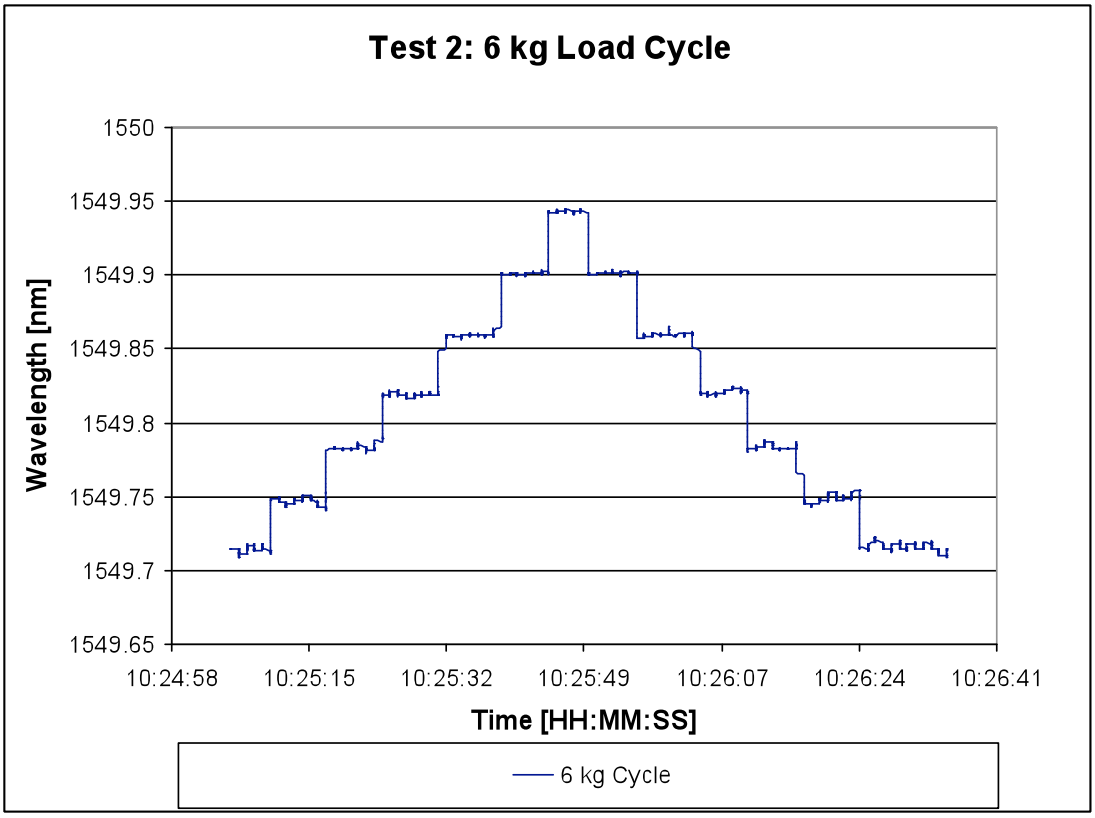

Figure 3.13a 6 kg load cycle (function of time)

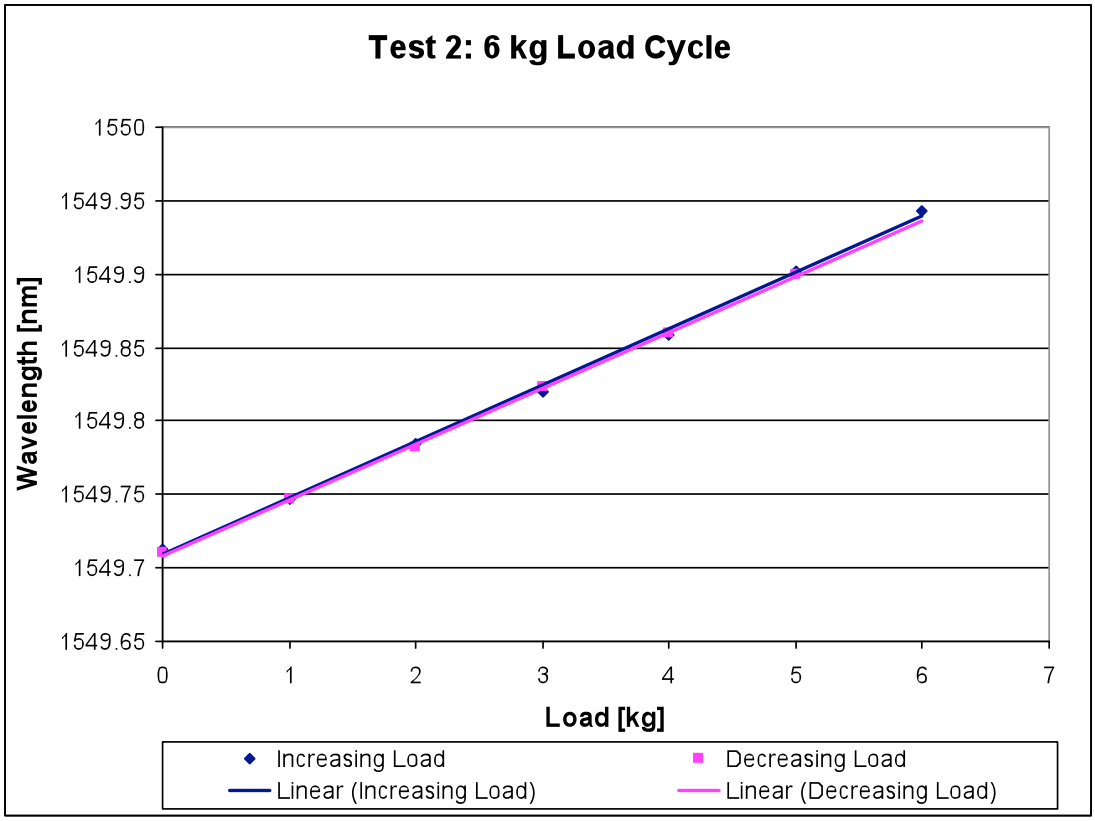

Figure 3.13b 6 kg load cycle (function of load)

Whilst the T702 went through stage-1 calibration, stage-2 calibration could not be carried out as this takes place post-final assembly and soak testing. Having discussed this with the Engineers at Avery, it was agreed that the error in this result is most likely to be system error due to a lack of final calibration of the T702.

In order to analyse the repeatability of the system, five cyclic tests were performed following the same process i.e. 6 kg was added and removed in 1 kg increments and decrements. The five increasing results and five decreasing results are shown in Figures 3.14a and 3.14b respectively.

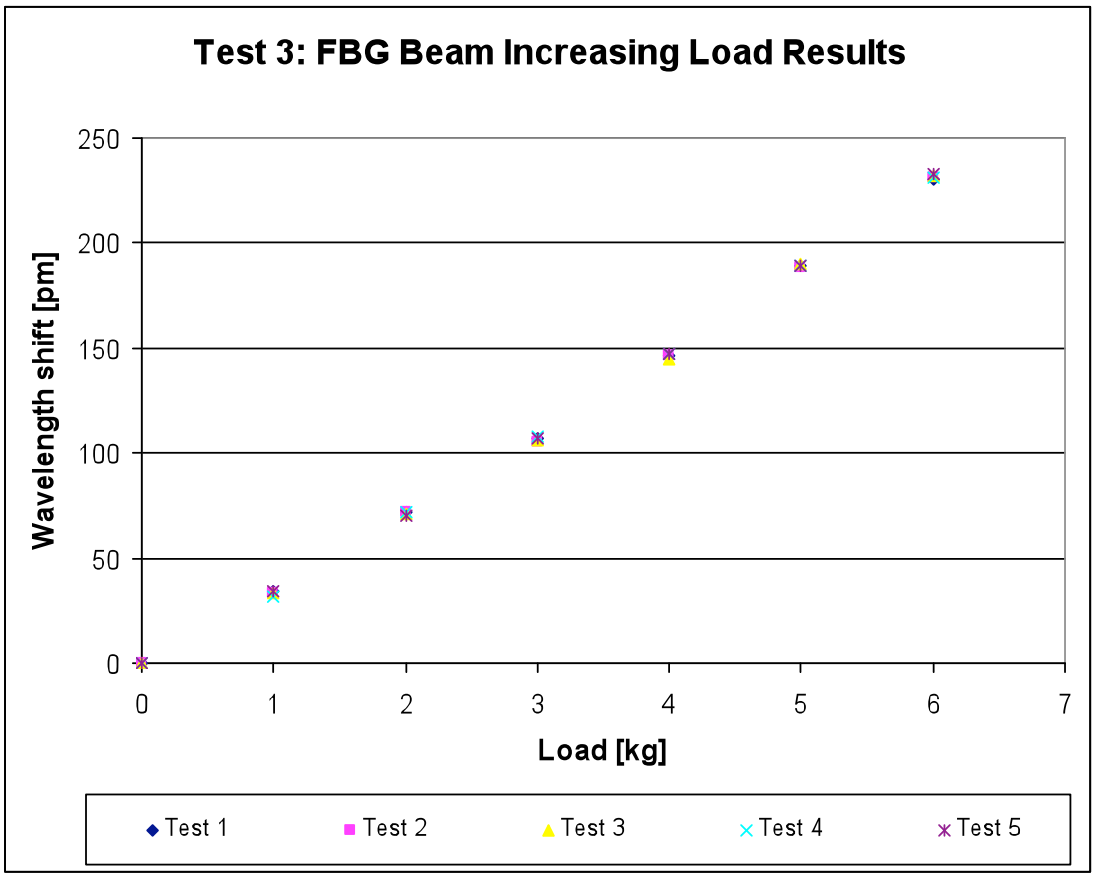

Figure 3.14a Five 6 kg load cycles – increasing load

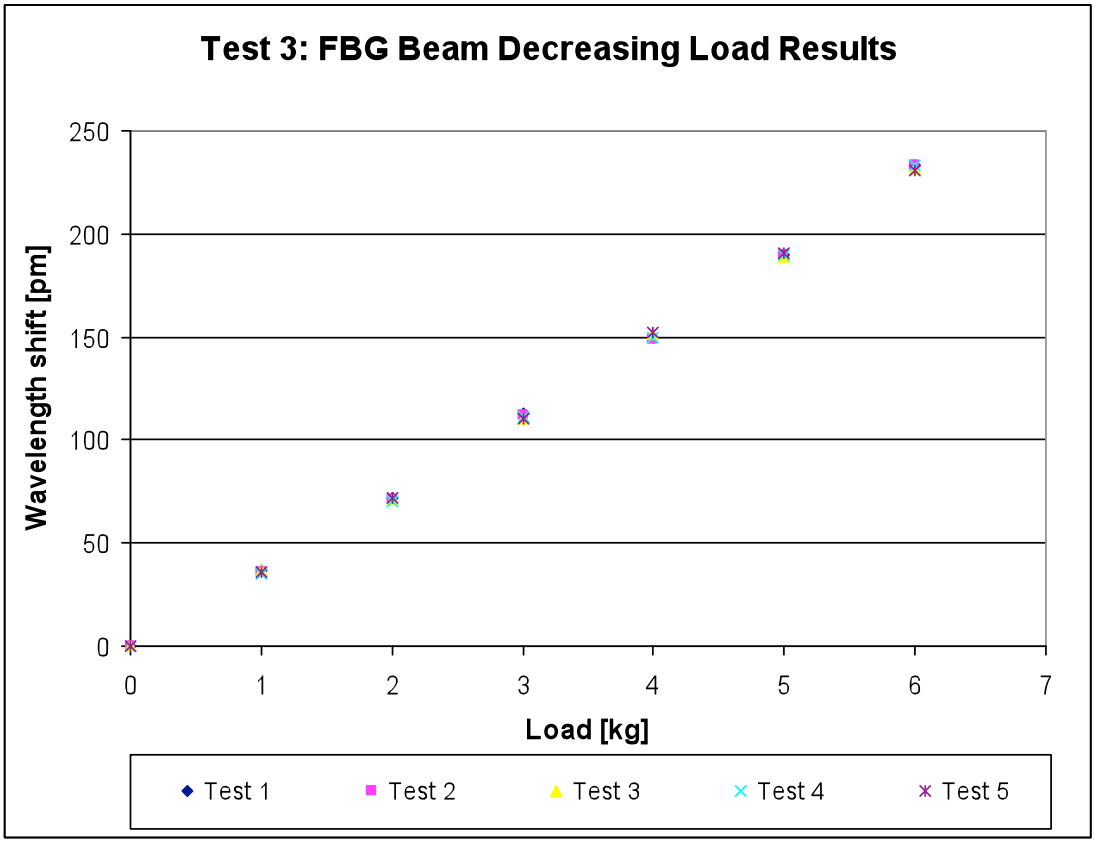

Figure 3.14b Five 6 kg load cycles – decreasing load

As can be seen, under temperature-controlled conditions, the wavelength shift induced is both highly linear and repeatable. It should be noted that in order to gain commercial certification, cycle numbers in the tens-of-thousands are required. Performing such a high volume of cycles was not feasible for this work due to time and equipment availability. It can take many months for a certification process to complete. Table 3.3 summarises the five cyclic results.

Test N°	Increasing load FBG max shift (pm)	Decreasing load FBG max shift (pm)
1	230	233
2	231	233
3	232	232
4	231	233
5	233	231

Table 3.3 Summary of results from Test 3

One of the most important factors in load cell design for weighing is that no matter where the load is applied on the weighing pan, the measured load should be the same. This was tested with the FBG cell by placing loads in different locations on the weighing pan, and measuring the induced shift. Test 4, illustrated in Figure 3.15, shows a 1 kg weight being applied to all five LPs (LP 1 ⇒ LP 5) on the weighing pan.

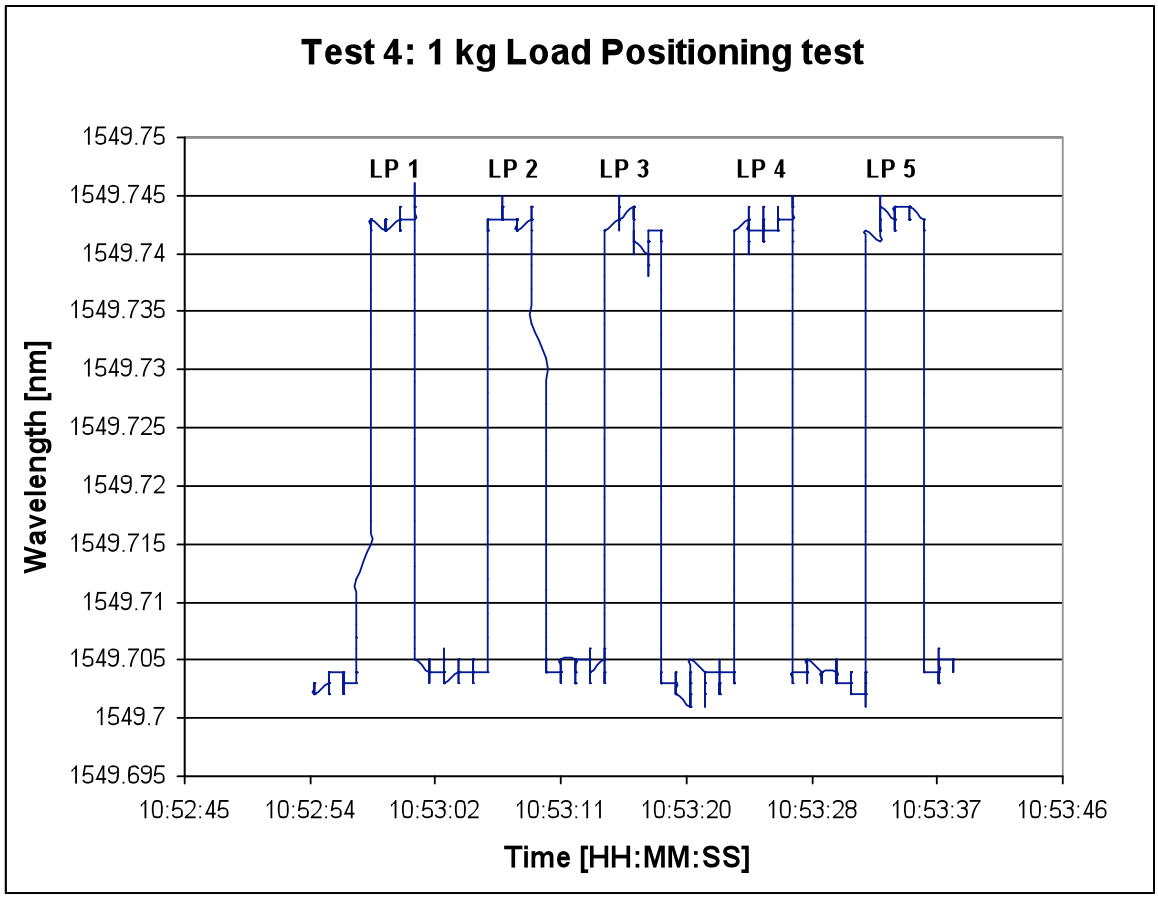

Figure 3.15 Positional loading of a 1 kg load

The above result shows five distinct measured loads in the form of five peaks on the trend. From left to right, the five peaks represent the five loading positions illustrated on Figure 3.5 (LP 1 – LP 5).

To further investigate the linearity with respect to positional loading, the four corners (LP 2 – LP 5) of the weighing pan were loaded and unloaded in 1 kg increments. I.e. to begin with, LP 2 was loaded with 1 kg, then a further 1 kg added to LP 3, and so on until all four corners were loaded. The process was reversed for unloading. The results of this test are shown in Figures 3.16a and 3.16b.

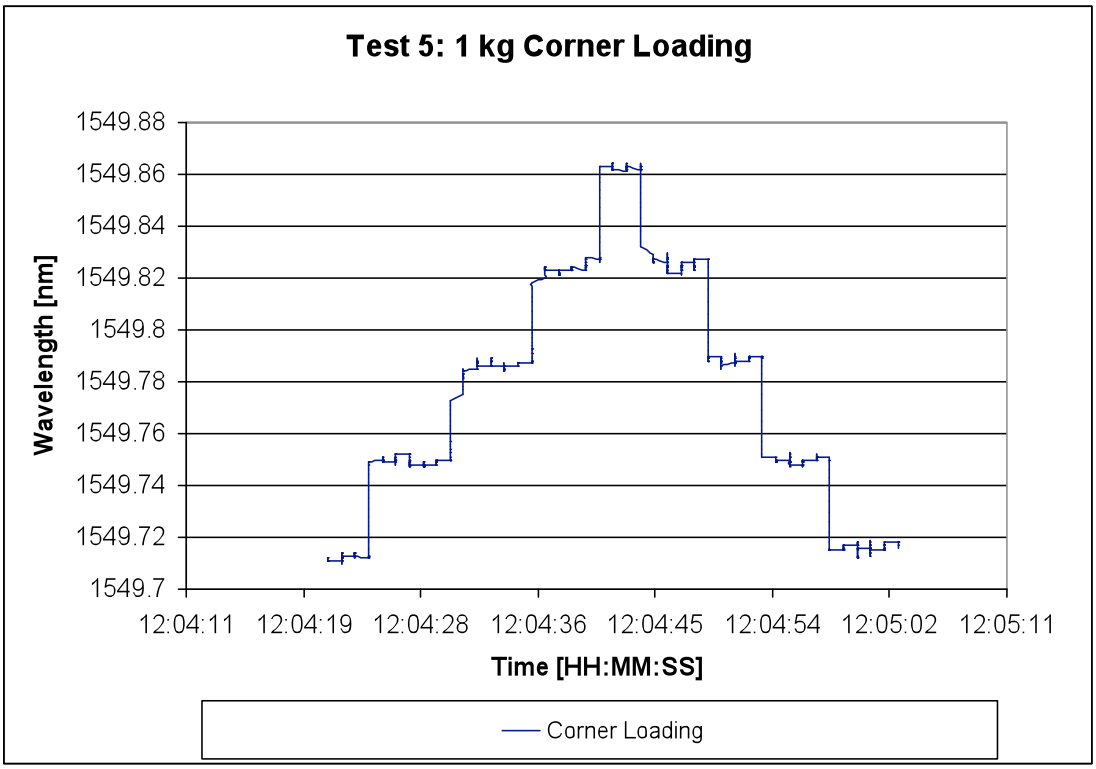

Figure 3.16a Corner loading in 1 kg increments (function of time)

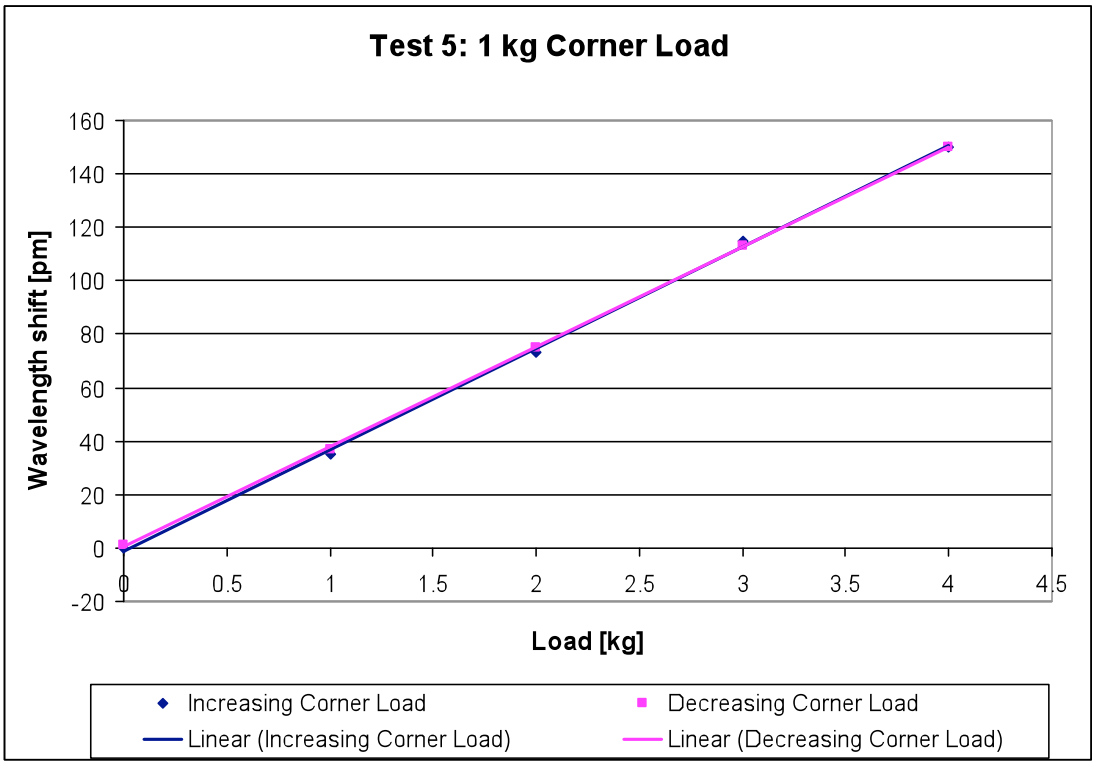

Figure 3.16b Corner loading in 1 kg increments (function of load)

As with the result shown in Figure 3.13b, the above result in Figure 3.16b yields some errors between incremental and decremental load values. The largest error is present at the 1 kg load point, where the wavelength difference between incremental and decremental

loading was 3.24 pm. Again, and considering the FSI resolution, this adds credibility to the conclusion that the result is limited by the system rather than the instrumentation itself.

Also, as with the Single Point strain gauge load cells, Avery's T702 systems are designed to measure loads in the region of grams to 1000 kg. Test 6, illustrated in Figure 3.17, shows a 100 g load cycle.

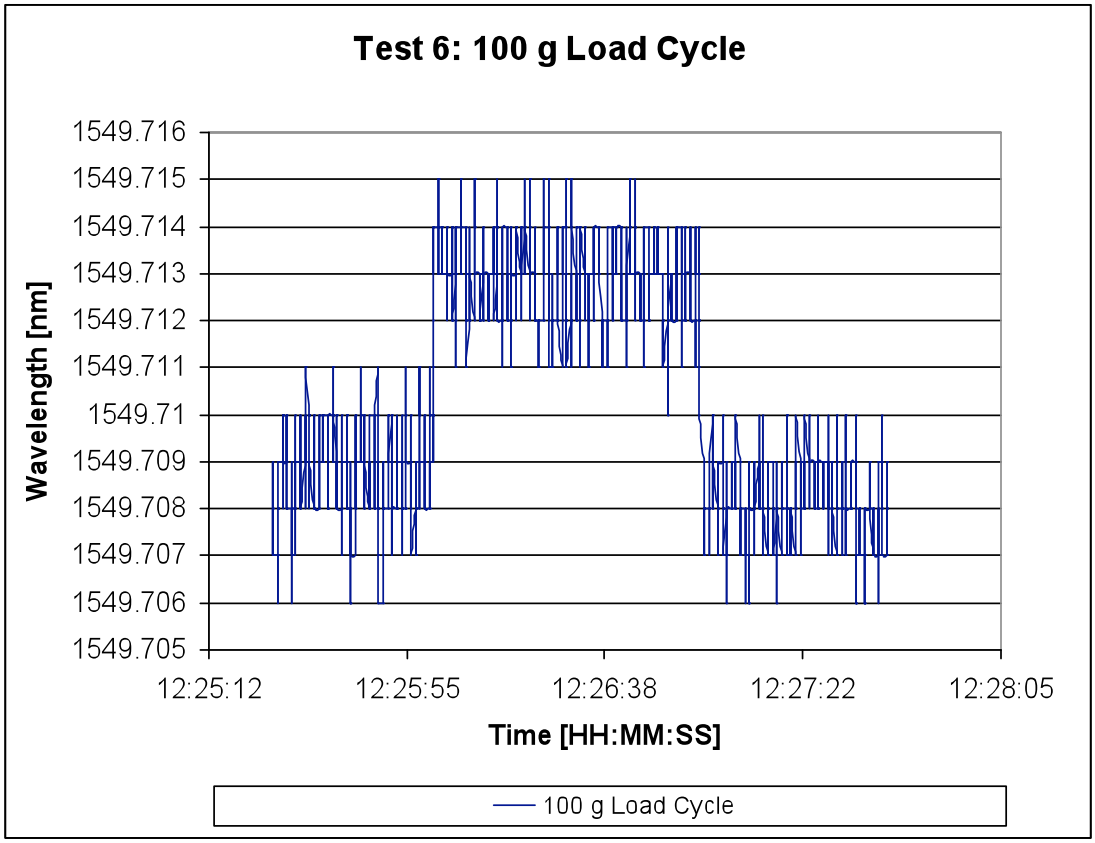

Figure 3.17 100 g load cycle

Despite the noise present on the trace, even at such a minuscule load, there is a clearly identifiable load cycle, represented by a 5 pm increase in wavelength as the load was applied, and returning to its initial wavelength once the load was removed.

3.4 Dynamic loading for rail Weigh-In-Motion

Part of the project was aimed at studying the feasibility of using FBGs as a means of detecting train axle loads, with the eventual aim of having an optical WIM system. Optical WIM systems have considerable advantages over their electrical counterparts, these advantages include:

- Electrical sensor signals, unless appropriately packaged, can become corrupted by electromagnetic interference. FBG sensors are immune to such interference

- For multi-sensor WIM systems, a large amount of cabling is required which has to be managed trackside. Numbers of optical sensors, running into the hundreds, can be multiplexed in a single length of fibre

There are already a number of optical techniques reported for railway WIM, and also some commercial systems already being deployed worldwide. Manellea *et al* demonstrated that a WDM multiplexed array of FBG sensors could be directly bonded to a pre-treated section of rail and used to measure dynamic strain [4]. SensorLine GmbH has produced a system based on microbending, which can be used to infer axle loads of a passing train [5]. A case study produced by Sensornet & SOAM Consultants demonstrated a Brillouin based distributed sensing system, which can be used to monitor train axle loads as well as track infrastructure integrity monitoring [6].

Early discussions with colleagues from Aston University, Avery UK and Avery USA revealed that bonding fibres directly to the track was not commercially practical, therefore the obvious solution was to design some form of patch with embedded sensors. The patch, in its entirety, could then potentially be bonded to pre-treated rail in-situ. The advantage here, as well as providing extra protection for the fibre, is that the precise positioning of the fibre is accounted for at the patch fabrication stage, rather than at the bonding stage. At present, the logistics if implementing a WIM system is vast. Current systems cannot be bonded in-situ. Instead, a section of track, usually in the region of 5 m, is removed from the active rail line and transported to Avery where the electrical WIM system is fitted. The Avery site in Smethwick, UK currently fits systems to rails from Europe, North America, Asia and Australasia. The reason for shipping to the site is due to the complexity of fitting the electrical system. It is hoped that further research into bonding techniques, which is not in the scope of this work, could lead to an optical WIM system being fitted and calibrated in-situ, without the need for removing any sections of track.

3.4.1 Shear strain and bending moment theory

Figure 3.18 diagrammatically illustrates the concept of shear strain and bending moment when a force is applied to a beam.

A beam needs to be analysed to deduce the maximum stress it can withstand, which can then be used for real applications to determine the maximum stress said beam can safely induce. Beyond this, it is also a requirement to determine the maximum deflection the

beam will experience when subjected to the determined maximum load. To determine the maximum stress, a bending moment diagram and shear force diagram needs to be produced.

The shear moment diagram is constructed by moving a section along the beam from the origin and summing the forces to the left of the origin. When the equilibrium condition is reached, it means that the forces either side of the section are equal, from this the resisting shear force of the section can be obtained.

The bending moment diagram is obtained in similar fashion, except in this case, the bending moment is the sum of the product of each force and its distance (D) from the section. The distributed loads can then be calculated by summing the product of the total force and the distance (D) of the centroid of the distributed load [7].

A detailed analysis of shear stress and bending moment theory is reported by Megson [8].

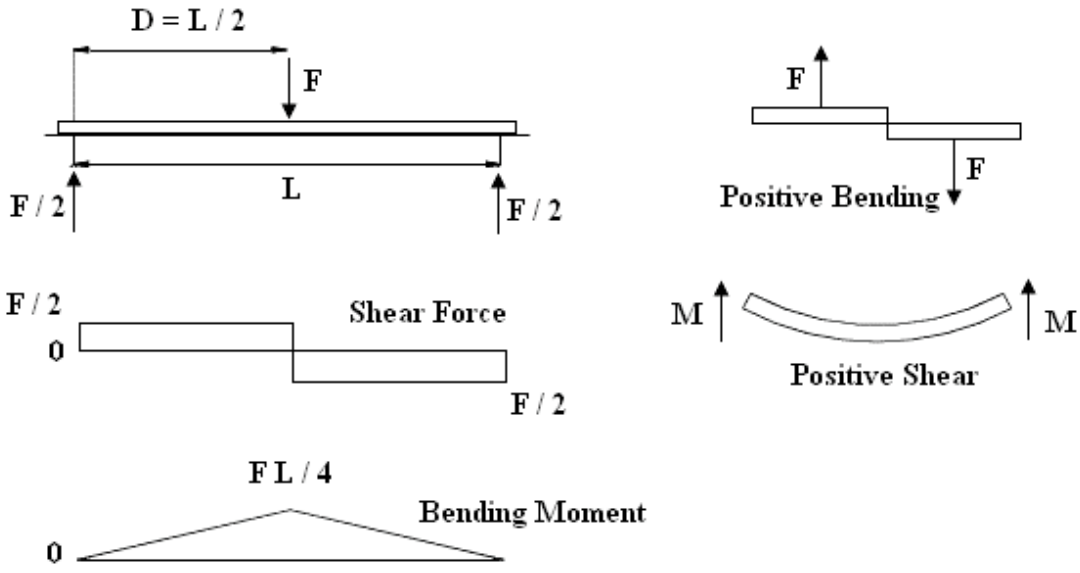

Figure 3.18 Shear force and bending moment diagram

Where L is the length of the beam (m), F is the applied force on the beam (N), M is the moment (Nm) and D is the distance along the beam (m).

3.4.2 Patch requirement

The railway track to be tested on is an I-beam configuration. The rail web has a flat section 50 mm wide where it is desired to locate the sensors. Two patch designs were ordered from

Insensys. One configuration has a single-FBG, the other patch configuration had two FBG sensors, positioned at an angle of ± 45° relative to the neutral axis, to measure shear in the web.

Compensation for thermal strains in the track and thermal variations of the sensors was not required as only dynamic signals were measured. Testing also took place in a temperature-controlled environment, which removed any temperature-induced wavelength shift. It should be noted however that for field implementation, temperature compensation would be vital to obtaining accurate load measurements.

3.4.3 FBG sensors

Individual Bragg grating sensors were laminated into e-glass / epoxy composite patches, which can be multiplexed together with armoured cable to form a desired array. The patches were pre-built in controlled conditions and were appropriately tested and certified by Insensys prior to shipping. An example of the single-FBG patch is pictured in Figure 3.19.

Figure 3.19 Single patch

As can be seen, the patch is mounted on peel ply, which is removed immediately prior to bonding.

As the FBG can be interrogated from either end, both ends were pig-tailed and thus provided an element of redundancy. The fibre pigtails were 900 microns in diameter.
The patch was designed to have low stiffness so that it would not impact on the overall properties of the structure to which it was to be mounted. The surface to which the patch is to be bonded, i.e. the track, was treated prior to bonding.

For simplicity of design and fabrication, the first patch designed housed a single-FBG with the sensor running horizontally through the patch with reference to the x-axis. The patch was designed to measure the wavelength shift induced by the FBG when a force was applied to the track. Comparatively, the single-FBG patch was both far easier to fabricate by Insensys as it did not require precise angular positioning of the FBG, and significantly cheaper. The latter advantage was particularly attractive to Avery as a commercial option.

However, even before the patches were fabricated, based on existing theory regarding shear force, it was collectively accepted that a double-FBG patch with the FBGs mounted at ± 45° to the neutral axis would induce the maximum stress, ergo the maximum positive and negative wavelength shifts for the tension and compression FBGs respectively. The double-FBG patch however was not without its disadvantages. The double-FBG patch was both considerably lager and more than double the price of its single-FBG patch counterpart. It also required two separate fibres within the patch as a limitation of the Insensys system was that grating the minimum separation was 2.5 m, obviously in such a small patch this was impossible. See section 2.6.3.2 on the limitations of TDM interrogation. Admittedly, this could be overcome using a WDM interrogation technique, but that in itself has inherent disadvantages.

Figure 3.20 shows the detailed design of both the single and the double patch.

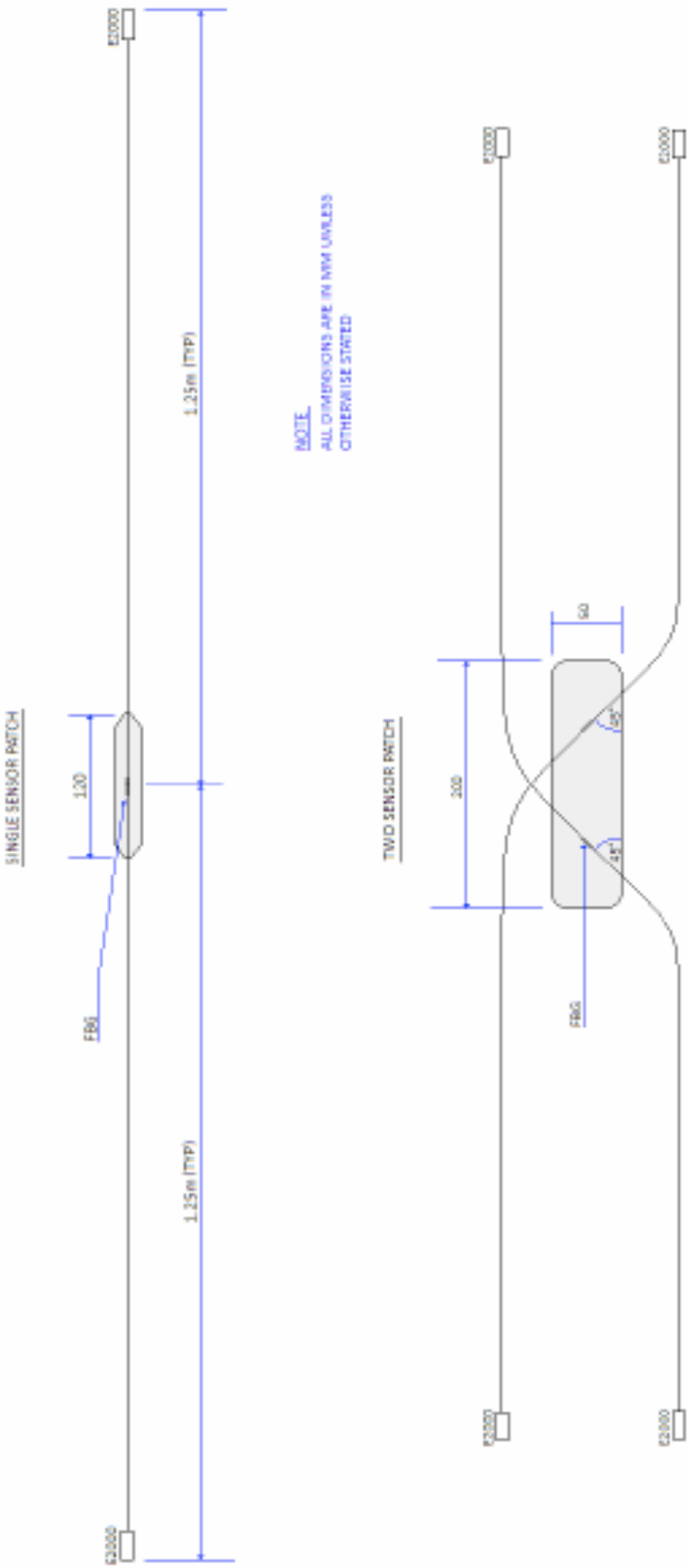

Figure 3.20 Patch designs

3.4.4 Bonding the patches

Prior to bonding the patches, the section of track Avery were able to source for testing was treated in much the same way as it would be for bonding their electrical strain gauge WIM sensors. The adhesive used for this testing was a standard RS Cyanoacrylate gel and activator. Just prior to bonding a final cleaning and de-greasing process was performed.

Once the gel and activator come into contact with each other, the bond is formed within seconds. Therefore it was vital the patch was accurately positioned. This was helped greatly by the design of the double sensor patch in particular as it fitted perfectly with the 50 cm flat area of the I-beam.

Figure 3.21 is an image of the pre-treated track.

Figure 3.21 Pre treated track

First, the patch was accurately positioned and then placed under a section of tape at one end to form a hinge. Cyanoacrylate gel was then applied to the under side of the patch, whilst the activator was sprayed onto the track surface. Then quickly, but carefully, laying the patch down applying finger pressure horizontally away from the hinged side, the patch was bonded into place.

Whilst the patch was secured within just a few seconds, the patch was left for the recommended 24 hours at room temperature to cure for the bond to complete.

3.4.5 Single patch experimental configuration and procedure

Figure 3.22 shows a front-end view of the I-Beam track, illustrating the patch position relative to the flat web.

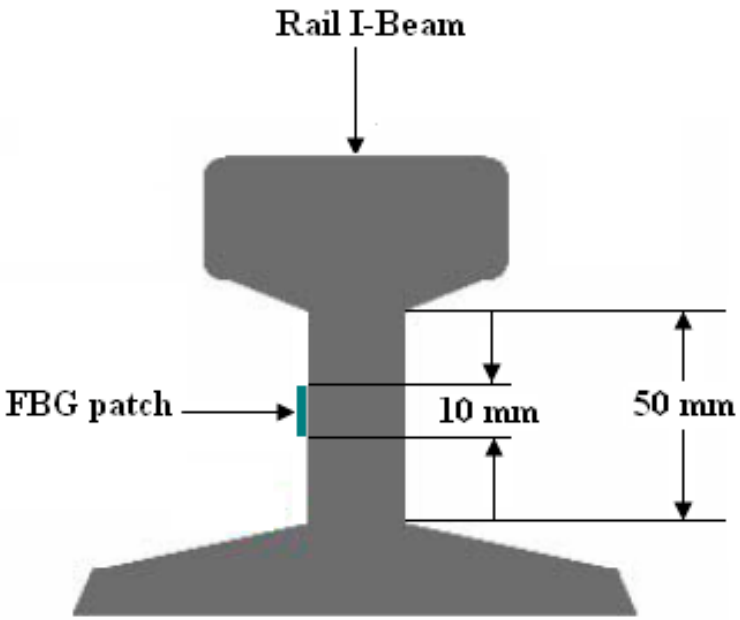

Figure 3.22 Single FBG patch

Figure 3.23 is a picture taken of the single-FBG patch bonded to the rail.

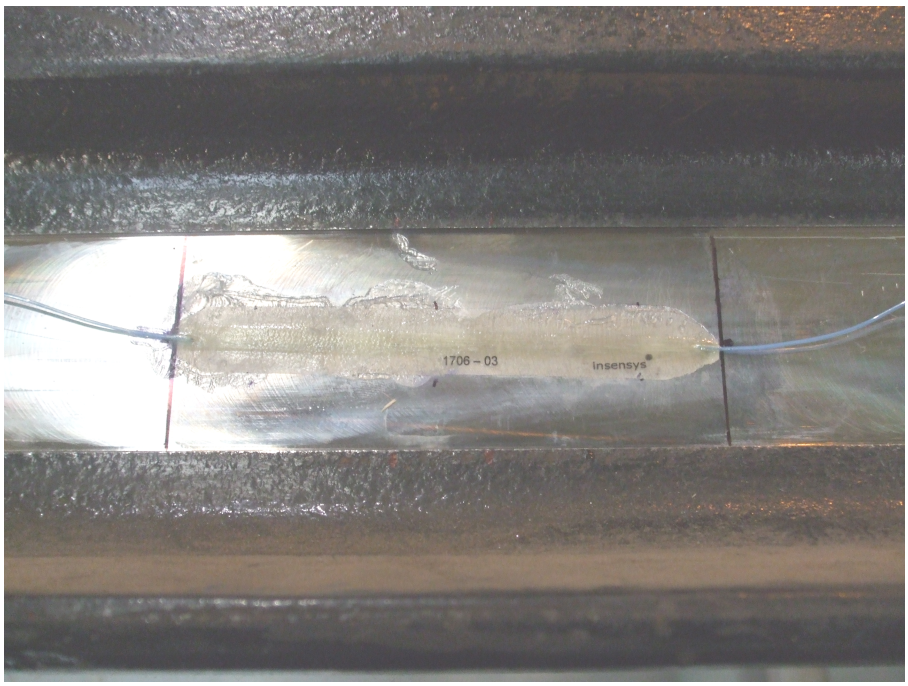

Figure 3.23 Picture of the single FBG patch

The experimental configuration consisted of the Insensys FSI and a laptop. The arrangement is shown if Figure 3.24.

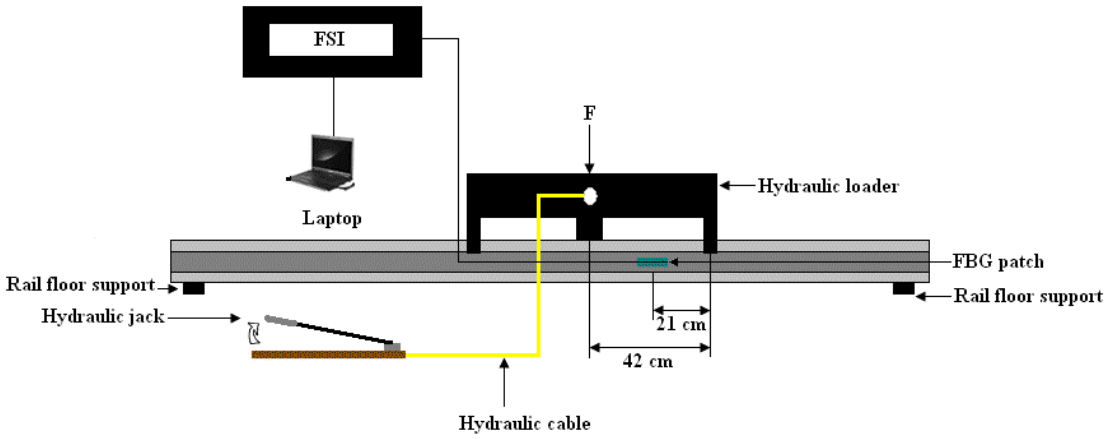

Figure 3.24 Experimental configuration for the single patch

The procedure for performing these tests was to use a piece of manual hydraulic loading equipment that allows the application of load up to 13,000 kg. This equipment is pictured in Figure 3.25.

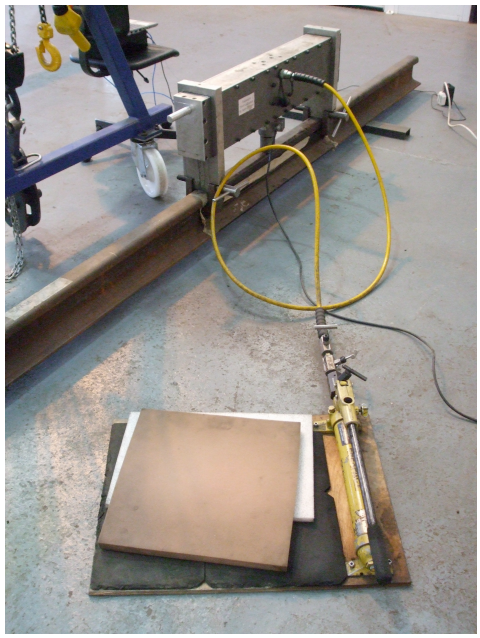

Figure 3.25 Hydraulic loading equipment

The rail was positioned over two floor supports and lowered into place using a hydraulic crane at the Avery Weigh-Tronix rail test facility. A hydraulic loader was then positioned over the track, such that the patch centre was exactly half way between the downward force load and the end clamp, maximising the response of the FBG sensors, see section

3.4.1 for details. The load was manually applied by hand by means of a hydraulic jack handle, which effectively pumped hydraulic fluid to the loader, applying the load. The applied load was visually monitored on an LCD display connected to the hydraulic loader. The data was captured using the Insensys FSI, running at 30 Hz, connected to a laptop.

There were significant limitations of Avery's hydraulic loader. These were:

- As the load was manually applied, it was difficult to apply the exact desired load for each test, which may account for some of the error in the results
- The loader did not maintain its load; therefore constant human intervention was required in an attempt to maintain the load. Maximum deviance from each load for the tests presented in this chapter was ± 5 kg
- There was no facility to do complete cyclic loading, i.e. the load could not be removed in 1000 kg decrements. No matter how much load was applied, the load release mechanism released all hydraulic load back to zero load

3.4.6 Single FBG patch results

The results presented in this section illustrate test results obtained by applying 13,000 kg of load. Figure 3.26 is the initial cycle test showing wavelength shift as a function of time. The 'step-up' trend on the increasing wavelength line is indicative of the manual application of the load in a ratcheting effect. Note that the following five results representing five load tests are plotted as wavelength shift as a function of load. This was made possible by logging the time at each 1000 kg interval, then matching that time with the associated wavelength in the .txt file. These five test cycles are shown in Figures 3.27a-e.

Finally Figure 3.28 illustrates the five test cycle traces combined.

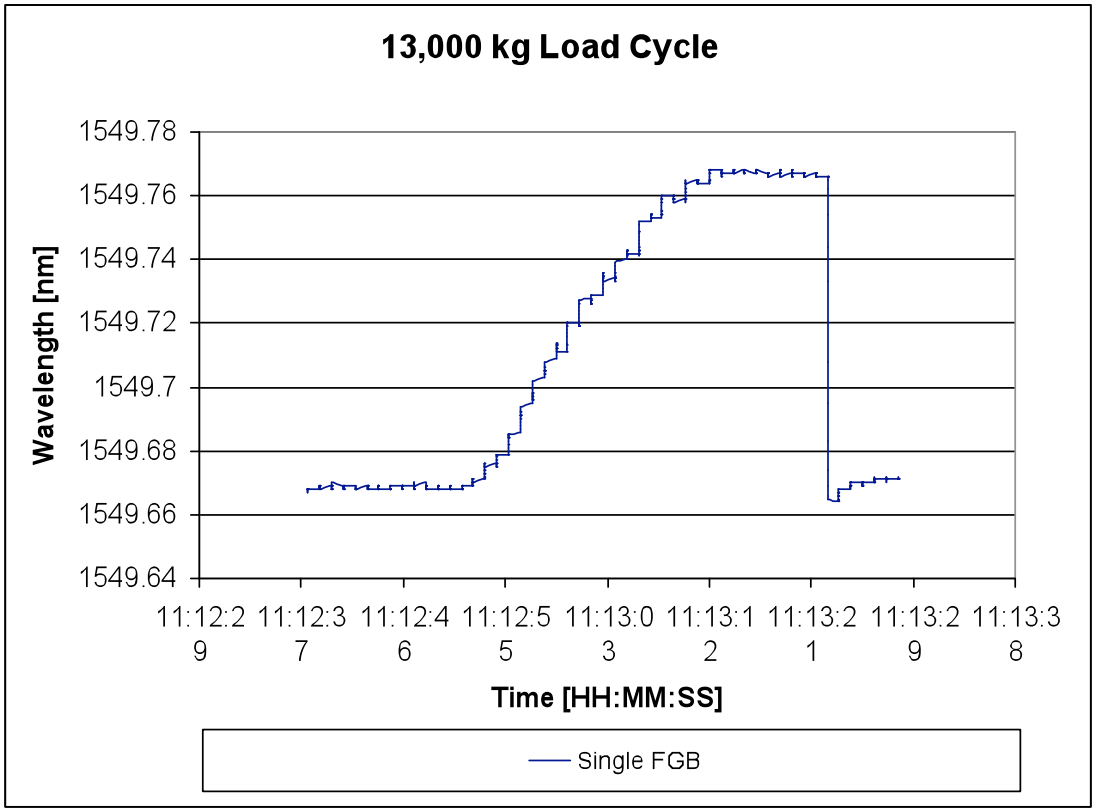

Figure 3.26 0 kg ⇒ 13,000 kg initial cyclic load test

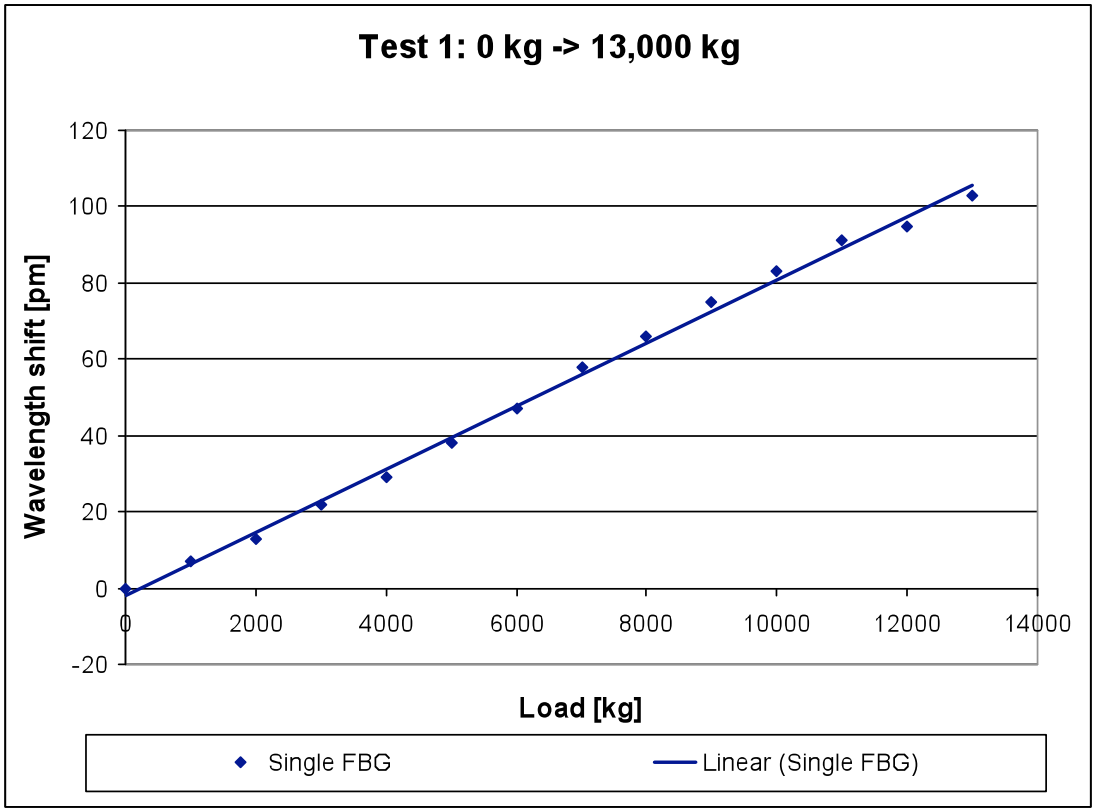

Figure 3.27a Test 1 result

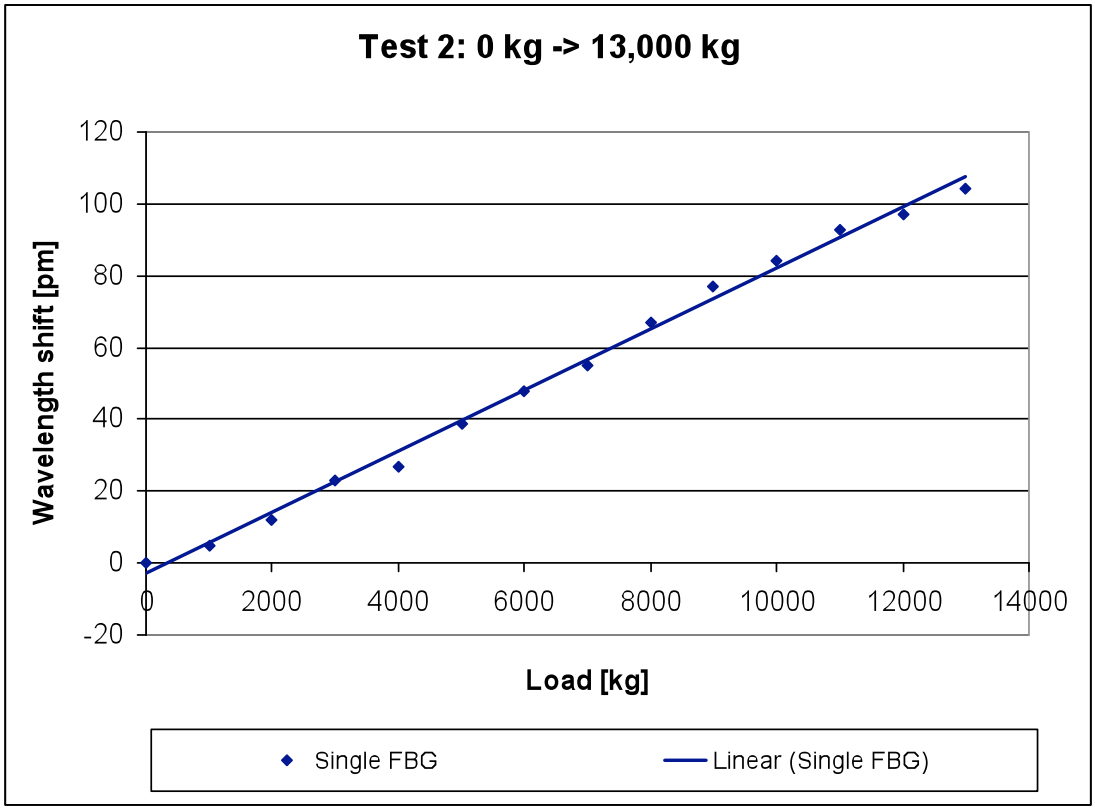

Figure 3.27b Test 2 result

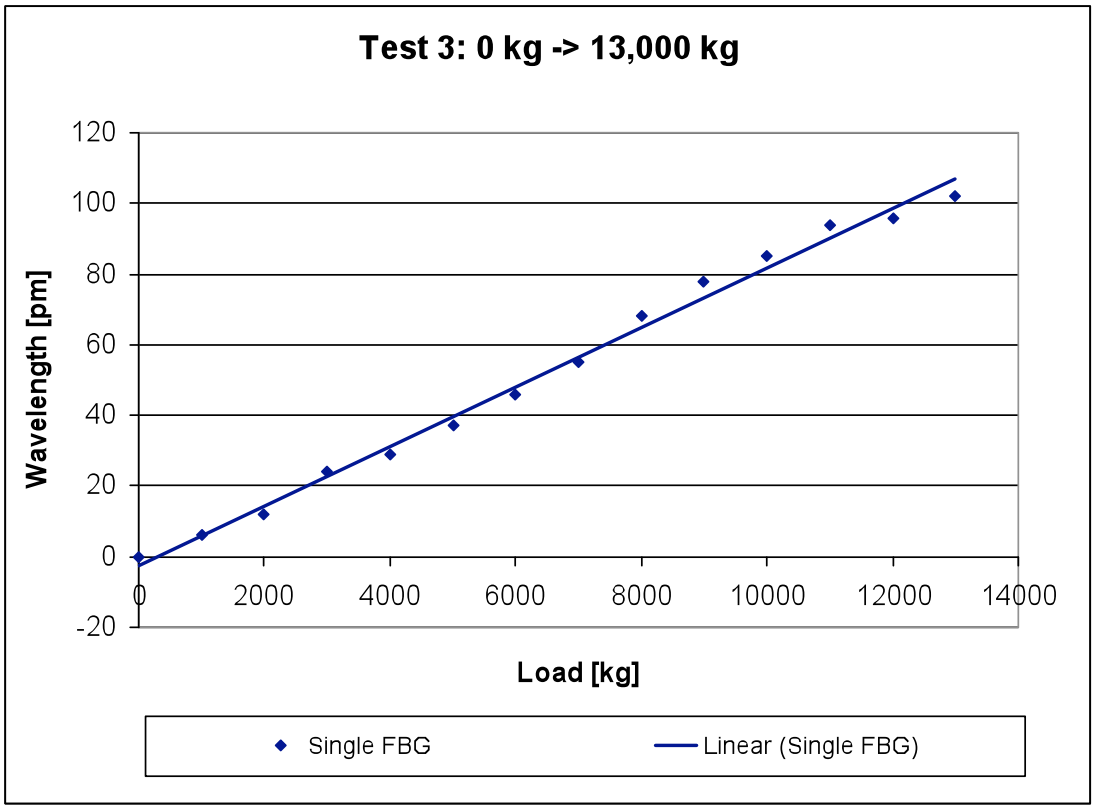

Figure 3.27c Test 3 result

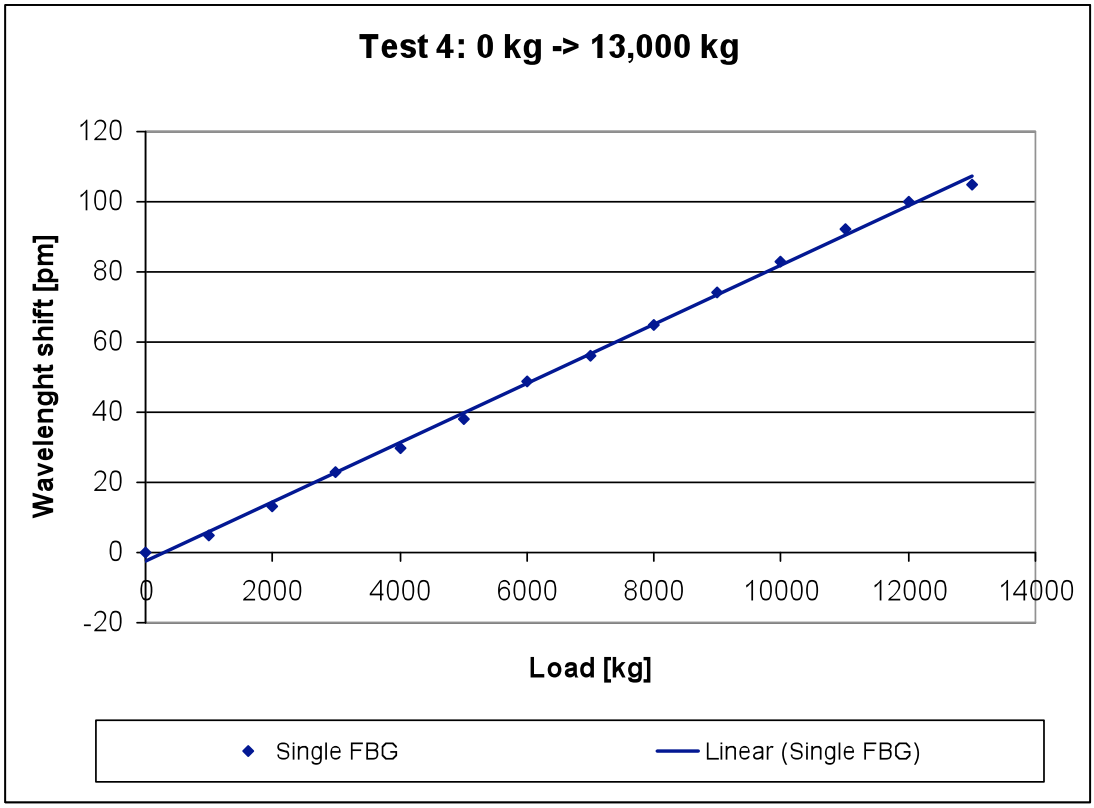

Figure 3.27d Test 4 result

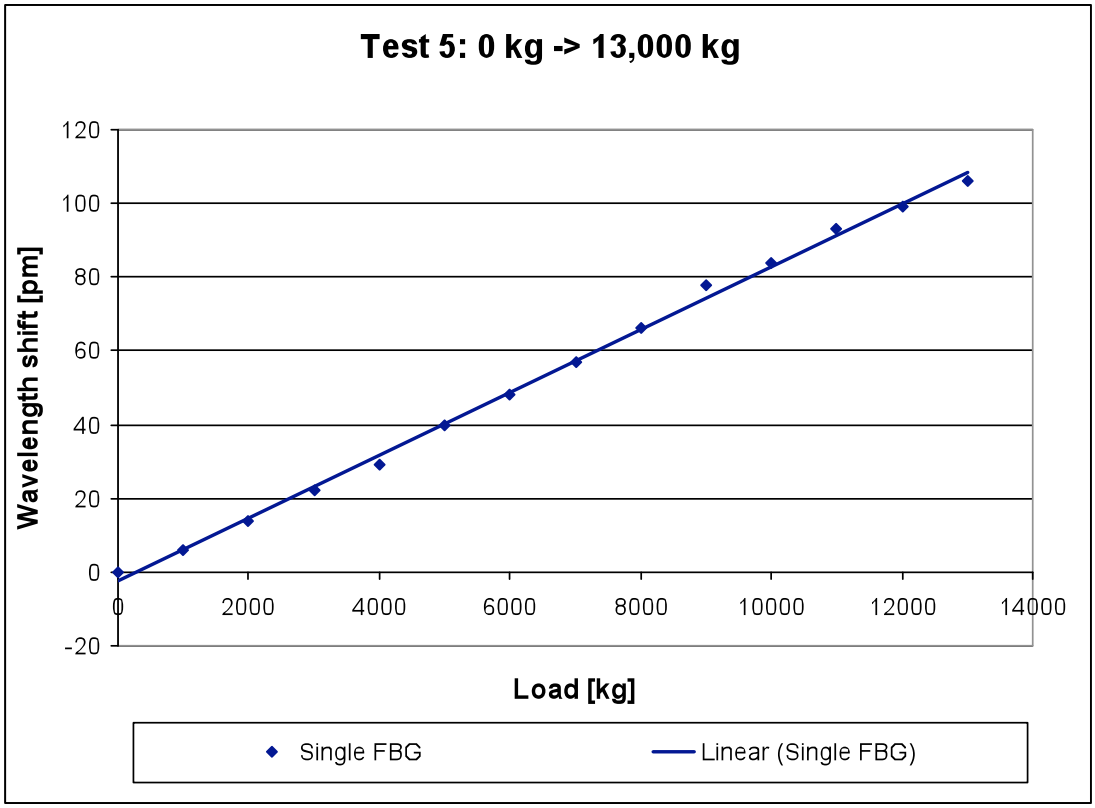

Figure 3.27e Test 5 result

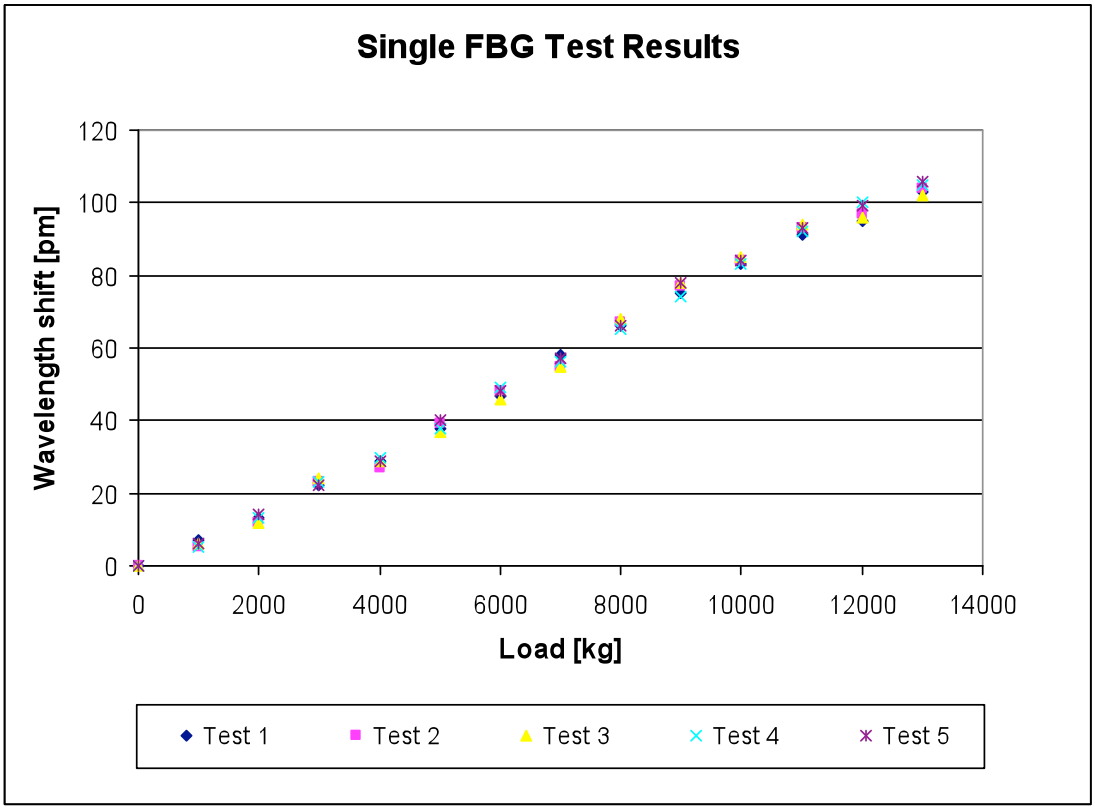

Figure 3.28 Single FBG sensor responses from Tests 1-5

Table 3.4 summarises the results obtained from the five tests.

Test N°	FBG max shift (pm)	Achievable sensitivity (pm/kg)
1	103	0.0079
2	104	0.0080
3	102	0.0078
4	105	0.0080
5	106	0.0081

Table 3.4 Summary of single patch results

Typically, train axle loads do not exceed 12,000 kg. Testing over a weight range of 0 kg to 13,000 kg ensured the sensor was subjected to loads greater than would be experienced in-situ.

3.4.7 Double patch experimental configuration and procedure

Figure 3.29 shows a front-end view of the I-Beam track, illustrating the patch position relative to the flat web.

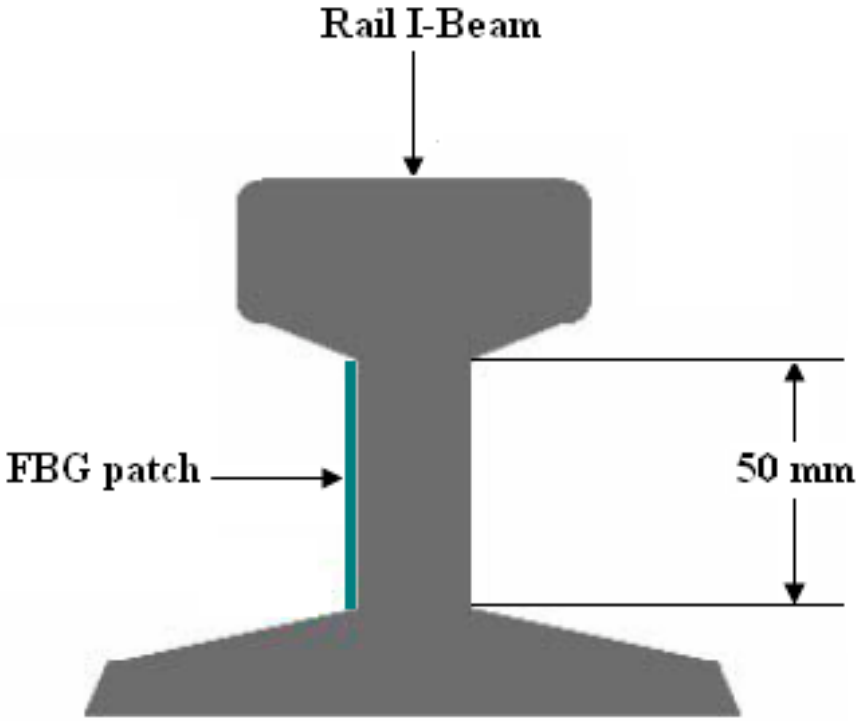

Figure 3.29 Double FBG patch

Figure 3.30 is a picture taken of the bonded patch.

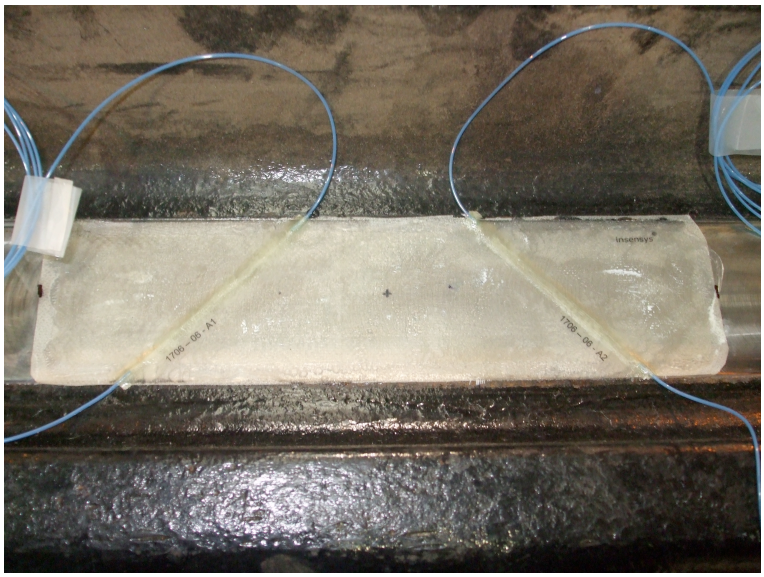

Figure 3.30 Picture of the double FBG patch

The arrangement is shown if Figure 3.31.

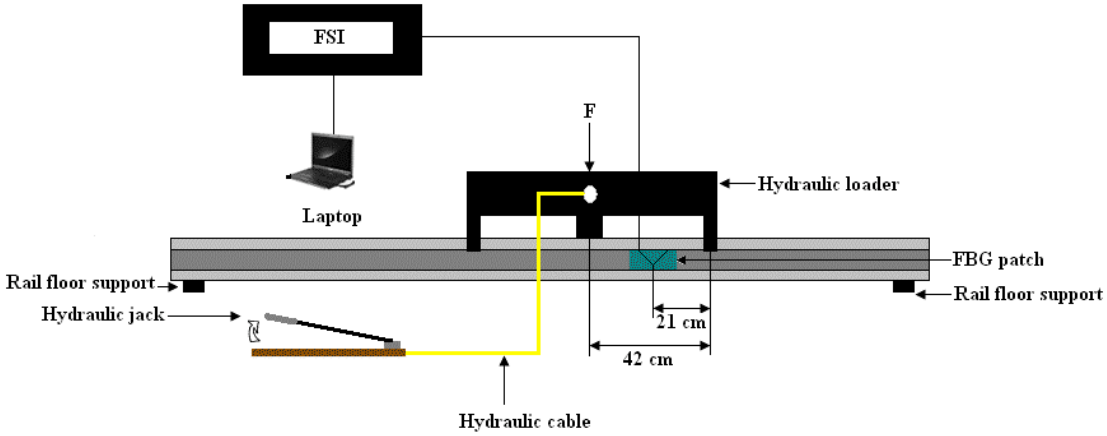

Figure 3.31 Experimental configuration for the double patch

Note that the experimental procedure for the double patch was identical to the single patch procedure, as described in section 3.4.5.

There were two primary reasons for pursuing a patch designed with FBGs mounted at ± 45° to the neutral axis. Firstly, as highlighted in sections 3.4.1 and 3.4.2, ± 45° is the orientation that induces the maximum shear in the web. It is for this reason that the FBGs mounted at ± 45° to the neutral axis induce a larger shift than that of an FBG mounted in parallel to the neutral axis, as is the case with the single-FBG patch. The second was to perform a performance comparison with Avery's current commercial electrical WIM system. There were ancillary reasons for investigating the double-FBG patch design, however these are commercially sensitive and it has been requested by Avery Weigh-Tronix that those details not be included in this thesis.

3.4.8 Double FBG patch results

Figure 3.26 represents the initial cyclic load test. The test begins at zero load, and then 13,000 kg was applied and held for a period of time before the load was released. The traces in Figure 3.32 illustrate the absolute wavelength shifts, clearly depicting one of the two FBGs in tension (magenta trace) and the other in compression (blue trace).

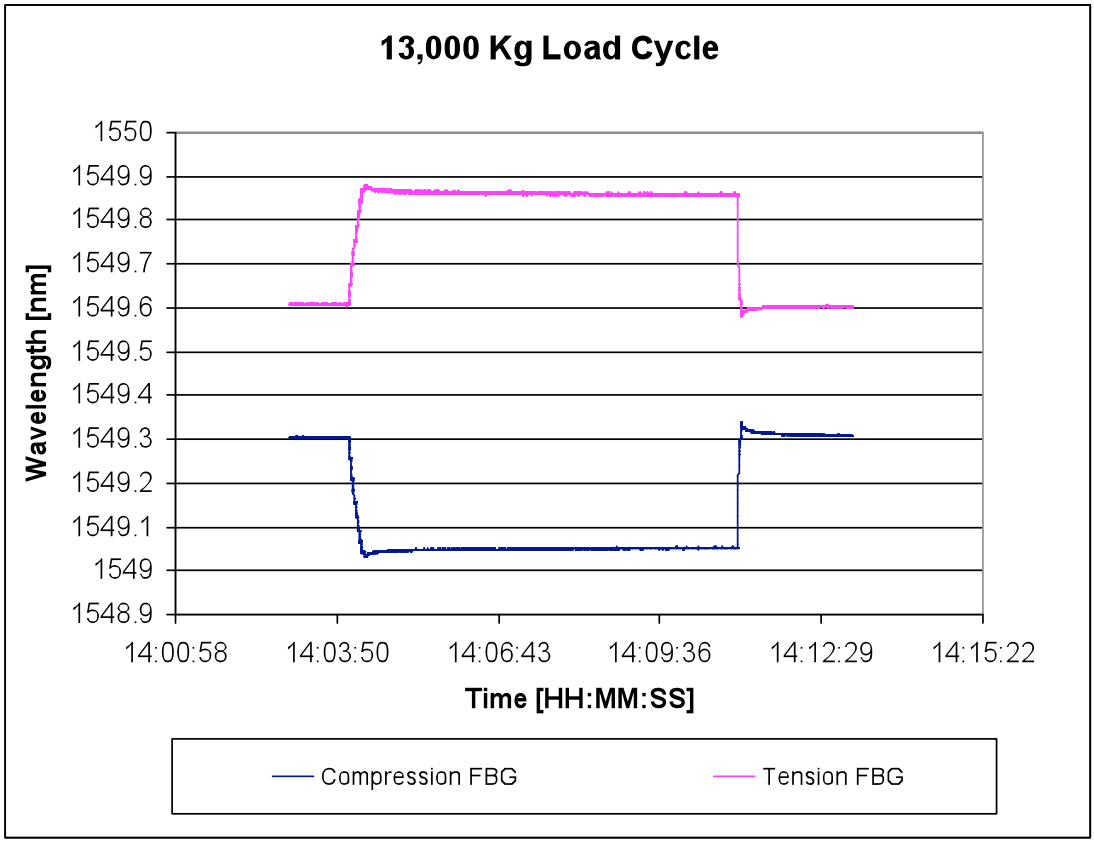

Figure 3.32 0 kg ⇒ 13,000 kg ⇒ 0 kg initial cyclic load test

The first result obtained utilising the double-FBG patch is shown in Figure 3.32. The result highlights that with two FBGs mounted at ± 45° to the neutral axis, the tension sensor (magenta trace) experiences a red shift, whilst the compression sensor (blue trace) experiences a blue shift. The test highlights that the tension FBG induces a shift of 255 nm whilst the compression FBG induces a shift of 256 nm. Reasons for the shift being slightly different could be inaccurate positioning of the sensors in the patch at the patch fabrication stage, or inaccurate positioning of the load-applying device to the track relative to the patch. Summing the two wavelength shifts, for 13,000 kg of load, a shift of 511 pm is produced. Translating that relative to the applied load, it yields a possible sensitivity of 25.44 kg/pm. A plot of the combined sensor shifts is shown in Figure 3.33.

Figures 3.34a-e illustrate five 0 kg ⇒ 13,000 kg test results. The results depicted again show the tension sensor (magenta trace) and the compression sensor (blue trace), with measurement points at 1,000 kg intervals. The results clearly show good repeatability, numerical data is presented in Table 3.5, whilst overlays of the five results are presented in Figures 3.35a and 3.35b.

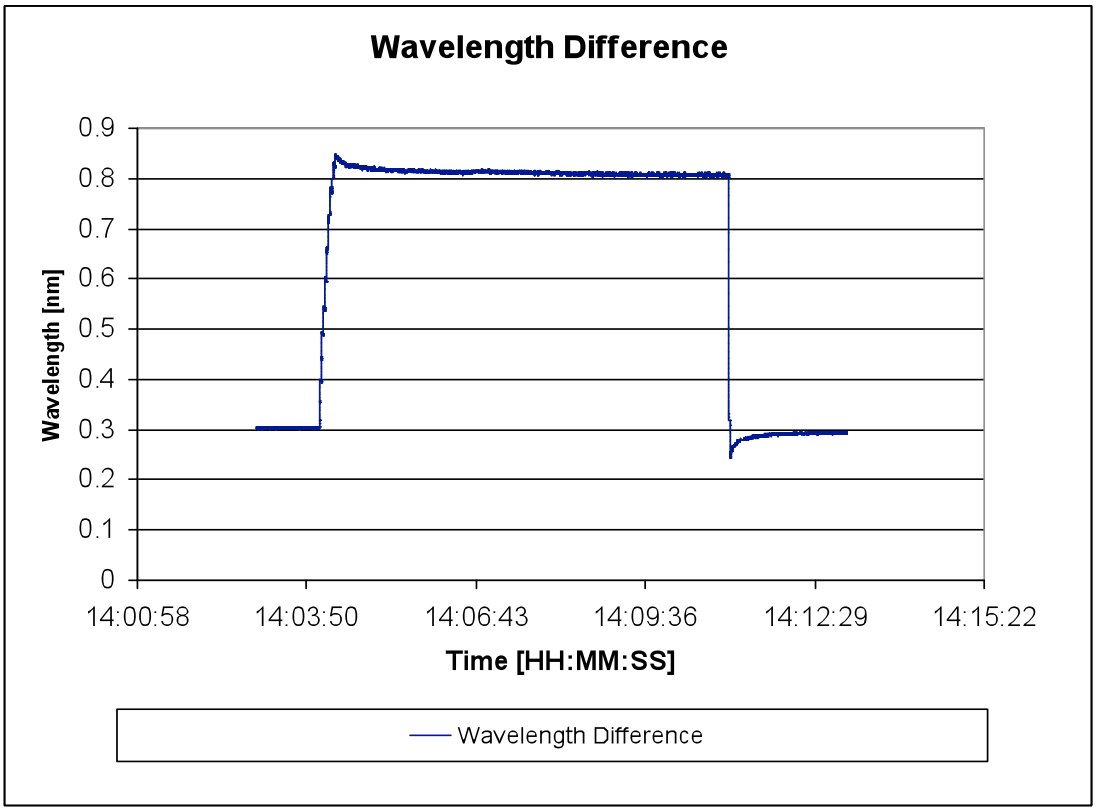

Figure 3.33 0 kg ⇒ 13,000 kg ⇒ 0 kg load cycle – combined response

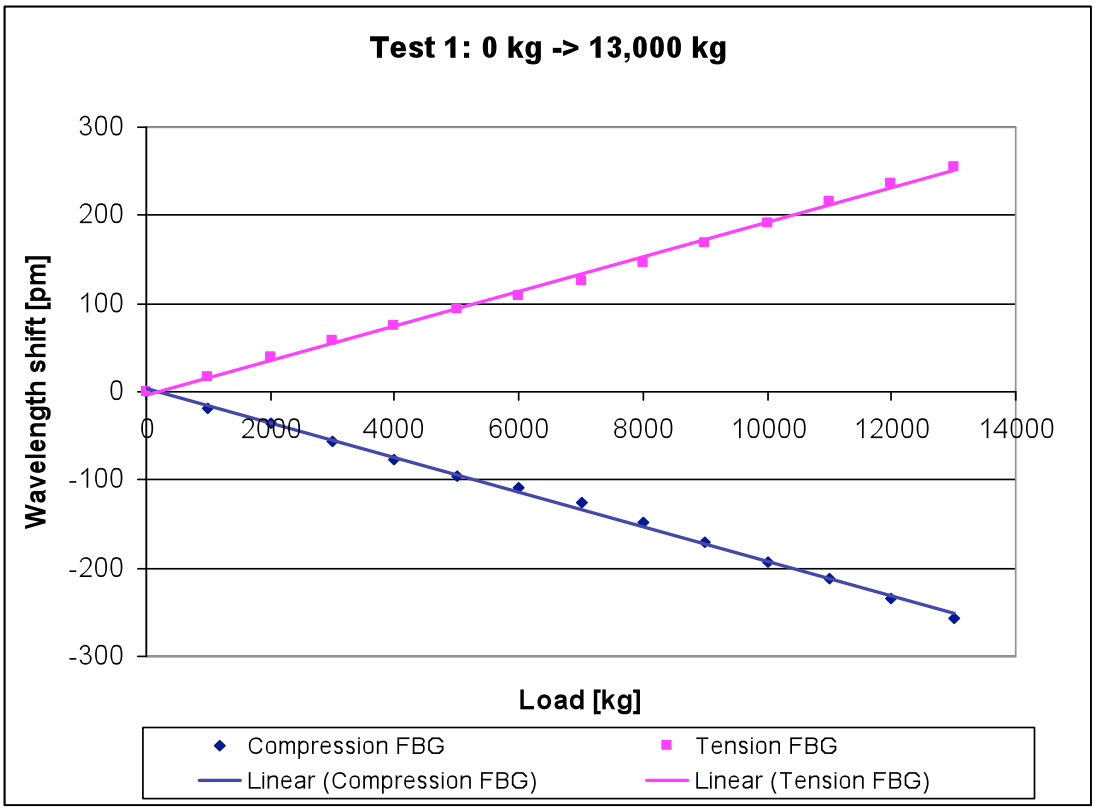

Figure 3.34a Test 1 result

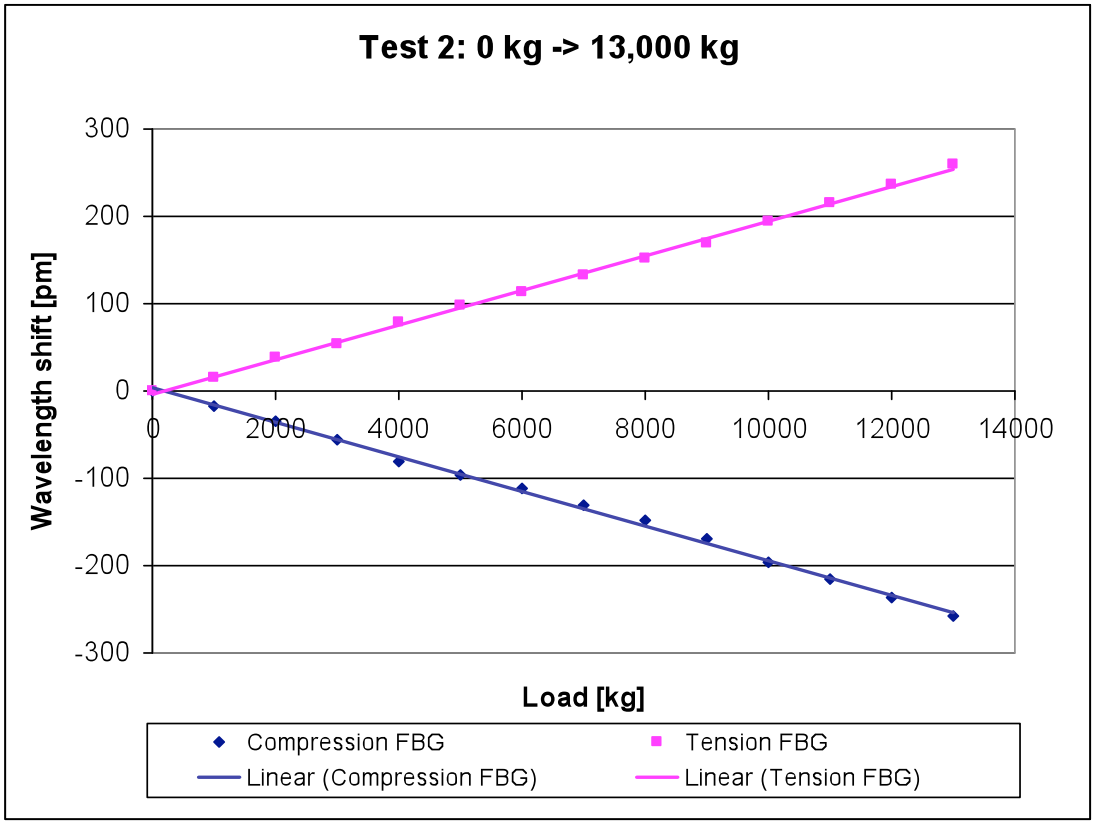

Figure 3.34b Test 2 result

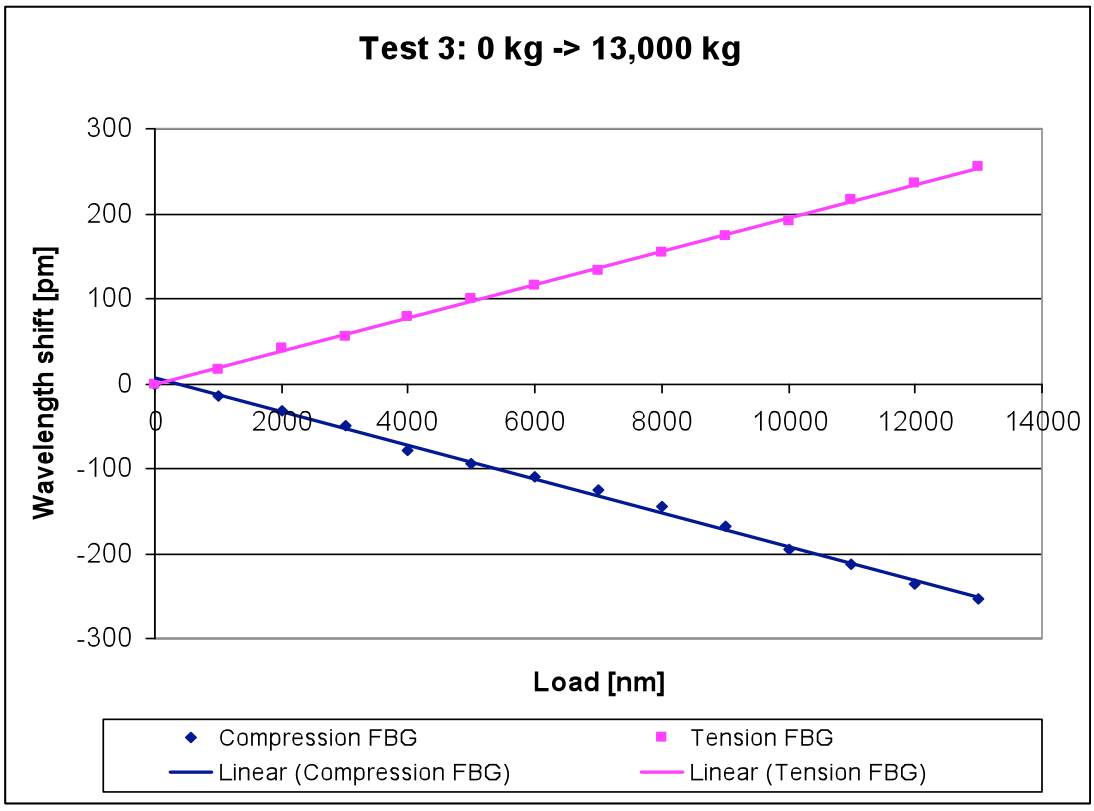

Figure 3.34c Test 3 result

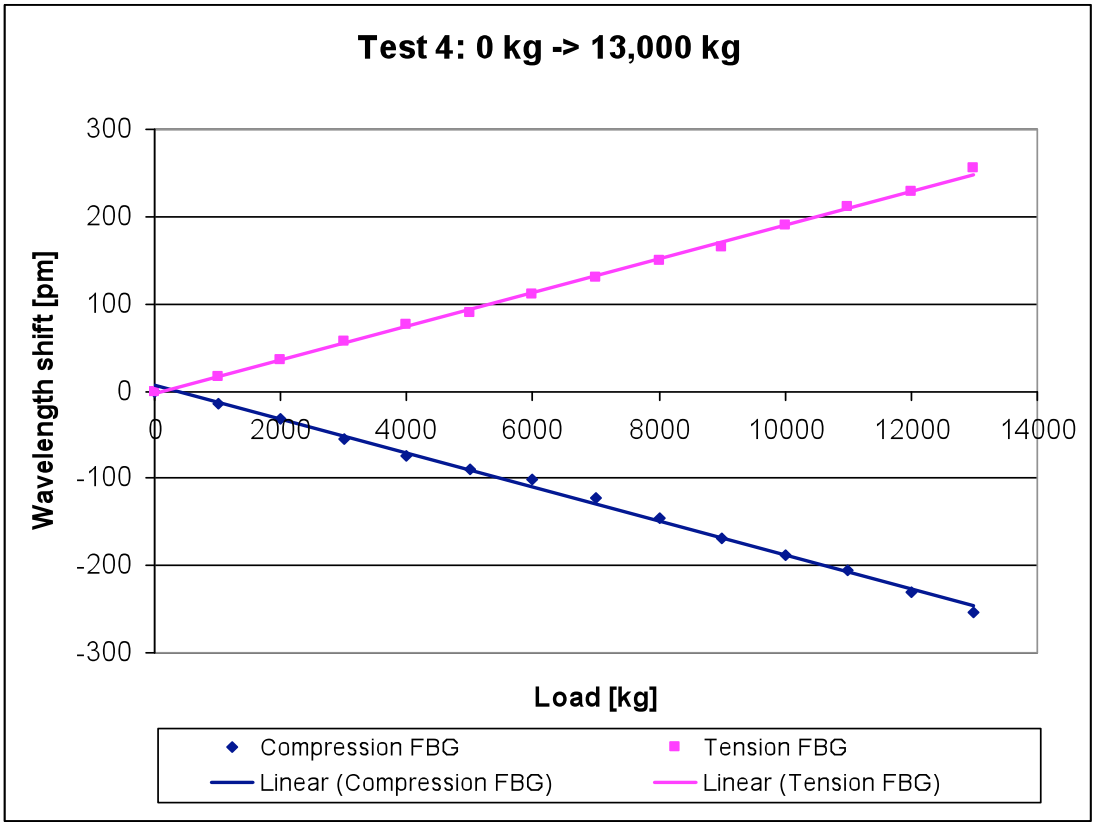

Figure 3.34d Test 4 result

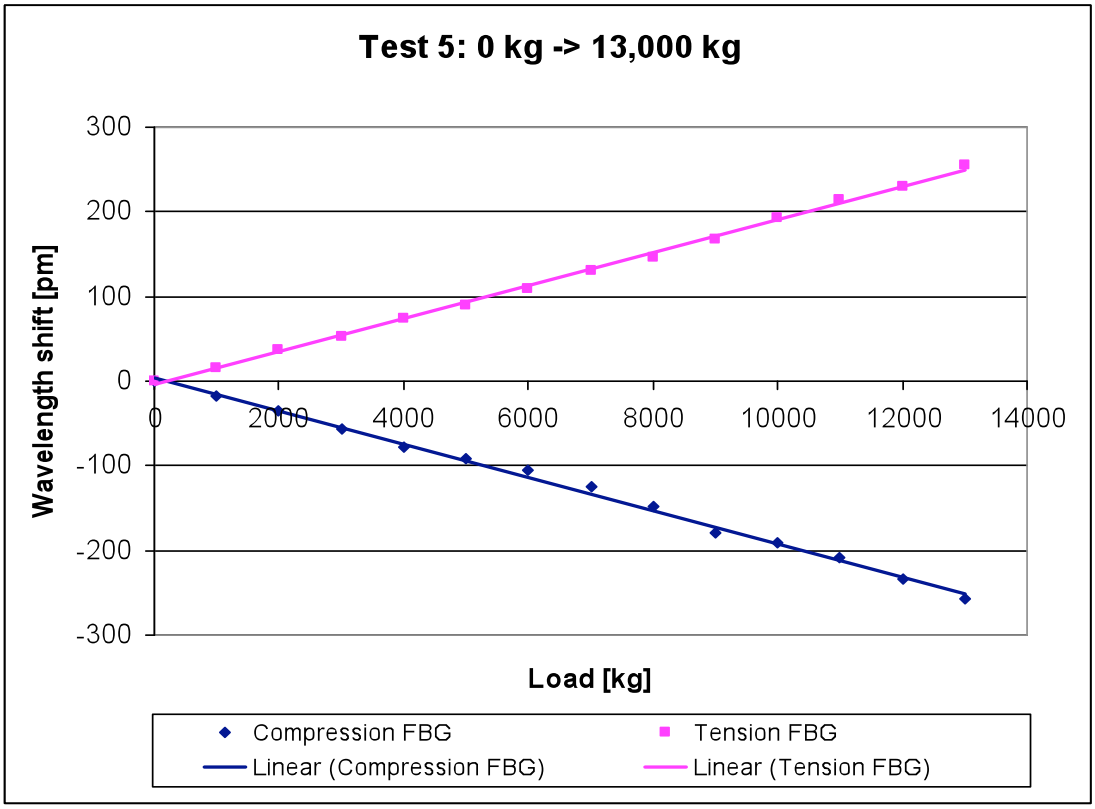

Figure 3.34e Test 5 result

Table 3.5 summarises the results obtained from the five tests.

Test N°	Compression FBG max shift (pm)	Tension FBG max shift (pm)	Wavelength difference (pm)	Achievable sensitivity (pm/kg)
1	-257	255	512	0.0394
2	-258	259	517	0.0398
3	-254	256	510	0.0392
4	-254	256	510	0.0392
5	-258	255	513	0.0395

Table 3.5 Summary of double patch results

Figures 3.35a and 3.35b show the combined responses of the compression and tension sensors respectively.

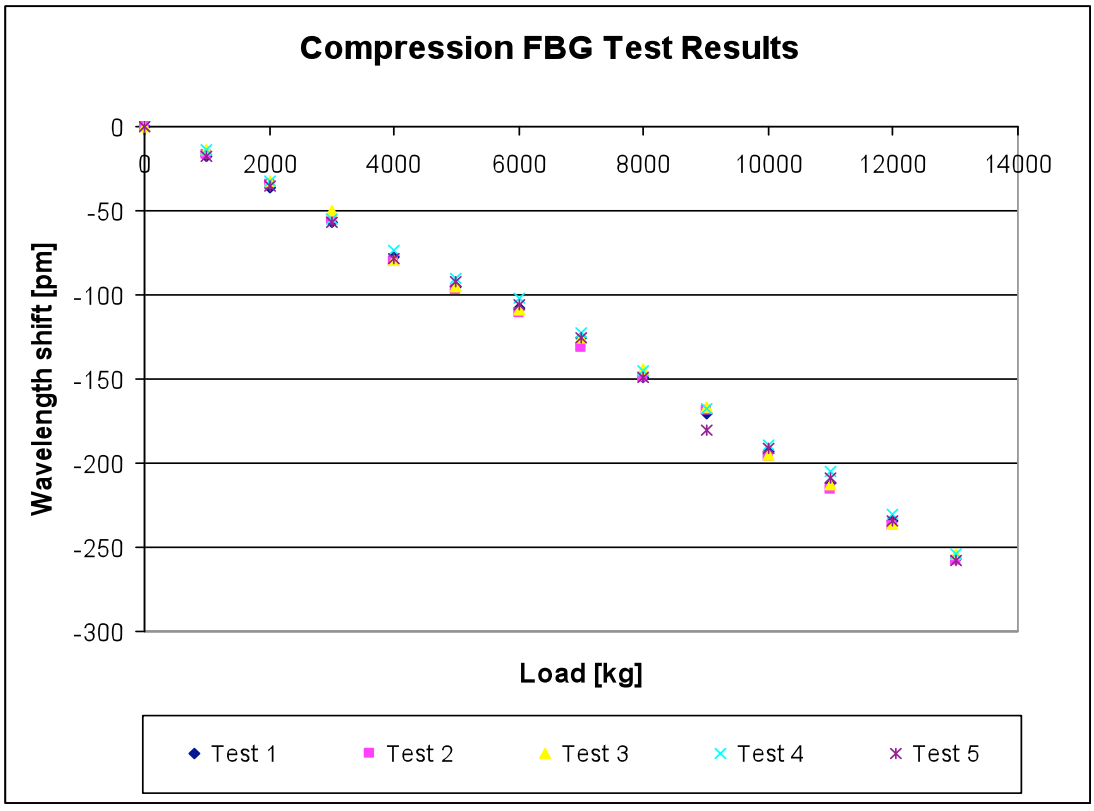

Figure 3.35a Compression FBG sensor responses from Tests 1-5

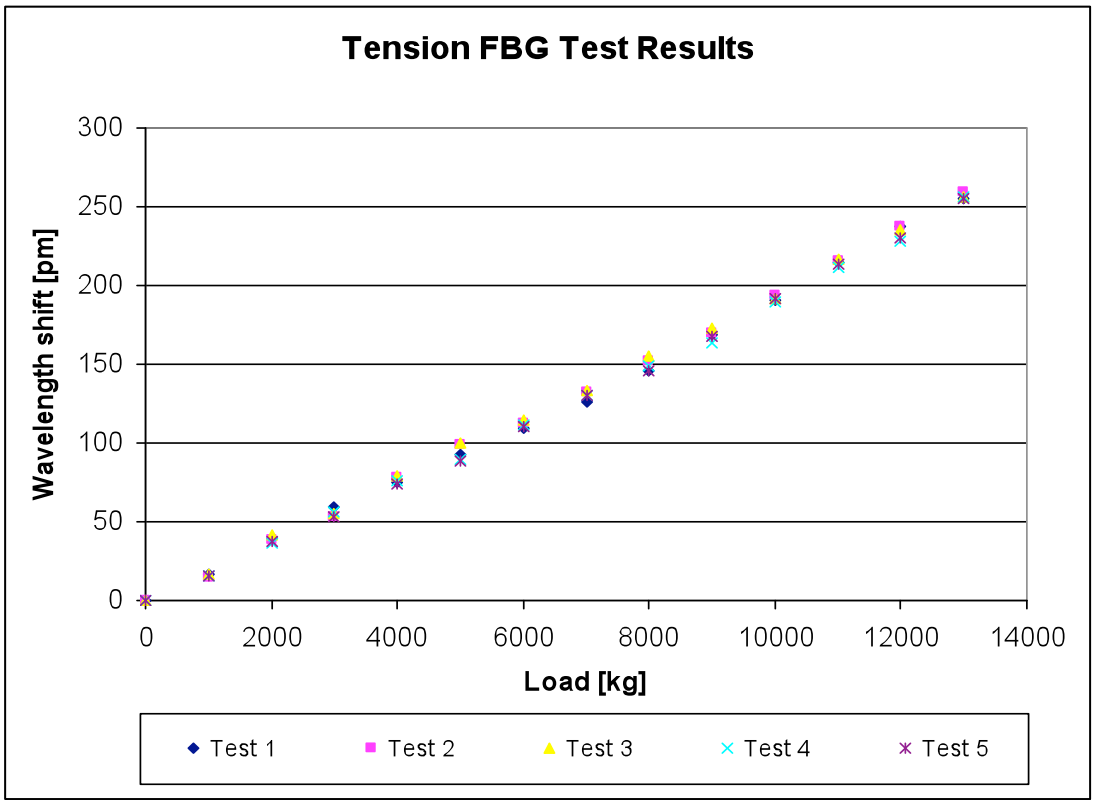

Figure 3.35b Tension FBG sensor responses from Tests 1-5

Results from the single-FBG patch tests showed that although the response was highly linear, the achievable sensitivity was too low for it to be feasibly developed into a commercial viable option for Avery. The double-FBG patch was designed to replicate an optical equivalent of Avery's current electrical rail WIM configuration. The largest shear strain is induced at ± 45° to the applied force; hence the reason why the FBG mounted at ± 45° induces a larger strain than the single-FBG sensor, which is mounted horizontally along the neutral axis. Combining this with the double patch having sensors mounted at ± 45° i.e. one in tension, the other in compression, as the load was applied, the tension FBG experienced a red shift, the compression FBG a blue shift. Summing the difference yields a total wavelength shift more than five times larger than the single-FBG patch.

In all tests with the rail patches, the most likely cause or error is experimental technique. The equipment was rather limited in that the load had to be manually applied, and then maintained as the equipment could not maintain an applied load without human intervention. The load was maintained within ± 5 kg of the targeted loaded.

3.5 Chapter conclusions

In this chapter, a detailed description of optical load sensing techniques for both static and dynamic loading had been reported, providing the foundation of research for any future endeavours Avery wish to pursue in optical load monitoring.

For the static loading tests, the initial work with the cantilever demonstrated a system, which was highly linear, highly repeatable and exhibited good sensitivity. Following on, the work described shows the novel integration techniques used to integrate FBGs into the framework of one of Avery's current electrical systems. The sensitivity achieved during this testing shows real potential that FBG sensors are a viable alternative to their electrical counter parts, if used in the appropriate application. Loads as small as 100 g were detected using the FBG / T702 hybrid load cell, and using a 15 kg load, a sensitivity of 41.3 pm/kg was determined. The system also showed high linearity and good repeatability over a series of cyclic load tests.

Even though no active dynamic testing could be performed, the intended application of the Insensys FBG patches was in dynamic rail WIM. To the best of the authors' knowledge, this is the first reported instance of embedding FBGs in e-glass in a ± 45° configuration to measure shear force.

The single-FBG patch yielded good linearity over the 13,000 kg measurement range, however the sensitivity was poor. Due to the limited area where the track was pre-treated for bonding, the only area this patch could be bonded to was near the neutral axis; therefore low sensitivity is not surprising. The double-FBG patch, with two FBGs mounted at ± 45° to measure shear in the web, yielded sensitivity five times greater than that of the single patch. This is due to the positioning of each grating relative to the neutral axis inducing a larger shift on both FBGs, and also the fact that one FBG was in tension and the other in compression. Calculating the difference between the two FBG wavelengths could then be used to infer applied load.

A crucial element of optical sensing is the interrogation of information encoded by the sensor; this chapter has demonstrated the Insensys FSI TDM-based system is an ideal solution for Avery's optical rail WIM ambitions.

3.6 Future work

It has since been decided that the best way to proceed regarding the static loading is to develop an all-new system rather than integrate the optical technology into their current product range. This has opened up the scope of the work to include investigating a variety of new avenues of research, including:

- Sensor configurations
- Materials
- Signal processing techniques such as Neural Networks
- Epoxies and bonding techniques

As it was not possible to conduct dynamic testing on live or test rail track, certainly an element of future research should include some active rail testing.

From the offset, for a rail WIM system, Avery envisioned a system that could be fitted in-situ. In order for commercial in-situ fitting of rail systems to be feasible, the following areas need to be further researched:

- In-situ treatment of the track. If the track is to remain in place, the area where the system is to be fitted must be properly treated before any system can be bonded. Currently this is done at the Avery installation facility
- The technique used for fitting the system to the track is vitally important. Far more work needs to be done on researching different glues and epoxies, as well as on the bonding process itself
- The current system undergoes rigorous calibration tests before it is returned to site to be re-fitted to the rail network. For any system to yield accurate results, calibration is essential. Therefore an in-situ calibration process must be devised

3.7 Chapter references

[1] G. L. Rossi, P. Maggiorana and C. C. Rondini, "*Development of a load cell based fiber Bragg grating sensors*", Proceedings of SPIE, vol. 5144, p 585, 2003

[2] E. Udd, W. L. Schulz, J Semi, K. Corona-Bittick, J. Dorr, K. Slattery, H. M. Laylor and G. McGill, "*Fiber optic smart bearing load structure*", Proceedings of SPIE, vol. 3587, pp. 40-48, 1999

[3] T. Matsumura, K. Nakamura and S. Ueha, "*A load cell using an optical fiber Bragg grating with inherent mechanical temperature compensation*", Optical Fiber Sensors Conference Technical Digest, vol. 1, pp. 347-350, 2002

[4] F. Mennella, A. Laudatia, M. Esposito, A. Cusano, A. Cutolo, M. Giordano, S. Campopiano and G. Breglio, "*Railway Monitoring and Train Tracking by Fiber Bragg Grating Sensors*", Proceedings of SPIE, vol. 6619, pp 66193H-1, 2007

[5] Web address: www.sensorline.de/forps. Accessed July 2009

[6] Web address: www. Sensornet.co.uk. Accessed July 2009

[7] Web address: www.roymech.co.uk. Accessed March 2010

[8] T. H. G. Megson, "*Structural and stress analysis*", 2nd Edition, Elsevier Butterworth Heinmann, 2005

4 Fuel level sensing techniques using single and multiple fibre Bragg grating based diaphragms systems

4.1 Chapter preamble

Fuel gauging systems in modern commercial aircraft are largely based on electrical capacitive sensing probes, which infer fuel level by continuously monitoring the capacitance value as fuel level changes. The capacitance value varies due to the differing dielectric values of air and fuel. In 2005, the UK Technology Strategy Board funded the Airbus led Integrated Wing (IW) collaborative R&T programme. Part of this programme was designed to investigate the feasibility of replacing the existing electrical sensing technology with optical sensing technology. This chapter will explore both single-sensor and multi-sensor level sensing techniques utilising FBGs, which have been either bonded to, or placed directly in contact with, a diaphragm that deforms under increasing isotropic hydrostatic pressure. In this case, the increasing hydrostatic pressure arises from an increase in liquid depth. Although the majority of the experimental work in this chapter is novel, it is based upon the wealth of work already carried out by other researchers working on FBG based sensors.

The advantages of using OFS over their electrical counterparts has been listed and discussed in Chapter 2, so the reader is highly encouraged to frequently refer back to Chapter 2 for an in-depth evaluation of OFS. However, to briefly recap, the main advantages of OFS are:

- Immunity to electromagnetic interference
- Lightness and compactness
- Remote interrogation
- Can operate in harsh, flammable and explosive environments
- Multiplexing capabilities

Clearly, in the highly flammable environment of an aircraft fuel tank, the advantages of removing any electrical components are stark, and the advantages of OFS listed above illustrate that they lend themselves aptly to this application.

Numerous optical liquid level sensing techniques have been previously reported. Examples include:

- Morris *et al* reported a liquid level sensor based on collimated light in a waveguide being coupled out at the air-liquid interface due to the increase in the external refractive index [1]
- Gao *et al* reported the design and characterization of a fibre optic level sensor based on measuring the attenuation of light in the fibre due to microbending [2]
- Welss reported a fluorescence-based optical liquid level sensor, where light is coupled into a fluorescent slab. In a slab-air interface condition, light within the slab is guided. However upon reaching the liquid, light is lost into the liquid. Liquid level can then be inferred by measuring the fluorescence power [3]
- Khaliq *et al* reported a liquid level sensor based on measuring the minimum attenuation value of a characteristic peak of a LPFG [4]

The proof-of-concept work in this chapter will be based on measuring the wavelength shift of a single FBG, or multiple FBGs, induced by a change in hydrostatic pressure caused by liquid level change. Whilst the aim is to develop a fuel level sensor, the liquid used for testing in these experiments is water, for safety purposes as well as for convenience. Even though fuel is less dense, the trend of the responses to variations in liquid level should be similar as fuel is only marginally less dense than water.

The chapter begins with an introduction to the current technology deployed in today's Airbus commercial aircraft, followed by a brief description of the basic principles of hydrostatic pressure in liquids.

The chapter continues by introducing the concept of diaphragm deflection induced by varying hydrostatic pressure, and how incorporating an FBG sensor and monitoring the Bragg wavelength can lead to the measurement of physical measurands. In section 4.5 details are provided on the design, fabrication, experimental arrangement and procedure, and finally the results obtained from performing testing on the aluminium/steel sensing system. Following on, the need for an aerospace compliant system is introduced, followed by analysis of the materials chosen. The chapter then discusses in detail the design, fabrication and assembly procedures for both the PPS sensor housing and Kapton

diaphragm. The experimental system and procedure is presented followed by the results obtained from the series of tests performed on this system.

Section 4.9 introduces the concept of a multi-FBG sensor based system and the advantages such a system possesses. The design of the multi-FBG sensing system is then presented, followed by a series of diagrams and images depicting the system design and experimental arrangement. The experimental procedure is discussed outlining the subtle differences between testing the single-FBG and multi-FBG systems. The results are then presented and summarized.

The chapter concludes with a summary and discussion of the results presented, followed by a brief summation of possible future work.

4.2 Current technology

Before presenting the experimental work, it would be prudent to review the current technology deployed in commercial aircraft. Whilst this section cannot describe the technology in detail due to confidentiality restrictions, the basic concepts and principles can be conveyed. The details in this section are a brief summation of the Introduction to Fuel Gauging Systems and Techniques technical document produced by Airbus UK Ltd [5].

The most prominent technique for measuring fuel level in commercial aircraft is by using electrical capacitive sensors.

4.2.1 Capacitance probe design

The capacitance probe is formed from two concentrically positioned aluminium tubes, which form the electrodes of the capacitor. The outer electrode is formed from corrosion protected precision aluminium alloy, whilst the inner electrode is formed from a precision parallel alloy. The inner electrode is placed inside the outer electrode and the entire unit is fixed in position within the aircraft fuel tank using fuel resistant support pins. Figure 4.1 illustrates the basic design concept for the probe.

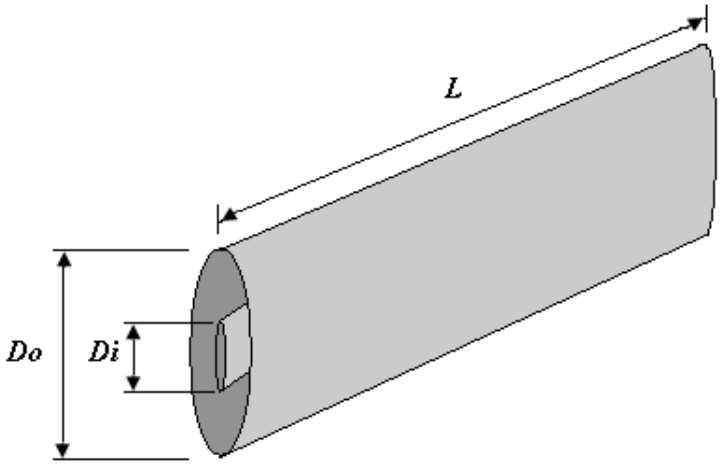

Figure 4.1 Concentric capacitance probe design

If the probe is completely in air, the capacitance, C, can be calculated by:

$$C = \frac{\pi \varepsilon_o K L}{\ln(D_o / D_i)}$$ **Equation 4.1**

where C is the capacitance in picofarad (pF), ε_o is the vacuum permittivity constant (8.85), K is the dielectric constant (1 for air), L is the length of the probe in metres, D_o is the diameter is the outer tube and D_i is the diameter of the inner tube.

However when the probe is immersed in fuel, in effect two separate probes are formed. One equivalent to the immersed length with the dielectric constant of fuel, the other equivalent to the remaining length in air, with the dielectric constant of air. This is diagrammatically illustrated in Figure 4.2. Note that the dielectric constant of fuel is approximately 2.1times greater than that of air.

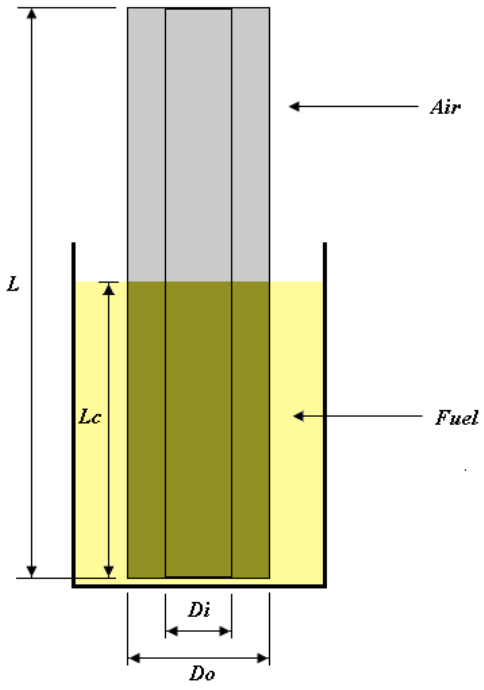

Figure 4.2 Illustration of probe partially immersed in aviation fuel

Under this condition, equation 4.1 can be modified to accommodate the above effect, and the capacitance can now be calculated using the following formula:

$$C = \left[\left(\frac{\{\pi\varepsilon_o\}}{\ln\{D_o/D_i\}}\right)(K_F - 1)L_C + C_E\right] \qquad \textbf{Equation 4.2}$$

where C is the total capacitance, L_C is the immersed length, K_F is the dielectric constant of fuel, C_E is the sensor empty capacitance, ε_o is the vacuum permittivity constant (8.85), D_o is the diameter is the outer tube and D_i is the diameter of the inner tube.

As the dielectric constant of fuel is approximately 2.1 times greater that of air, when the capacitance probe is completely immersed in fuel, the capacitance measured will be approximately 2.1 times greater than when the probe is surrounded only by air.

It should also be noted that the dielectric constant and density of aviation fuel varies according to a number of parameters. These include temperature, pressure, fuel contamination and the addition of fuel additives. Therefore when using capacitive sensors, the dielectric constant and density of fuel must also be measured. These are relatively complex operations; therefore it is beyond the scope of this thesis to provide an in-depth review of such measurement techniques beyond stating they must be performed in order to obtain accurate fuel level readings.

4.3 Principles of pressure in a fluid

When a fluid is static, it exerts a force perpendicular to any surface it comes into contact with, in the case of the work in this chapter, the diaphragm surface. This is the same force as humans feel as they dive deeper underwater. Even though the liquid as a whole is at rest, the liquid molecules are actively moving around. The force exerted by the liquid is caused by said molecules colliding with the diaphragm surface.

If the diaphragm was exposed to liquid on both sides, the pressure exerted on both sides of the diaphragm would be equal. Consider a force F, exerted equally on both sides of a diaphragm of area A, the pressure p exerted on the surface is defined as:

$$p = \frac{F}{A}$$ **Equation 4.3**

Atmospheric pressure p_a is the pressure of the earth's atmosphere. Variations in this value can be caused by weather variations or variations of altitude. At sea level the earth's atmospheric pressure is approximately 1013 mb or 29.92 inHg.

If a diaphragm is sealed over an air cavity such that the internal atmospheric pressure remains constant as the external pressure increases due to liquid level change, then the pressure p at a given depth h will be greater than the internal atmospheric pressure p_a. Therefore the hydrostatic pressure p_h, can be expressed as:

$$p_h = p_a + \rho g h$$ **Equation 4.4**

where ρ is the liquid density (kg/m^3), g is the gravitational acceleration (m/s^2) and h is the height of the liquid. Note the density of water is 1000 kg/m^3, whilst the density of JA-1 aviation fuel is approximately 805 kg/m^3.

4.4 Principles of diaphragm behaviour when exposed to variations in hydrostatic pressure

Providing the deflection of a diaphragm is less than the thickness of the diaphragm itself, the output is proportional to the to the applied pressure. However it should be noted that the general response of a diaphragm is non-linear, and as the deflection increases, the response becomes increasingly non-linear. A rule-of-thumb for diaphragm design is that the deflection at the diaphragm centre must not be greater than the diaphragm thickness,

and to ensure the response remains in the linear region, central deflection should be limited to ¼ of the diaphragm thickness.

4.4.1 FBG/diaphragm based sensor

The proposed concept in this chapter consist of a diaphragm bonded and sealed over an air cavity with a FBG either bonded to, or placed directly in contact with, the diaphragm such that any change in the external pressure will result in diaphragm deformation. This is conceptually illustrated in Figure 4.3

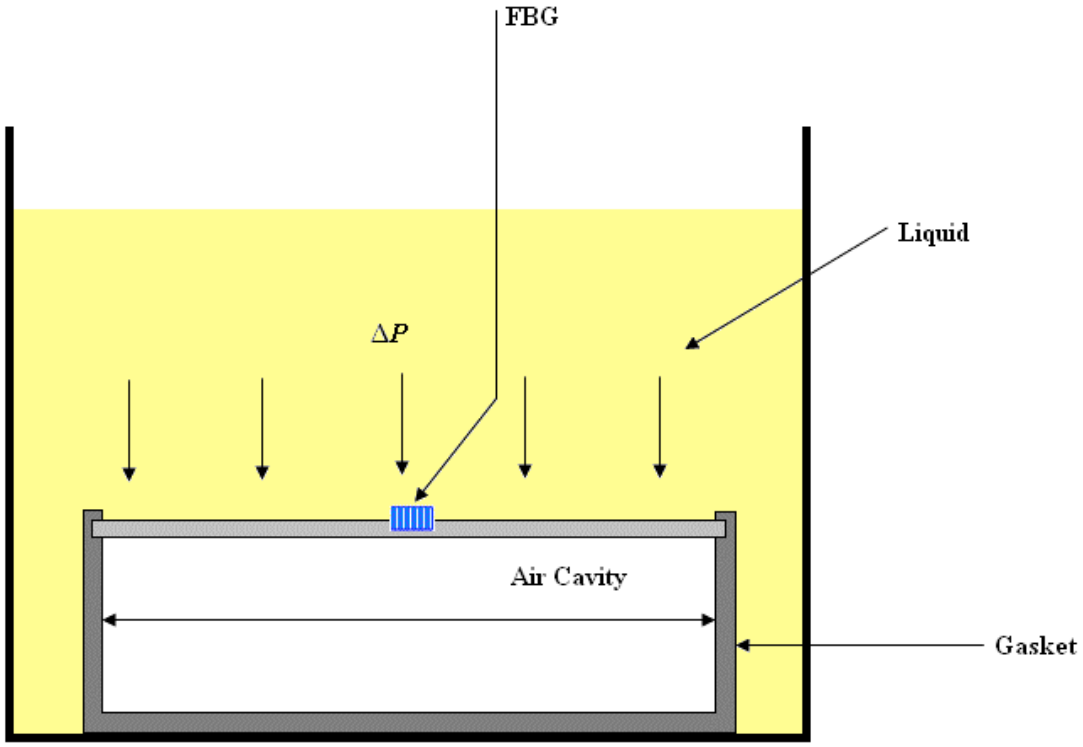

Figure 4.3 Concept of FBG based pressure sensor

A round diaphragm of diameter $2a$ and thickness t is deflected when there is an external pressure increase owing to increasing liquid level. This in turn causes stresses to appear across the diaphragm disk, and with a FBG in place, these stresses can be measured.

The centre deflection Y_c (mm), is given by the following equation as long as the material remains within the elastic region [6]:

$$Y_c = \frac{3PR_0^4(1-\upsilon^2)}{16t^3E} \qquad \textbf{Equation 4.5}$$

where P is pressure (Pa), R_0 is the radius of the diaphragm (mm), t is the diaphragm thickness (mm), υ is Poisson's ratio (dimensionless) and E is Young's modulus for the diaphragm (Pa).

The maximum strain $\varepsilon_{\max}$, at the circumference of the diaphragm is a linear function in relation to the pressure difference Δp, and is given as:

$$\varepsilon_{\max} = \left[\frac{3(1+\upsilon)\Delta p}{8E} \left(\frac{a}{t} \right)^2 \right] \qquad \textbf{Equation 4.6}$$

The pressure difference Δp, is then given as:

$$\Delta p = \left[\frac{8E_{\varepsilon_{\max}}}{3(1+\upsilon)} \left(\frac{a}{t} \right)^{-2} \right] \qquad \textbf{Equation 4.7}$$

The resultant deformation of the diaphragm will change the physical fibre dimensions resulting in a change in the Bragg wavelength λ_B. The wavelength shift $\Delta\lambda_B$, caused by this deformation is given as:

$$\Delta\lambda_B = \lambda_B(1-\rho_e)\varepsilon_{\max}$$

where λ_B is the initial Bragg wavelength and ρ_e is the photo-elastic coefficient of the fibre.

A detailed analysis of general membrane deflection has been previously reported by Wan *et al* [7].

By monitoring the wavelength shift of the FBG, the level of liquid can be inferred by the magnitude of said shift. For a more in-depth analysis of Bragg grating sensitivity to strain, refer to Chapter 2.

4.5 Single sensor continuous level sensor housing

The concept for a single-FBG level sensor is based on the design of an aluminium gasket, which houses a shim-steel diaphragm with a FBG bonded directly to it. Figure 4.4a-c is the CAD image and technical designs of the gasket and retaining ring.

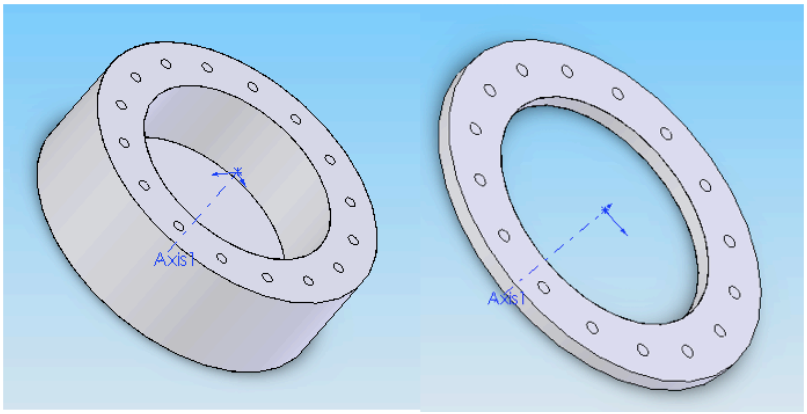

Figure 4.4a CAD design "Finish Image"

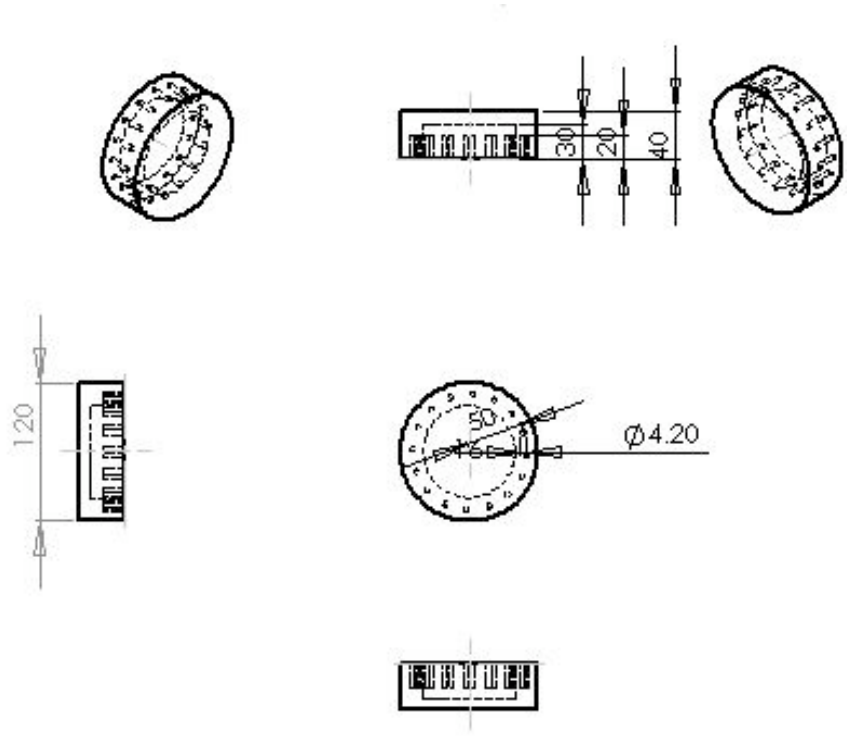

Figure 4.4b Technical design of the gasket base

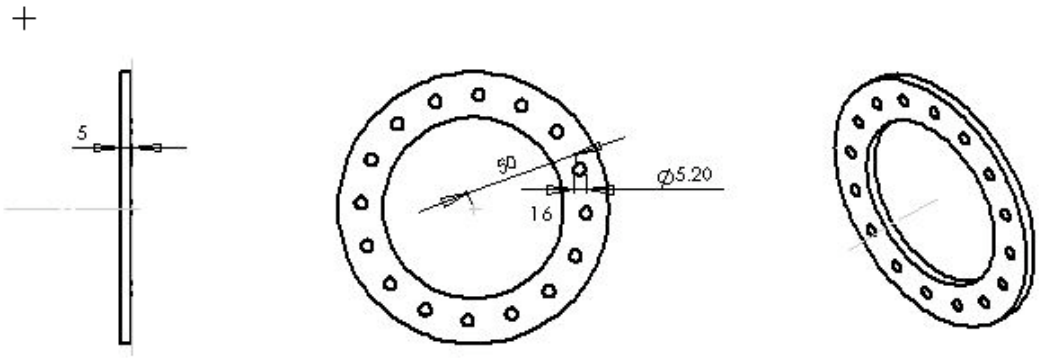

Figure 4.4c Technical design of the gasket retaining ring

RPS Engineering manufactured the gasket, along with the numerous shim-steel circular diaphragms used in this series of experiments.

To fix the diaphragm in position, a silicone rubber sealant (Instant Gasket) was placed around the rim of the diaphragm on both sides, and this effectively sandwiched the diaphragm between the base and retaining ring. 16 screws were then used to hold the base and retaining ring together creating a seal once the sealant has cured for 24 hours. To complete the seal, a thin layer of Instant Gasket was brushed around the external joint where the retaining ring meets the base. This forms the sealed air cavity within the base/underneath the diaphragm.

The FBG was bonded centrally on the diaphragm surface using RS two-part epoxy. A thin layer was brushed onto the diaphragm surface, the fibre was then positioned, and finally another thin layer of epoxy was brushed over the fibre. This was then left to cure at room temperature for a further 24 hours.

Figures 4.5a and 4.5b is a diagram of the complete sensor housing system, and a photograph of the assembled sensing unit, respectively.

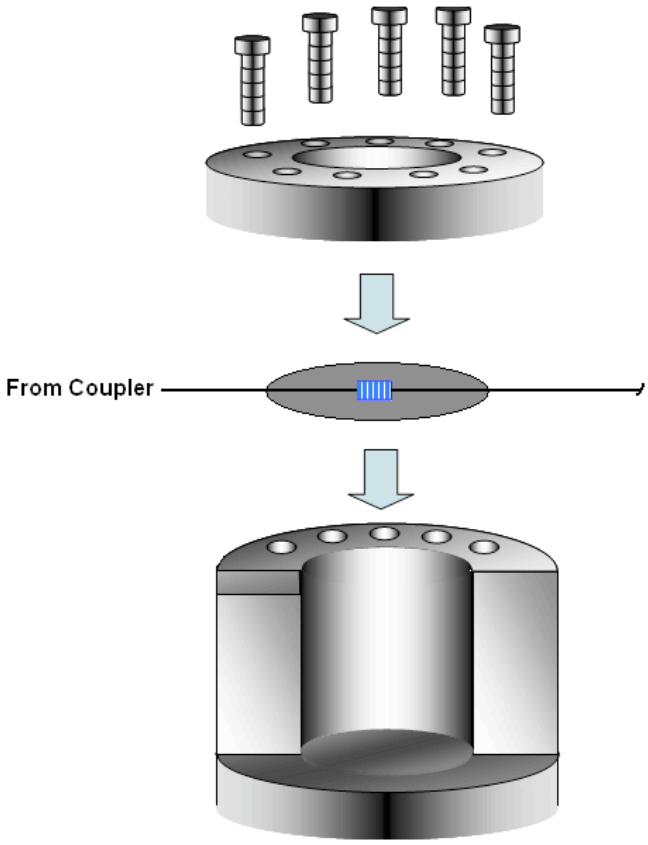

Figure 4.5a Diagram of the aluminium sensor housing

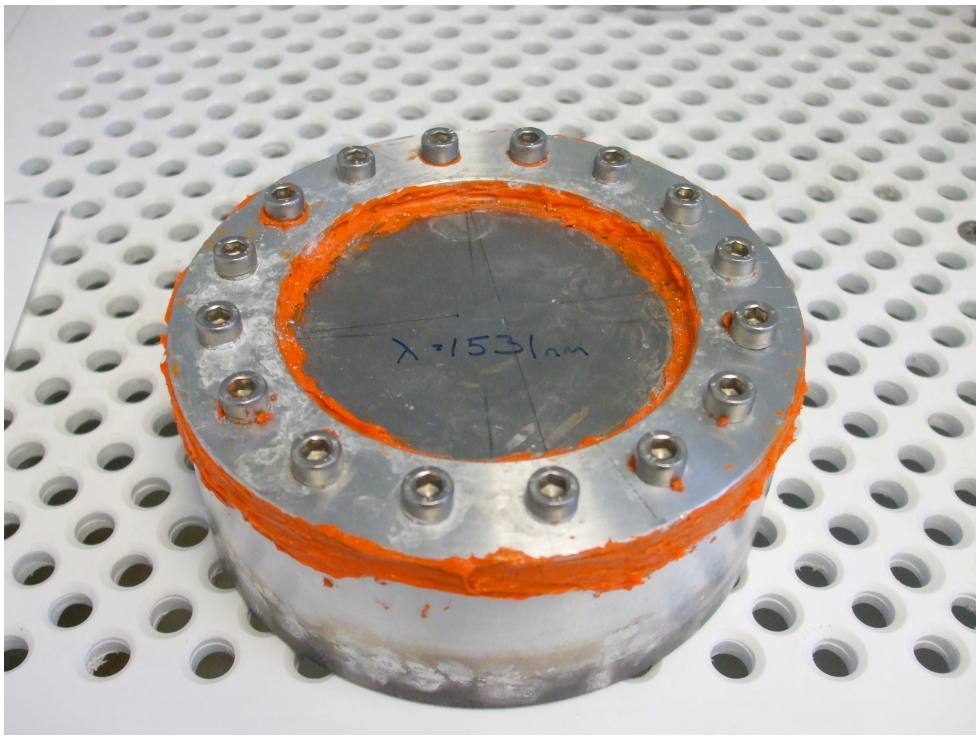

Figure 4.5b Picture of the aluminium sensor housing / steel diaphragm

4.6 Proof-of principle experimental results from exposing the sensor to hydrostatic pressure variations

This section will outline the experimental procedure for the hydrostatic pressure variation experiments and then present the experimental results obtained.

4.6.1 Experimental arrangement and procedure

The sensing gasket was positioned at the base of a modified storage tank capable of containing water up to a depth of 50 cm. The water was added by simply feeding a hose from a tap directly into the storage tank. The water was then allowed to reach equilibrium for no less than three hours for each test. The sensor housing was placed on a base plate with an extended handle for manual level control. A ruler was attached to the handle to monitor the sensor position relative to the depth. By hand the sensor level was varied and readings were taken at 1 cm intervals.

As the Ibsen I-MON 400e interrogation unit measures wavelength shift as a function of time, to obtain a specific depth, the time was manually logged at each level point. Therefore wavelength shift as a function of depth could be plotted.

The experimental arrangement consisted of an AFC broadband source, a 50:50 coupler, the Ibsen I-MON 400e interrogation unit and a laptop. The FBG was illuminated by the broadband source and the I-MON unit interrogated the reflected spectrum. The data was then saved in the form of a .txt file to the laptop. For more details on the Ibsen I-MON 400e, refer to Chapter 2.

The optical system and complete experimental arrangement are illustrated in Figures 4.6a and 4.6b respectively.

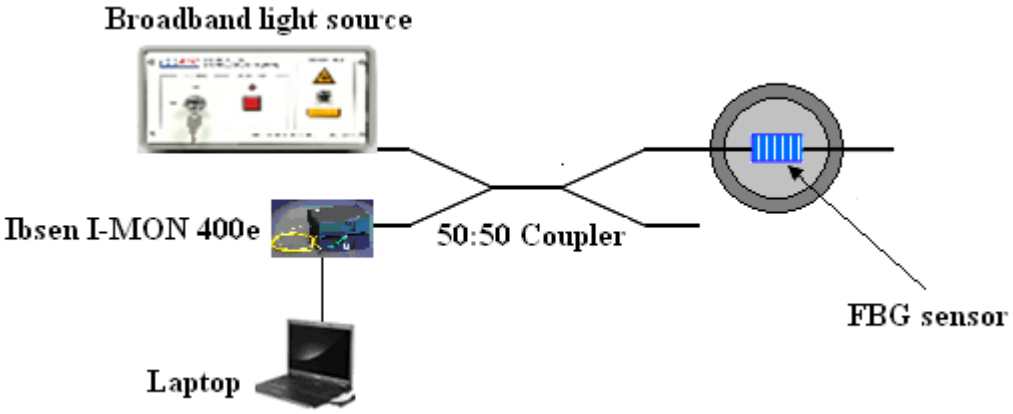

Figure 4.6a Schematic of the optical circuit

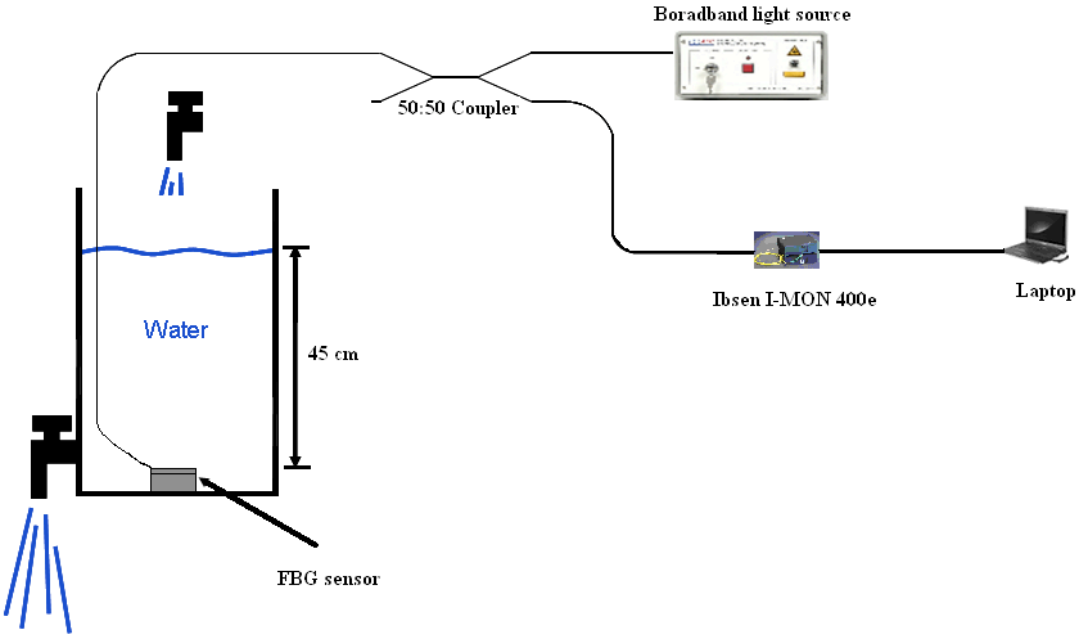

Figure 4.6b Schematic of the complete experimental arrangement

The initial experiments involved testing a number of aluminium diaphragms of varying thickness to test for sensitivity to hydrostatic pressure variations. RPS Engineering fabricated three diaphragms to test with the aluminium sensor housing. Table 4.1 outlines the specifications for each diaphragm.

Diaphragm	Thickness
D1	0.6 mm
D2	0.4 mm
D3	0.2 mm

Table 4.1 Aluminium diaphragm test specimen details

4.6.2 Experimental results from aluminium diaphragms

Prior to designing and manufacturing a sensing system constructed from aerospace-compliant materials, it was necessary to perform proof-of-principle experiments to demonstrate the capability of such a design to Airbus and the associated IW partners.

Initially three diaphragm thicknesses were tested with a single FBG bonded centrally to the shim-steel diaphragm surface. The thicknesses for the respective diaphragms are listed in Table 4.1.

Once the testing had been completed and the results discussed with the IW partners, the diaphragm yielding the result most conducive to further testing was interrogated in more detail by performing hydrostatic cyclic testing to analyse the repeatability of the system.

4.6.2.1 0.6 mm-thick steel diaphragm (D1)

Figure 4.7 shows the wavelength induced shift induced by a FBG on the 0.6 mm-thick steel diaphragm. The sensor was initially submerged under 45 cm of water, and then raised at 1 cm intervals to the point where the sensor was at the water surface. Note that as the sensor position is elevated 5 cm from the gasket base, the results represent a 45 cm level change, from 50 cm to 5 cm.

The encouraging aspect is that result is highly linear. However the sensitivity to hydrostatic pressure variations is relatively small. The overall shift is 47.2 pm, giving a sensitivity of 1.049 pm/cm of level change.

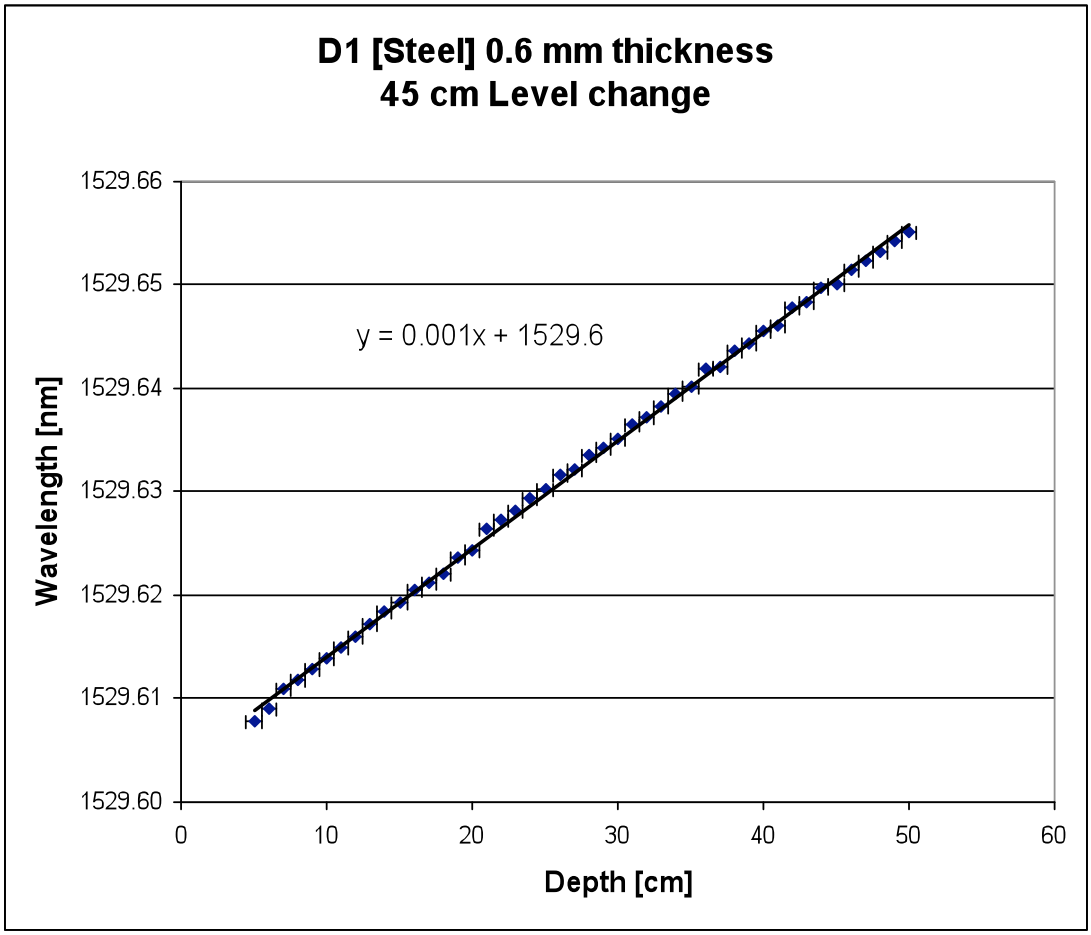

Figure 4.7 The result from of the 0.6 mm-thick steel diaphragm

4.6.2.2 0.2 mm-thick steel diaphragm (D2)

The next test conducted was using a 0.4 mm-thick steel diaphragm. The results of the test are shown in Figure 4.8.

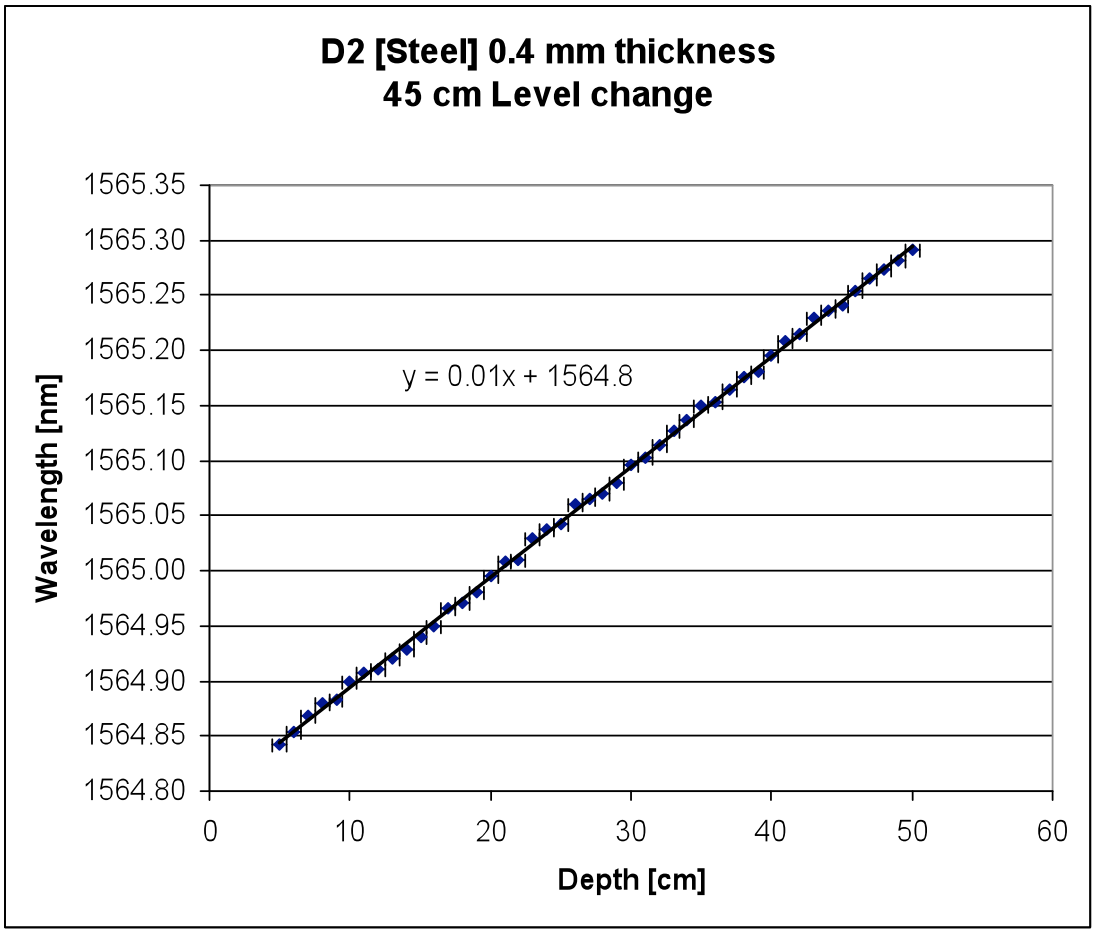

Figure 4.8 The result from of the 0.4 mm-thick steel diaphragm

The result from the 0.4 mm-thick diaphragm was again encouraging. Again the response is highly linear, however as expected, this diaphragm induced a larger deformation than D1. This resulted in a larger wavelength shift being observed. Over the 45 cm measurement region, the overall wavelength shift was 448.8 pm, yielding a possible sensitivity of 9.973 pm/cm of level change. This level of sensitivity meant the specified sensitivity set by the IW project could be achieved using such a system.

4.6.2.3 0.2 mm-thick steel diaphragm (D3)

The final test conducted was using a 0.2 mm-thick steel diaphragm. The results of the test are shown in Figure 4.9.

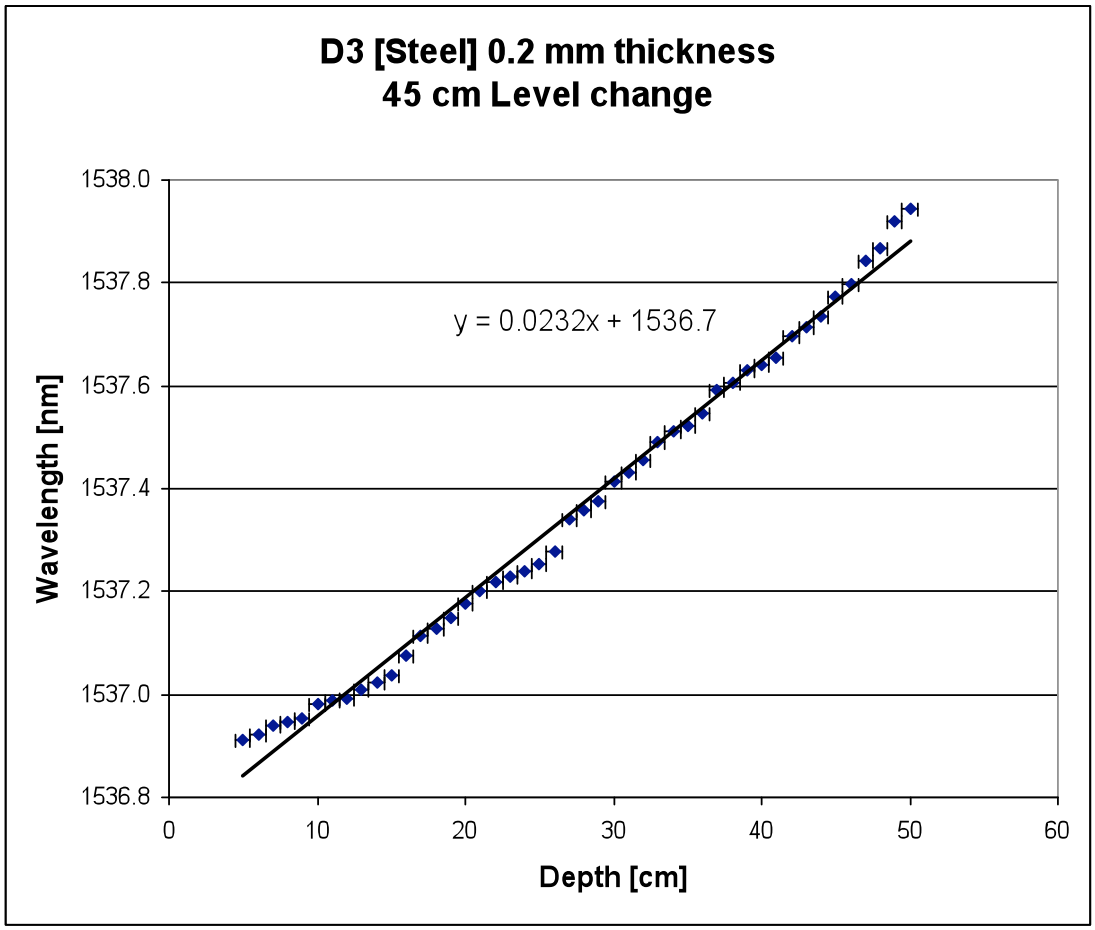

Figure 4.9 The result from the 0.2 mm-thick steel diaphragm

Despite seeing a further increase in sensitivity, diaphragm D3 demonstrated considerable non-linearity in its response to hydrostatic pressure variations. The overall wavelength shift measured over the 45 cm sensing region was 1031.6 pm, yielding a possible sensitivity of 22.924 pm/cm of level change.

Of the three steel diaphragms tested, the most encouraging result in terms of linearity and sensitivity came from diaphragm D2. To ensure the feasibility of such a system, further testing was required in order to analyse its repeatability. Note that cyclic repeatability tests were performed on diaphragm D2 only.

4.6.2.4 Analysis of diaphragm D2

One of the key requirements for such a system is the reproducibility of the sensor response. Therefore the next stage of testing was to perform cyclic tests to observe the repeatability of the sensor.

The experimental procedure was identical to that of the initial testing, however for this series of tests, complete cycles were performed. Initially the sensor was at the base of the tank and raised in 1 cm intervals. When the sensor reached the water surface, it was subsequently lowered in 1 cm intervals back to the tank base, giving a complete cyclic result. Five cycles were performed.

4.6.2.4.1 Calculation of estimated central deflection

The central diaphragm deflection for diaphragm D2 was estimated using equation 4.5. Shim steel was used by RPS to fabricate the diaphragm, therefore figures of 200 GPa and 0.3 for Young's modulus and Poisson's ratio were used respectively. As the maximum depth the sensor could experience was 45 cm, a figure of 4565 Pa was calculated based on fresh water at a temperature of 20°C.

$$Y_c = \frac{3PR_0^4(1-\upsilon^2)}{16t^3E}$$

$$Y_c = \frac{3\times 4565\times 60^4\times(1-0.3^2)}{16\times 0.4^3\times 200{,}000{,}000{,}000}$$

$$Y_c = \frac{3\times 4565\times 12960000\times 0.91}{16\times 0.064\times 200{,}000{,}000{,}000}$$

$$Y_c = \frac{161.51\times 10^9}{204.8\times 10^9}$$

$$Y_c = 0.789mm$$

4.6.2.4.2 Results from diaphragm D2

The initial test result is depicted in Figure 4.10a. It involves cycling the liquid depth over a 45 cm range in 1 cm intervals for both increasing (magenta trace) and decreasing (blue trace) depth. Each measurement point on the graph depicts a 1 cm incremental or decremental depth interval. The experiment technique was to vary the liquid level to the required depth, log the time at which said depth was achieved, then manipulate the data in the Insensys .txt file to extract the wavelength information for the given time. From this, wavelength as a function of depth could be plotted.

Figure 4.10b depicts the same data set, however 100 pm of absolute wavelength has been deducted from the increasing measurement points to add graph clarity.

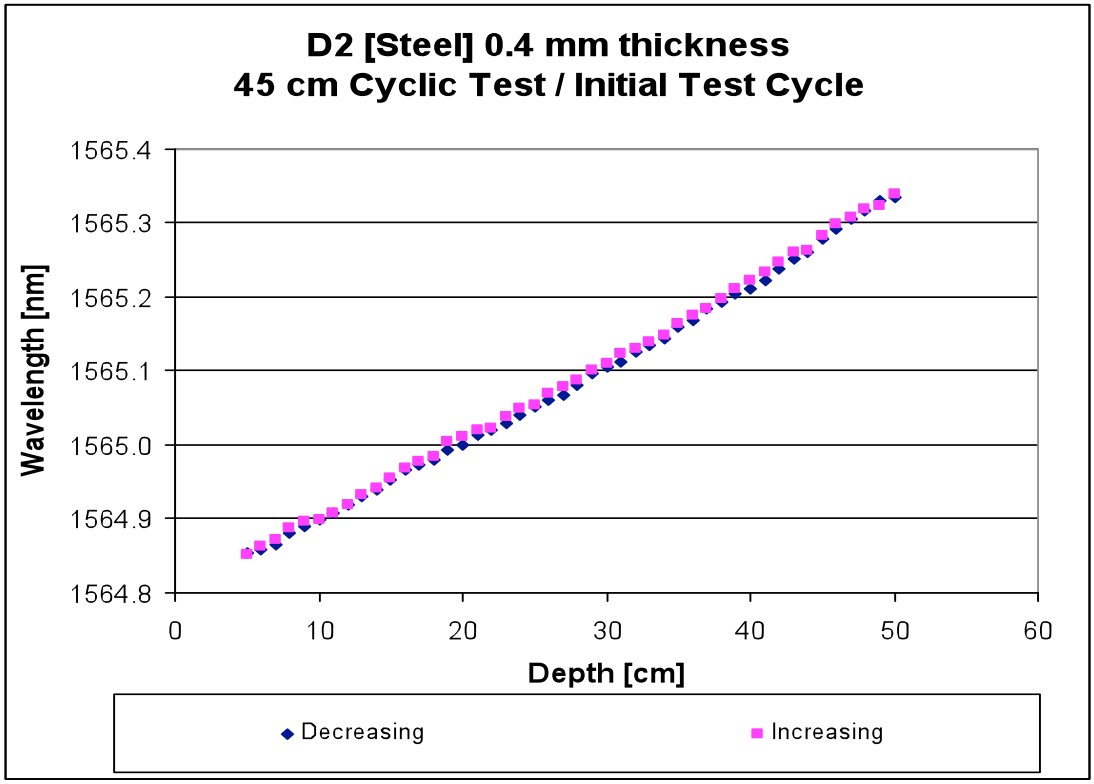

Figure 4.10a Cyclic response from the test cycle

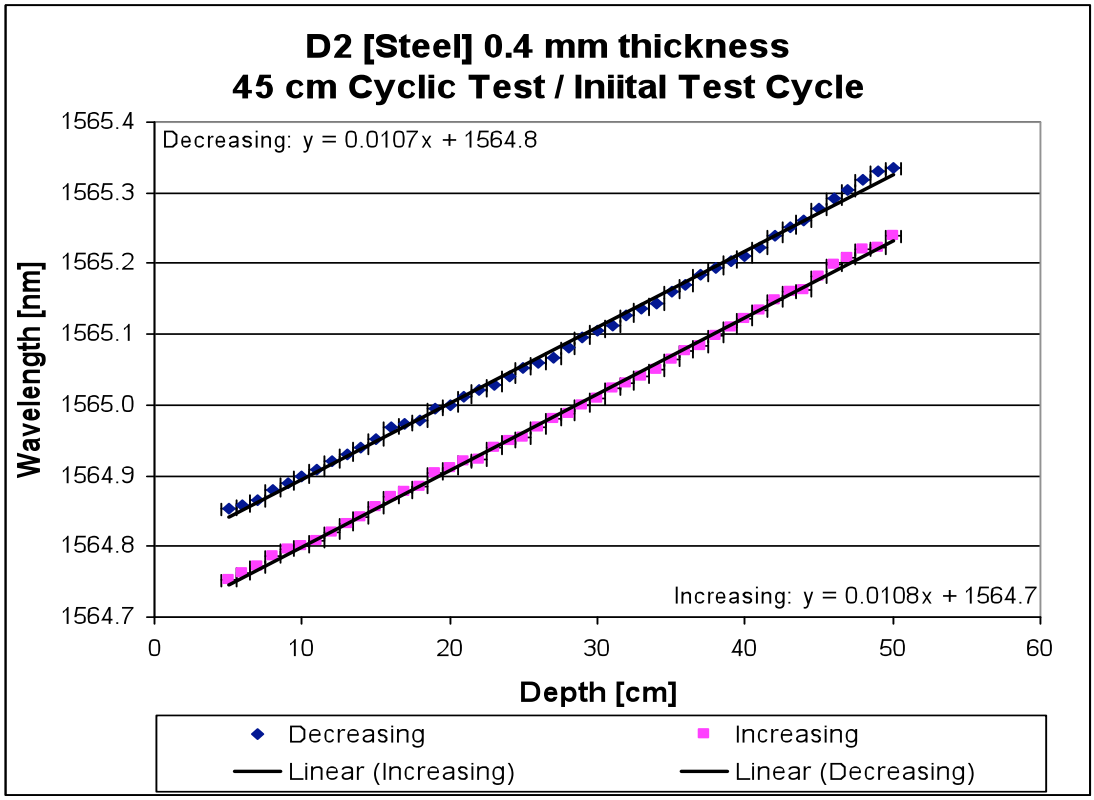

Figure 4.10b Cyclic response from the test cycle with 100 pm subtracted from the increasing result to add graph clarity

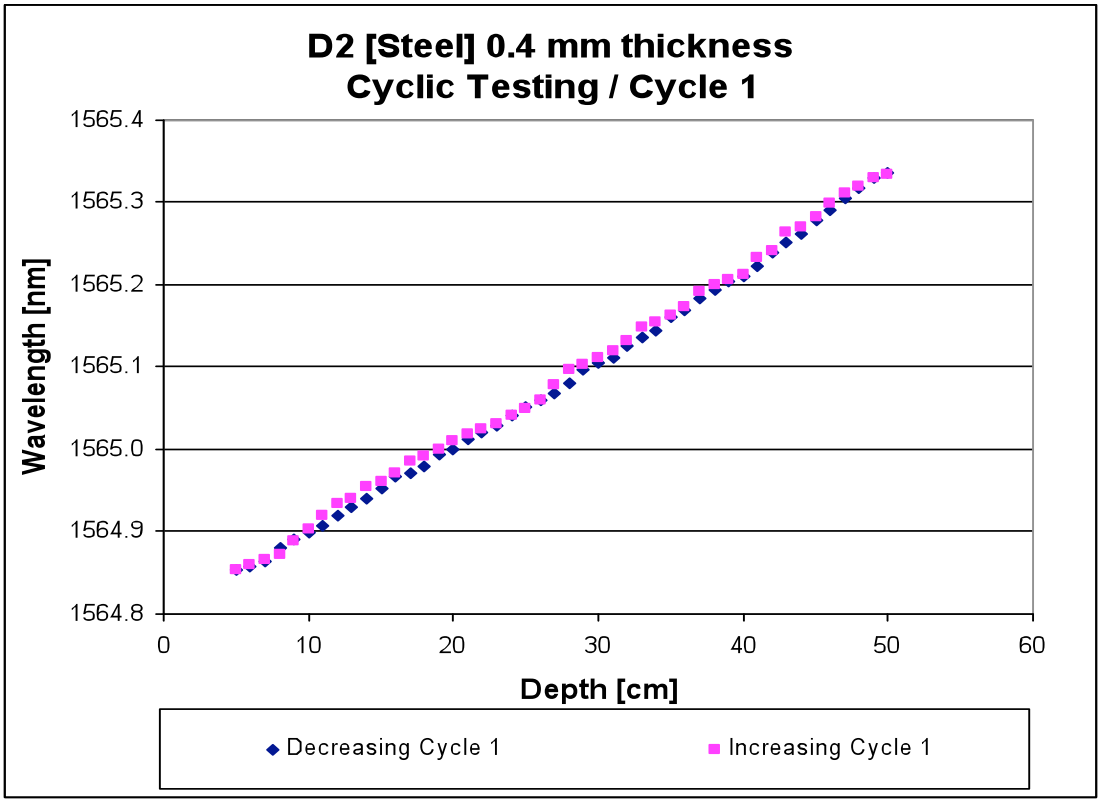

Figure 4.11a Cyclic response from cycle 1

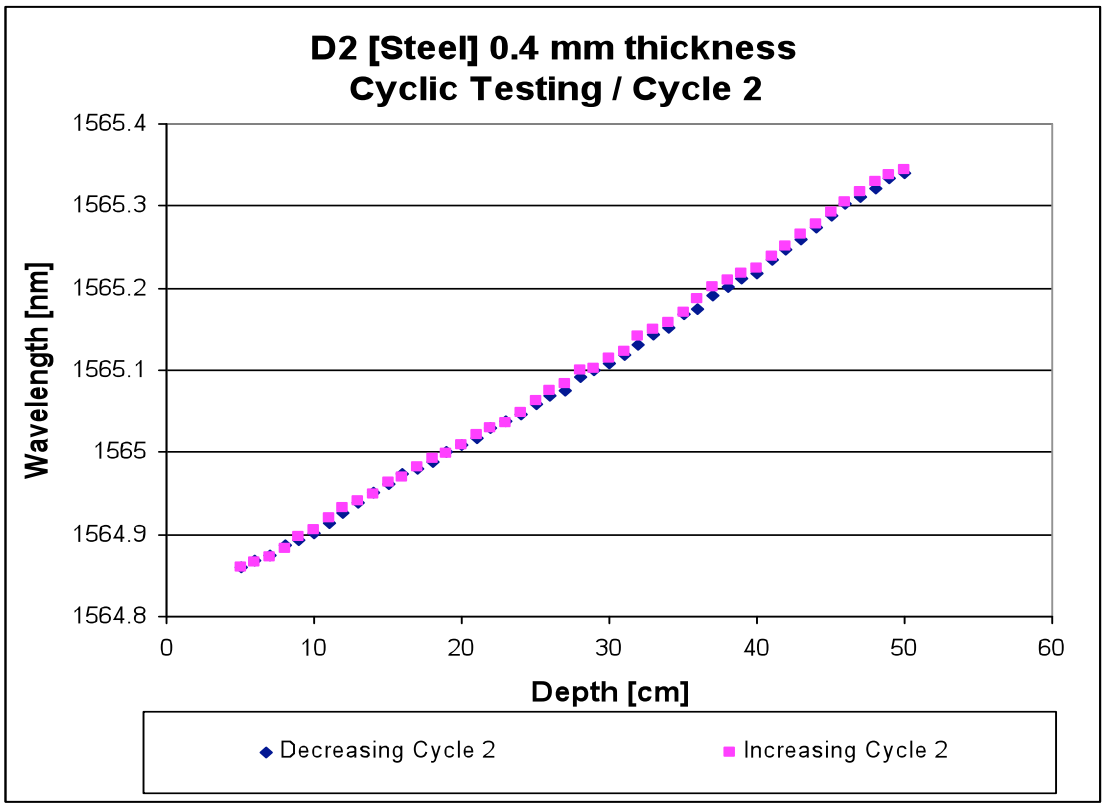

Figure 4.11b Cyclic response from cycle 2

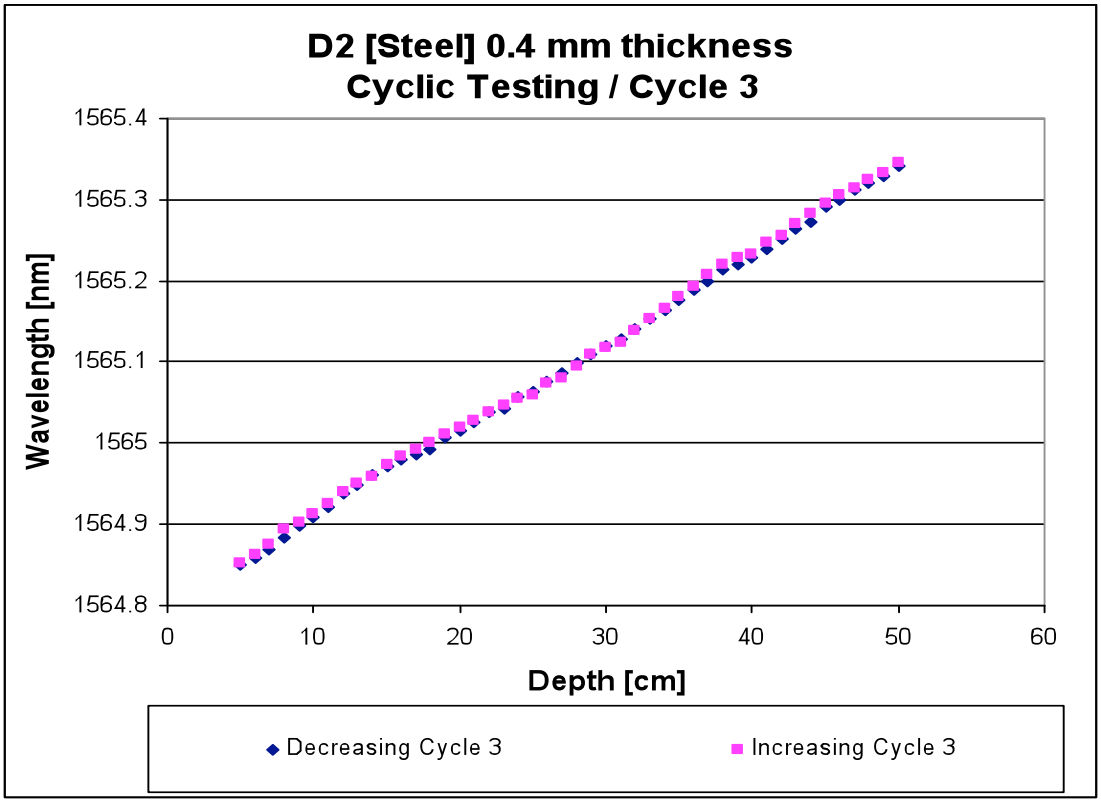

Figure 4.11c Cyclic response from cycle 3

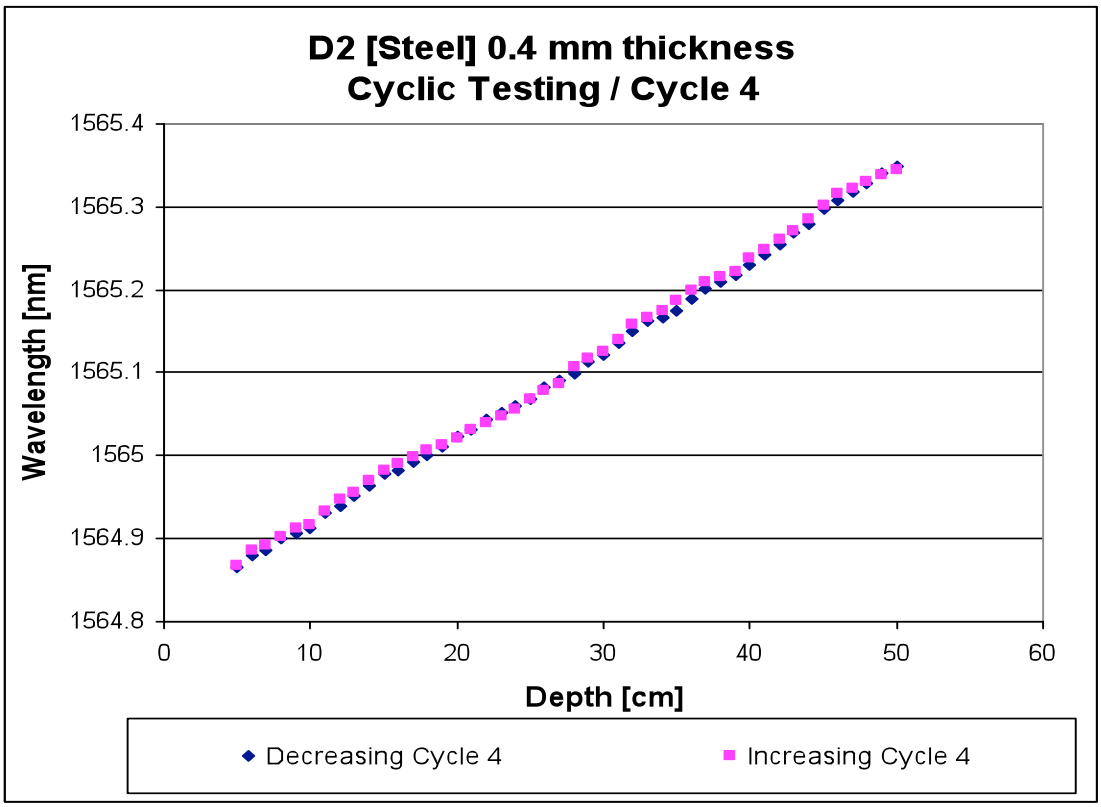

Figure 4.11d Cyclic response from cycle 4

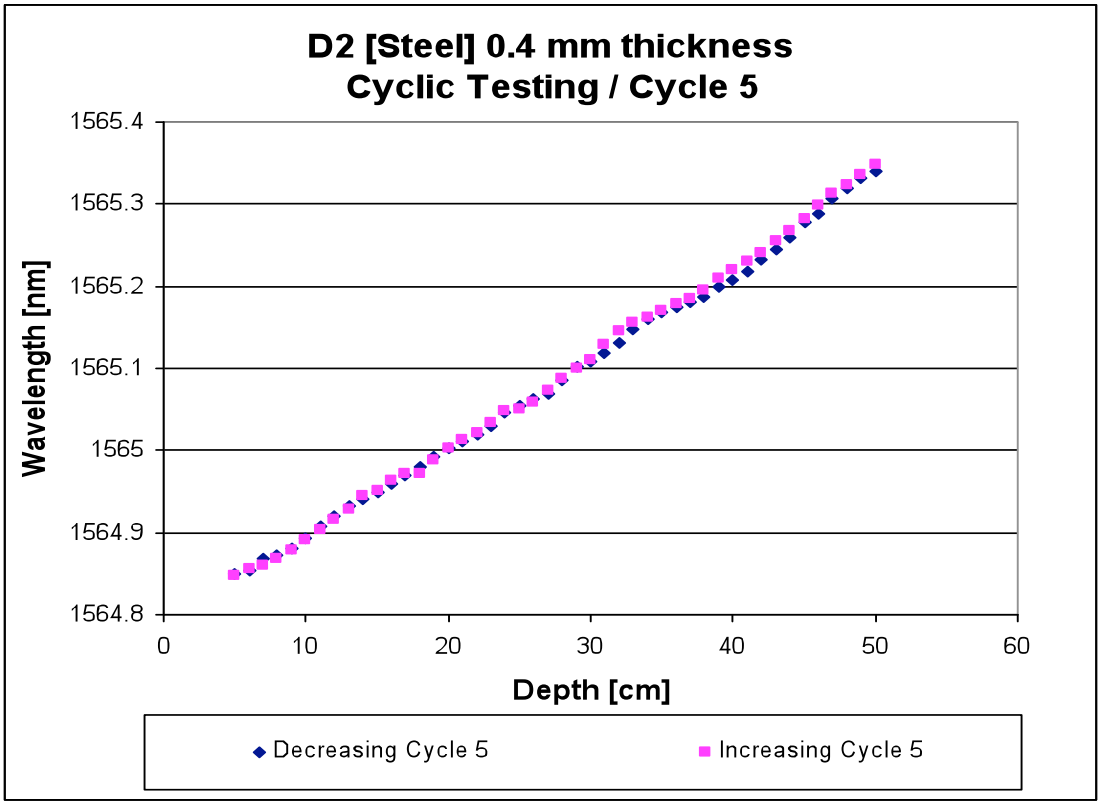

Figure 4.11e Cyclic response from cycle 5

After performing the initial test cycle, cyclic testing was then performed to investigate the repeatability of the system. Figures 4.11a-e depicts five test cycles over the 45 cm measurement range. Like the initial cycle test depicted in Figure 4.10a, the magenta trace indicates increasing depth whilst the blue represents decreasing depth. Whilst an analysis of the wavelength response, sensitivity and linearity can be found in Tables 4.2 and 4.3, Figures 4.11a-e clearly show the system is repeatable over the complete cycle. It is hypothesized that the two main causes for the difference in wavelength between increasing and decreasing depths are temperature (this system was not temperature compensated) and reading error.

Figures 4.12a and 4.12b show the five decreasing and increasing depth responses taken from the five cycles depicted in Figures 4.11a-e combined, whilst 4.13a and 4.13b show the same results with 100 pm deducted from each subsequent result respectively.

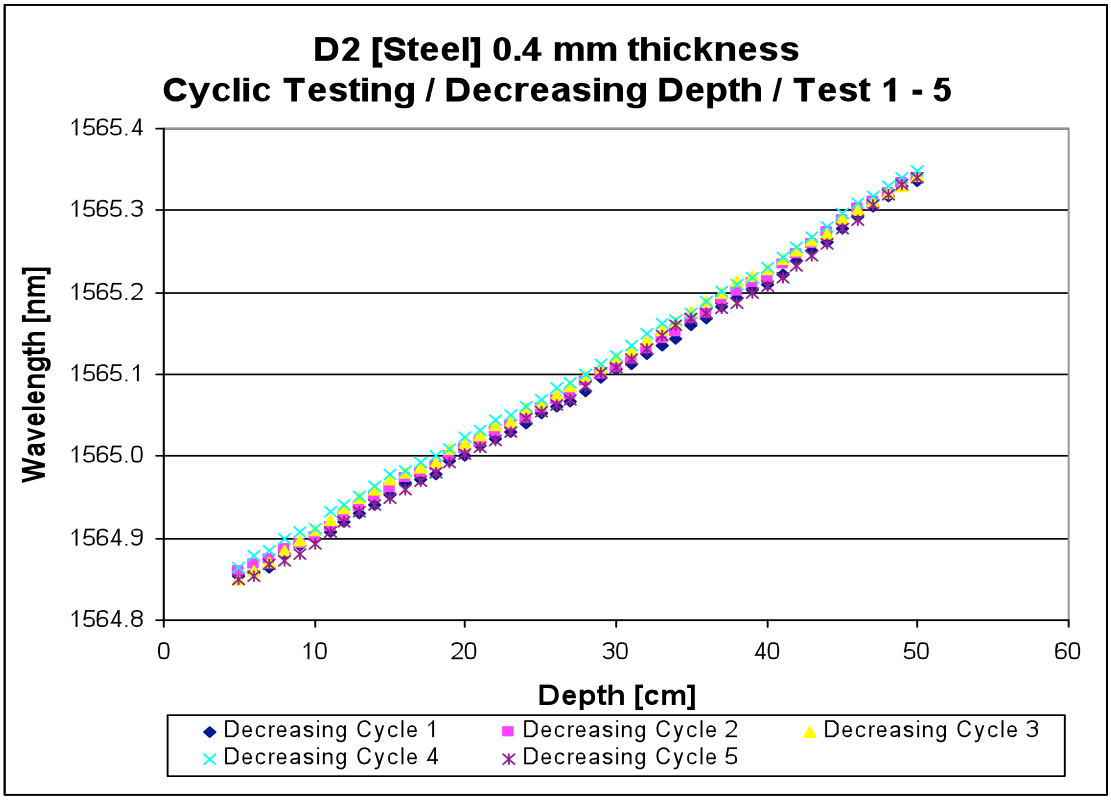

Figure 4.12a Cycles 1-5 combined (decreasing depth)

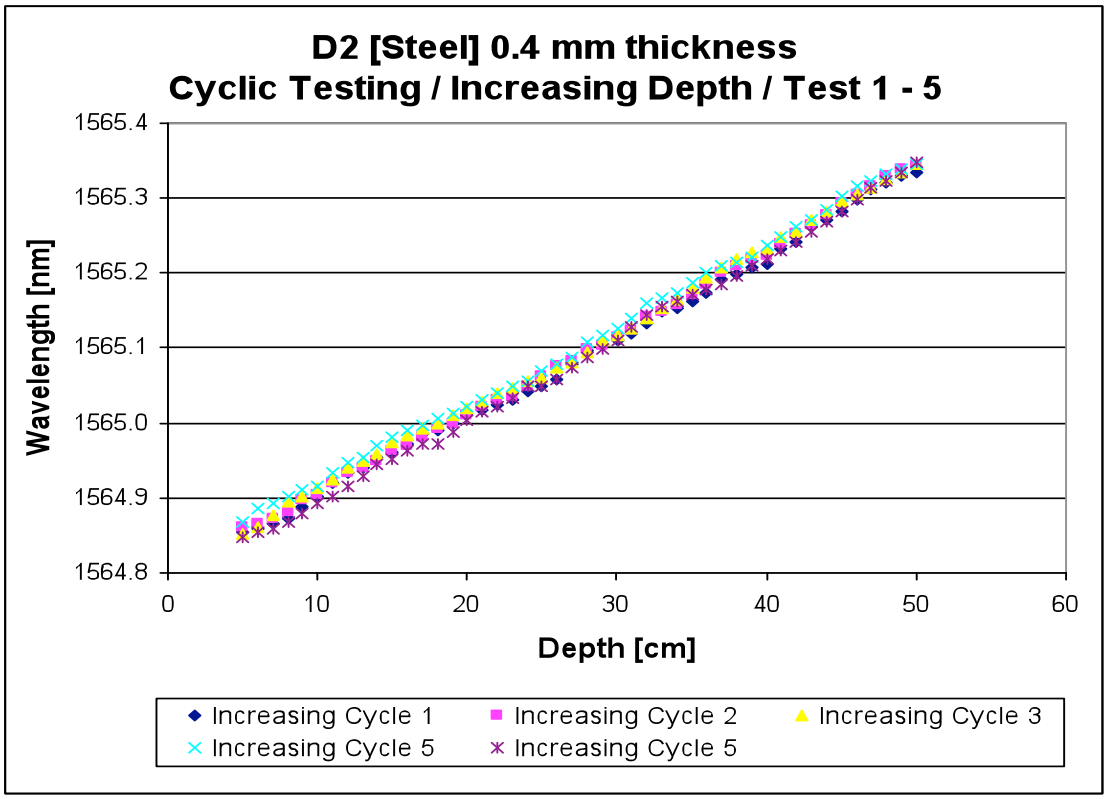

Figure 4.12b Cycles 1-5 combined (increasing depth)

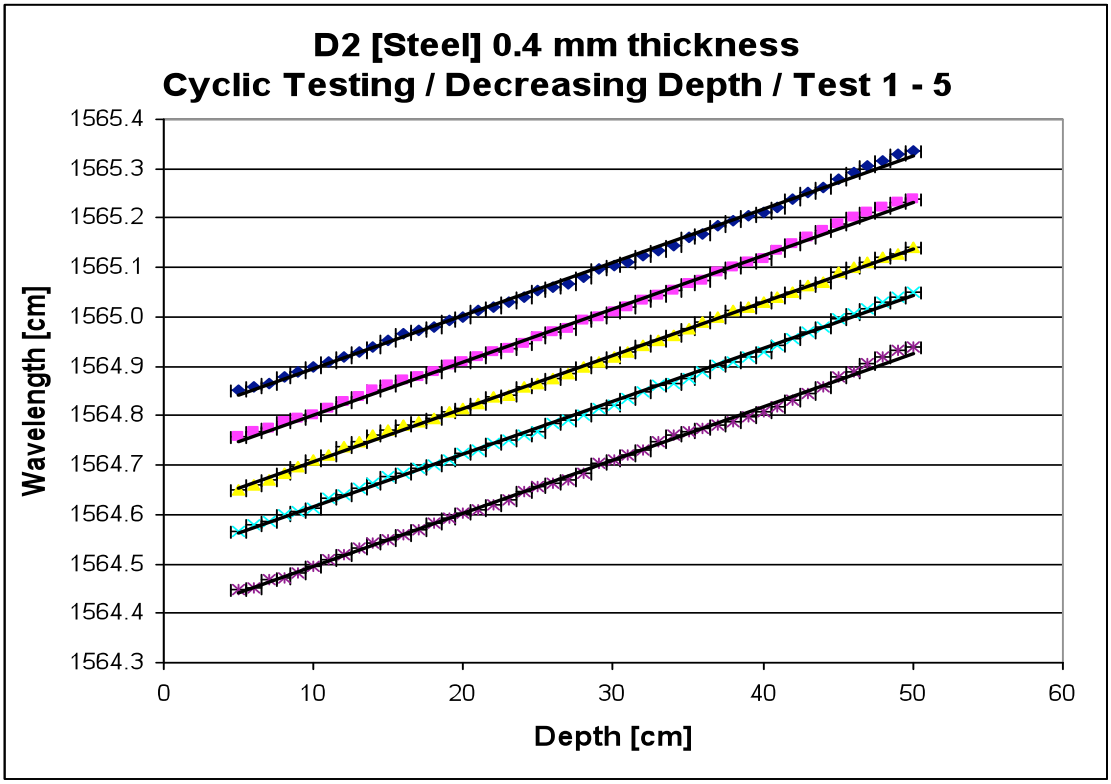

Figure 4.13a Cycles 1-5 combined (decreasing depth), 100 pm subtracted from each subsequent result to add graph clarity

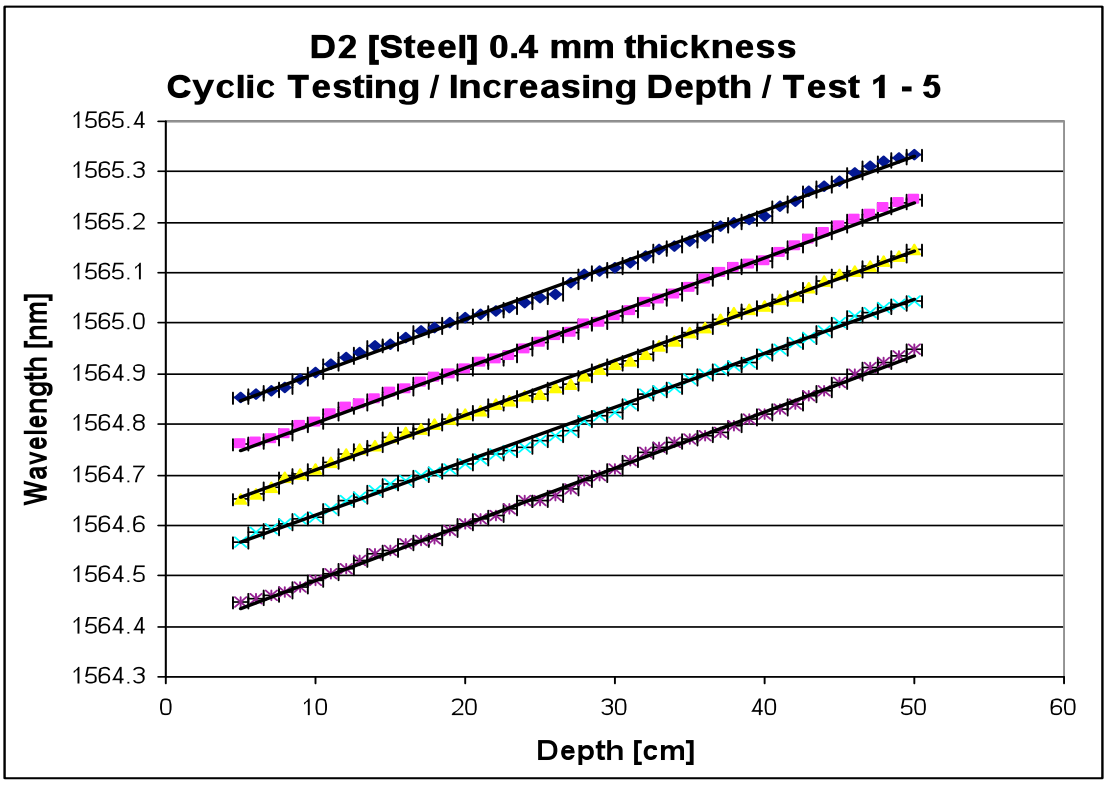

Figure 4.13b Cycles 1-5 combined (increasing depth), 100 pm subtracted from each subsequent result to add graph clarity

Cycle N°	Decreasing Δλ (pm)	Increasing Δλ (pm)	Decreasing sensitivity (pm/cm)	Increasing sensitivity (pm/cm)
1	482.5	481	10.722	10.689
2	481	483	10.689	10.733
3	492	494	10.933	10.978
4	484	478	10.756	10.622
5	490	501	10.889	11.133

Table 4.2 Steel diaphragm cyclic results – wavelength / sensitivity analysis

Cycle N°	Decreasing linear equation	Increasing linear equation
1	y = 0.0107x + 1564.8	y = 0.0107x + 1564.8
2	y = 0.0108x + 1564.8	y = 0.0109x + 1564.8
3	y = 0.0108x + 1564.8	y = 0.0108x + 1564.8
4	y = 0.0106x + 1565.8	y = 0.0107x + 1565.8
5	y = 0.0108x + 1565.8	y = 0.0111x + 1565.8

Table 4.3 Steel diaphragm cyclic results – linearity analysis

Tables 4.2 and 4.3 summarise the results obtained from testing the 0.4 mm-thick steel diaphragm, D2.

Table 4.2 represents the wavelength data and resulting sensitivity of each cycle. What is evident from these results is that the wavelength shifts for increasing and decreasing depth, though similar in terms of order of magnitude, do vary slightly. For increasing depth, max Δλ is 23 pm, and for decreasing depth Δλ is considerably less at 9 pm. As stated earlier, this could be due to temperature or reading error. The former is not a trivial matter. Many factors are involved in the system when the sensor is not temperature compensated. Firstly, as the experiment was not conducted in a temperature-controlled environment, the water temperature would quite clearly vary with time. These temperature changes would also have an affect not only on the sensor, but also on the sensor housing. Whilst aluminium exhibits clear advantages which lend themselves well to the aerospace industry, such as lightweight and resistance to corrosion, it also has a relatively high coefficient of thermal

expansion (23) when compared to other materials such as metal (11). This means that as the temperature varies, the physical dimensions of the sensor housing are also likely to vary. It is hypothesised that with appropriate temperature compensation, the wavelength shifts for increasing and decreasing depth points would marry far better.

Table 4.3 presents the equations of linearity for the results depicted in Table 4.2. Again, with appropriate temperature compensation, and the derivation of a more accurate reading technique, is hypothesised the repeatability would be further improved. One such technique for improving the accuracy of reading the liquid level would be to use a laser range finder. Positioned about the storage tank and pointing towards to the liquid surface, as the liquid level varied, so would the distance between the laser range finder and liquid surface. Digital laser range finders now can be purchased with sub-mm accuracy. The author suggests that whilst this should be the next course of action, it is beyond the scope of this thesis.

The results from this series of experiments proved to be very encouraging, and after discussions with Dr P.D. Foote of BAE SYSTEMS, it was decided that this approach should be further investigated. The obvious next stage was to construct a new sensor from aerospace compliant materials so that it could be tested at the fuel testing facility based at Airbus UK in Filton, Bristol.

4.7 Sensor fabricated from aerospace compliant materials

After evaluating a number of materials for both the sensor housing and diaphragm, PPS and Kapton polyimide film were chosen respectively. This sensor was designed and fabricated in-house using the Photonics Research Group workshop facilities. The work in this section was partly carried out in collaboration with Executive Scientist Dr P.D. Foote. Both the design and fabrication of the sensing system was carried out collaboratively, whilst the fabrication of the FBGs and practical experiments were carried out solely by the author of this thesis.

4.7.1 Polyphenylene sulphide (PPS)

PPS is a semi-crystalline high performance thermoplastic used in a number of industries. Its key features of heat, chemical and flame resistance have seen PPS components used in products ranging from automobiles to kitchen appliances. PPS is easily machinable which was a vital attribute for the work presented in this chapter as the sensor housing had to be

fabricated from a solid PPS rod of 40 mm in diameter. Also its resistance to kerosene and low thermal expansion coefficient make it a highly suitable material, given it will be exposed to aviation fuel and experience large temperature variations throughout the flight profile.

4.7.2 Kapton polyimide film

Kapton polyimide film was developed by DuPont. Like PPS, Kapton has been used in a number of applications from the coating of optical fibres to the fabrication of flexible electronic circuits. Kapton has also been used as a coating for both military and civil aircraft cabling, and has even been utilised by NASA on both the Space Shuttle and to support solar sails for long-term space vehicles. Critically, it has been previously reported that Kapton is an effective diaphragm material for use in automotive engine sensors and manifolds. Other key attributes of Kapton include its ability to operate in temperatures ranging from -269°C up to 400°C. Kapton is also resistant to a number of corrosive chemicals, including aviation fuel.

4.7.3 Design and fabrication of the PPS sensor housing

As Kapton has a lower Young's modulus (2.5 GPa) than shim-steel, for a diaphragm of fixed diameter and thickness, the Kapton diaphragm induces greater deformation than its shim-steel counterpart for a given hydrostatic pressure. Therefore it was decided to reduce the dimensions of the PPS sensor housing, which has the obvious advantage of taking up less volume in the prime realestate that is the inside if an aircraft fuel tank. The dimensions of PPS rods available for purchase ultimately limited the design, with the largest PPS rod available being 40 mm in diameter.

The PPS sensor housing is identical in principle to the aluminium sensor reported earlier in this chapter. It consisted of a base and retaining ring, which could then be used to secure a diaphragm in position, creating an airtight seal using Instant Gasket. The only addition to the design was a fibre delivery tube protruding from one side of the PPS base, allowing the fibre to be protected as it entered the sensor housing.

The design of the sensor is depicted in Figures 4.14a and 4.14b

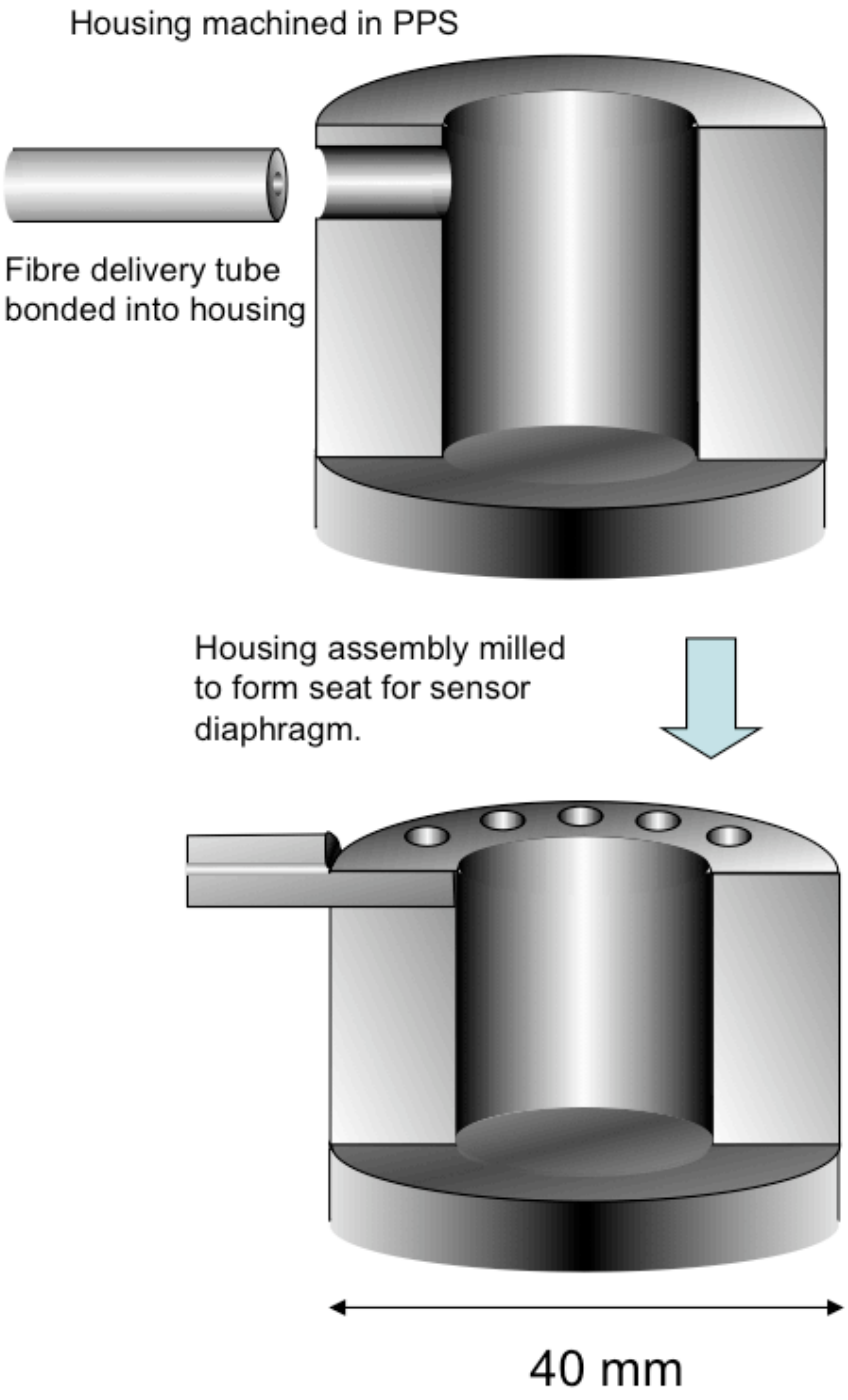

Figure 4.14a PPS sensor base design

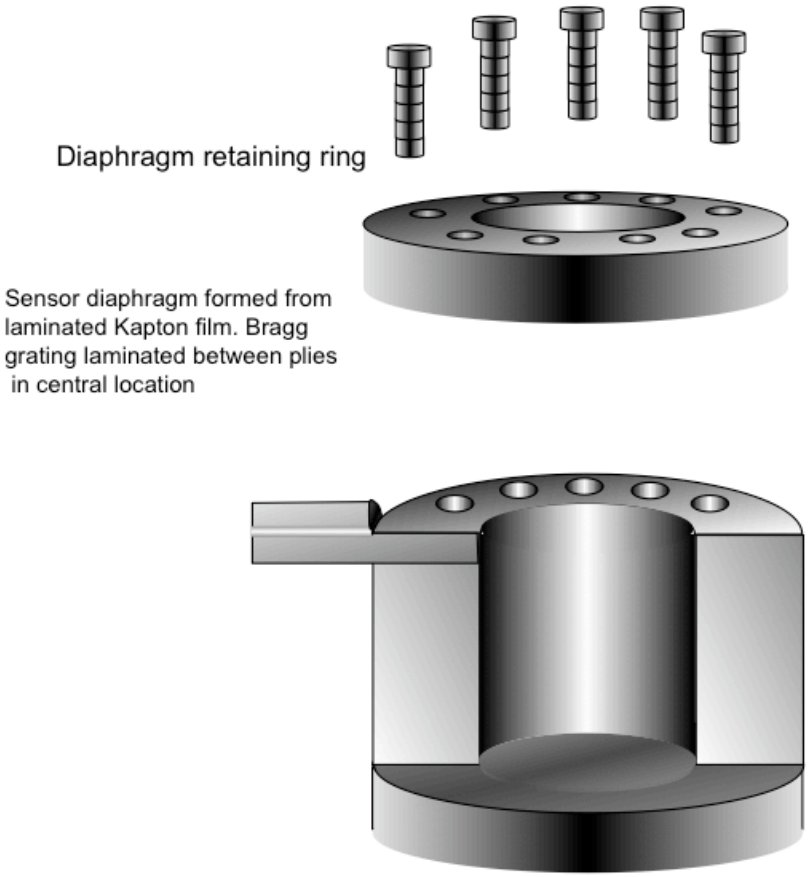

Figure 4.14b PPS sensor system, complete with retaining ring

The fabrication process was as follows:

- PPS rod was cut to the desired length, 50 mm
- The PPS rod was then mounted in the lathe and the cavity was milled out. The cavity was 24 mm in diameter, leaving an 8 mm rim to allow for the addition of screw holes
- The eight screw holes were then marked off and drilled, each hole was separated by 45°
- The top 5 mm of the rod was then cut off using the band saw, creating the retaining ring
- A smaller PPS section of length 30 mm and a 10 mm diameter, was then centrally drilled creating the fibre delivery tube

- A hole for the fibre delivery tube was drilled into the sensor base. The fibre delivery tube was then bonded to the sensor base using 2-part epoxy and left to cure for 24 hours
- All surfaces were then milled to create smooth level surfaces to allow good contact between the base and retaining ring
- Finally, the screw holes were then tapped to suit M3 screws

4.7.4 Design and fabrication of the Kapton diaphragm

The Kapton was to act as the diaphragm. Two sheets of Kapton film were used, with a single FBG fabricated in SMF-28 fibre effectively sandwiched between the two sheets. Figure 4.15 illustrates the construction process of the Kapton diaphragm.

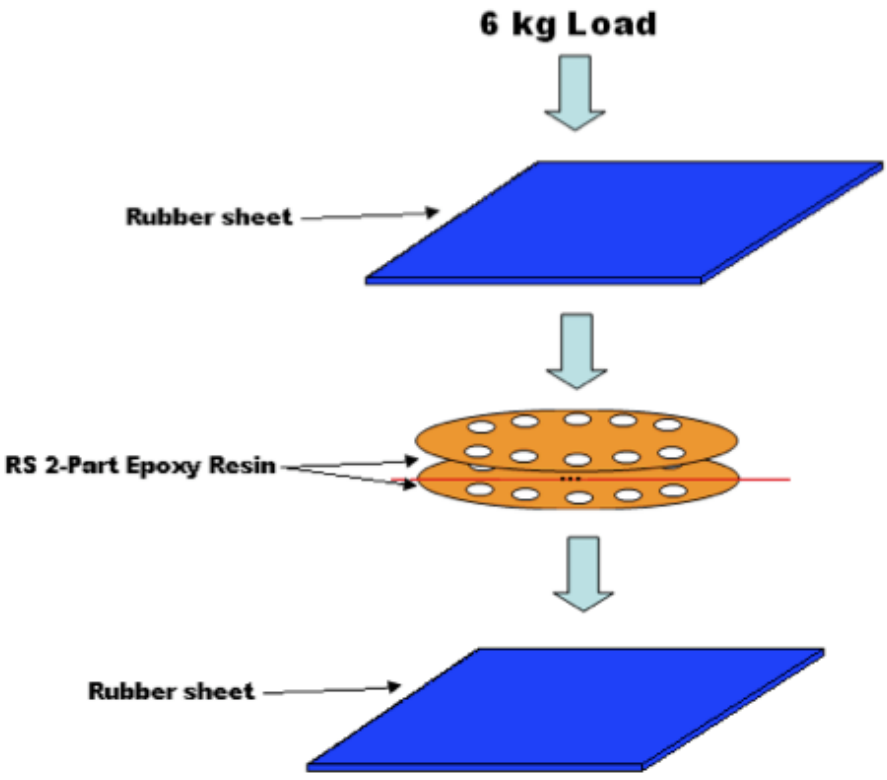

Figure 4.15 Kapton diaphragm construction

The fabrication process was as follows:

- Two Kapton sheets were cut to 40 mm in diameter
- The centre line of the sheets were marked to aid fibre positioning

- Both bonding sides of the Kapton sheets were generously coated with 2-part epoxy, and the fibre was positioned along centre line, aligning the FBG centre with the diaphragm centre
- The top layer of Kapton was then placed in position, sandwiching the fibre between the two Kapton sheets, forming the diaphragm
- Finger pressure was then used to edge out any visible air bubbles in the epoxy
- The diaphragm was itself temporarily sandwiched between two sheets of conforming rubber, and 6 kg of load was applied to help create the bond
- This was left to cure for 24 hours
- Finally, the eight holes were punched out to align with the holes in the PPS base and retaining ring

Each Kapton film was 0.05 mm thick, however as it was difficult to control the epoxy thickness, it was difficult to predict the diaphragm thickness. The diaphragm thickness was measured using a micrometer after the epoxy had cured; it measured 0.42 mm thick.

4.7.5 Final assembly of the sensor

The final stage of sensor assembly was simply to mount the diaphragm between the base and retaining ring. This was done using the eight screws, and Instant Gasket to create the seal. The final assembly is diagrammatically shown in Figure 4.16a and pictured in Figure 4.16b.

The fabrication process was as follows:

- A small rim of Instant Gasket was placed around the 8 mm rim of the sensor base
- The Kapton diaphragm was then placed in position, and the retaining ring placed on top
- The eight screws were then screwed in, creating a tight seal between base, diaphragm and retaining ring
- Finally, a small amount of Instant Gasket was smeared around the seal to further prevent any leakage

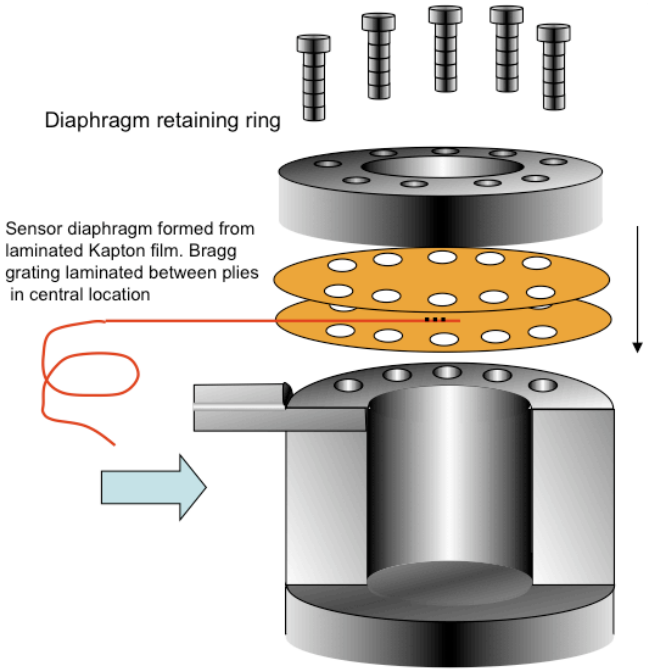

Figure 4.16a Diagram of the final assembly

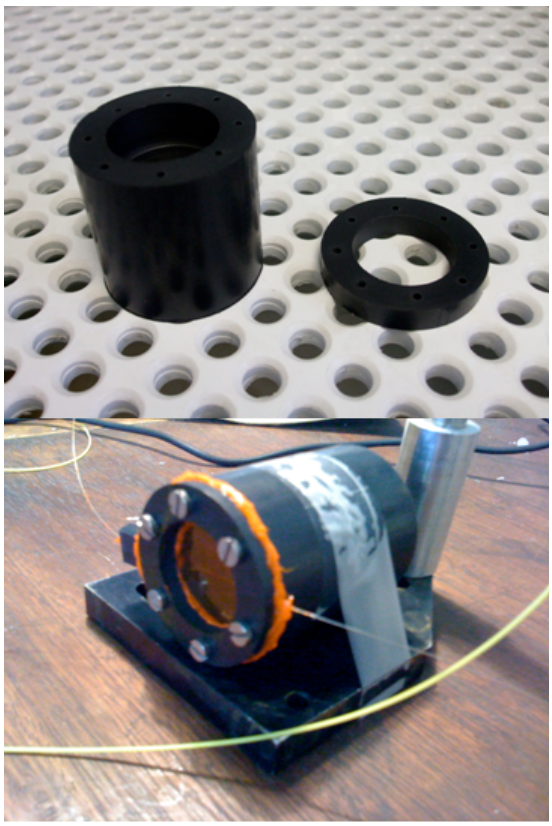

Figure 4.16b Picture of pre and post final assembly

4.8 Experimental arrangement and procedure

The experimental procedure for these experiments was, in principle, the same as that of the aluminium/shim-steel sensor experiments. The only difference here being that because the FBG used was a 4% reflectivity FBG centred at 1550 nm, the senor was interrogated using the TDM-based Insensys FSI. The system schematic is depicted in Figure 4.17.

Figure 4.17 System schematic

The experimental procedure was identical to that of the aluminium/shim-steel sensor system experiments, for a detailed experimental procedure description, refer to section 4.6.1. However to briefly reiterate the most important aspects, the water was allowed to reach equilibrium in the storage tank for no less than three hours before conducting any testing. The sensor depth was then manually controlled, taking readings at 1 cm intervals. Like the Ibsen I-MON 400e, the Insensys FSI logs wavelength as a function of time, therefore the time was logged against each discrete sensor depth. The wavelength for a given depth could therefore be determined by looking up the wavelength for a given time log. Wavelength could then be plotted as a function of depth.

4.8.1 Calculation of estimated central deflection

The accurate calculation of the central diaphragm deflection is quite complicated due to the fact that the RS 2-part epoxy used to bond the 2 sheets of Kapton together will greatly affect the diaphragms' response to pressure. Therefore the figure obtained from this calculation should be considered as a rough estimate. From the DuPont Kapton Polyimide film general specification datasheet, the values for Young's modulus and Poisson's ratio are 2.5 GPa and 0.34 respectively. The Kapton diaphragm radius was 20 mm, and using a digital micrometer measured 0.42 mm in thickness. The same pressure used to calculate the shim-steel diaphragm deflection, 4565 Pa, was used here also.

$$Y_c = \frac{3PR_0^4(1-\upsilon^2)}{16t^3E}$$

$$Y_c = \frac{3\times 4565\times 20^4\times(1-0.34^2)}{16\times 0.42^3\times 2{,}500{,}000{,}000}$$

$$Y_c = \frac{3\times 4565\times 160000\times 0.91}{16\times 0.074\times 2{,}500{,}000{,}000}$$

$$Y_c = \frac{2\times 10^9}{2.96\times 10^9}$$

$$Y_c = 0.676mm$$

4.8.2 Experimental results from Kapton diaphragm D4

The initial test performed was a 45cm depth reduction test to measure the wavelength shift as a function on depth change. The sensor unit was initially at the tank base and subsequently rose in 1 cm intervals. Figure 4.18 shows the result from this test.

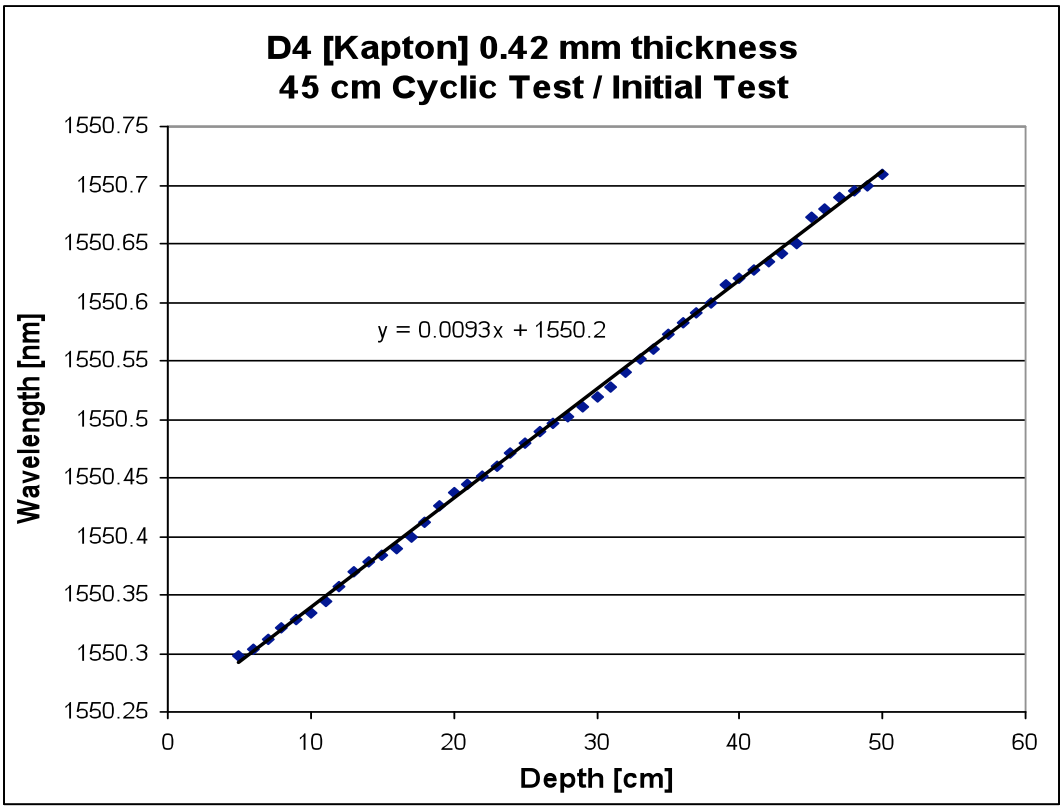

Figure 4.18 The result from the 0.42 mm-thick Kapton diaphragm

The above result demonstrates that the Kapton diaphragm gives good linearity over the entire measurement region. The wavelength shift induced over the 45 cm measurement region was 334 pm, which could provide a sensitivity in the region of 7.422 pm/cm of

level change. This result is encouraging as the sensitivity is comparable to the result obtain from the aluminium diagram D2, however diaphragm D2 had a much greater surface area than the Kapton diaphragm D4.

Cyclic testing was then performed to interrogate the repeatability of the sensor. Again like the aluminium/shim-steel system, five full cycles were performed. Each cycle involved the sensor initially starting at the tank base, being raised in 1 cm intervals until reaching the water surface, then being lowered in 1 cm until finally reaching the tank base. Figure 4.19a is the result taken from the initial test cycle. Figure 4.19b is the same result with 100 pm deducted from the increasing result to add graph clarity.

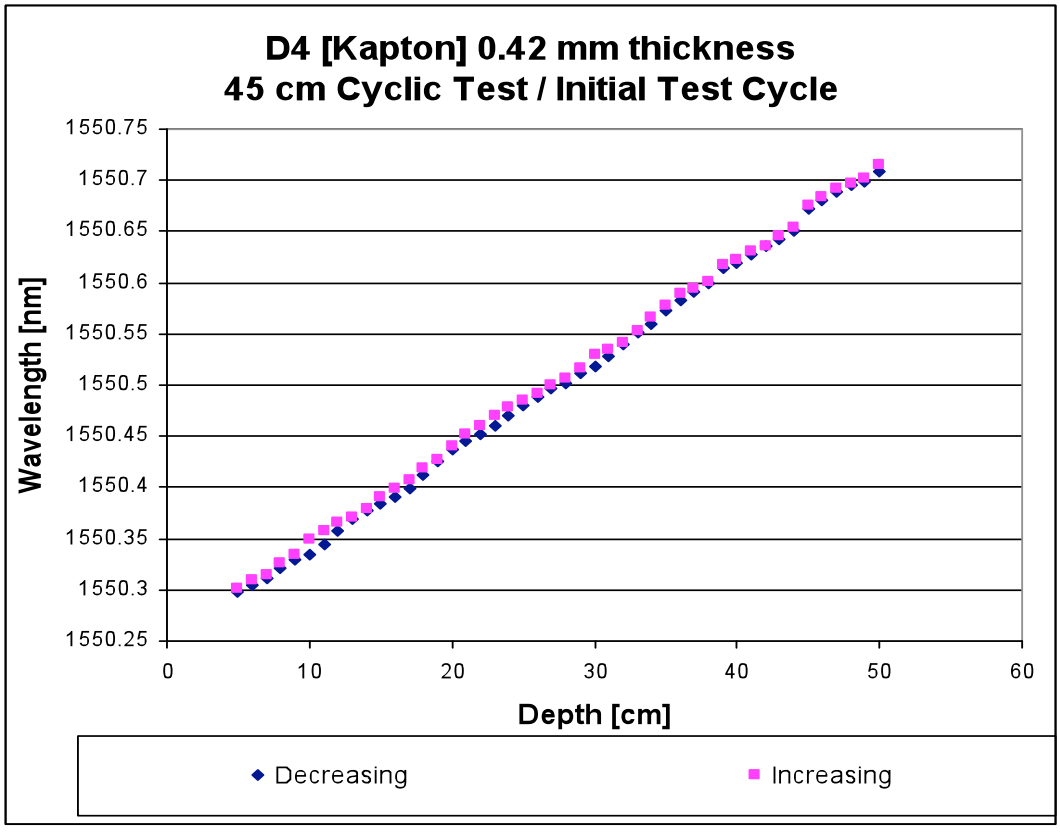

Figure 4.19a Cyclic response from the initial test cycle

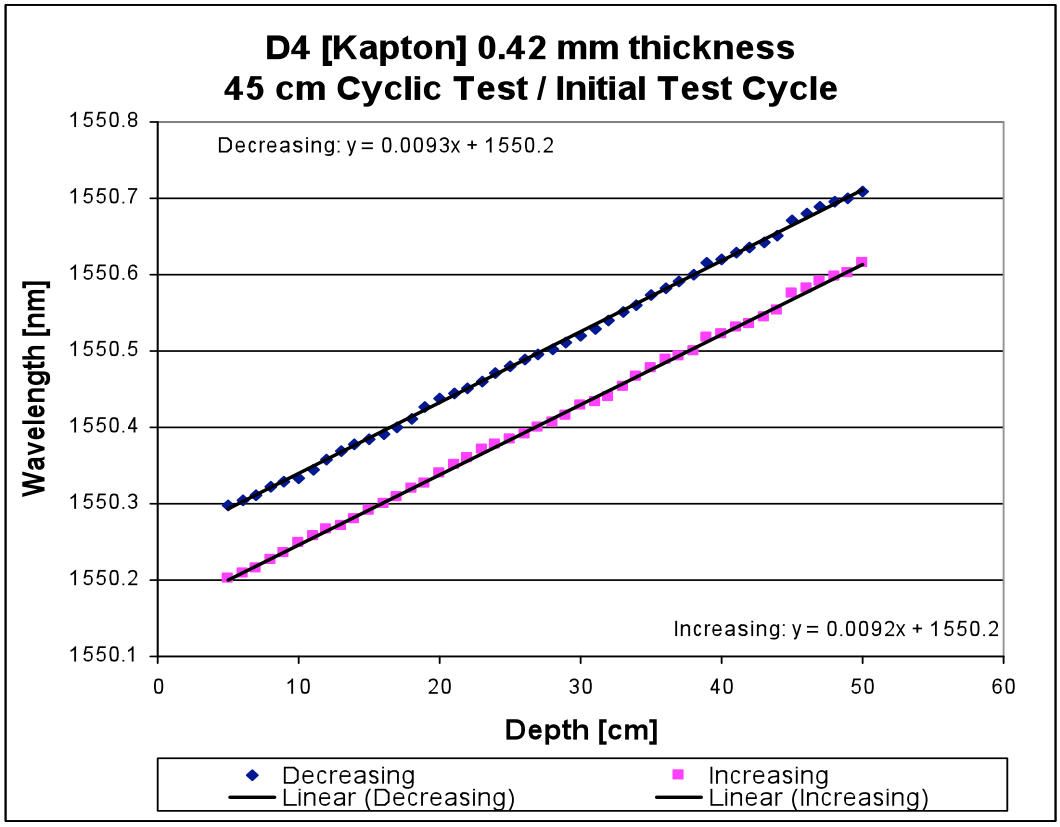

Figure 4.19b Initial test response from Test 1 with 100 pm subtracted from the increasing result to add graph clarity

The previous result demonstrated the Kapton diaphragm gave good linearity over the complete measurement range. It also demonstrated the repeatability over the complete cycle. Five further cycles were then performed to further investigate the behaviour of the system.

Figures 4.20a-e show the five cyclic responses

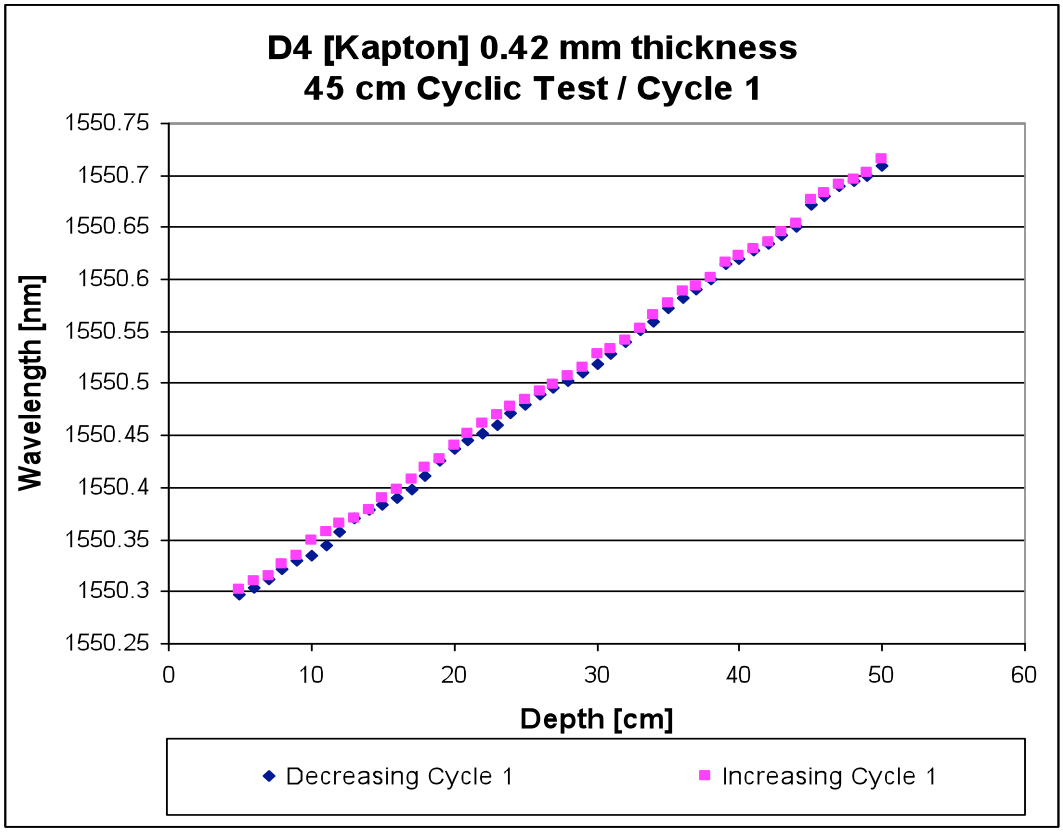

Figure 4.20a Cyclic response from cycle 1

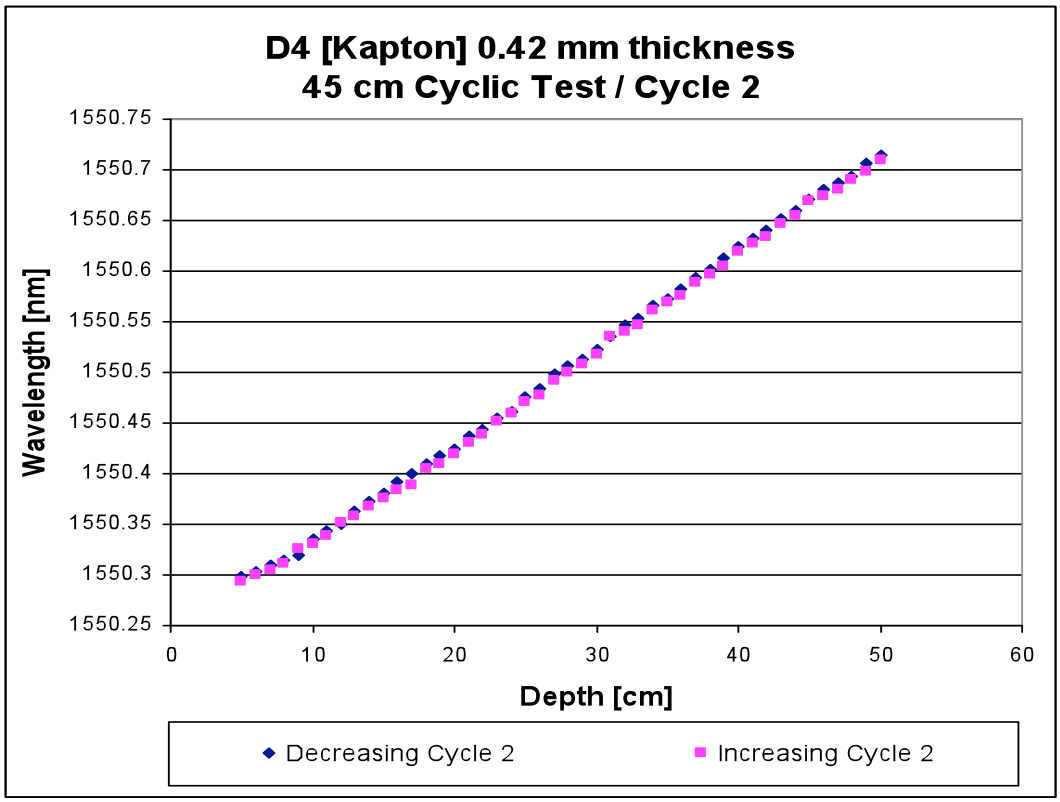

Figure 4.20b Cyclic response from cycle 2

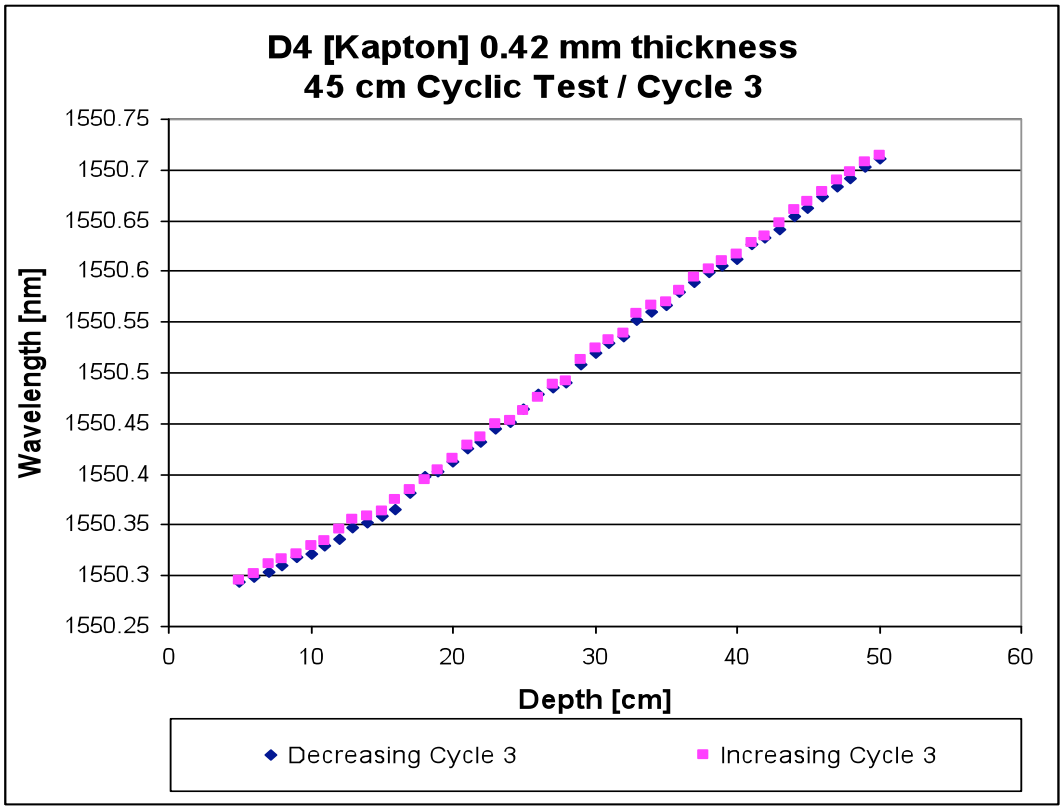

Figure 4.20c Cyclic response from cycle 3

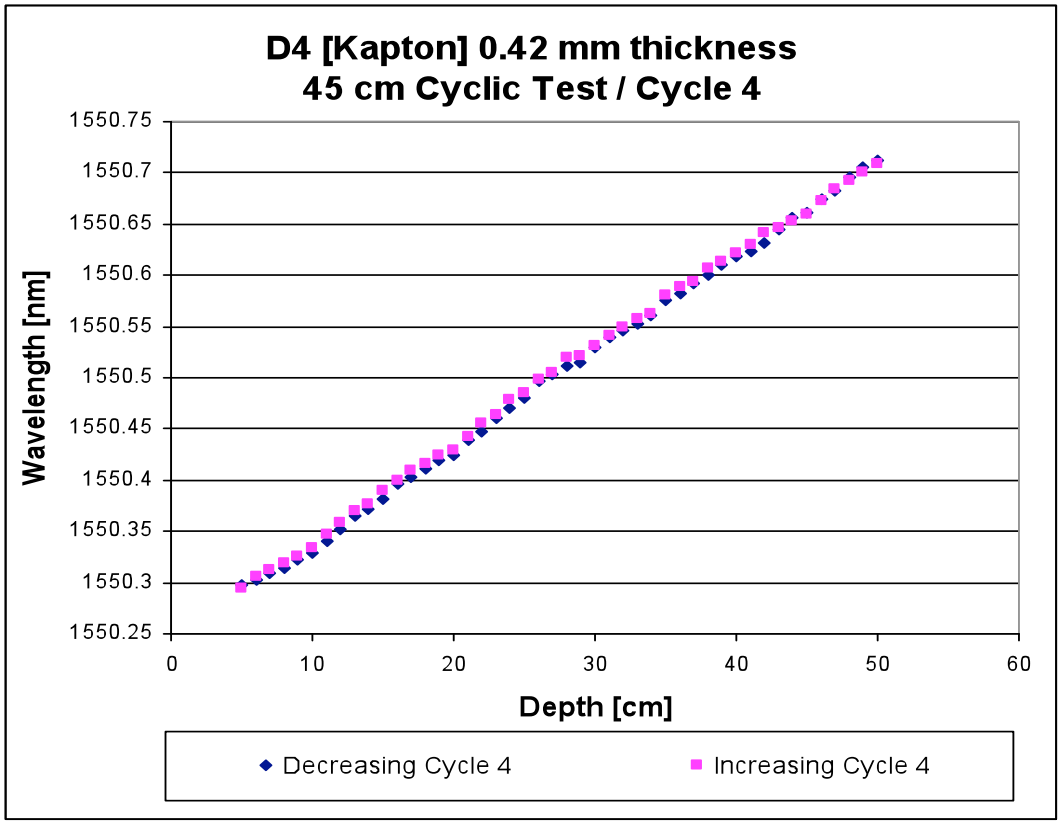

Figure 4.20d Cyclic response from cycle 4

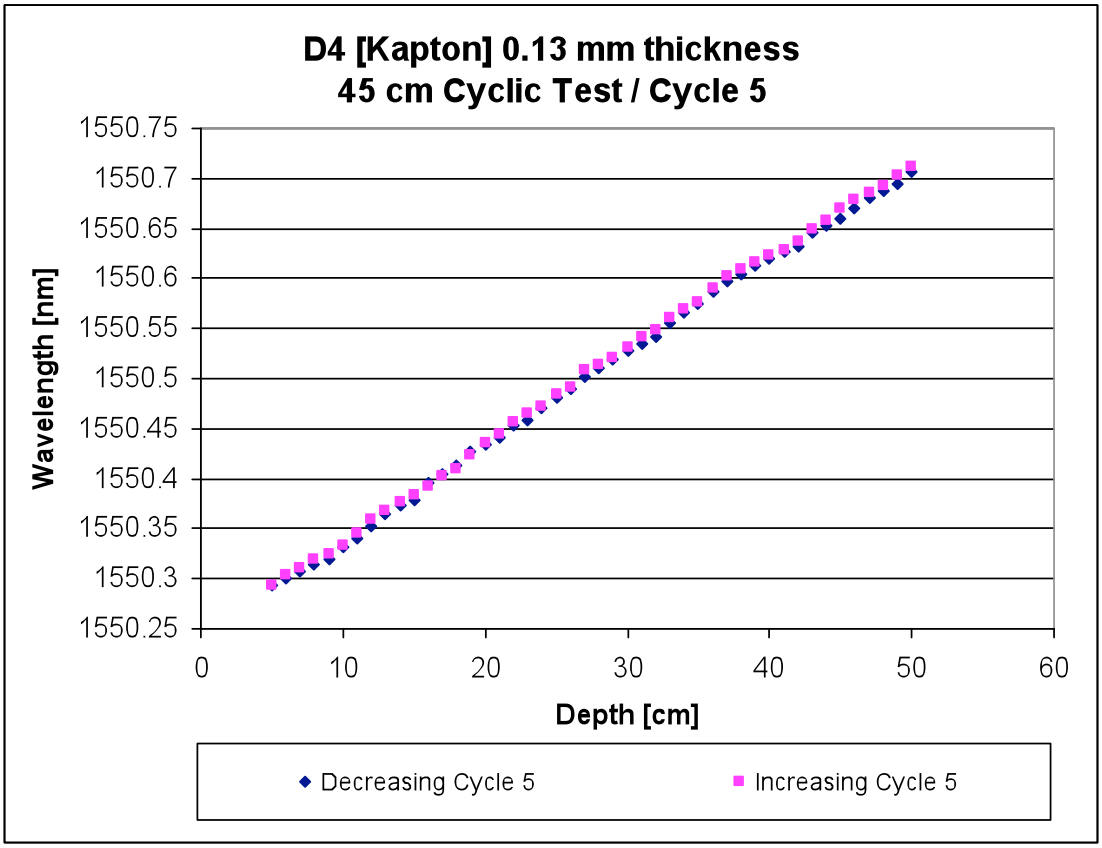

Figure 4.20e Cyclic response from cycle 5

Figures 4.21a and 4.21b show the five decreasing and increasing depth responses combined, whilst 4.22a and 4.22b show the same results with 100 pm deducted from each subsequent result respectively.

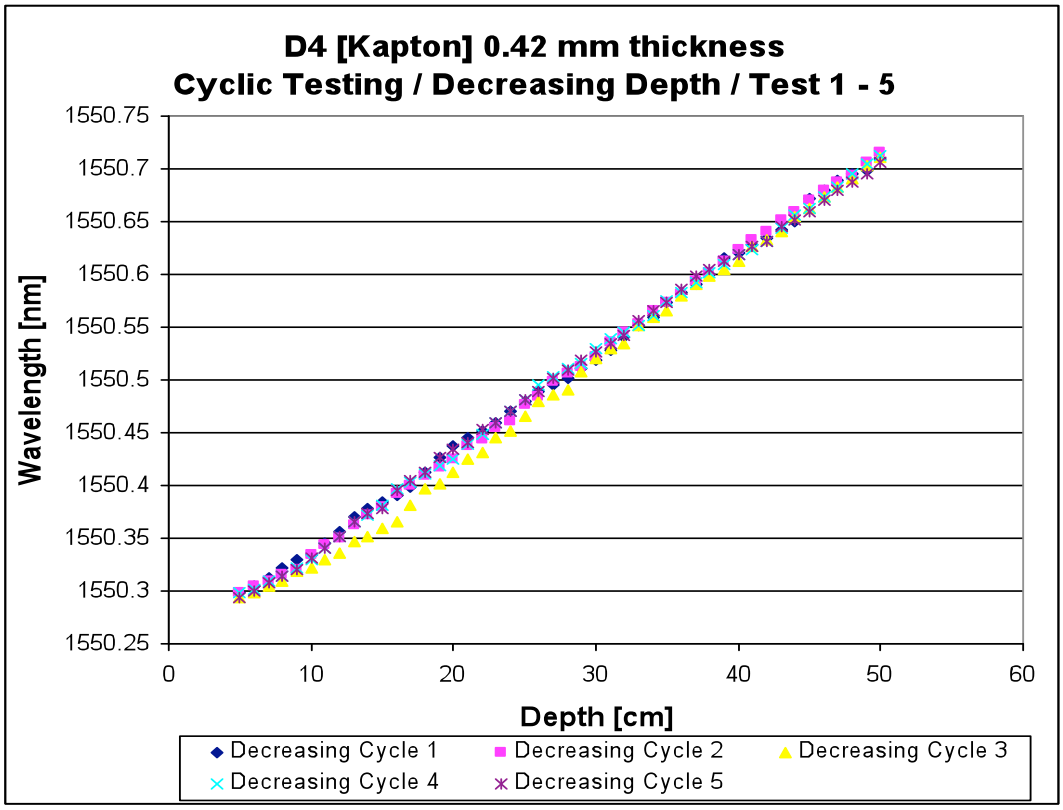

Figure 4.21a Cycles 1-5 combined (decreasing depth)

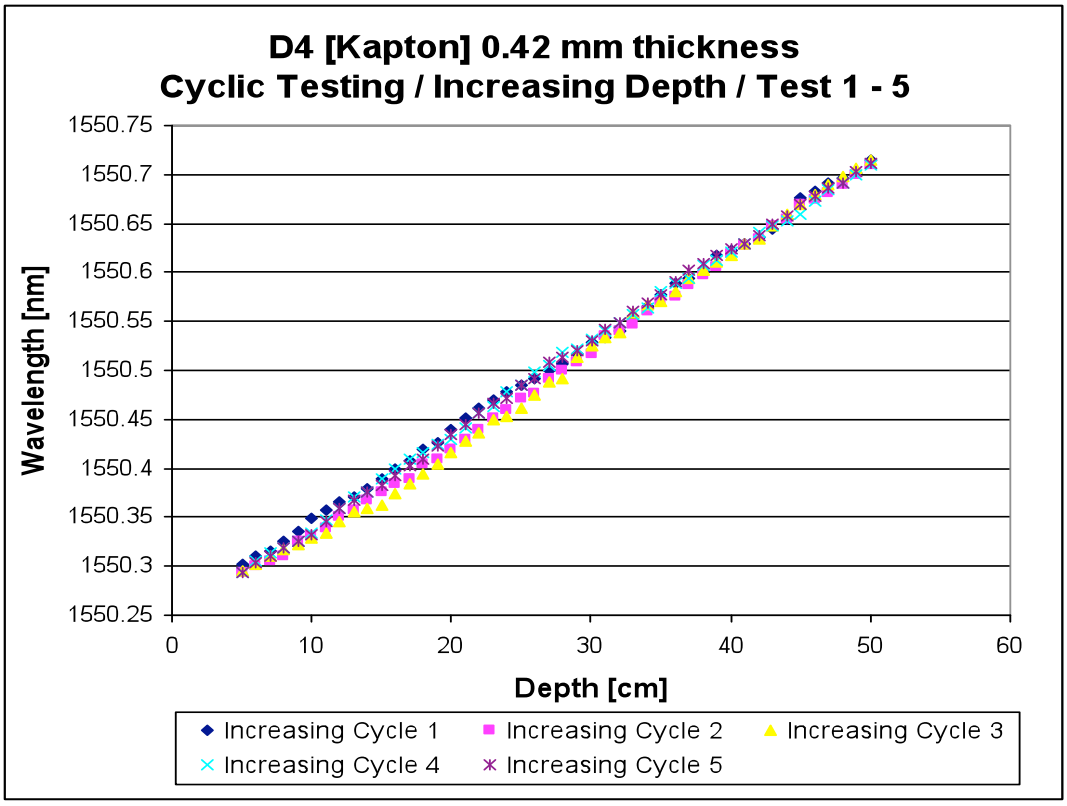

Figure 4.21b Cycles 1-5 combined (increasing depth)

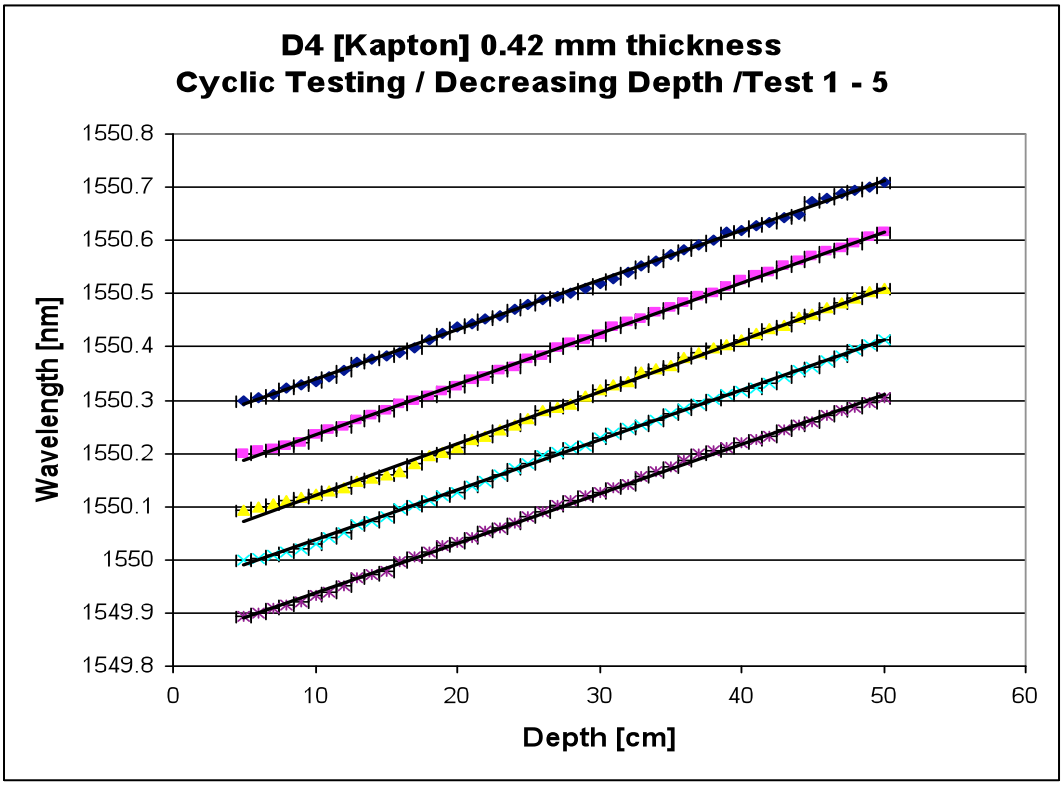

Figure 4.22a Cycles 1-5 combined (decreasing depth), 100 pm subtracted from each subsequent result to add graph clarity

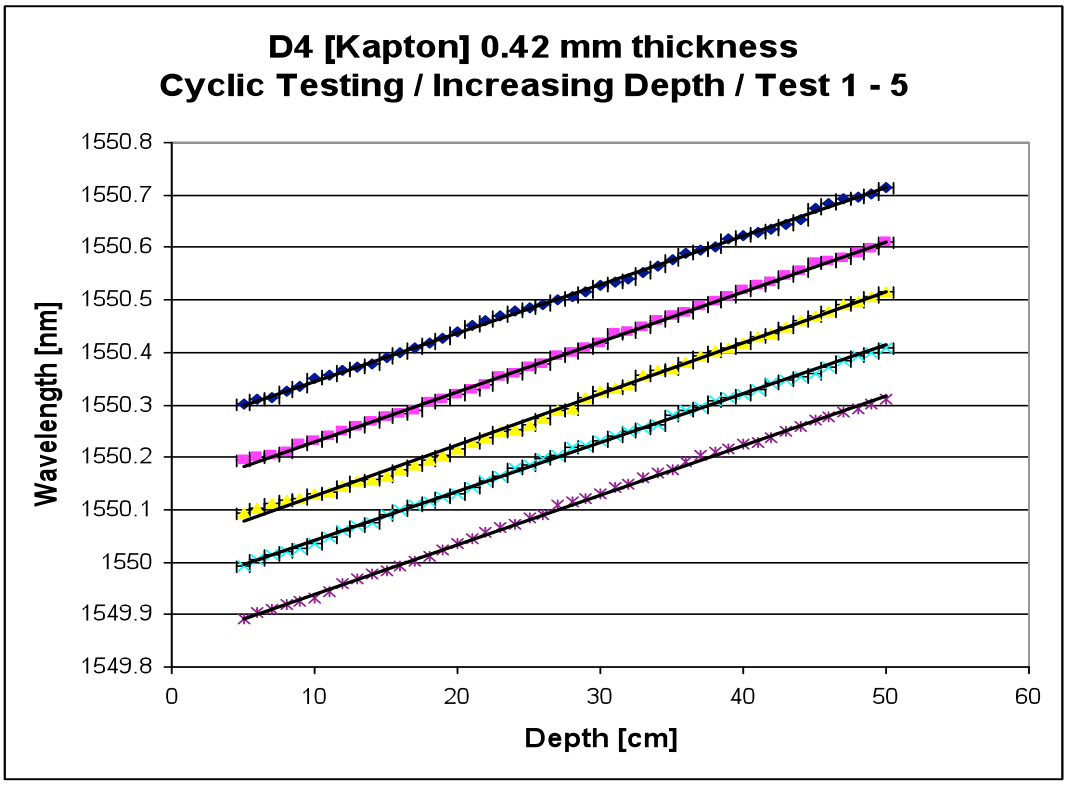

Figure 4.22b Cycles 1-5 combined (increasing depth), 100 pm subtracted from each subsequent result to add graph clarity

Tables 4.4 and 4.5 summarise the results obtained from testing the 0.42 mm-thick Kapton diaphragm.

Cycle N°	Decreasing Δλ (pm)	Increasing Δλ (pm)	Decreasing sensitivity (pm/cm)	Increasing sensitivity (pm/cm)
1	411	413	9.133	9.178
2	417	412	9.267	9.156
3	417	420	9.267	9.333
4	414	412	9.200	9.222
5	412	418	9.156	9.289

Table 4.4 Kapton diaphragm cyclic results – wavelength / sensitivity analysis

Cycle N°	Decreasing linear equation	Increasing linear equation
1	y = 0.0093x + 1550.2	y = 0.0092x + 1550.3
2	y = 0.0095x + 1550.2	y = 0.0095x + 1550.2
3	y = 0.0097x + 1550.2	y = 0.0097x + 1550.2
4	y = 0.0094x + 1550.2	y = 0.0093x + 1550.2
5	y = 0.0093x + 1550.2	y = 0.0095x + 1550.2

Table 4.5 Kapton diaphragm cyclic results – linearity analysis

4.9 Multi-FBG based level sensor

Whilst the vast majority of the work conducted in this chapter is based on single-FBG level sensing, the possibility of using a multi-FBG based sensor was also explored. Although the issue of sensitivity can be overcome to a certain degree with the single-FBG system by varying the physical dimensions of the sensor housing and diaphragm, by virtue of understood diaphragm behaviour, the system is limited to the amount of deflection it can induce before the diaphragm enters the non-linear region. Though in principle, the single-FBG system described in the previous section could be multiplexed together to create a multi-sensor system, the proposition of deploying multiple gratings in a single sensor housing was an attractive one, and so was explored.

There are numerous advantages to housing multiple sensors in a single sensor element, some of these include:

- Increased system redundancy
- Possibility of greater sensitivity, accuracy and resolution
- Can detect fuel adulteration
- As well as continuous sensing, the system could also provide a discrete measurement. The exact measurement would depend of sensor separation.

4.9.1 Multiple sensor continuous and discrete level sensor housing

The design of the multiple sensor system consists of a square aluminium tube, with windows drilled at equidistant positions along it. As the system was to be fabricated in-house, aluminium was chosen as it is a material that is relatively easy to machine. FBGs were then fabricated in hydrogenated SMF-28 fibre at positions aligning with the window positions such that the FBG centre aligns with the window centre. In this case the diaphragm material was heat shrink. Once the sensors were in position, heat shrink was placed and shrunk over the tube forming a diaphragm over the window region. Once the heat shrink was in position, Instant Gasket was used to seal the sensing area. Figures 4.23a and 4.23b is a diagrammatical representation and image of the system respectively.

The system consisted of three FBG sensors positioned over 9 mm diameter holes spatially separated by 150 mm.

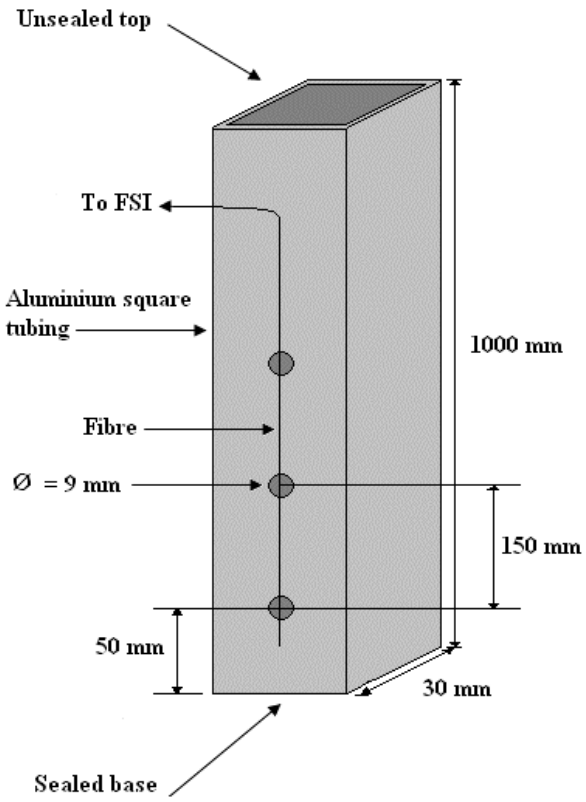

Figure 4.23a Diagram of the aluminium tube sensor arrangement

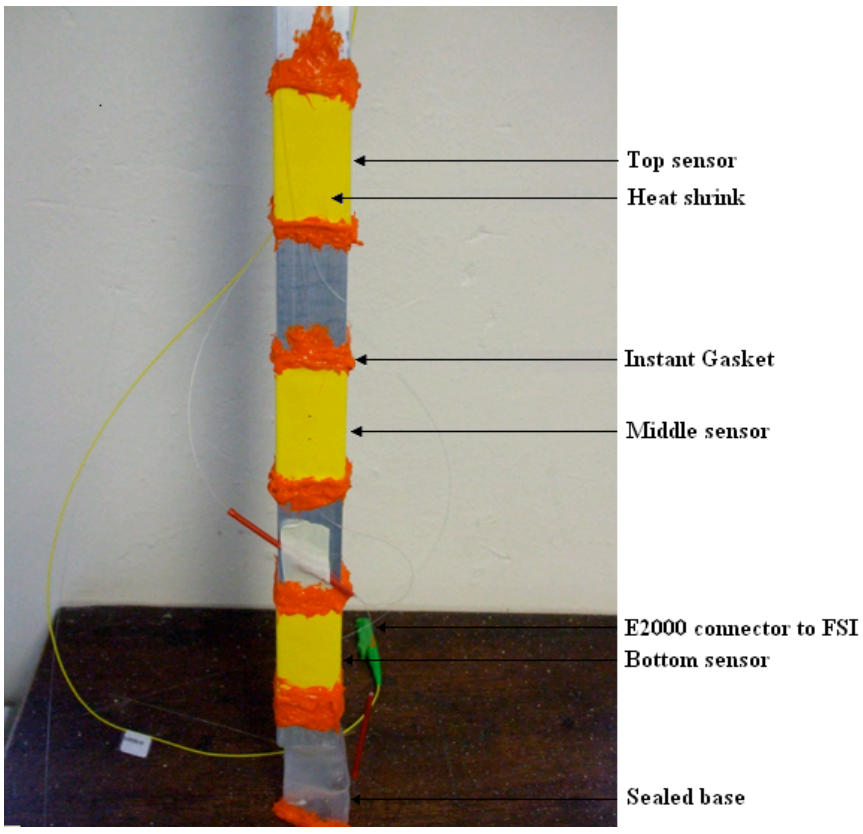

Figure 4.23b Picture of the aluminium tube sensor arrangement

With the tube sealed at the bottom, and open at the top, the atmospheric pressure inside the tube remains relatively constant, and only varies with atmospheric variations. The system relies on increasing hydrostatic pressure deforming the diaphragm causing the fibre to become elongated, which results in a red wavelength shift. When not immersed in any liquid, the internal pressure matches the external pressure; therefore the diaphragm is not deformed. However, as the sensors become immersed in the liquid and the depth increased, the external (hydrostatic) pressure begins to increase. It is this increasing hydrostatic pressure, which caused the diaphragm to deform.

4.9.2 Experimental arrangement and procedure

The FBG sensors used in these experiments were ~ 1550 nm 4% reflectivity FBGs specifically designed to be used with the Insensys FSI. The system is depicted in Figure 4.24. Note that operating limitations of the FSI require 2.5 m spacing between each sensor, which is not depicted in the diagram.

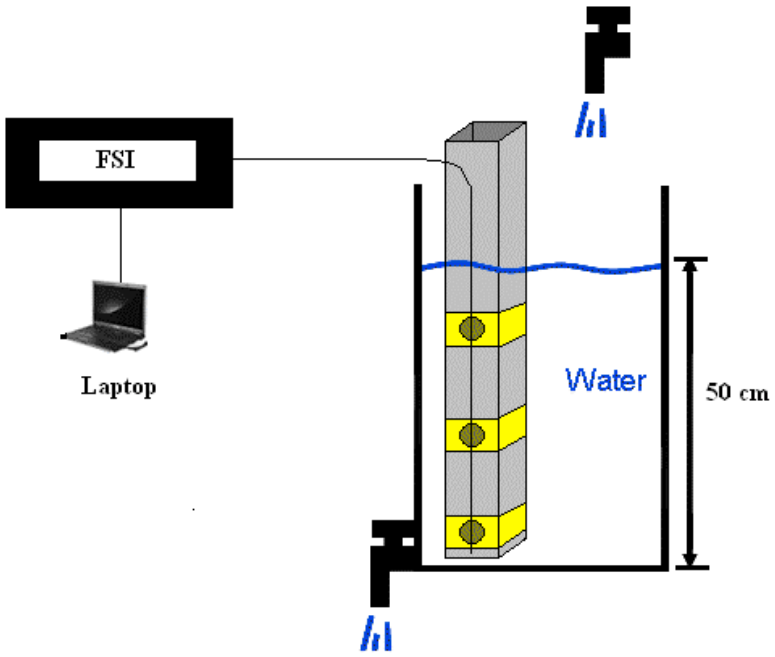

Figure 4.24 System schematic

Like earlier experiments, the water was allowed to reach equilibrium for no fewer three hours before conducting the experiments. The primary difference here is that whereas before, the sensor position was varied relative to liquid depth, in the case the tube was fixed in position and the liquid depth varied. After liquid had been loosed out via the tap, adding fresh tap water would defeat the object of allowing the water the reach equilibrium.

Therefore the water was released into a second storage tank and was added back into the test tank to maintain water continuity.

The sensor positions relative to the tank base are listed in Table 4.6.

Sensor	Position relative to base
Top	350 mm
Middle	200 mm
Bottom	50 mm

Table 4.6 Sensor positions relative to the tank base

To ensure all three sensors were submerged to allow each to respond to hydrostatic pressure changes, the liquid depth was varied between 35 cm and 50 cm, giving a 15 cm measurement region.

4.9.3 Experimental results from multi-sensor system

Figure 4.25a-c represents the responses from the top, middle and bottom FBG sensors respectively.

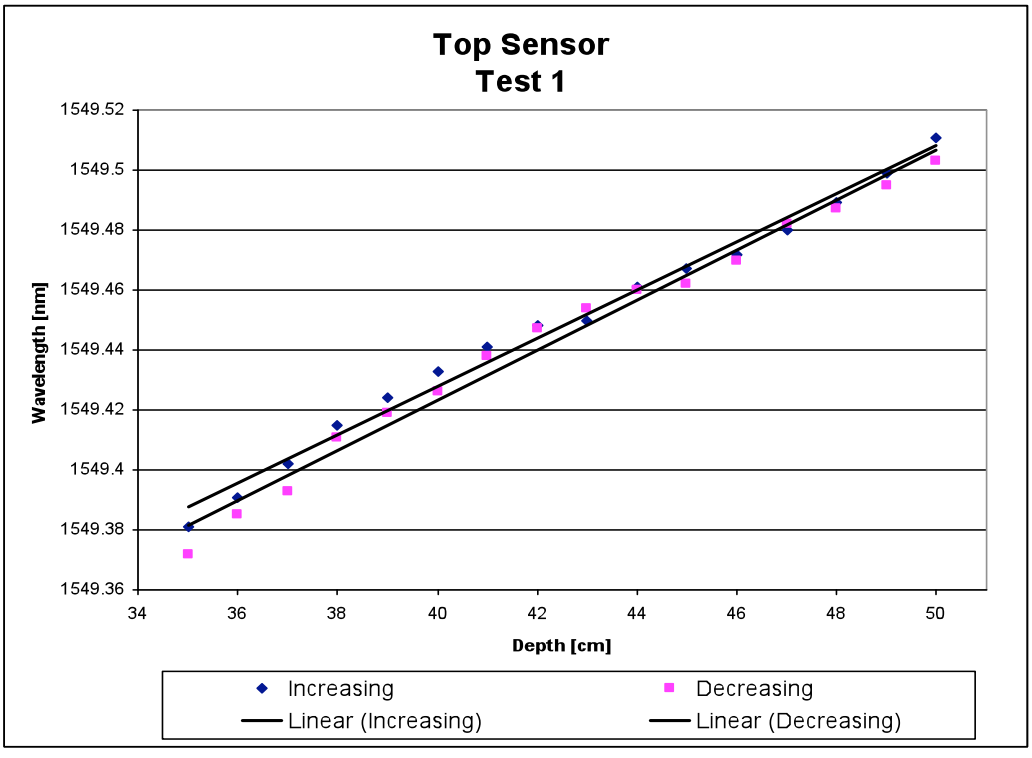

Figure 4.25a Top sensor response

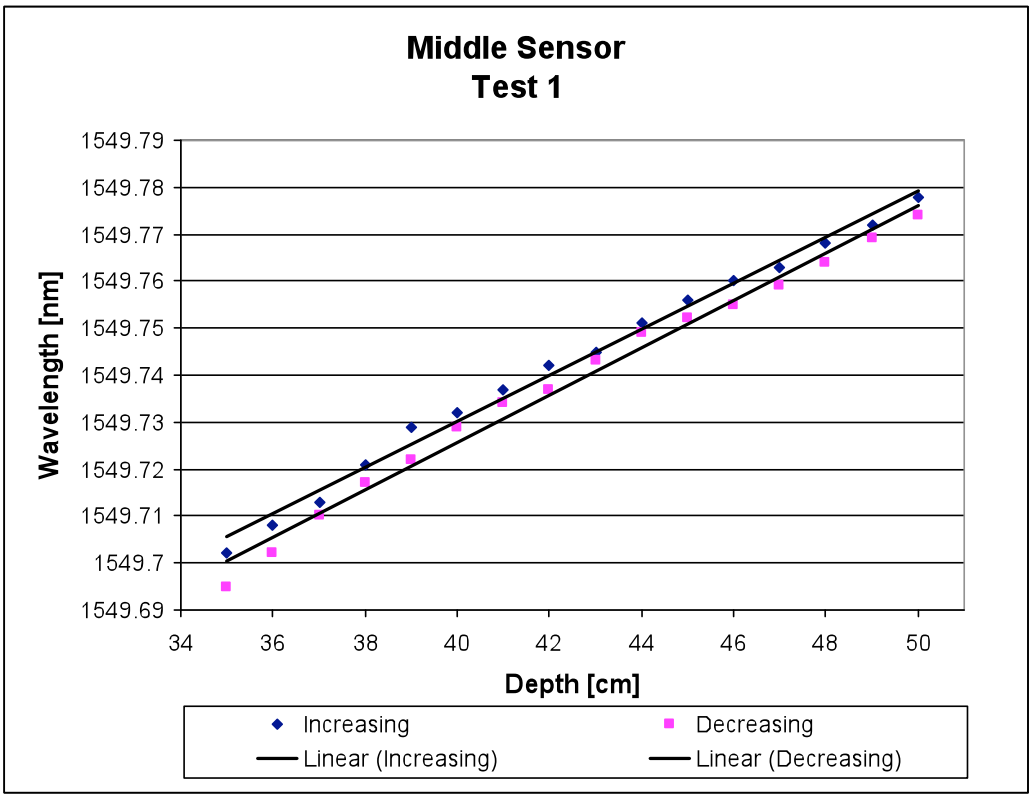

Figure 4.25b Middle sensor response

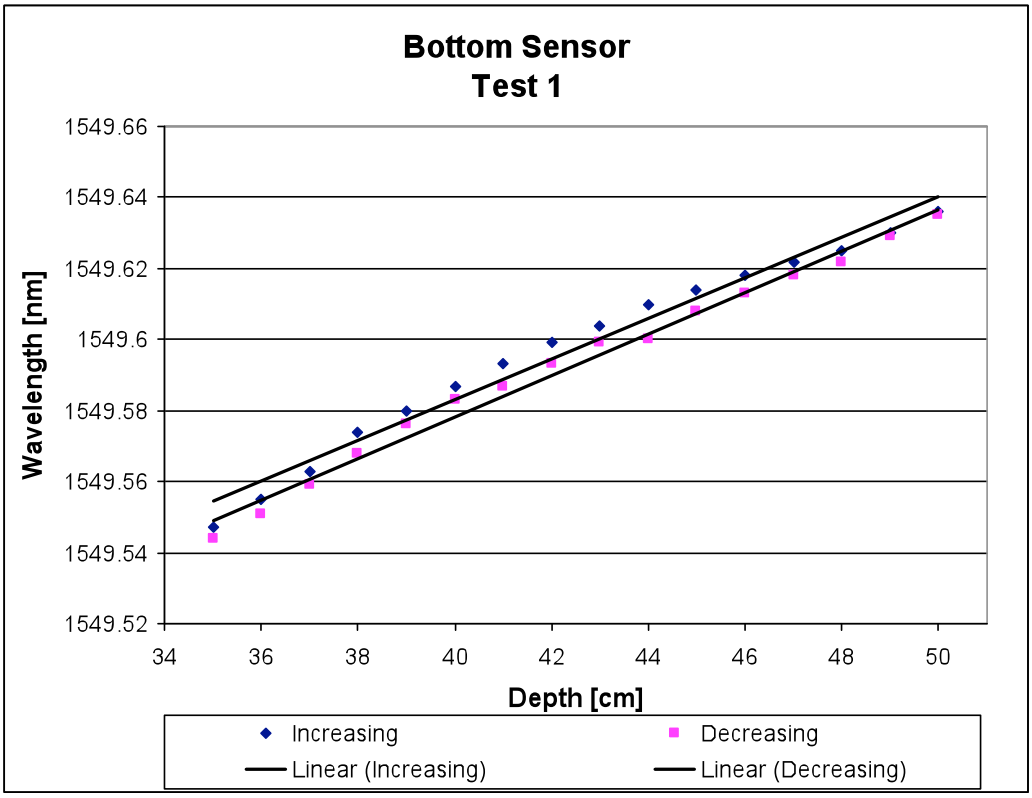

Figure 4.25c Bottom sensor response

Tables 4.7 and 4.8 outline the findings from the above result. The primary reason for the different sensitivities measured is most likely to be attributed to the positioning of the sensors over the drilled holes, and the amount of epoxy used. Ideally, all three sensors would be bonded in the exact same position using the exact same amount of epoxy. In practice, the positioning and bonding process was not controlled enough to guarantee this, therefore it is highly probable that small variations in grating positioning and epoxy quantity exist. If this should be the case, different sensitivities should be expected.

Sensor	Decreasing Δλ (pm)	Increasing Δλ (pm)	Decreasing sensitivity (pm/cm)	Increasing sensitivity (pm/cm)
Top	131	130	8.733	8.667
Middle	79	76	5.267	5.067
Bottom	91	89	6.067	5.933

Table 4.7 Multiple sensor system – wavelength / sensitivity analysis

Cycle N°	Decreasing linear equation	Increasing linear equation
Top	y = 0.0083x + 1549.1	y = 0.0080x + 1459.1
Middle	y = 0.0050x + 1549.5	y = 0.0049x + 1549.5
Bottom	y = 0.0058x + 1549.3	y = 0.0057x + 1549.4

Table 4.8 Multiple sensor system – linearity analysis

4.10 Proposed temperature compensation techniques

Although temperature compensation has been discussed in detail in Chapter 2, this section will briefly introduce temperature compensation techniques for both the single- and multi-FBG based systems.

For the single-FBG unit, temperature compensation could be achieved by adding a second unstrained reference FBG close to the sensing FBG. Zhou *et al* presented this technique in detail [8]. The sensor bonded to the diaphragm would experience both strain and temperature effects, whilst the unstrained grating would only experience temperature effects. In real terms for the system presented in this chapter, the design would consist of a two-layer diaphragm system. The sensing grating would be bonded to the top diaphragm

(sensing diaphragm), which is the diaphragm exposed to the liquid. A second diaphragm (reference diaphragm), of the same material and with the same dimensions, would sit underneath the sensing diaphragm, close enough for it to experience near identical thermal conditions. The reference grating would be bonded to this reference diaphragm. The reference diaphragm is not exposed to the external liquid and therefore will only alter in dimension due to temperature variations. With both the sensing and reference grating experiencing the same ΔT, the only difference between the two gratings is the strain-induced shift experienced by the sensing grating. To avoid creating a second pressure sensor by sandwiching air between the sensing diaphragm and reference diaphragm, a hole in the reference diaphragm would allow the air to flow freely into the main chamber. In the absence of this hole, deformation of the sensing diaphragm would in turn deform the reference diaphragm. The result would be an inaccurate temperature response.

Another proposed temperature compensation technique is to deploy multiple sensors at different location on the sensing diaphragm. The proposed theory being multiple gratings in different locations would experience different strains, whilst all sensors would experience more or less the same temperature effect. Therefore the temperature component can be isolated from the strain component. With this technique, the reference diaphragm is surplus to requirements, in effect making it a less complicated system to fabricate.

4.11 Chapter Conclusions

In conclusion, two novel diaphragm/FBG based level sensors have been demonstrated and discussed. Both systems have shown the potential to interrogate liquid level by measuring the strain induced by FBG sensors bonded to, or positioned directly underneath, a diaphragm which deforms due to isotropic hydrostatic pressure variations. These experiments have crucially shown the optical sensing systems presented can produce the sensitivities required by Airbus, as well as producing good linearity and repeatability. The main advantage of replacing the current electrical sensors with optical sensors is the removal of all electrical sources from within the fuel tank, eliminating the potential risks posed by sparks. The multiplexing capabilities of optical sensors also mean large numbers of sensors can be installed and interrogated.

The first system, though only a single-FBG based system, has shown real promise in terms of its sensitivity and linearity over cyclic testing. It is also feasible that such a system could be multiplexed into a much larger sensing array consisting of numerous single-FBG sensors, which has the advantage of system design and scale flexibility.

The multi-FBG system has also shown good sensitivity and linearity during cyclic testing. The multi-FBG system has advantages including system redundancy, possibility of fuel adulteration detection, and discrete level sensing. This system is also similar in design to the current capacitance probes, therefore it is envisaged that the system could be installed requiring minimal modification to current aircraft fuel tank design.

Both systems are also scalable in terms of the levels they can sense. Early testing showed that for a specific depth, different diaphragm thicknesses exhibit different sensitivities. As fuel tank dimensions vary greatly, depending on tank position and between aircraft types, it is suggested that these systems could be easily adapted to suit all tank volumes/dimensions simply by choosing an appropriate diaphragm thickness to attain the required sensitivity.

4.12 Future Work

The work in the chapter was designed to provide Airbus with an insight into the feasibility of using FBG sensors as a means of measuring fuel level in aircraft fuel tanks. The systems reported in this chapter have shown real promise, however the conditions of a controlled laboratory environment are far less hostile than those found inside aircraft fuel tanks over the complete flight profile. For any of the systems presented in the chapter to be a viable replacement for the capacitance sensors currently deployed, far more investigation is required into compensating against other external effects inducing:

- Temperature
- Density
- Acceleration
- Gravity

Based on the fuel tank parameters being known and assuming the aircraft attitude and pitch are also known, inputting the measured fuel level, fuel density, aircraft pitch and roll will yield the fuel volume.

One of the primary issues in aircraft fuel tanks is fuel adulteration from a number of contaminants, including water. Although no practical work in this chapter has been performed to attempt to detect fuel contaminants, the author proposes a novel technique for detecting contaminants based on the different contaminants having different densities. For a given liquid, the increase in hydrostatic pressure is linear with an increase in depth. Based on the fact the trend is linear, any deviation from the linear trend indicates change in the liquids' density. As the FBG separation on the multi-sensor system described in section 4.9 are equidistant, the approach of monitoring the trend line could be tested on this system. For example, the density for J A-1 is ~805 $kg.m^{-3}$ at 20°C. At the same temperature, water is ~ 1000 $kg.m^{-3}$. In the absence of water, the measured pressure, therefore the wavelength shift, should be linear. If water is present in the tank, usually found near the bottom, the sensor immersed in water will deviate from the linear trend.

Another area where further work is needed is system robustness testing. Whilst both systems have shown good results in laboratory conditions, the environment of a live aircraft is far more extreme over the flight cycle. Large temperature variation, atmospheric

pressure variations, vibration, debris in the tanks, and bacteria forming on the sensors are just some of the factors which need to be combated before these systems could be effectively deployed.

At the time of producing this thesis, work is underway on fabricating a new version of the single-FBG sensing unit presented in sections 4.7 and 4.8, as well as an aerospace compliant version of a multi-FBG sensing unit system presented in section 4.9. When suitably satisfied these two systems are ready for fuel testing, they will be tested at the Airbus fuel testing facility based at Airbus UK Ltd in Filton, Bristol, UK.

4.13 Chapter references

[1] J. A. Morris and C.R. Pollock, "*A Digital Fiber-Optic Liquid Level Sensor*", Journal of Lightwave Technology, vol. LT-5, Iss 7, pp. 920-926, 1987

[2] J. Z. Gao, Y.L. Zhao and Z.D. Jiang, "*Design and performance characterization of a fibre optic sensor for liquid level monitoring*", Journal of Physics: Conference Series 13, pp. 77-80, 2005

[3] J. D. Welss, "*Fluorescent optical liquid-level sensor*", Optical Engineering, vol. 39, pp. 2198-2213, 2000

[4] S. Khaliq, S. W. James and R. P. Tatam, "*Fiber-optic liquid-level sensor using a long-period grating*", Optics Letters, vol. 26, pp. 1224-1226, 2001

[5] Airbus UK Limited, "*Introduction to Fuel Gauging Systems and Techniques*", confidential document, 2006

[6] M. F. Ashby, "*Materials selection in mechanical design – 2nd edition*", Oxford, UK, p. 389, 1999

[7] K-T. Wan, S. Guo and D. A. Dillard, "*A theoretical and numerical study of a thin clamped circular film under an external load in the presence of a tensile residual stress*", Thin Solid Films, pp. 150-162, 2002

[8] Z. Zhou and J. Ou, "*Techniques of temperature compensation for FBG strain sensors used in long-term structural monitoring*", Proc of Asian Pacific Fundamental Problems to Opto- and Microelectronics (APCOM), pp. 465-471, 2004

5 Fuel level sensing utilising long period fibre grating based refractive index sensors

5.1 Chapter preamble

A great deal of interest has been focused on executing fuel level measurements in numerous areas, such as the in the fuel tanks of aircraft, rockets, and automobiles. In many cases, electrical sensors are inappropriate or simply not feasible because of the hazards posed by sparks in potentially explosive environments. Electrical sensors will also be undesirable when electromagnetic interference can overwhelm the signals generated by them. Fuel level sensors using optical fibres hold particular promise as replacements for the existing sensing technologies, especially as they can operate in potentially explosive environments. Sensors based on purely optical level sensing techniques have been previously described [1][2].

Optical FBG techniques attract much attention due to their significant feature of wavelength encoding, which allows the removal of influences from system variables such as source intensity and attenuation. Most of those reported FBG based sensors based on the measurement of strain, pressure and weight are greatly affected by environmental variables such as temperature, pressure and gravity.

There are two techniques for determining liquid level using LPFGs. The first is to measure the transmission value of an attenuation band [3], and the second is to monitor the resonant wavelength shift of an attenuation band [4]. The former technique has been previously reported, however to the best of the authors knowledge, this is the first instance of measuring fuel level by monitoring a shift in the resonant wavelength of an attenuation band.

The chapter begins with a brief overview of LPFGs utilised in other fields as refractive index sensors. Sections 5.3 and 5.4 present the experimental results obtained when exposing the uncoated and titanium oxide coated LPFGs to variations in fuel level respectively. Section 5.5 compares the results obtained in sections 5.3 and 5.4. As the presence of water in aviation fuel is a significant issue, sections 5.6 and 5.7 present the possibility of using a LPFG to detect the presence of free water in fuel and simulation

results respectively. A detailed theoretical description of LPFGs can be found in Chapter 2.

5.2 Overview of LPFGs utilised as refractive index sensors

As has been previously described, the sensitivity of LPFGs occurs due to the dependence of the phase matching condition on the cladding modes' refractive indices. The effective indices of these cladding modes $n_{cl,m}^{eff}$ are dependant on the difference between the RI of the cladding n_{cl}, and the RI of the surrounding medium n_{sur}. This sensitivity to variations in the surrounding RI is evident when observing the grating spectrum by either a change in the resonant wavelength and/or in the minimum transmission value of the attenuation band. The higher order modes yield higher sensitivity, and occur as the RI of the surrounding medium approaches the RI of the cladding [5]. The sensitivity to changes of the surrounding RI has been widely used as RI based sensors in numerous applications including liquid level sensing [3][4][6], chemical sensing [7], organic sensing [8], solution concentration sensing [9] and tuneable spectral filtering [10]. Other such instances of LPFG based sensors being deployed to measure parameters such as bend sensing based on peak splitting [11] and fuel quality control [12] have also been reported.

5.3 Experimental results from exposing long period fibre gratings to variations in liquid level

5.3.1 Experimental arrangement and procedure

The experimental arrangement consists of an optical broadband source to illuminate the LPFG and an Optical Spectrum Analyzer (OSA) to interrogate the transmission spectrum. Each LPFG was suspended in free space between two fixed points ensuring the fibre was under a constant tension throughout the experiments, and was placed within a u-tube. The u-tube used was designed in-house and fabricated at the School of Chemistry, University of Birmingham. The fuel level could then be increased by adding the fuel into the vacant arm of the u-tube, and decreased via the tap at the base of the u-tube. The experimental arrangement is illustrated in Figure 5.1a and pictured in Figure 5.1b.

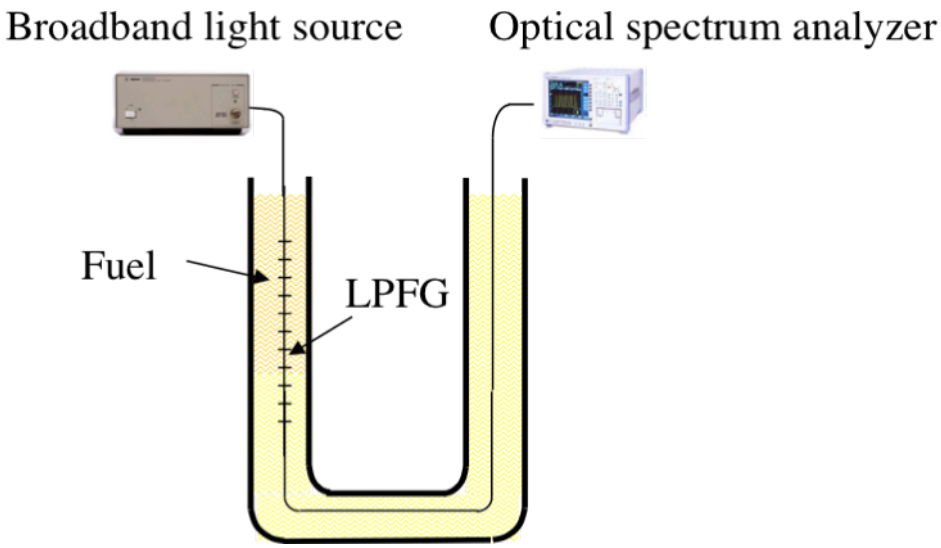

Figure 5.1a Experimental arrangement for fuel level sensing

Figure 5.1b Picture of the experimental arrangement

The data was captured using a National Instruments GP-IB connection from the OSA to a PC, and a LabVIEW trace capture program.

5.3.1.1 Agilent 83437A broadband light source

The optical broadband source used for the experiments in this chapter was an Agilent 83437A, which houses four independently driven edge emitting LEDs (EELED). Each EELED operates in its own wavelength window. The operating wavelengths are given in Table 5.1.

EELED N^{o}	Operating wavelength (nm)	Diode power (dBm)
1	1550	-17
2	1310	-13
3	1430	-13
4	1650	-17

Table 5.1 Operating wavelengths of the EELEDs [13]

Optical couplers are then used to couple the light from the four EELEDs to combine the light to a single output.

5.3.1.2 Ando AQ6317V Optical Spectrum Analyzer

The OSA used to interrogate the transmission spectrum of the LPFGs in these experiments was the Ando AQ6317B. Key features of this OSA include:

- Wavelength range 600 nm to 1750 nm
- Wavelength resolution as high as 0.015 nm
- Wavelength accuracy of ±0.02 nm (1520 to 1580 nm), ±0.04 nm (1580 to 1620) and ±0.05 nm (600 to 1620)
- Level accuracy ±0.3 dB

5.3.2 1000 μm period uncoated LPFG

The transmission profile of the 1000 μm period uncoated LPFG is illustrated in Figure 5.2. As can be seen, in the wavelength region of 1300 nm to 1700 nm, the LPFG couples the light to four cladding modes.

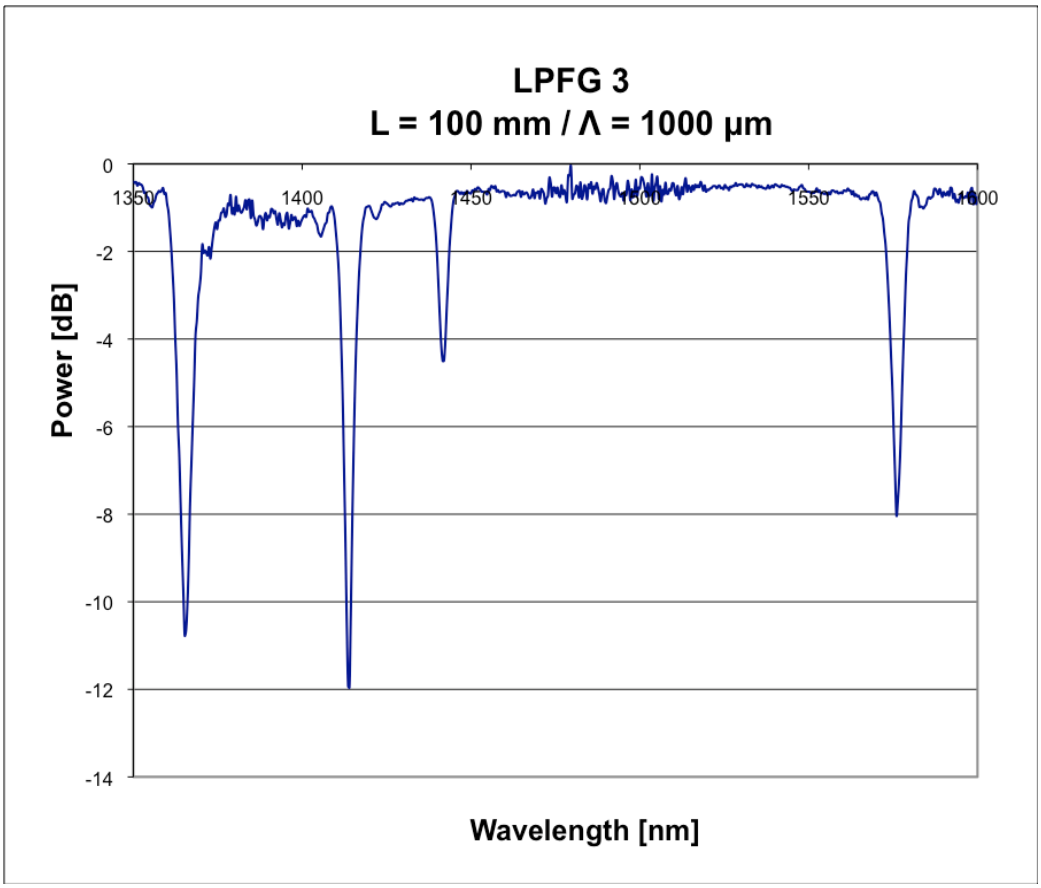

Figure 5.2 Pre-annealed transmission profile of the uncoated 1000 µm LPFG

Initial testing, observing all four attenuation bands, showed the most sensitive attenuation band was centred at ~1414 nm. The experimental procedure showed this attenuation band induced a resonant wavelength shift of 10.0 nm over the 10 cm measurement range, shifting from its resonant wavelength of 1413.2 nm in air to 1403.2 nm when fully immersed in fuel. Figure 5.3 illustrates this shift in wavelength over the 10 cm measurement range.

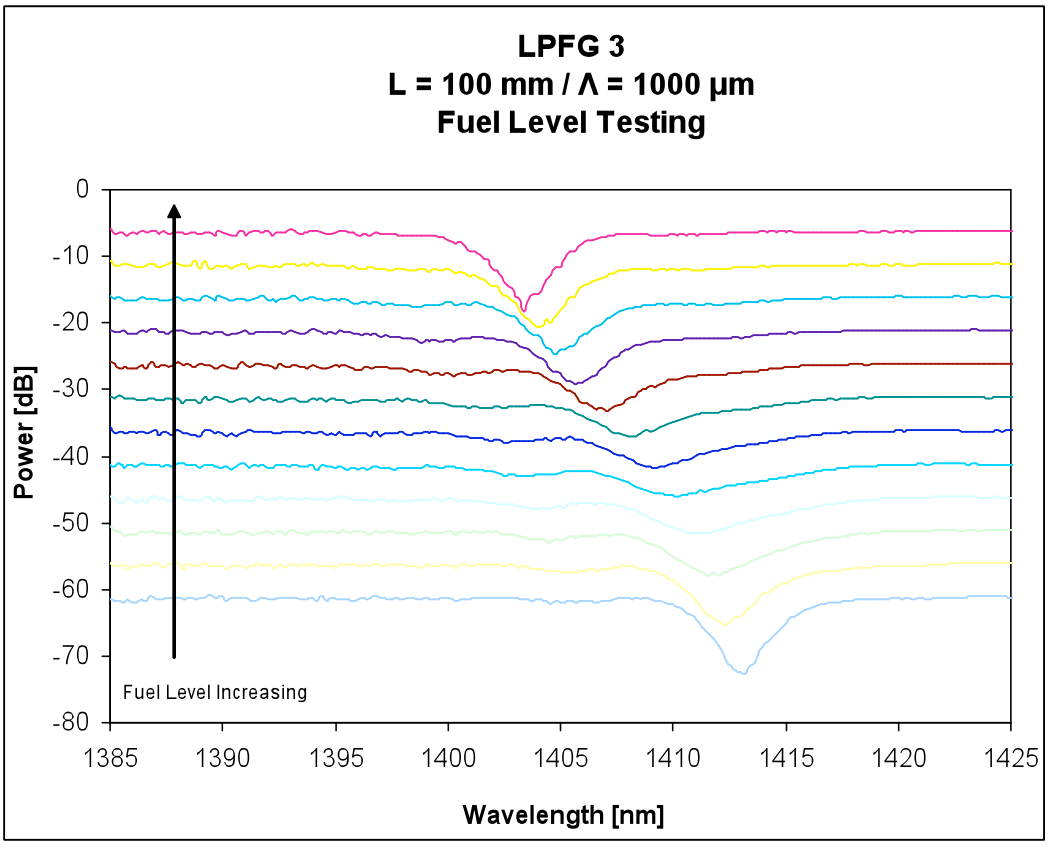

Figure 5.3 Plot of wavelength shift induced by increase in fuel level

It should be noted that 5 dB of transmission loss was added to each subsequent trace in Figure 5.3 to add clarity to the result.

Whilst the result shown in Figure 5.3 clearly shows a blue wavelength shift as the liquid level is increased, as is normally the case when the RI of the surrounding medium is lower than the cladding, it also shows the phenomenon of the peak strength cycling from strong ⇒ weak ⇒ strong as the liquid level was increased. Whilst in this particular situation, the dispersion condition results in a continuous shift of the resonant peak; in effect two separate LPFGs are still formed in series, yielding two separate attenuation bands corresponding to the two different RIs of the surrounding medium. From the theory discussed in Chapter 2, it is known that the strength of the attenuation peak, for a given LPFG length, varies with the amount of liquid that the LPFG is immersed in to. Equations 2.42 and 2.43 clearly show that the strength of the attenuation band will be at maximum when the LPFG is (a) surrounded by air, or (b) when the LPFG is completely immersed in the liquid to be measured. These are represented in Figure 5.4 at the initial wavelength,

1413.2 nm and the final wavelength, 1403.2 nm. For further discussion on this effect, refer to Chapter 2.

The result shown in Figure 5.4 demonstrates the linearity of the LPFG over the complete measurement range of fuel level variations. This is very important if the LPFG is to be employed as a sensor where variations in the external RI are to be measured and attributed to changes in fuel level. Figure 5.4 is a plot of resonant wavelength as a function of fuel level, which greatly emphasizes the linearity of this LPFG.

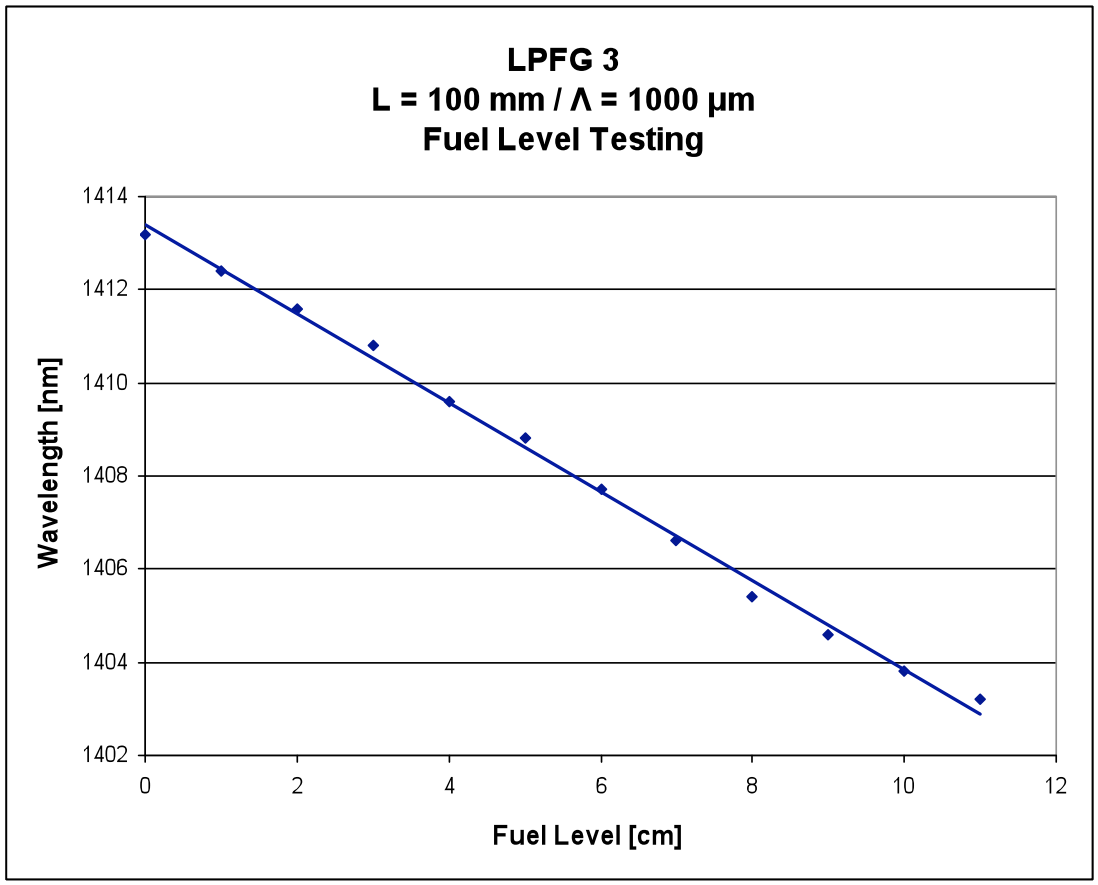

Figure 5.4 Plot of wavelength shift as a function of fuel level

The sensitivity of the uncoated LPFG to fuel level variations was found to be 1000 pm/cm.

5.3.2.1 1000 μm period uncoated LPFG cyclic testing

Whilst the above result provides an in depth analysis of the response of the LPFG to increasing fuel level, cyclic testing was performed to analyse the repeatability of the system. Five cycles were performed, increasing and decreasing the fuel level respectively and taking measurements at 1 cm intervals.

Figure 5.5a and 5.5b illustrates the five cyclic tests. Figure 5.5a represents the fuel level increasing; Figure 5.5b represents the fuel level decreasing.

As can be seen, there is little hysteresis within the complete range of the sensor output. The difference between the outputs of increased and decreased fuel levels mainly arose from the reading error of the fuel level.

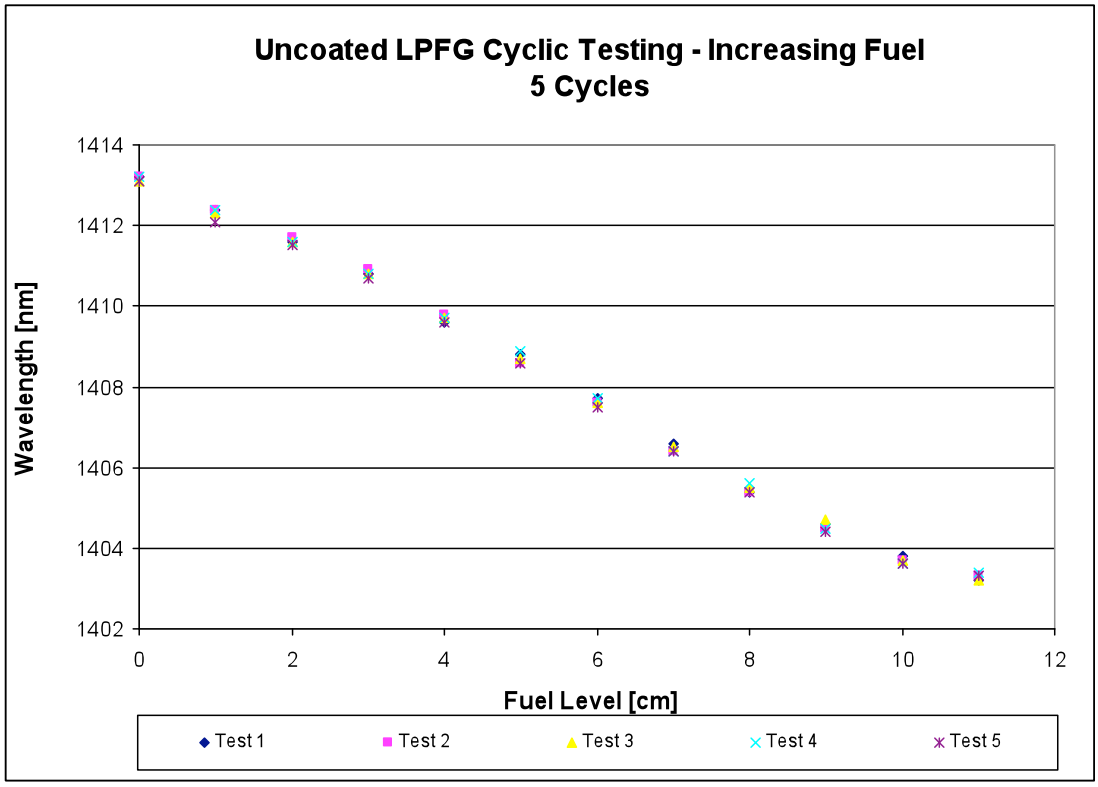

Figure 5.5a Uncoated LPFG cyclic testing (increasing fuel)

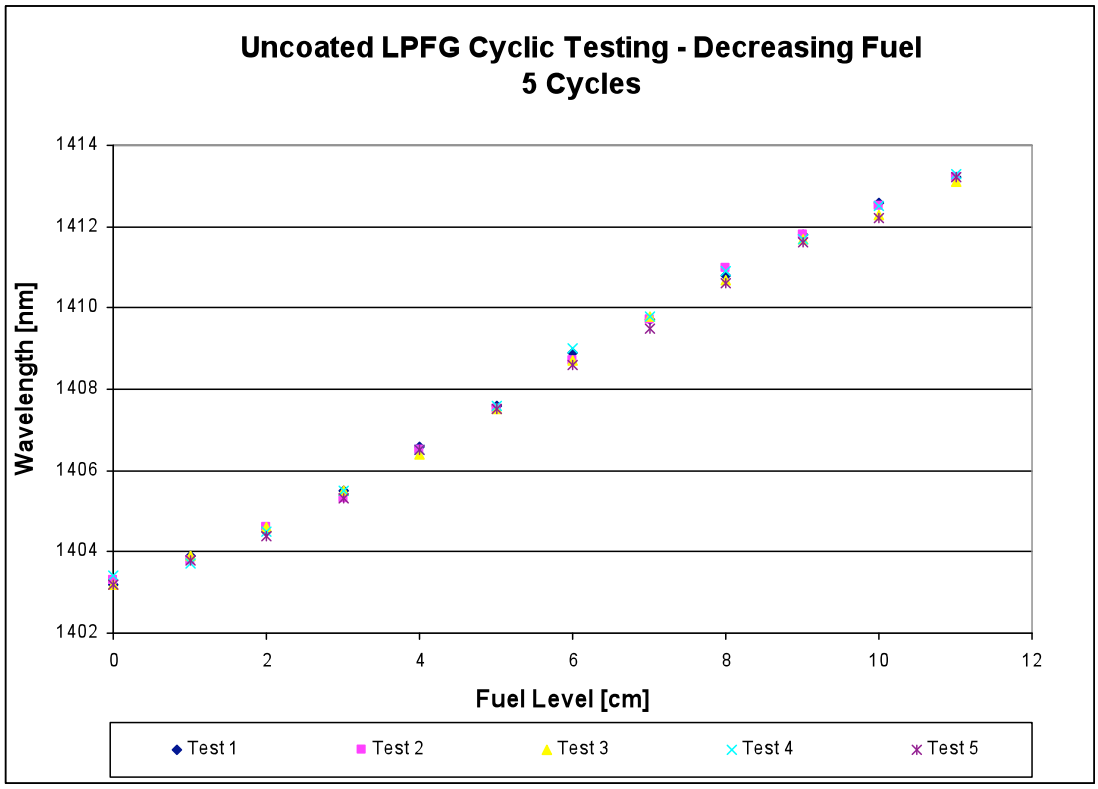

Figure 5.5b Uncoated LPFG cyclic testing (decreasing fuel)

5.4 Enhancing refractive index sensitivity by applying a sol-gel dip-coated derived Titanium-Oxide (TiO_2) coating

The initial reason for investigating the possibility of coating the fibre was to add a degree of physical strength. As the envisaged application for this sensor was an in-situ fuel level sensor for aircraft fuel tanks, it quickly became apparent that there would be a need for some type of engineering to increase the strength/survivability of such as sensor, and a coating was one of several options. Research into numerous possible coatings revealed that there were multiple advantages of coating the fibre with Titanium Oxide (TiO_2) in addition to increasing the overall strength of the fibre. Firstly, in an aircraft fuel tank there is the significant problem of bacterial adhesion to the glass fibre. Figure 5.6a-d depicts various images of cyanobacteria and the respective damage it can cause.

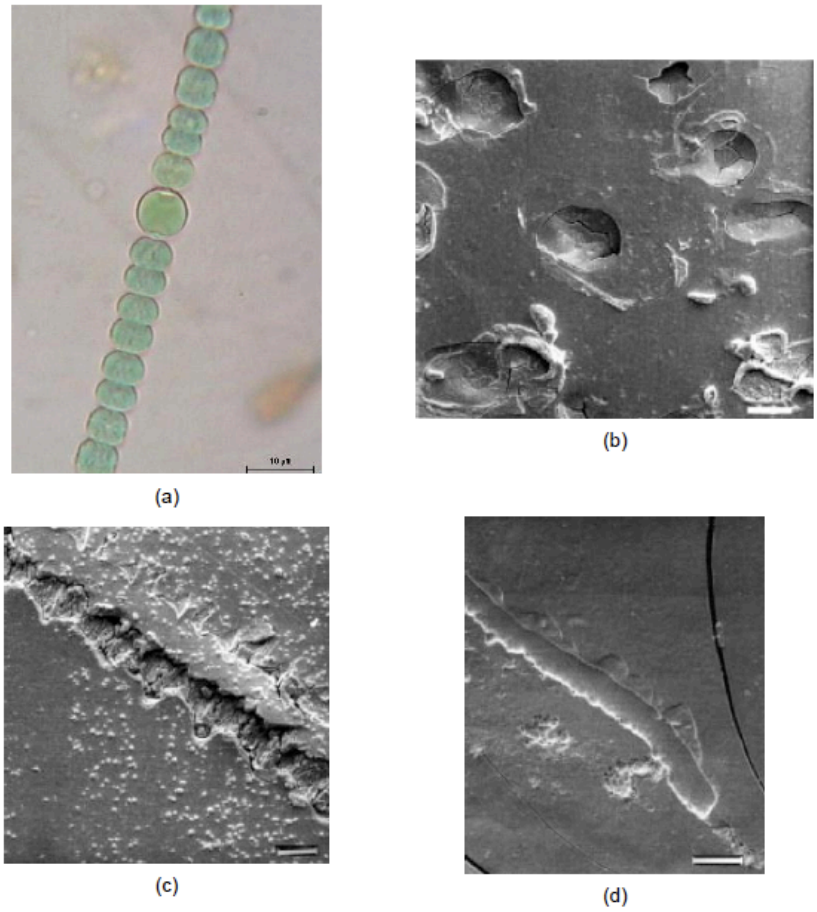

Figure 5.6 (a) An image of a typical cyanobacteria [BAE SYSTEMS report], (b) Bio pitting of glass, (c) Etched pattern on glass caused by a cyanobacteria, (d) Presence of crack and etching [14].

Li *et al* has demonstrated that by coating the fibre surface with the photocatalitically active metal oxide TiO_2, the bacterial adhesion can be reduced by 10 to 50% [15]. This technology is similar to the now commonly employed self-cleaning windows used in buildings. It has also been reported in the same work that applying UV illumination at 245 or 340 nm, 100% of the bacteria is killed. This is due to the coating becoming hydrophilic under UV illumination. In the case of self-cleaning windows in buildings, the UV light is provided by sunlight. The other advantage of applying a TiO_2 coating is that by doing so, the sensitivity to variations of the surrounding medium is increased, as shown by Davies *et al* [16]. If an optical fibre is coated with a different material, the effective refractive index of the cladding is modified. If the coating material is of a higher value than that of the cladding, the result is an increase in the effective refractive index of the cladding [17]. The end result is an increase in the sensitivity to RI variations so long as the condition $n_{cl,m}^{eff} \leq n_{co}^{eff}$ is satisfied. Davies *et al* has previously reported that the values of $n_{cl,m}^{eff}$ yielding

high RI sensitivities are achievable by choosing optimal combinations of coating thickness and RI [16].

5.4.1 Preparation of TiO_2 coatings for optical fibres

The sol-gel dip-coating method is a versatile method for the preparation of coatings. Different shaped objectives like glass slides and fibres can be coated with this sol-gel method. For sol-gel synthesis, typical precursors are metal alkoxides such as titanium or silicon, water and acid, base and also alcohol can be used as a solvent. In aqueous environments, together with an acid or base catalyst, alkoxides begin to hydrolyse and condensate, which in turn leads to the formation of particles in the sol. Sols are colloidal suspensions of solid particles (about 1-1000 nm) in a liquid. In the alkoxide based sols, the size of the particles and particle aggregation depend on the pH and sol concentration. Particle sizes in alkoxide based sol are typically between 2-10 nm. If the sol is very diluted, the gelation of the sol can be a very slow process or the sol can become stable. A gel can be considered to be formed when a continuous solid skeleton encloses continuous liquid phase. During the dip-coating process, the substrate, in this case SMF-28 optical fibre, is immersed into the sol and withdrawn from the sol at a constant speed. During the film deposition particles from the sol are deposited on the fibre surface and the solvent is evaporated. The deposited gel can be further heat-treated in order to densify the coating. Dip-coating can be done at room temperature. Typically sol-gel produced materials are nanoporous because of the nature of the sol. A sol contains nano particles and after gel formation and drying these particles are very close to each other and the pores are formed in-between said particles. For the dip-coating system used for this work, the film thickness can be controlled by either changing the speed at which the fibre is removed, and/or the viscosity of the sol. By using a slow withdrawal speed the sol has more time to drain from the substrate and a thinner coating layer will be deposited. Whereas if a high withdrawal speed is used the sol has less time to drain and more particles will be deposited on the surface leading to a thicker films. The particle concentration of the sol affects the sol viscosity and has an effect on the film thickness. If the particle and aggregate concentration in the sol is low, thinner films are deposited compared to films that have been deposited from the sol with a high particle concentration. The refractive index of the film mainly depends on the coating material, e.g. TiO_2 coatings [16][18].

The sol-gel method is used to prepare the titania coatings to be applied to the optical fibre. Typically, in sol-gel method metal alkoxides are used as precursors for oxides. Precursors

for titania sol are tetraisopropyl orthotitanate (TIPT, [$Ti(OC_3H_7)_4$]), ethanol, deionised water, 65 % HNO_3 and polyethylene glycol with molecular weight 400 (PEG). The used water to alkoxide mole ratio (R) of the sol is one and alkoxide to ethanol mole ratio is four. Hydrolysis and condensation is done in acidic conditions. Coating is prepared by dipping the optical fibre into the sol and withdrawn from the sol with a constant speed of 20 mm/min. A dip-coating device is used to prepare the coatings and the withdrawal speed is controlled with the device. Coatings are done at room temperature (T=21-23ºC) and atmosphere in the relatively humidity of 38-50%. Fibres are washed gently with ethanol and dried before dip-coating. After the dip-coating films were heat-treated at 100 ˚C for 30 min [16].

A LPFG with a period of 1000 μm and a length of 10 cm was written into presensitised Corning SMF-28 fibre and sent for coating. Dr. Reeta Viitala of the Turku Biomaterials Centre, University of Turku, Finland, coated the LPFG utilised in this chapter. Table 5.2 lists the grating parameters.

LPFG N^o/Λ	Withdrawal speed	Coating thickness	Coating refractive index
6/1000 μm	20 mm/min	147.6 nm	1.96

Table 5.2 LPFG with specified coating thickness and refractive indices.

5.4.2 1000 μm period TiO_2 coated LPFG

The transmission profile of the 1000 μm period LPFG that was sent for coating is illustrated in Figure 5.7. As can be seen, in the wavelength region of 1300 nm to 1700 nm, the LPFG couples the light to four cladding modes.

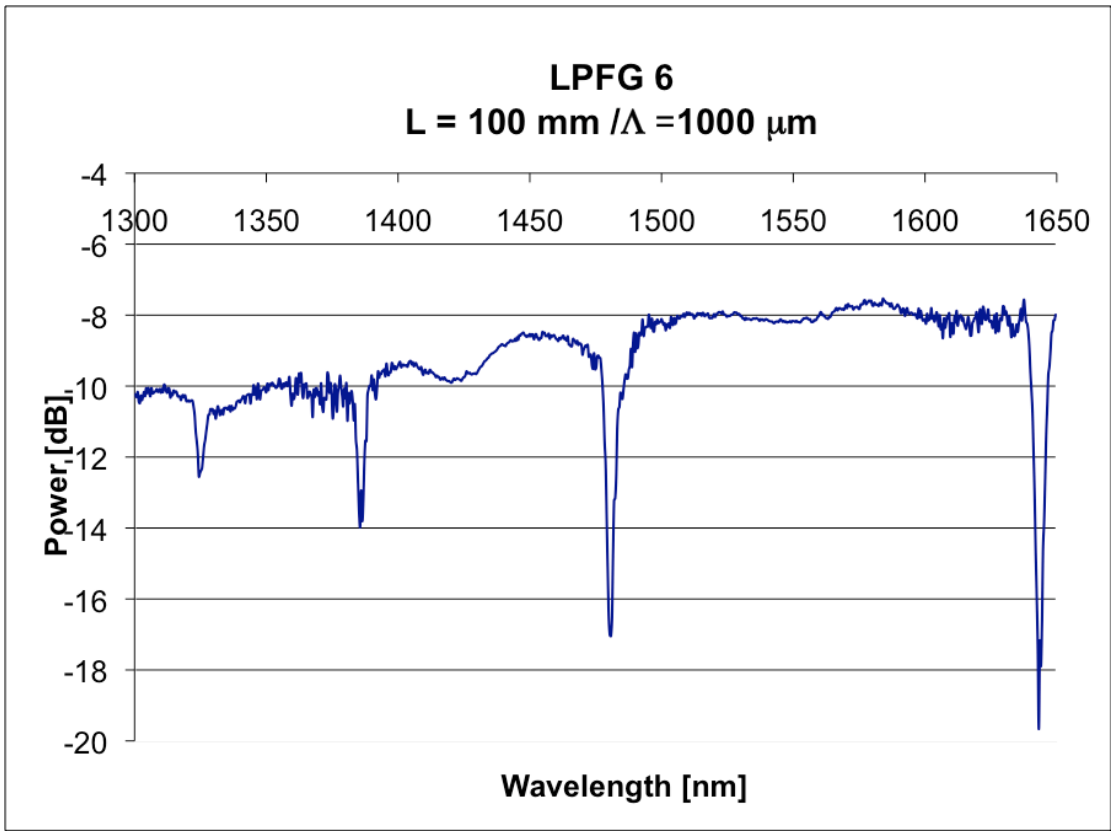

Figure 5.7 Pre-annealed transmission profile of the coated 1000 μm LPFG

After coating, and following the same procedure of initially observing all four attenuation bands, it showed the most sensitive attenuation band was centred at ~1328 nm. The experimental procedure showed this attenuation band induced a resonant wavelength shift of 12.4 nm over the 10 cm measurement range, shifting from its resonant wavelength of 1328.0 nm in air to 1315.6 nm when fully immersed in fuel. Figure 5.8 illustrates the resonant wavelength shift over the 10 cm measurement range.

Again, please note that 5 dB of transmission loss was added to each subsequent trace in Figure 5.8 to add clarity to the result.

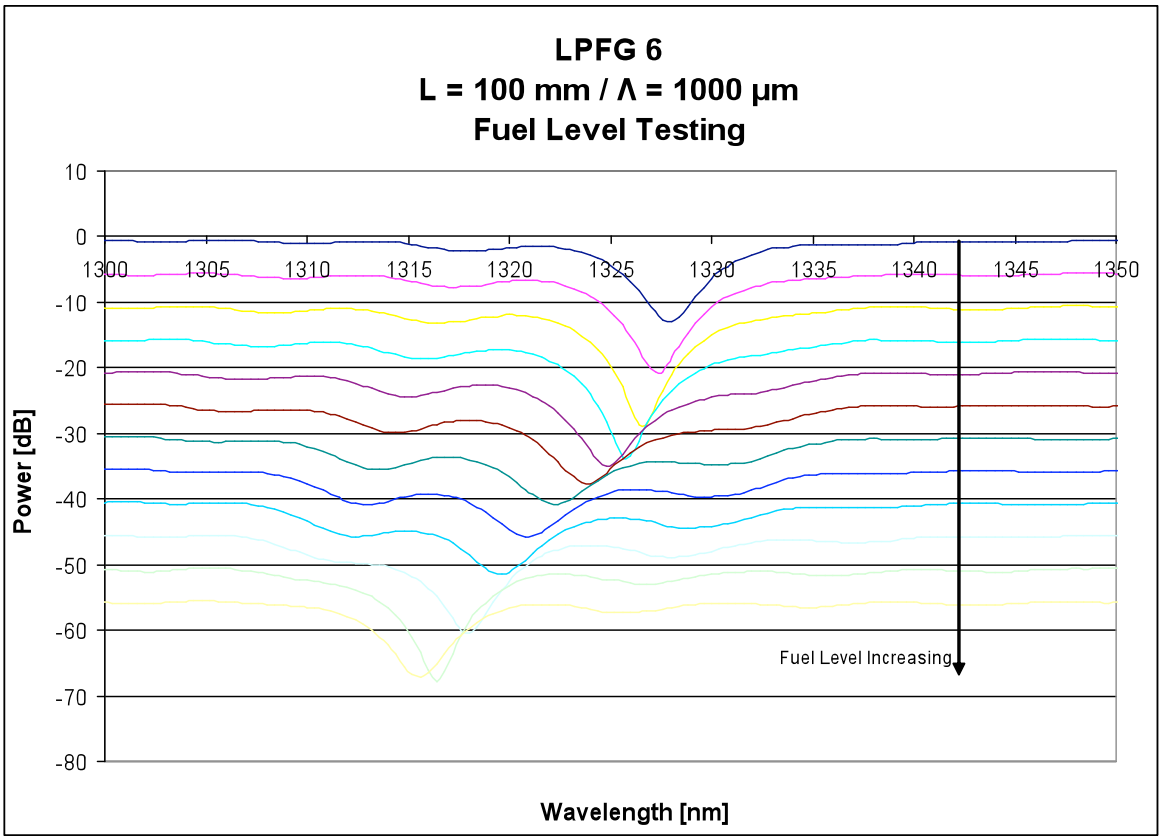

Figure 5.8 Plot of wavelength shift induced by increase in fuel level

Like the uncoated LPFG, the above result demonstrates very good linearity over the complete measurement range, as shown in Figure 5.9. As previously stated, this is very important if the LPFG is to be employed as a sensor where variations in the external RI are to be measured and attributed to changes in fuel level. Figure 5.9 is a plot of resonant wavelength as a function of fuel level, which greatly emphasizes the linearity of this LPFG.

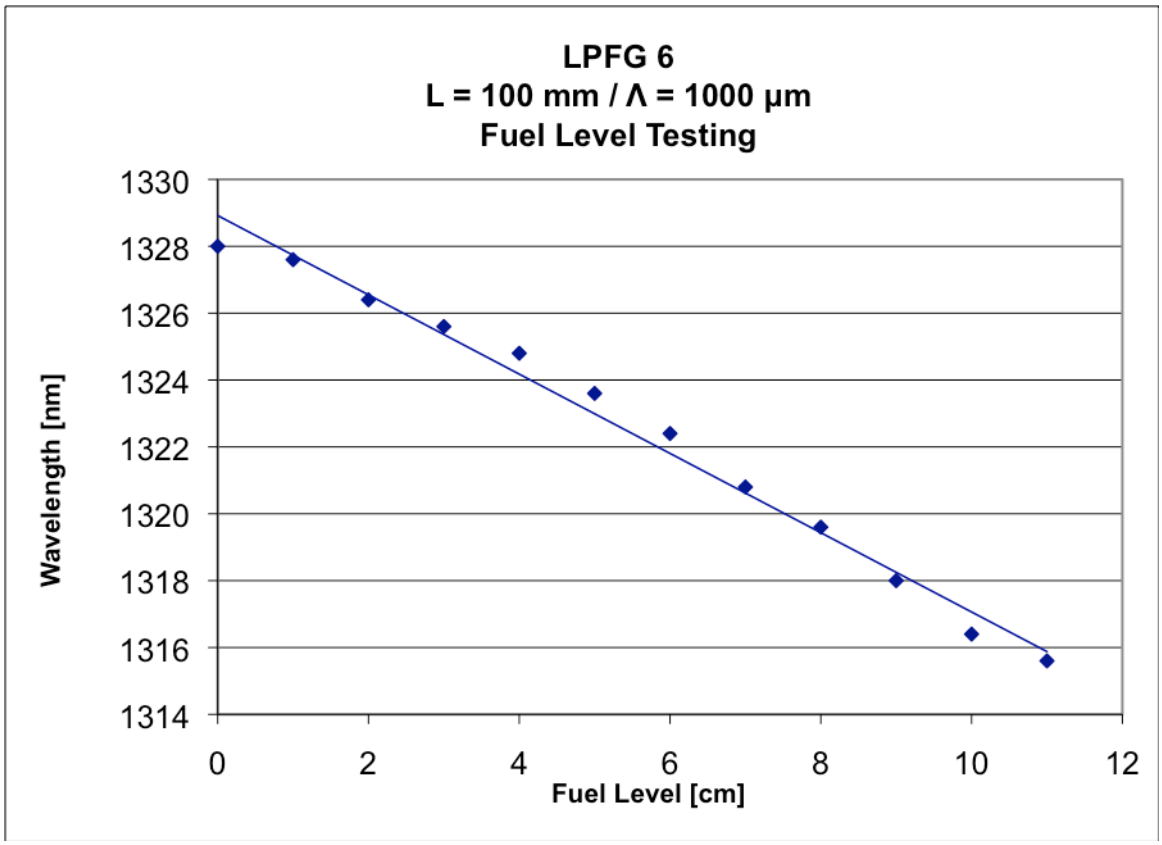

Figure 5.9 Plot of wavelength shift as a function of fuel level

The sensitivity of the uncoated LPFG to fuel level variations was found to be 1240 pm/cm.

5.4.2.1 1000 µm period TiO_2 coated LPFG cyclic testing

Again whilst the above result provides an in depth analysis of the response of the LPFG to increasing fuel level, cyclic testing was again performed to analyse the repeatability of the system. Five cycles were performed, increasing and decreasing the fuel level respectively and taking measurements at 1 cm intervals.

Figure 5.10a and 5.10b illustrates the five cyclic tests. Figure 5.10a represents the fuel level increasing; Figure 5.10b represents the fuel level decreasing.

As can be seen, like the uncoated LPFG, the repeatability over the complete sensor range is very good. The difference between the outputs of increased and decreased fuel levels is again attributed to reading error of the fuel level.

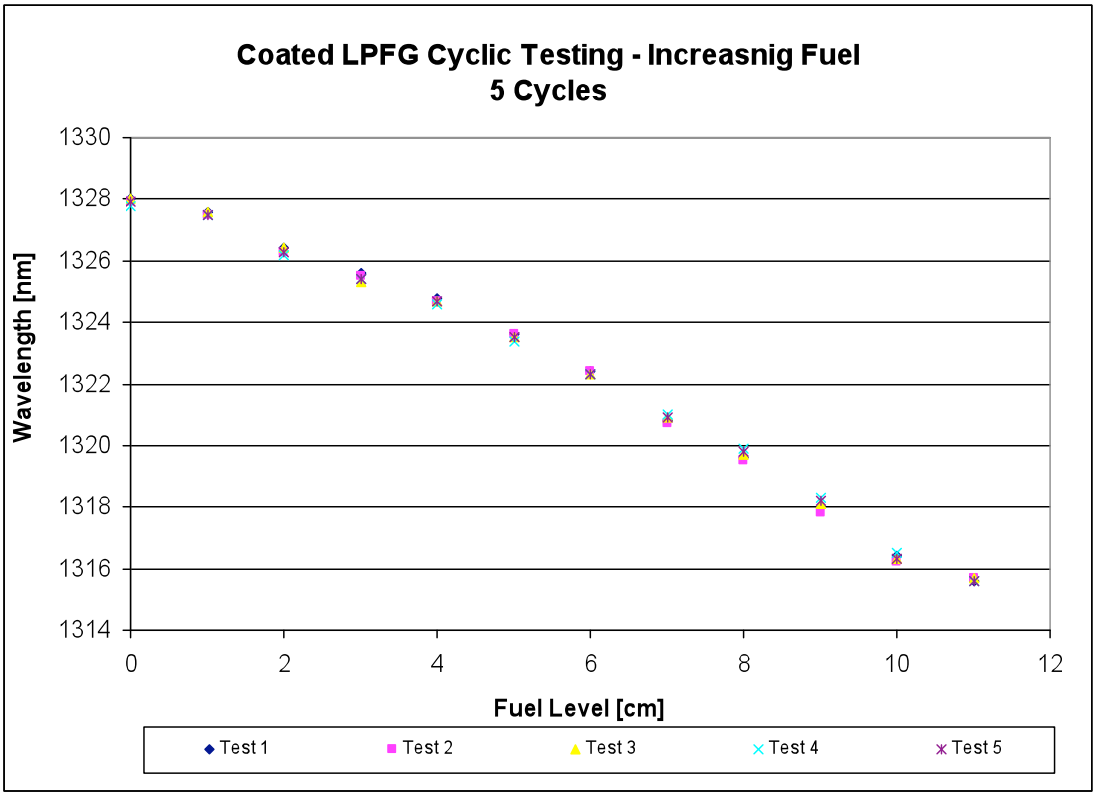

Figure 5.10a Coated LPFG cyclic testing (increasing fuel)

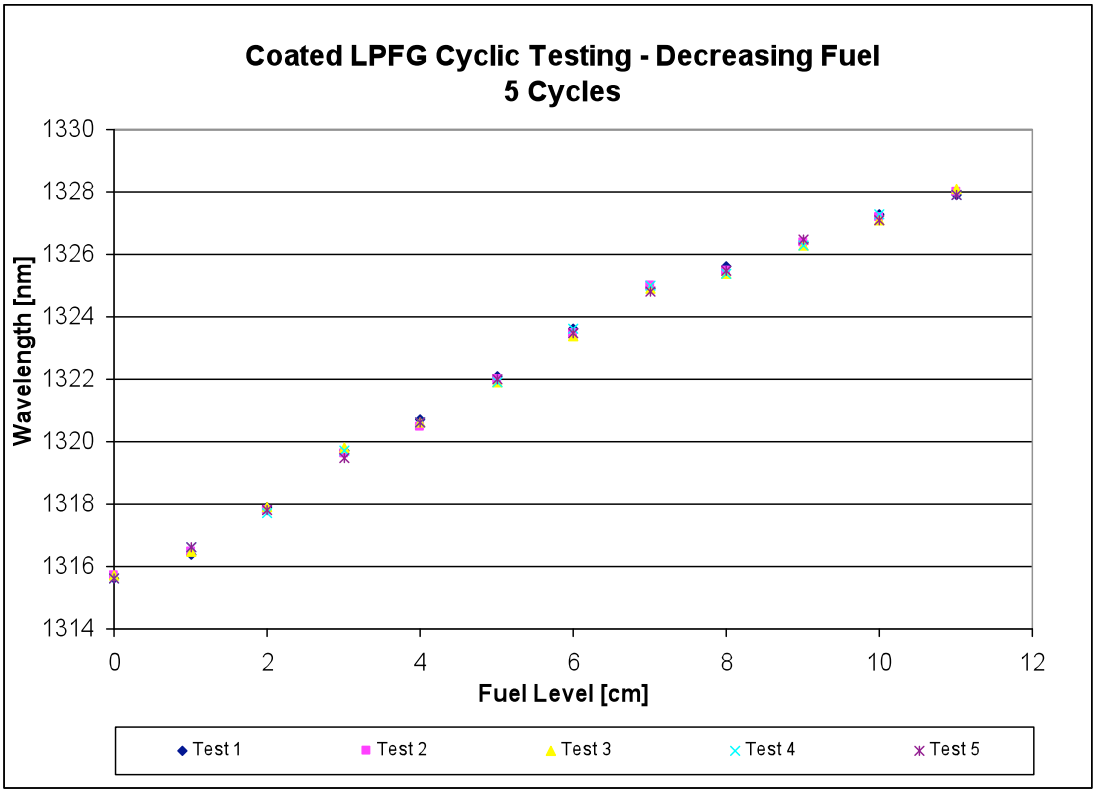

Figure 5.10b Coated LPFG cyclic testing (decreasing fuel)

5.5 Comparison of uncoated and TiO_2 coated LPFGs

The section will compare the results illustrated in Figures 5.3 and 5.8. Testing showed that the coated LPFG produced an overall shift 2.4 nm larger than that of the uncoated LPFG. Figure 5.11 shows the response of both the uncoated and coated LPFGs; clearly illustrating that the larger relative wavelength shift was induced by the coated sensor.

Compared with the uncoated LPFG, the coated sensor produced a sensitivity 24% greater than the uncoated sensor.

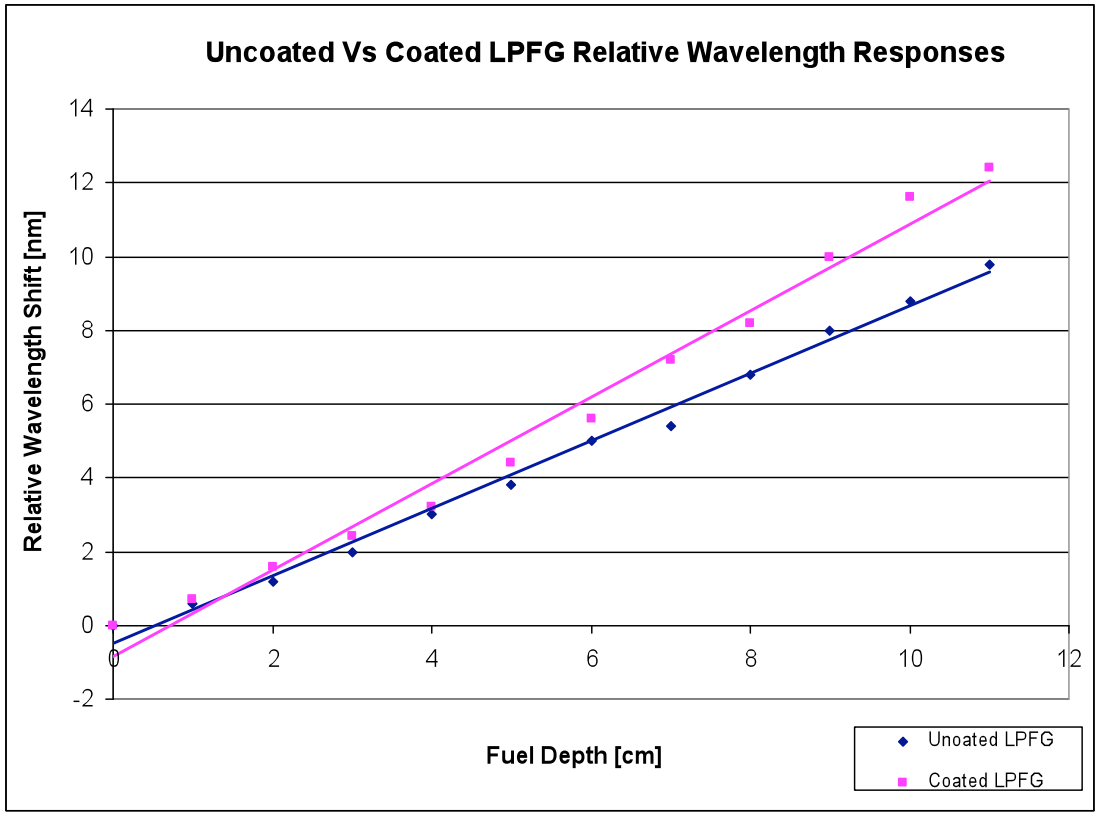

Figure 5.11 Comparison of responses between the uncoated and coated LPFGs

5.6 Detection of free water in fuel

One of the most common causes of aviation fuel adulteration is the presence of water. Water can enter the fuel tank via two methods:

- Fuel already contaminated by water can be injected into the aircraft fuel tanks during refuelling
- Moisture in the air during flight can form condensation in the fuel tanks

This is not a trivial issue. A British Airways Boeing 777-236ER enroute from Beijing Capital International Airport crash-landed just short of the runway at its destination, London Heathrow Airport on 17 January 2008 after an 8,100 kilometres flight.

A September 2008 interim report from the Air Accident Investigation Branch (AAIB) found the most likely cause to be icing in the fuel delivery system. This would have restricted fuel flow to the engines as thrust was demanded during the final approach to Heathrow. Because temperatures in flight had not dropped below the 777's designed operating parameters, the AAIB recommended Boeing and Rolls-Royce take interim measures on Trent 800 powered 777s to reduce the risk of ice restricting fuel delivery, and that European and American regulatory authorities consider the risks to similar aircraft and review their certification criteria accordingly.

In early 2009, Boeing sent an update to aircraft operators, identifying the problem as specific to the Rolls-Royce engine oil-fuel flow heat exchangers. Other aircraft, or Boeing 777 aircraft powered by GE or Pratt and Whitney engines, are not affected by the problem [19].

To date there is no in-situ water contamination detection system in place in any commercial aircraft. The current way to rid the fuel tanks of water is to periodically drain them during scheduled maintenance. Following on from the fuel level measurement, and expanding the on IW project remit, the work in this section looks at the feasibility of using a LPFG to detect free water in fuel.

5.6.1 Experimental arrangement and procedure

The technique used in this section is based upon measuring the minimum transmission value. The experimental arrangement is depicted in Figure 5.12.

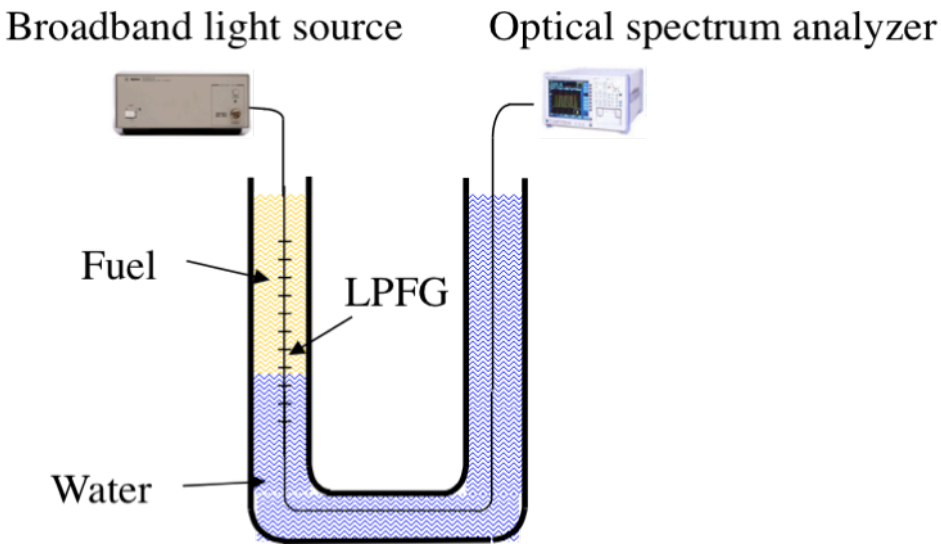

Figure 5.12 Experimental arrangement for detecting free water in fuel

In principle, the experimental procedure is the same as with the fuel level sensor. In this case, the LPFG is initially fully immersed in fuel, and then water is added to the vacant arm of the u-tube, thus increasing the amount of water that covers the LPFG. As described earlier, the result is the formation of two separate LPFGs. One LPFG will have an effective length equal to that covered by fuel (which has a RI of 1.44), and another LPFG with an effective length equal to that covered by water (which has a RI of 1.33). Theory discussed in Chapter 2 describes how the minimum transmission value for a given attenuation band is dependant upon the LPFG length.

Figure 5.13 is a plot depicting the change the respective transmission bands as water is added to fuel.

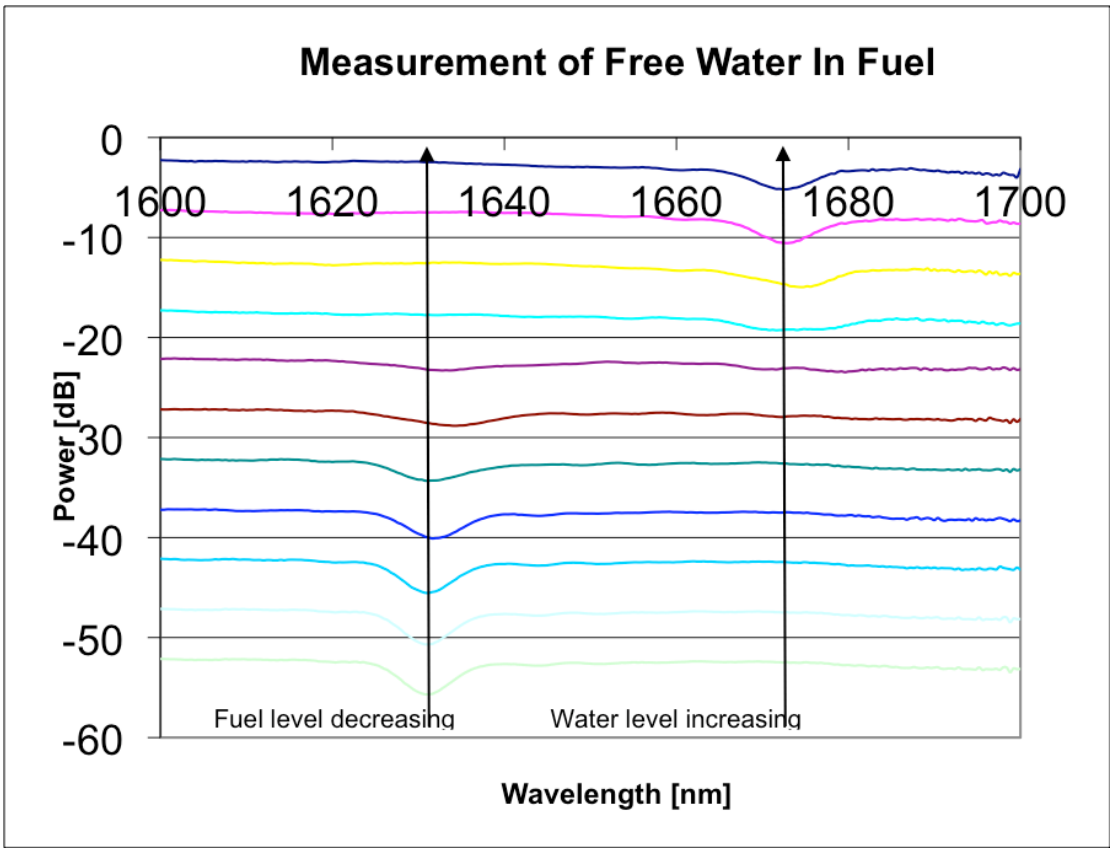

Figure 5.13 Measurement of the addition of water to fuel

As previously stated, initially the LPFG was completely immersed in fuel, and subsequently water added to the vacant arm of the u-tube in 1 cm intervals, and a trace capture was taken at each interval. This was repeated to the point where the LPFG was completely immersed in water. From Figure 5.13, the two characteristic peaks are clearly evident and varying in minimum transmission value as the ratio of water and fuel changes. The characteristic attenuation band for fuel is centered at ~1631 nm and the characteristic peak for water is centered at ~1673 nm. As expected, as the water level increased, the minimum transmission value of the characteristic fuel peak began to decrease in strength, whilst the characteristic water peak began to grow at the higher wavelength.

Figure 5.14 is a plot of minimum transmission value for both the fuel peak (magenta) and water peak (blue) as the water level is increased.

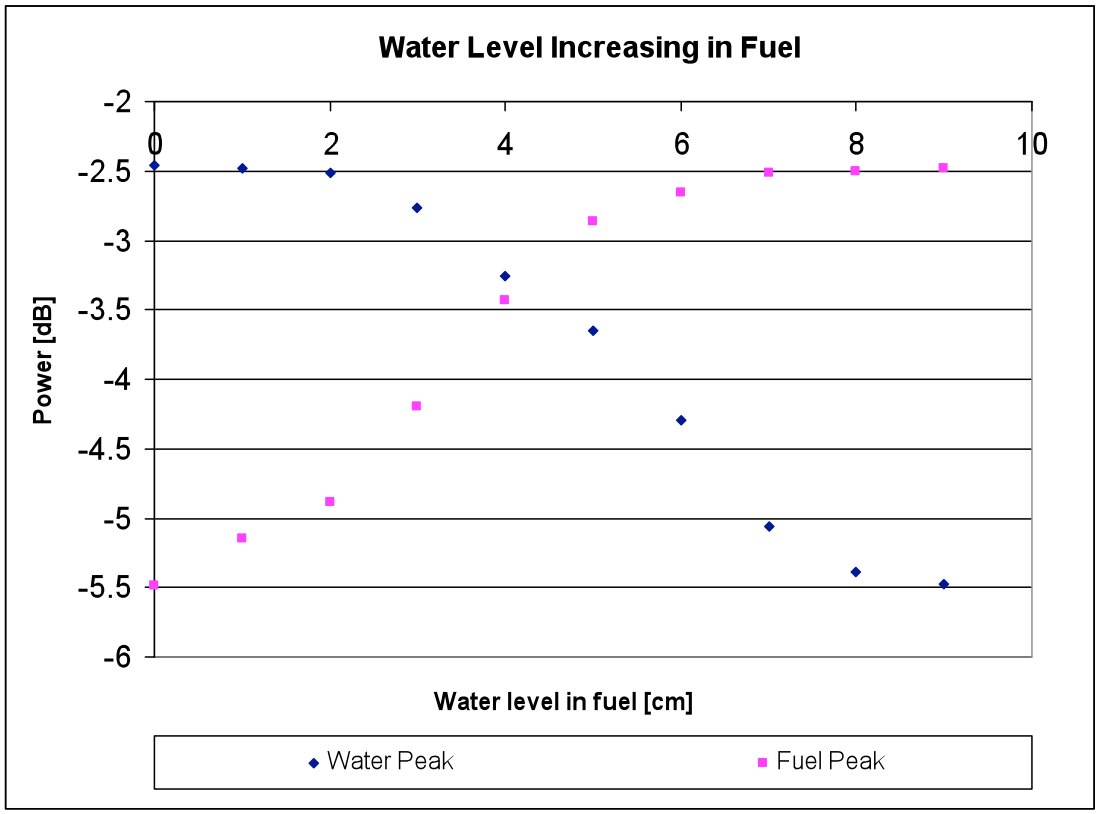

Figure 5.14 Traces of decreasing fuel level and increasing water level as a function of minimum transmission value

As can be seen from Figure 5.14, on both the water and fuel peak, there is a non-linear region in the -2.5 dB loss region. It is hypothesised that in fact at this point the LPFG completely immersed in fuel and therefore not depicting any further wavelength shift. One of the limitations of the experimental procedure is that liquid level is read manually, and the practical set-up made it difficult to obtain accurate depth measurements. Like with the experiments performed in Chapter 4, these experiments would benefit from the use of a laser range finder to determine, with far greater accuracy, the actual liquid depth.

For practical implementation, either one or both characteristic peaks could be illuminated by means of a surface-emitting LED (SLED) and photodetectors could be employed to detect the transmitted power. The amount of water in the fuel could then be determined by the measurement of one characteristic peak, or the ratiometric response of both characteristic peaks.

5.6.1.1 Free water in fuel cyclic testing

Like the fuel level sensing application, to analyse the repeatability of this system, cyclic testing was conducted to observe the sensor response over a number of cycles. 5 cycles

were performed, the results are presented in Figures 5.15a and 5.15b. Figure 5.15a shows how the power of the fuel peak at ~1373 nm reduces in strength as the water level is increased, oppositely Figure 5.15b shows the power of the water peak at ~1631 nm increase as water level is increased. Figures 5.15a and 5.15b demonstrate the system has good repeatability over the complete range when undergoing cyclic testing. Like the fuel level results, the difference between each of the five cycles is mainly attributed to reading error of the fuel/water level.

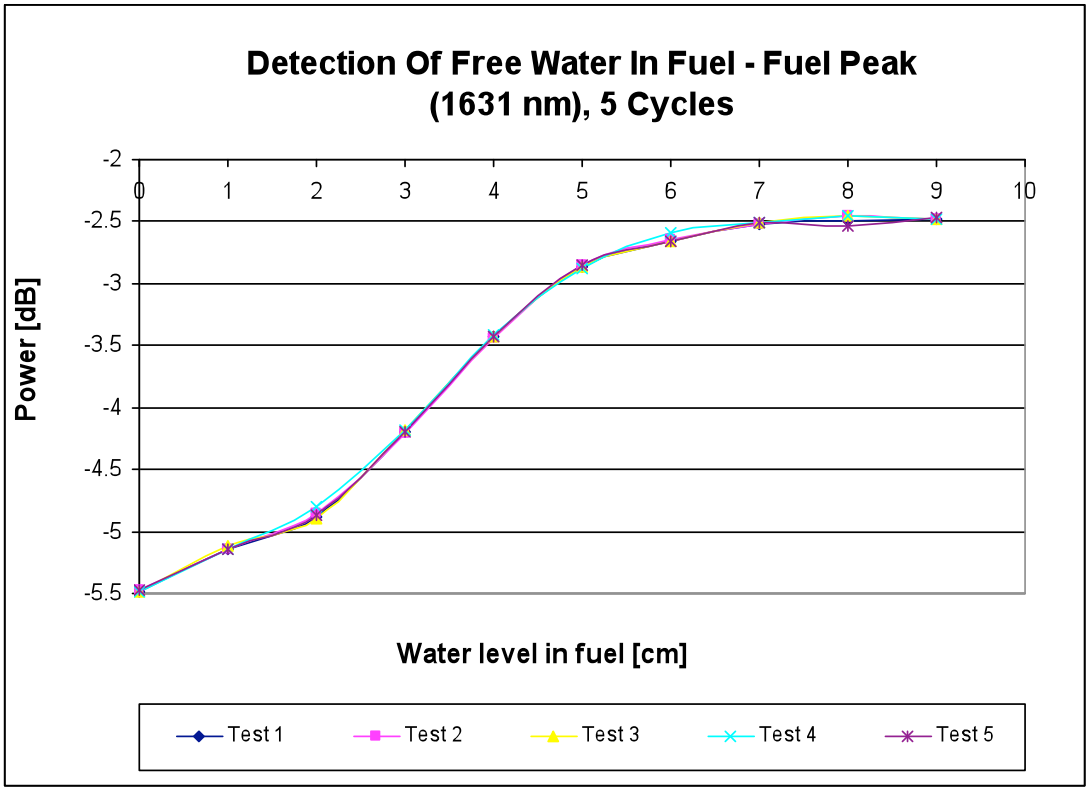

Figure 5.15a Result of the characteristic fuel peak as water level increases

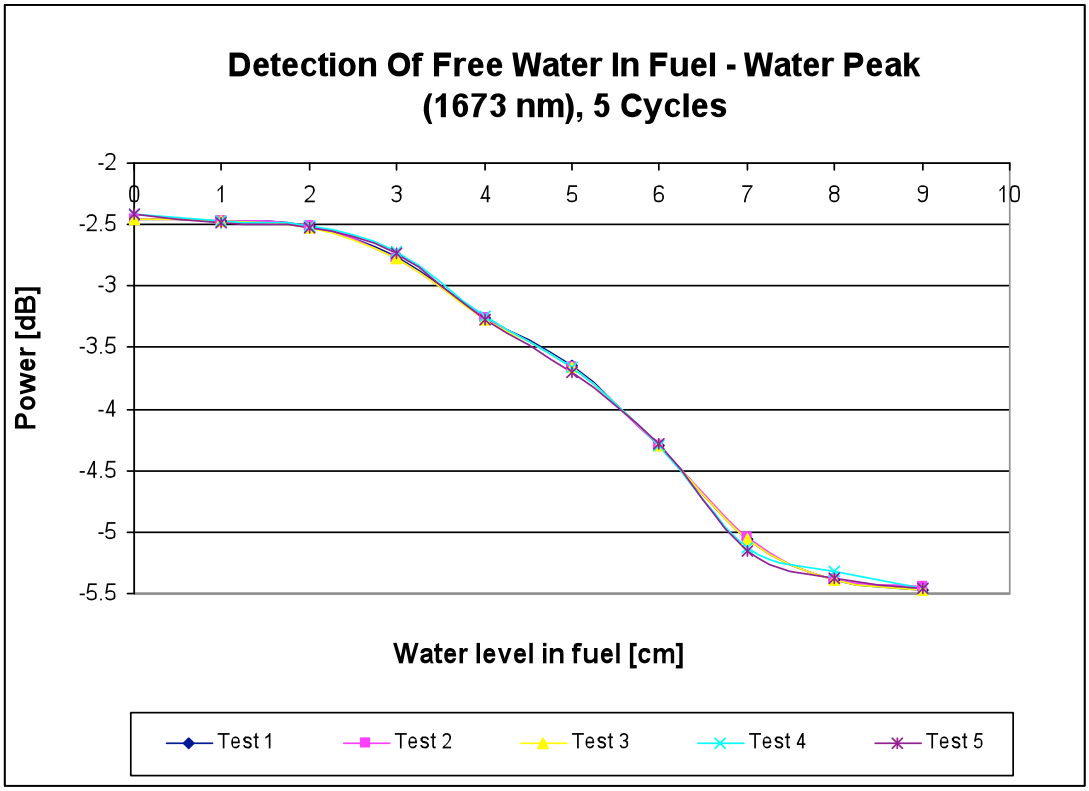

Figure 5.15b Result of the characteristic water peak as water level increases

5.7 Optiwave IFO_Grating 4.0 simulations

After completing the practical experimental work, it was deemed prudent to attempt to replicate the experiments. There are a number of reported techniques for modelling LPFGs, [20]–[22], to name a few. Despite these reported techniques, it was decided to use the simulation package known as Optiwave IFO_Grating 4.0. This simulation tool allows an LPFG to be simulated by defining the key parameters of both the transmission medium i.e. the fibre, the surrounding medium and the LPFG itself.

Fatale *et al* [23] has previously reported that IFO_Grating software can simulate effectively a single LPFG by cascading two separate LPFGs of varying parameters. In said article, two LPFGs were simulated in a cascaded effect to form a Phase-Shifted LPFG. It is this technique that was employed to simulate the effect of a LPFG exposed to varying surrounding RI values of varying length, attributed to the LPFG being progressively immersed.

The experimental LPFGs were of 10 cm in length and had a periodicity of 1 mm. These parameters were therefore used in the IFO_Grating, as were the defined RI values of

1.4512 and 1.4440 for the fibre core and cladding respectively. Also simulated were the physical dimensions of the fibre and surrounding medium, with the fibre core, fibre cladding and surrounding medium radii values of 4.15 μm, 58.35 μm and 10 μm being used respectively. As the LPFG was immersed in aviation fuel, RI values of 1 and 1.44 were used to simulate the surrounding RI of air and fuel respectively, and the length of the two cascaded LPFGs, L1 and L2 were altered to match the immersion depth. An example would be to consider the LPFG immersed 2 cm into the fuel. To simulate this response, LPFG_A would have the surrounding RI set to 1, and have a length of 8 cm. LPFG_B would have the surrounding RI set to 1.44, and have a length of 2 cm.

5.7.1 Simulation results obtained from simulating the uncoated LPFG (LPFG 3)

As with the experimental LPFG, the simulation produced a LPFG with four distinct couplings, at 1370 nm, 1415 nm, 1445 nm and 1570 nm. The results of each coupling is illustrated in Figure 5.16a-d

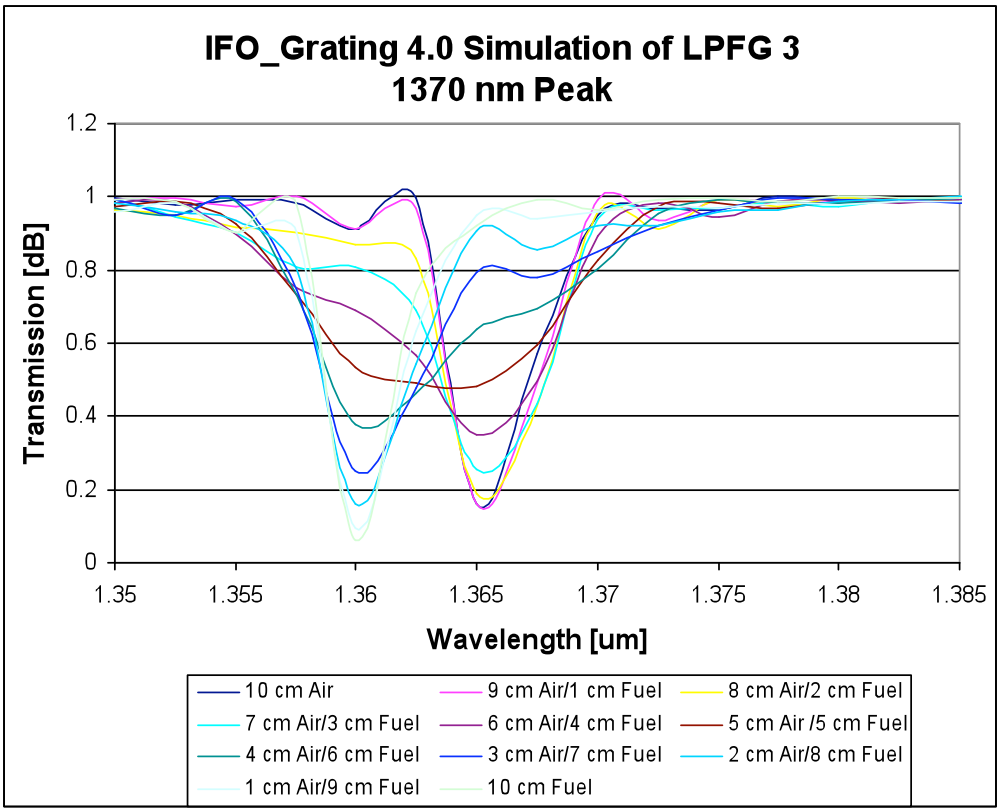

Figure 5.16a IFO simulation of the 1370 nm peak

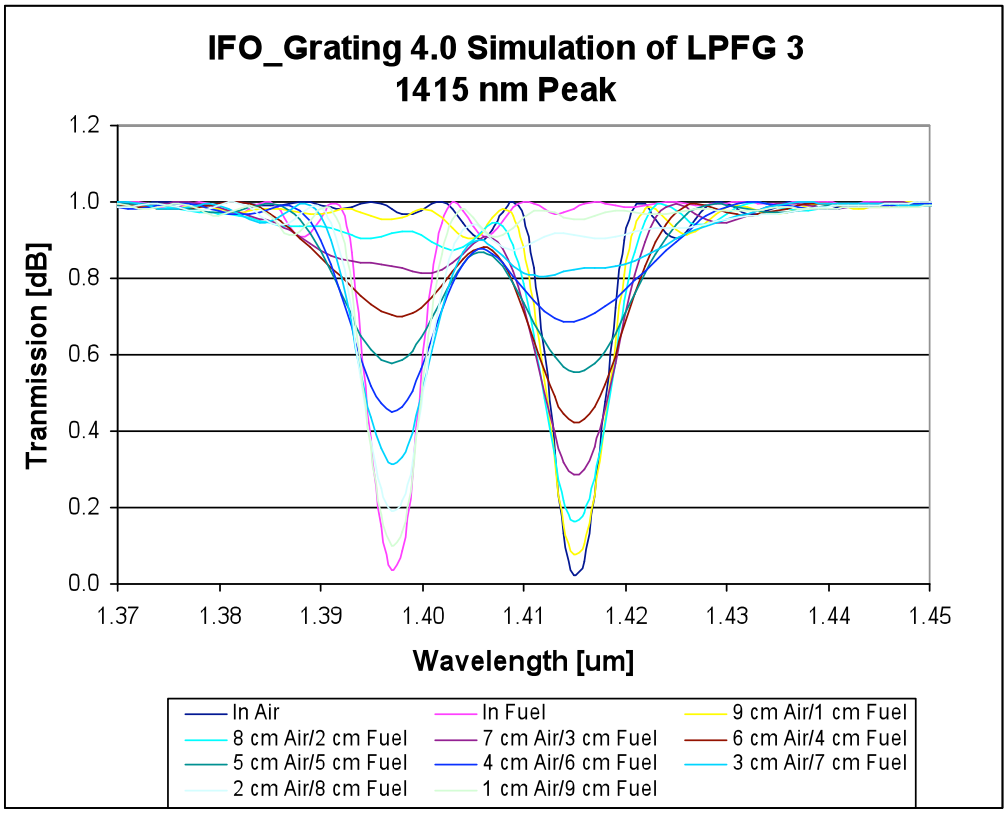

Figure 5.16b IFO simulation of the 1415 nm peak

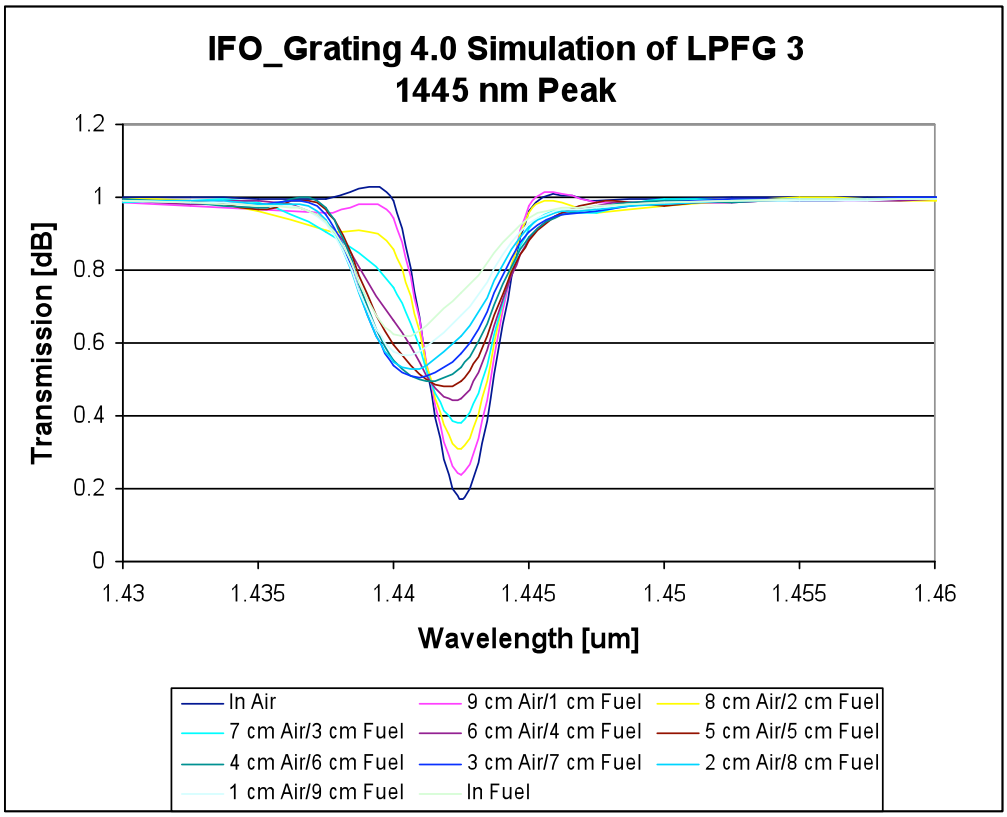

Figure 5.16c IFO simulation of the 1445 nm peak

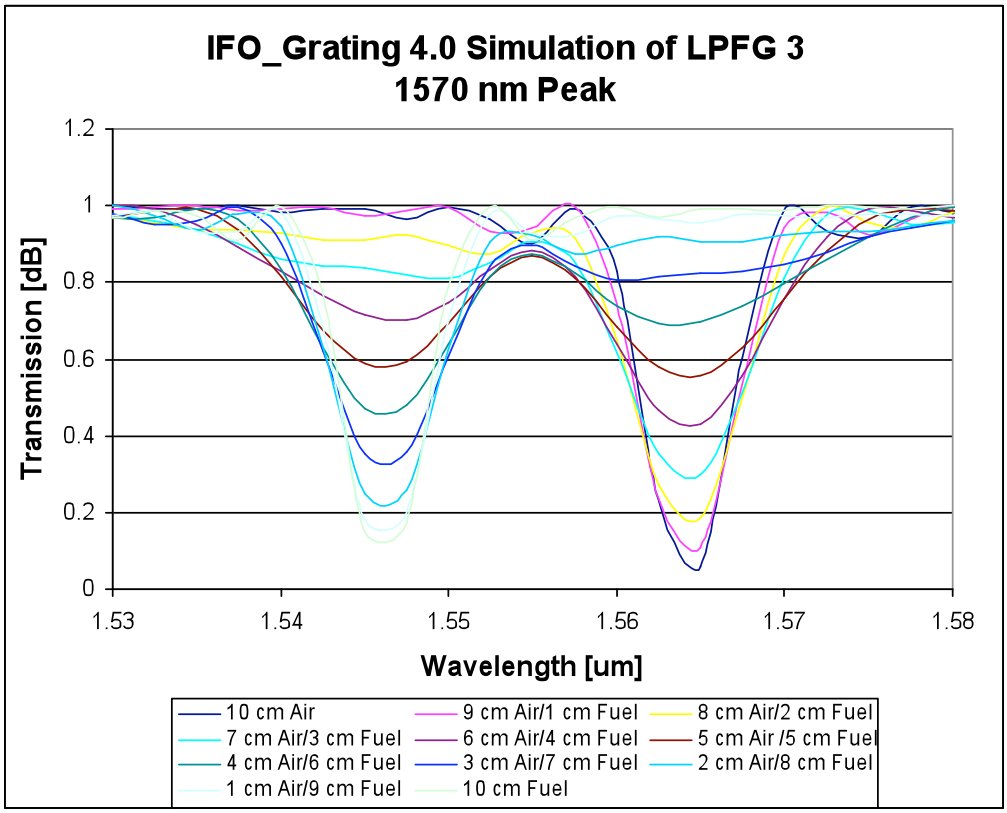

Figure 5.16d IFO simulation of the 1570 nm peak

Analysis of LPFG 3 focussed on the peak at 1414 nm, as this peak exhibited the continuous linear shift as the LPFG was progressively immersed in fuel. Whilst the three other core/cladding couplings yielded variations in the transmission value on peak loss central wavelength, it was only the loss band at 1414 nm that exhibited the aforementioned continuous shift. As can be seen from Figure 5.16b, the continuous shift is not present. Rather the effect that is seen is that of only variations associated with the minimum transmission. That being said, the absolute wavelength of the peak and the magnitude of the relative wavelength shift do correspond to the experimental results.

Experimentally, fully in air the central wavelength of the loss band was 1413.2 nm and fully in fuel the central wavelength reduced to 1403.2 nm. This gives an experimental shift of 10 nm. In the IFO_Grating simulations, the central wavelength of the loss band in air 1412.4 nm, reducing to 1399.2 nm when simulating the LPFG being fully immersed in fuel. This gives a simulation shift of 13.2 nm

Considering an alternative simulation peak, when comparing the simulations with the experimental results obtained from testing LPFG 3, the peak that most replicates the

resonant blue wavelength shift is the 1445 nm peak shown in Figure 5.16c. Here it can be seen that as the fuel level is increased in the simulation, the strength of the attenuation band decreases, and a blue shift is exhibited. Both traits are also seen in the experimental results obtained from testing LPFG 3. However, there are some discrepancies. Firstly, in the experimental result, when the LPFG is immersed fully in fuel, the strength of the attenuation peak grows back to a strength similar to its strength when in air. Theory discussed on the minimum transmission value in Chapter 2 illustrates that this in fact should occur. However, in the case of the simulation, clearly the strength of the peak when fully immersed in fuel is far weaker than that of the peak fully in air. Secondly, the magnitude of the wavelength shift in the practical experiment was 10 nm, in the simulation the shift was ~ 2 nm.

There are a number of factors that may result in the error between the experimental and simulated values and trends. These include, but are not exclusive to:

- The physical characteristics of the experimental LPFG may vary slightly from the exact simulated values owing to fabrication error, parameters including period, length and strength
- The physical fibre values such as the core RI and radius and cladding RI and radius may differ from the simulated values used
- The RI of the fuel may not be exactly 1.44, which was the simulated value used
- The LPFG was placed under a small amount of tension in the fibre-holder, which may have resulted in slight variations of the peak loss wavelengths
- Annealing the LPFG results in a blue shift in the peak loss wavelength. This affect can not be simulated in the IFO_Grating software

Attempts to simulate the TiO_2 coated LPFG using IFO_Grating were unsuccessful. In the IFO software, an extra layer was added between the cladding and the surrounding medium using the values supplied by Dr. Reeta Viitala (coating thickness: 147.6 nm, coating RI: 1.96). When running the software, no attenuation bands were present on the spectrum, suggesting that no cladding mode couplings were simulated. It is hypothesised that this is a software limitation.

5.7.2 Simulation results of free water in fuel

The method used to simulate free water in fuel was identical to the method used above for air and fuel. In this case, two cascaded LPFGs were simulated, this time one with an RI of 1.44 (fuel) and the other with an RI of 1.33 (water). Initially the LPFG was simulated to be completely immersed in fuel, followed by the simulated addition of water in 1 cm increments to the condition where the LPFG was fully immersed in water.

Figure 5.17 illustrates the result of simulating free water in fuel.

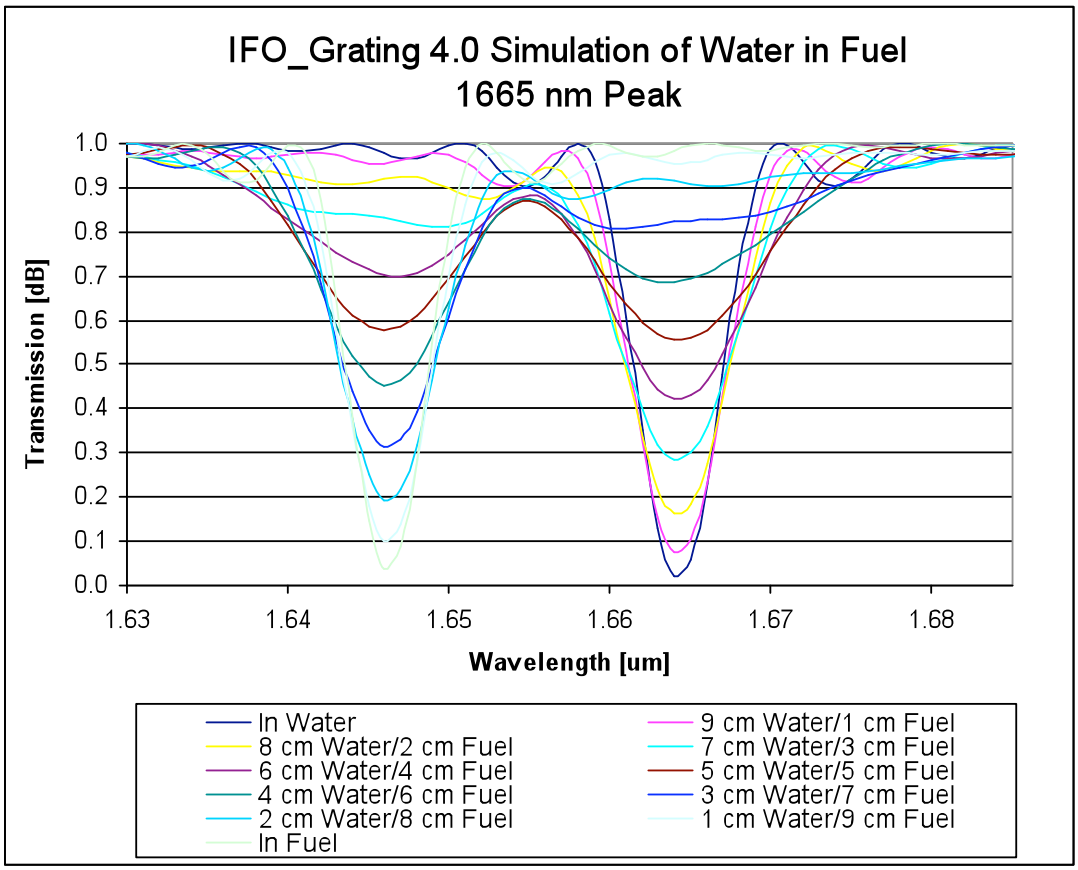

Figure 5.17 IFO simulation of free water in fuel

Though the wavelengths of the peaks are different in the simulation when compared to the experimental result, in this case the trend of the fuel attenuation peak reducing in strength as water is added, whilst the water attenuation peak grows replicates the experimental result.

For the experimental result, the fuel and water peaks were at 1673 nm and 1631 nm respectively. The simulated fuel and water peaks were at 1664 nm and 1645 nm. Though the size of the shift between the peaks are different, 42 nm experimentally, 19 nm in the

simulation, this difference could be attributed to one or more of the reason listed earlier in this section.

5.8 Chapter Conclusions

This chapter began by providing an overview of where LPFGs have previously been deployed as sensors based on their sensitivity to changes of the external medium. It is obvious that such sensor types hold considerable promise for level sensing applications beyond those in aircraft fuel tanks.

Results from the initial fuel level testing using the uncoated LPFG were presented and discussed showing that a sensitivity of 1000 pm/cm was achievable with a 10 cm LPFG having a periodicity of 1 mm. The chapter has also presented the reasoning for coating a LPFG, specifically with TiO_2. The practical results, showing the increased sensitivity over its uncoated counterpart have also been presented. The TiO_2 coated LPFG, which was of the same length and periodicity as the uncoated LPFG, produced a sensitivity of 1240 pm/cm, which is a 24% increase in overall wavelength shift compared to the uncoated LPFG. It also showed both sensors showed good linearity over the entire measurement region.

An introduction to fuel adulteration by the presence of water was introduced. Following on, a novel technique for the measurement of free water in fuel based on monitoring the minimum transmission value was also presented and discussed. It illustrated how for a given coupled mode, two distinct attenuation bands were evident on the transmission spectrum; one attributed to the LPFG immersed in fuel, and the other to the LPFG immersed in water.

As a single LPFG sensing element can measure multiple parameters, it is feasible that further investigation could produce a design for a single sensor element that could measure fuel level, temperature and free water in fuel. Such as system is highly likely to be an attractive alternative to the electrical (capacitance) counterparts currently deployed in the Airbus family of aircraft.

However, it is clear that the deployment of such a sensor in an aircraft fuel tank environment will require a concerted effort to appropriately engineer and package the sensor to ensure its survivability under the harsh conditions.

5.9 Future Work

There is still a significant amount of work to be done in this area before a practical sensor is ready for implementation into a live aircraft environment. This section will briefly highlight some of the areas for possible future work.

- Whilst TiO_2 has proved to be advantageous in numerous areas such as increased sensitivity and the reduction of bacterial adhesion, other coatings should be explored. One such issue that may arise in-flight as the fuel becomes more "waxy" due to low temperatures is fuel retention on the glass fibre. Should this occur, it would provide a false reading. Therefore it maybe possible to coat the fibre with a material that reduces surface tension. Work by Regan *et al* has already demonstrated that Teflon coated fibre has numerous advantages, including the increase in sensitivity [24]. Whilst it has not been specifically reported that Teflon coated fibre would reduce liquid retention on the fibre due to surface tension, the nature of Teflon would lend itself to having this effect

- It would also be prudent to test a wide range of TiO_2 coating thickness and refractive indices in order to determine if the sensitivity can be increased further

- In an aircraft environment, there are a number of factors that would compromise the life of such a sensor. One of the main areas where further work is needed is in the engineering of the system to ensure its survivability in a live aircraft environment to combat against factors such as vibration and free ice floating in the tanks, which would most likely break a freely suspended fibre

- Attempt to more accurately simulate the LPFG responses for air and fuel, and free water in fuel, as well as developing an effective technique for simulating coated LPFGs

Another area of work that has been pursued, though in its infancy, is that of utilising Tilted Fibre Bragg Gratings (TFBGs) as a sensor for measuring liquid level.

For a TFBG with a tilted angle $\delta < 45°$, radiated light is coupled from the forward-propagating core mode into the backward-propagating cladding modes [25]. The technique proposed here is based on measuring the transmission spectrum of the TFBG. For the investigation described in this thesis, the TFBG used was fabricated by exposing SMF-28

fibre to UV irradiation through a phase mask, where the mask was tilted to produce the tilted angle of the photo-induced fringes. The TFBG was suspended between two fixed points and was gradually immersed in water. The transmission spectrum was monitored using a broadband light source and an OSA as the water level was varied. Figure 5.18a shows the captured transmission responses of one of the TFBGs with a length of ~14 mm and tilt angle of 9.2° against a varying water level. From Figure 5.18a it can be seen that once the TFBG is immersed in water, the original loss bands start to reduce and new loss bands are generated and get stronger as the water level increases. When the TFBG is fully immersed the original loss bands totally disappeared. The peak loss of one of the loss bands (as marked in Figure 5.18a) is plotted against varying water level and shown in Figure 5.18b. The sensor output shows a parabolic response to the varying water level. The main limitations in this experiment is the reading error of the water level, however by studying the fit of the data to the trend line and looking at some theoretical modelling, the measurement resolution could be as good as 15 μm depending on the position on the curve.

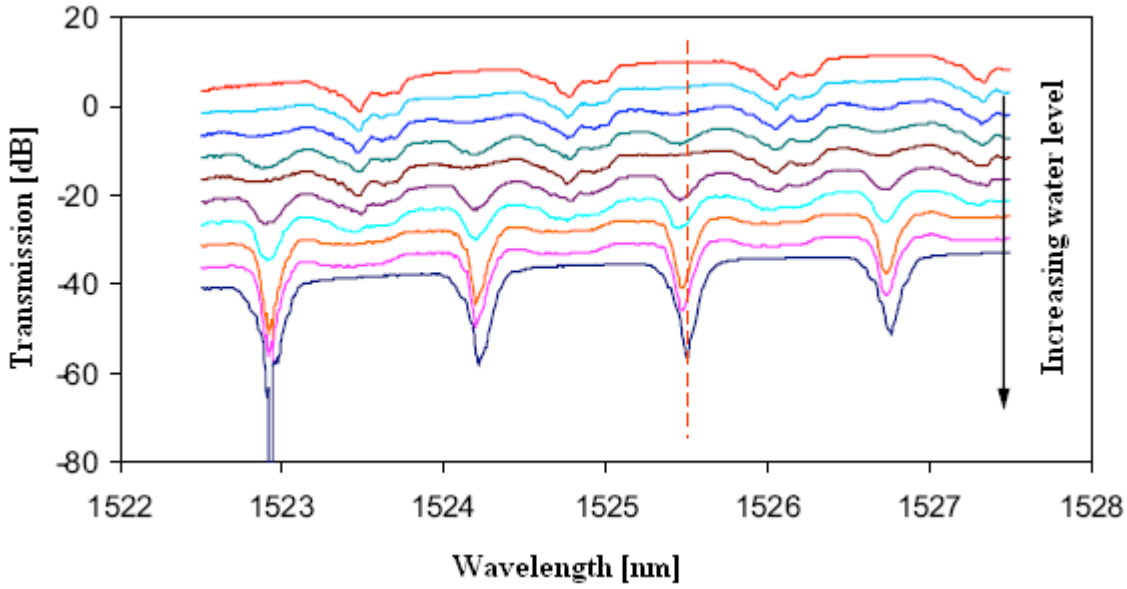

Figure 5.18a TFBG transmission loss as a function of water level

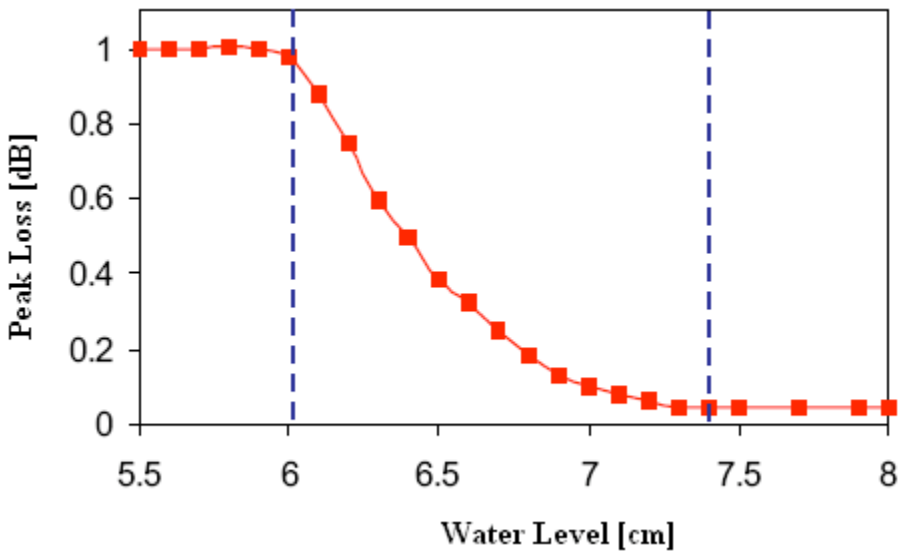

Figure 5.18b Peak loss as a function of water level

In the above result, the two dashed lines indicate the TFBG region. As expected, either side of the dashed line, there is no change in peak strength as the TFBG is not the region of liquid level change.

Like LPFGs, the sensitivity of TFBGs to varying liquid level arises from the fact that the effective refractive index of a cladding mode is dependent on the RI of the surrounding medium. When the external RI varies, the phase matching condition of the TFBG changes giving rise to the spectral change in TFBG loss band. TFBGs with smaller or larger tilted angles show similar responses to varying liquid level. For a liquid with larger RI (but less than the RI of the cladding) the sensor will show a larger responsivity thus higher resolution. By simply assigning a laser diode to one of the loss band peaks one can monitor the liquid level change. The low thermal sensitivity of the TFBG [25], especially when compared to LPFGs, offers simplicity and reliability for accurate liquid level measurement in hazardous environments.

As stated earlier, the TFBG stage was not progressed beyond proof-of-concept. To further explore TFBGs as a means of level sensing, the author suggests that a wide range of tilt angles δ, and grating strengths, should be tested to find the combination which gives maximum sensitivity. Beyond this, the issues of survivability exist for TFBGs as they do with LPFGs. Therefore the future work suggestions listed earlier section for LPFGs regarding survivability in an aircraft fuel tank must also be considered valid for TFBGs.

5.10 Chapter References

[1] D. A. Jackson, "*High precision remote liquid level measurement using a combination of optical radar and optical fibers*" in Proc. First Int. IEE Con. Optical Fiber Sensors (London, England), vol. 221, pp. 100-103, 1983

[2] T. Guo, "*Temperature-insensitive fiber Bragg grating liquid-level sensor based on bending cantilever beam*", IEEE Photon. Technology Letters, vol. 17, pp. 2400–2402, 2005

[3] S. Khaliq, S. W. James, and R. P. Tatam, "*Fiber-optic liquid-level sensor using a long-period grating*", Optics Letters, vol. 26, pp. 1224-1226, 2001

[4] S. Grice, W. Zhang, K. Sugden and I. Bennion, "*Liquid level sensor utilising a long period fibre grating*" Proceedings of SPIE, vol. 7212, 2009

[5] H. Patrick, A. D. Kersey and F. Bucholtz, "*Analysis of the Response of Long Period Fiber Gratings to External Index of Refraction*", Journal of Lightwave Technology, vol. 16, pp. 1606-1642, 1998

[6] V. I. Kopp, V. M. Churikov, G. Zhang, J. Singer, C. W. Draper, N. Chao, D. Neugroschl and A. Z. Genack, "*Single- and double-helix chiral fiber sensors*", Journal of the Optical Society of America, vol. 24, pp. 48-52, 2007

[7] X. Shu and D. Huang, "*Highly sensitive chemical sensor based on the measurement of the separation of dual resonant peaks in a 100μm period fibre grating*", Optical Communications, vol. 17, pp. 65-69, 1999

[8] T. Allsop, L. Zhang and I. Bennion, "*Detection of organic compounds by a long period fibre grating optical sensor with optimized sensitivity*", Optical Communications, vol. 191, pp. 181-190, 2001

[9] R. Falciai, A. G. Mignani and A. Vannini, "*Long period gratings as solution concentration sensors*", Sensors Actuators, vol. B74, pp. 74-77, 2001

[10] S. Yin, K. W. Chung and X. Zhu, "*A novel all-optic tunable long period grating using a unique double cladding layer*", Optical Communications, vol. 196, pp. 181-186, 2001

[11] Y. Liu, L. Zhang, J. A. R. Williams and I. Bennion, "*Bend sensing by measuring the resonance splitting of long-period fiber gratings*", Optics Communications, vol. 193, pp. 69-72, 2001

[12] R. Falate, M. Müller, J. L. Fabris and H. J. Kalinowski, "*Long Period Gratings in Standard Telecommunication Optical Fibers for Fuel Quality Control*", Annals of Optics, vol. 5, 2003

[13] Web address: www.agilent.co.uk. Accessed March 2009

[14] A. A. Gorbushina and K. A. Palinska, "*Biodeteriorative processes on glass: experimental proof of the role of fungi and cyanobacteria*", Aerobiologia, vol. 15, pp. 183-191, 1999

[15] B. Li and B. E. Logan, "*The impact of ultraviolet light on bacterial adhesion to glass and metal-oxide coated surfaces*", Colloids and Surfaces B: Biointerfaces, vol. 14, pp. 153-161, 2005

[16] E. Davies, R. Viitala, M. Salomäki, S. Areva, L. Zhang and I. Bennion, "*Sol-gel derived coating applied to long-period gratings for enhanced refractive index sensing properties*", Journal of Applied Optics, vol. 11, 2009

[17] D. R. Lide, "*CRC Handbook of Chemistry and Physics*", 81st edition, ISBN-13: 978-0849304811, CRC Press, 2000

[18] C. J. Brinker and G. W. Scherer, "*Sol-gel science*", Academic Press, San Diego, USA, 1990

[19] AAIB, "*AAIB Interim Report 2: Accident to Boeing 777-236ER, G-YMMM at London Heathrow Airport on 17 January 2009*", Department for Transport, 2009

[20] T. Erdogan, "*Fibre Grating Spectra*", Journal of Lightwave Technology, vol. 15, pp. 1277-1294, 1997

[21] R. Kashyap, "*Fiber Bragg Gratings*", Optics and Photonics, Academic Press, San Diego, 1999

[22] A. Othonos, K. Kalli, "*Fiber Bragg Gratings: Fundamentals and Applications in Telecommunications*", Artech House Inc, Boston, 1999

[23] R. Fatale, O. Frazao, G. Rego, O. V. Ivanov, H. J Kalinowski, J. L. Fabris and J. L. Santos, "*Bending sensitivity dependant on the phase shift imprinted in long-period gratings*", Measurement Science and Technology, vol. 18, pp. 2132-3130, 2007

[24] F. Regan, B. D. MacCraith, J. E. Walsh, K. O. Dwyer, J. G. Vos and M. Meaney, "*Novel Teflon-coated optical fibres for TCE determination using FTIR spectroscopy*", Vibrational Spectroscopy, vol. 14, pp. 239-246, 1997

[25] K. Zhou, L. Zhang, X. Chen and I. Bennion, "*Low thermal sensitivity grating devices based on ex-45° tilting structure capable of forward-propagating cladding modes coupling*", Journal of Lightwave Technology, vol. 24, pp. 5087-5094, 2006

6 Thesis Conclusions

This thesis has presented novel sensing solutions for both industrial weighing and aerospace applications. In both applications, the results presented in this thesis have shown that Bragg grating based sensors, be they FBG or LPFG, yield high enough sensitivities to make them viable options as replacements for current their electrical and/or mechanical counterparts.

6.1 Industrial Weighing

The work presented in this thesis based on industrial weighing has described the design and implementation of FBG interrogation techniques for both static and dynamic weighing equipment. At the very beginning of this project Avery Weigh-Tronix expressed a strong desire to, where possible, integrate this technology into their current systems. The purpose of this was to enable Avery to, in effect, "test the water" with the technology whilst remaining comfortably familiar with the overall system.

For static loading, the research focussed on implementing FBG sensors into Avery's FX220 system. However before pursuing this, the technology was demonstrated to Avery by an initial 'proof of concept' experiment in which a cantilever-based system was designed and fabricated. Not only did these proof of concept experiments give an insight into the achievable sensitivity of FBG sensors, it also gave the engineers at Avery a first glimpse of the technology in operation. The experiments were conducted in a temperature-controlled environment using the Insensys FSI as a means of interrogating the sensor. The results obtained from the proof of concept experiments proved highly encouraging, with a sensitivity in the region of 111 pm/kg being achieved. Not only did these initial experiments exhibit good sensitivity, they also demonstrated high linearity and repeatability over a series of cyclic tests.

This initial series of experiments led to the implementation of a FBG sensor into an Avery Weigh-Tronix FX220 top-pan based weighing system. After considering numerous options as to how the FBG sensor should be integrated, it was decided to modify the T702 vibrating beam from the FX220 system. A T702 beam was sent to RPS engineering where a 200 μm V-groove was milled along the centre beam. On its return, the FBG was bonded into this groove using Avery's standard electrical strain gauge bonding adhesive, Micromeasurements 610 epoxy. As with the proof of concept series of experiments, this

series of tests was also conducted in a temperature-controlled environment. The initial load of 15 kg was applied to determine the sensitivity of the system, which proved to be in the region of 41.3 pm/kg. The follow-up cyclic tests again showed the system to be highly linear, and repeatable over a number of cycles. It is of paramount importance in industrial weighing applications that the induced strain is independent of position, which basically means it does not matter where the load is positioned on the weighing pan, the same load is measured. Positional testing was performed to determine if the FBG induced different magnitudes of wavelength shift if a constant load was positioned on different locations around the pan. The results clearly showed that the sensor measures the same wavelength shift no matter where the load is placed.

One of the most encouraging aspects to arise from these experiments is that Avery's product range is scalable. Basically the weighbridge system used for measuring the axle loads for large vehicles is, in effect, a larger version of their desktop scale system (albeit more complex). Therefore there is no reason why FBG technology cannot be further developed and implemented into any of Avery's static loading markets.

Not only were Avery interested in static loading; they were also interested in dynamic loading applications. Based on the fact that some of Avery's competitors were already investing in rail WIM technology using FBG sensors and backed up by findings from early market research, it was decided rail WIM should be the application to be investigated.

The system consisted of a full-scale piece of treated railway track. Two configurations of e-glass sensing patches were designed, and subsequently manufactured by Insensys. These patches were then bonded to a pre-treated area of the track using a Cyanoacrylate gel and activator. Loads were then applied by means of a manually controlled hydraulic loading jack. As with the static tests, the experiments were conducted in a temperature-controlled environment, and all components of the experiment were allowed to "soak" prior to conducting the tests.

Whilst the single patch exhibited a relatively low sensitivity (in the region of 0.0078 – 0.0081 pm/kg), the result was not surprising as the patch was bonded horizontally along the neutral axis of the rail. This was unfortunate, but unavoidable, as there was only a small area of the track where the patch could be bonded. The double FGB patch, which housed two FBGs positioned at ± 45° induced a much larger shift. The initial test yielded a total combined wavelength shift of 511 pm, which corresponds to a sensitivity in the

region 25.44 kg/pm. Subsequent testing showed this system to be highly linear and cyclic testing demonstrated good repeatability.

Whilst it would have been advantageous to take this system to live/active rail track to obtain real time dynamic results, no facility was available to conduct any such testing.

6.2 Fuel level sensing

The desire to remove any electrical source from within an aircraft's fuel tank was the driving force behind the aerospace related work presented in this thesis. Two novel grating based approaches were investigated, these were:

- A diaphragm-based system incorporating a single FBG or multiple FBGs, which measured hydrostatic pressure variations
- A LPFG sensor, based on measuring the change in the surrounding RI

Numerous configurations for the diaphragm-based system were tested. Initially, an aluminium gasket was designed which incorporated a steel diaphragm, to which a FBG was centrally bonded. The initial proof of concept experiments involved testing a series of steel diaphragms, each of different thickness to determine their sensitivities. Three diaphragms in total were tested. The thinnest of the three (0.2 mm) exhibited the highest sensitivity (22.924 pm/cm), however significant nonlinearity was present in the result. The thickest of the three (0.6 mm) was highly linear, however the sensitivity was reduced considerably (1.049 pm/cm). It was the medium thickness diaphragm (0.4 mm), which produced the most encouraging result. Whilst the result was highly linear, the sensitivity was markedly improved (9.973 pm/cm) when compared with the thickest diaphragm, which was within the specification set out by the IW project. Further investigation of the 0.4 mm thickness diaphragm demonstrated good repeatability over a series of cyclic tests.

Convinced that this approach was a feasible option, follow-up research focussed on producing an aerospace compliant equivalent. After evaluating a number of materials for both the sensor housing and diaphragm, PPS and Kapton polyimide film were chosen respectively.

The experimental set-up and procedure was identical to that of the proof of concept series of tests. The sensitivity of the PPS/Kapton polyimide film system was approximately 7.442 pm/cm over the 45 cm depth range. Whilst this sensitivity is reduced when compared to

the aluminium/steel system, it must be noted that the diameter of the Kapton diaphragm was considerably less than the steel diaphragm. Despite Kapton possessing a lower Young's modulus than steel, it is believed that the smaller diameter of the Kapton diaphragm combined with the epoxy used to bond the Kapton sheets together added considerable rigidity, accounting for the reduced sensitivity. Increasing the diameter of the PPS gasket and Kapton polyimide would further increase the systems' sensitivity.

Whilst the above series of tests proved successful and work will be pursued beyond this thesis, an alternative approach was also investigated.

Novel work was presented pertaining to the investigation of a multi-FBG based system, where sensors were deployed at discrete points along an aluminium sensing tube. To enable a direct swap of technologies it is desirable in some ways for the optical system to be physically similar to the current capacitance based electrical system. The multi-FBG tube system goes some way to fulfilling this.

The advantages of this system were that as well as adding system redundancy in the event of FBG failure; the system could operate as both a continuous and discrete level sensor. Although the concept is sound, the issue of the differing sensitivities arising from the experimental results is most likely to be attributed to the lack of control during the bonding process, in terms of both sensor positioning and the amount of epoxy used. Ideally, all three sensors would have been positioned in identical positions of their respective holes, using a constant amount of epoxy being deposited at an exact location along the fibre. Although the proof of concept experiments has shown this approach is also a viable option, an aerospace compliant variant was not fabricated due to the fact that unless the sensor bonding process can be controlled, the same discrepancies between sensor sensitivities would be measured.

The alternative novel approach discussed was based on monitoring the wavelength shift of a specific attenuation band on the transmission spectrum of a LPFG. The concept arises from the fact that a LPFG is sensitive to variations of the surrounding RI. The initial proof of concept experiments involved suspending the 10 cm, 1 mm period LPFG within the glass u-tube and varying the level of fuel within the u-tube. A distinct blue shift on the attenuation band was clearly observed on the OSA, yielding a sensitivity of 1000 pm/cm. The response over the complete measurement range was highly linear. When compared to the diaphragm system, the sensitivity of the LPFG system is considerably higher.

Subsequent cyclic testing demonstrated the system was also highly repeatable. The fact this system was not temperature compensated, combined with the fact that surface tension may retain small amounts of fuel on the fibre surface may explain the slight variations in the wavelength values obtained for specific fuel depths during cyclic testing.

Past research has shown that TiO_2 has been used to reduce bacterial adhesion, which causes damage in the form of glass pitting. Coating a LPFG with TiO_2 with a high RI value has also been shown to increase sensitivity of a LPFG sensor due to the effective refractive index of the cladding being modified. LPFGs fabricated within the group were sent to Dr Reeta Viitala for TiO_2 coating using a dip-coating technique, which controls the thickness and surface quality of the coating. Testing of the TiO_2 coated sensor produced a sensitivity of 1240 pm/cm. When compared with the uncoated sensor, the sensitivity of the coated sensor is 24% greater.

Another novel aspect pertaining to the LPFG based system was the detection of free water in fuel. By monitoring the attenuation values of the characteristic peaks for a specific mode coupling, the amount of water covering the LPFG can be determined. Given that water is the most significant cause of fuel adulteration, possessing the ability to not only detect the presence of water, but also measure the quantity of water, is a significant advancement in fuel system monitoring technology. At present, no such real-time system exists.

The main issue with the LPFG based system is one of survivability. The operation of such a system is entirely dependant on the interaction between the cladding the surrounding medium. Any packaging solution proposed must ensure than this interaction can still occur. If a suitable packaging solution can be created, the LPFG is another candidate for replacing the current technology.

Bragg grating sensors show substantial promise in areas where large strain ranges, distance or potential explosion hazards make electrical sensors impractical. The work in this thesis has brought the practical realisation of the application of these sensors closer to being considered as viable replacements to their electrical and mechanical counterparts. With marketable applications in mind, the work has taken significant steps forward and resulted in a foundation of knowledge for commercial partners to build on in the future.

7 Publications

[1] S. Grice, W. Zhang, K. Sugden and I. Bennion, "*Liquid level sensor utilising a long period fibre grating*" Proceedings of SPIE, vol. 7212, 2009

[2] W. Zhang, S. Grice, K. Sugden and I. Bennion, "*Tilted Fiber Bragg Grating for Direct Liquid Level Sensing*", Optical Sensing and Metrology, CLEO EUROPE, 2009

[3] W. Zhang, K. Sugden, S. Grice and I. Bennion, "*Liquid level sensing by use of digital formatted optical spectrum spreading technique*", Journal Of The European Optical Society Rapid Publications, vol 4, 2009